

NORTHWESTERN UNIVERSITY

Colloidal matter and the road to trainable materials

A DISSERTATION

SUBMITTED TO THE GRADUATE SCHOOL
IN PARTIAL FULFILLMENT OF THE REQUIREMENTS

for the degree

DOCTOR OF PHILOSOPHY

Field of Materials Science and Engineering

By

Hector Manuel Lopez de la Cerda Rios

EVANSTON, ILLINOIS

October 2024

© Copyright by Hector Manuel Lopez de la Cerda Rios 2024

All Rights Reserved

ABSTRACT

Colloidal matter and the road to trainable materials

Hector Manuel Lopez de la Cerda Rios

The ability to create matter through the manipulation of single atoms remains elusive. This is due to the high energetic cost of manipulating single atoms and the complexity of chemical bonding. Thus the scientific and engineering community has moved towards creating matter using larger subunits that are easier to manipulate and functionalize. These colloidal systems, comprised of nanometer to micrometer sized particles, have been employed to create colloidal materials that have been shown to be analogs to atomic solids and hard condensed matter systems. However, considering how tunable these subunits have become, there is evidence that colloidal matter can be designed to have properties that resemble a sense of trainability, which has been assumed to be exclusive to animate matter. Training in materials consists of tuning a material's response by a cyclic exposure to an external stimulus, each cycle leading to a reconfiguration of its internal degrees of freedom. Exploiting this behavior can lead to a new paradigm for materials design. In this work we focus on the internal degrees of freedom of different colloidal systems to gain an empirical understanding of the requirements needed for trainable synthetic materials.

Acknowledgements

Doing science and being a part of this community is a labor of love. It takes time, patience, and a lot of support, especially when the times become turbulent. These nonlinearities can trap us in dark places, make us feel small, and wildly uncomfortable. I have been so lucky to be surrounded by people who have believed in me and in my dreams. I will always be indebted to them, but most importantly, they will always have in me a friend and a never-ending amount of time and support. I begin by thanking you mum for your unwavering support even when pursuing an undergraduate degree seemed difficult and teaching me that hard work does pay off. I thank you Uncle Salvador Sanchez Roman for believing in me and making it possible for me to study my undergraduate at Mexico's premier institute (UNAM) and teaching me so much about life. Thank you, Annaliese K. Ehlen, this PhD would have been impossible, truly, to finish without your love, support, wit, awesome ggplot skills, critical analysis of colloidal crystals, and the list could go on and on. I am an incredibly happy individual knowing you are my partner and together we will experience what the world has to offer. The union of two individuals is not only that, but of two families. I must say I am a doubly lucky person to have such loving and supporting parent in-laws, Anamary, and Matt Ehlen. They have embraced me like another family member and have made me feel at home no matter where we may be. Thank you, Anamary, and Matt, I can only hope that I have made you feel the same way. Thank you, friends, and family: Nick, Cecile, Abi, Karen, Alberto, Magui, Natalia,

Paola, Zoe, Sophie, for enlightening conversations, support, and love. I hope we may find more time to spend together in the near future!

On the professional side of things, I would not be equally or even more excited about pursuing a career in science than when I entered the PhD program without amazing collaborations and the support of my great advisor, Monica Olvera de la Cruz. Thank you, Monica, for always thinking and caring about your students. There is no doubt that you always put us students first, even when you are always so busy. You somehow always find the time to meet with us even when you are minutes away from heading out to the airport. Thank you, Edward P. Esposito, Shih-Yuan Chen, Michelle M. Driscoll, and Heinrich M. Jaeger, you have made our road towards discovery so intellectually stimulating and rewarding. I can only hope that I may replicate the environment of free thinking and exploration that you have instilled in our collaborations in the future with others.

Thank you all.

Dedication

I dedicate this to all my teachers who taught me to think critically from an early age.

Without you my perspective on life would be incomplete.

Table of Contents

ABSTRACT	3
Acknowledgements	4
Dedication	6
Table of Contents	7
List of Tables	9
List of Figures	11
Chapter 1. Introduction	27
Chapter 2. Self assembly of colloidal crystals using anisotropic particle cores	46
Chapter 3. The nature of colloidal crystal delocalization in a size-asymmetric system	69
Chapter 4. Insulator-to-metal transitions in colloidal crystals	102
Chapter 5. Mechanics of monolayers of superparamagnetic particles	139
Chapter 6. Manipulating the medium to create patterns	165
Chapter 7. Conclusions and Outlook	196

Bibliography	204
Appendix A. Supplementary information for Chapter 3	221
Appendix B. Supplementary information for Chapter 4	231
Appendix C. Supplementary information for Chapter 6	257

List of Tables

3.1	Simulation parameters.	77
4.1	Observed lattices, their properties, and the systems in which they occur.	110
4.2	Simulation parameters.	136
A.1	Temperature of onset of delocalization, melting, and existence of crystal lattices for varying number of small particle chains.	222
B.1	Comparison of potential energy landscape (theory) and interactive nead distribution (simulation) for all observed lattices.	242
C.1	Parameters used in all simulations.	262
C.2	Yukawa type potential parameters used in simulations to produce different microroller heights at $T = 0$ K.	263
C.3	Yukawa type potential parameters used in simulations to produce different passive particle heights at $T = 0$ K.	264
C.4	Yukawa type potential parameters used in simulations to produce different microroller heights at $T = 293$ K.	264

C.5	Yukawa type potential parameters used in simulations to produce different passive particle heights at $T = 293\text{ K}$.	265
-----	--	-----

List of Figures

- 1.1 Different self-assembled colloidal crystals using a bidispersed set of particles of different sizes grafted with hydrocarbon chains. This is adapted from Bodnarchuk et al. [8]. 30
- 1.2 Library of colloidal crystal lattices obtained by varying the geometric properties of the particles and DNA strand length and strength of their grafted DNA chains. This is adapted from Laramy et al. [18]. 33
- 1.3 Size asymmetry matters in DNA self-assembled colloidal crystals. If the particles are of equal size, there is negligible particle diffusion. However, if there is strong size-asymmetry, the smaller particles will hold the colloidal crystal but also diffuse among the larger particles, similar to electrons in a simple metal. This is adapted from Girard et al. [20]. 36
- 1.4 Modified material design paradigm with the inclusion of the concepts from training in materials. Training involves the reconfiguration of a material's internal degrees of freedom. 38
- 1.5 An example of reading out memory embedded in glassy granular matter. By shearing a trained system sequentially and in an increasing manner, a minimum is observed in the mean squared displacement

(MSD) of the particles at the value of $\gamma_{\text{mem}} = 0.06$ in (a) and values $\gamma_{\text{mem}} = \{0.04, 0.06\}$ in (b). The formation of minimum values or memories are reinforced as a product of the number of cycles. This is due to the appearance of steady state particle periodic orbits due to the cyclic oscillatory shearing. These graphs were adapted from Fiocco D. *et al.* [37].

41

2.1 A rod-based seed-mediated synthesis can be used to generate elongated rhombic dodecahedra with tunable ARs. (a) Schematics show a seed-mediated synthesis with a sphere or a rod seed and their resultant products. Green indicates an elongated side facet, and purple indicates a tip facet. (b) Seed AR and different [seed]:[Au³⁺] ratios can be used to tune product AR. The algorithmic analysis of several hundred nanoparticles per sample from transmission electron microscopy (TEM) images can be used to quantitate this relationship. (c) Representative TEM images show seed and product particles that correspond to the colors in the plot in (b). The scale bar represents 100 nm.

51

2.2 Elongated rhombic dodecahedra building blocks crystallized into multiple lattice symmetries. (a) As the AR of building blocks increases, the surface area (and thus number of DNA molecules) on elongated (green) facets increases, while the surface area of the tip (purple) facets remains the same. (b) TEM images show elongated rhombic dodecahedra before functionalization with DNA. From left

to right these particles have a minor edge length and corresponding coefficient of variation (CV) and AR of: 30.4 ± 2.4 nm (8.0% CV) and 1.1; 20.9 ± 1.4 nm (6.6% CV) and 1.6; 22.3 ± 1.2 nm (5.4% CV) and 2.8; 26.2 ± 1.9 nm (7.2% CV) and 4.3; 21.5 ± 2.4 nm (11.3% CV) and 5.0; 16.2 ± 2.4 nm (14.6% CV) and 9.0, as determined by algorithmic analysis of TEM images. The scale bar represents 100 nm and corresponds to all images in (b). For a complete list of synthetic conditions and particle dimensions. (c) Z-contrast TEM images show crystals formed from the elongated rhombic dodecahedra in (b). Images corresponding to ARs of 1.6, 4.3, 5.0, and 9.0 were sectioned (section thicknesses of 200, 400, 400, and 400 nm, respectively) to facilitate imaging. The scale bar represents 100 nm and corresponds to all images in (c). (d) Simulations show crystals of elongated rhombic dodecahedra with ARs that correspond to those in (b, c) (left to right: ARs of 1.15, 1.65, 2.85, 4.5, infinite). Images are cut through particles along the closest-packed plane and include the DNA beads that represent the sticky ends. (e) Indexed SAXS patterns correspond to the crystals in (c). From left to right, patterns index to FCC, pFCC, disordered FCC-like, BCT, mixture of BCT and HP, and HP. (f) Unit cells were determined from the corresponding SAXS patterns and EM images. Transparent unit cell box (gray) indicates a plastic crystal. The color bar indicates the series of phase changes.

2.3 Analysis of the number and location of DNA hybridization events for high AR particles. a Models show the DNA hybridization probability mapped to the particle surface based on simulations initialized in their most stable lattice (FCC, FCC, BCT, BCT, HP lattices, respectively). Each point on the particle represents a bead that may have DNA attached. The darkest color indicates the maximum (0.84) and the lightest color indicates the minimum (0.17) probability that the DNA attached to the bead hybridizes to DNA on an adjacent particle. The color scale corresponds to all models. b Analysis of the average DNA angle with respect to the surface normal vector is shown for an infinite rectangular prism initialized in a square planar (SP) vs. HP lattice. The HP plot corresponds to the model in a for the infinite rectangular prism. Dashed lines indicate the location of corners. Error bars represent the standard error determined from the angle of DNA with respect to the reference vector for strands attached to 32 different beads in the same position along x over 80 discrete time steps (at equilibrium). c Sectioned EM images (section thicknesses of 400 nm) show BCT and HP lattices. (top) EM images show sections cut across the square cross-section of the particles (approximately parallel to the lattice plane). (bottom and right) EM images show sections cut approximately perpendicular to the lattice plane. EM images for particles with AR=4.3 show lattices with multiple layers in registry, while images for particles with AR=5.0 show multi-layer

		15
	and single-layer lattices, and images of lattices formed from AR=9.0 particles show primarily single layers. Scale bars represent 200 nm.	61
3.1	System setup.	73
3.2	Definition of BCC lattice sites; comparison of energy landscape and interactive bead visitation frequency in simulation.	85
3.3	Visitation frequency of small particles in a BCC unit cell for low and high temperatures.	86
3.4	Lattice properties as a function of temperature and number of small particle linkers.	87
3.5	Lattice properties as a function of temperature and number of small particle linkers, compared between simulations with lattices that are and are not allowed to vibrate.	93
3.6	Visitation frequency of small particles in a BCC unit cell with suppressed lattice fluctuations for low and high temperatures.	94
3.7	Interaction potential energy from theory and simulation for linearly and exponentially expanding systems; theoretical free energy values for linearly and exponentially expanding systems.	95
4.1	System setup.	107
4.2	Phase diagrams, showing crystal type as determined by small:large particle number ratio, number of small particle chains, and temperature.	109

4.3	Average interaction energy as a function of lattice type.	116
4.4	Lattice properties as a function of temperature for 3:1 and 4:1 lattices.	118
4.5	Lattice properties as a function of temperature for 5:1, 6:1, 9:1, and 10:1 lattices.	123
4.6	Example of BCC/FCC phase coexistence in a 7:1 system.	125
4.7	Fraction of large particles in each phase as a function of temperature for 7:1 and 8:1 systems.	126
4.8	Lattice properties as a function of lattice composition for systems showing no phase transition.	129
4.9	Lattice properties as a function of lattice composition for systems showing phase transitions.	130
5.1	NP Sheet formation and measurement. (a) Self-assembly and deposition of nanoparticle sheets in schematic. (b) Characteristic TEM (left) and optical (right) micrographs of NP monolayer sheet on a copper TEM grid. Sheets that have torn partially free from the copper, as the one highlighted in the right image, are potentially mobile and are measured in subsequent experiments. (c) Experimental schematic. NP sheets on TEM grid are subjected to magnetic fields generated by permanent magnets in cylindrical Halbach arrays, with additional magnets added to control the field strength, measured with a linear Hall sensor. The surface is measured in each field by confocal reflectance microscopy. (d) NP sheet geometry and parameters.	144

5.2 Nanoparticle sheet deflection in applied external B-field.

(a) Confocal microscopy scans of a sheet without and with applied field. (b) Sheet deflection profiles for increasing B . Upper left inset: optical micrograph of the sheet. Dashed line indicates line scans for the deflection profiles. Lower right inset: Vertical deflection δ of the free corner of the sheet, normalized by the length L of the actuatable portion of the profile (in this case approximately half the diagonal of the square sheet). (c) Experimental and simulated deflections collapsed by the fitting function given by Eq. 5.3. Inset: Normalized deflection as a function of applied field from experiments on different sheets (squares) and simulations for Young's moduli from 0.5 to 5 GPa (circles).

147

5.3 Magnetization direction and magnitude in nanoparticle

sheets. (a) Single particle magnetization direction θ_m from molecular dynamics (MD) simulations, averaged over local surface orientations θ_n at different external field magnitudes. The angles θ_m and θ_n represent the deviations of the particle magnetic moments and of the local sheet normal from the direction of the applied field, respectively. If $\theta_m = \pi/2 - \theta_n$, then the magnetization remains in-plane. Dots: averages from simulation. Dashed lines: fitting function described in the text. (b) Magnetization as a function of local surface orientation for a range of external field strengths. Note how flat orientations of the sheet tend to suppress the magnetization due to stronger

demagnetizing fields. Inset: Single particle Langevin magnetization function. (c) Low-field and high field moment angle, evaluated directly for the simulation, and using the fitting functions described in the text for the experiments. (d) Same as (c), but for the moment magnitude. 150

5.4 **Non-uniform magnetic pressures.** (a) Simulated sheet at large applied field, with force per particle depicted by arrows. Black arrows: total force. Green and brown arrows: normal and tangential force components, respectively. The forces vary across the sheet, the strongest are near and at the edges. The normal and tangential components are typically of similar magnitude, as seen from the zoomed-in view, where the tangential component even exceeds the normal component. (b) Deflection of an initially flat sheet using only the normal or only the tangential force components. Black circles: Data from full magnetoelastic simulation as in Fig. 5.2. Green and brown circles: Purely elastic simulation applying only the normal (green) or tangential (brown) force components found in the magnetoelastic simulation. (c) Normal force distribution at low and high fields for simulated and experimental sheets. These images show the non-uniform nature of the magnetic forces, with normal pressures even changing sign across the sheet. 154

5.5 **Twisting sheets by changing the applied field orientation**
 (a) Deflections in fields with general direction are characterized by

two modes: mode i corresponds to deflection along the free diagonal; mode ii corresponds to twisting around the mode i diagonal, leading to undulations in the perpendicular direction. Red, blue: positive and negative deflections respectively. (b) End deflection of 1 GPa sheet at constant field strength (here, $B_{\text{ext}} = 0.12$ T) but varying direction. At fixed ϕ and increasing θ , the field rotates away from the vertical and deflection decreases. At fixed θ but increasing ϕ , the field rotates around the vertical axis, and for fields with substantial components in the xy plane, end deflection vanishes abruptly as the field rotates away from the free corner. (c) Deflection profiles for different θ at $\phi = \frac{\pi}{4}$, corresponding to mode i. Inset: 2D projection of simulated sheet with $\theta = \frac{\pi}{12}$ and $\phi = \frac{\pi}{4}$; profiles evaluated along dashed line. (d) Deflection profiles for different ϕ at $\theta = \frac{5\pi}{12}$, corresponding to mode ii. As ϕ approaches $\frac{3\pi}{4}$, undulations indicate twisting of the sheet. Inset: 2D projection of simulated sheet with $\theta = \frac{5\pi}{12}$ and $\phi = \frac{3\pi}{4}$; profiles evaluated along dashed line. (e) Curves indicate amplitude of mode i (orange) or ii (purple) as a function of ϕ for fixed θ , where darker lines of either color correspond to lower θ . The contribution of modes i or ii can be tuned by re-orienting of the field.

157

5.6

Actuating NP coated Aluminum. Fe_3O_4 NPs can be used as a surface coating to actuate non-magnetic structures. We demonstrate this by deflecting an aluminum sheet using a nanoparticle monolayer as depicted in the schematic. The bottom image is a composite

micrograph (magnified 50x) of the free end before and after application of the field. The Al sheet is ~ 1000 times thicker than the monolayer and $50 - 100$ times stiffer. Despite this, the NPs generate forces strong enough to deflect the Al sheet by $\delta/t_{\text{Al}} \sim 1$.

159

6.1 **Microrollers alter microstructure in passive suspensions.** We dope driven particles (microrollers) in a passive colloidal suspension, as demonstrated in the schematic (a) A small quantity of microrollers (driven particles) are added to a suspension of passive particles. (b) Microrollers contain a permanent magnetic moment, m , and are actuated by applying a uniform rotating magnetic field. This actuation generates strong advective flows, which scale with h_{roller} , the height of the particle above the surface; these flows are the driver for restructuring the passive suspension. (c) Microrollers restructure the passive suspension by modulating the mean local density; this restructuring becomes more and more apparent as we average over longer and longer times. (d) Restructuring of the passive suspensions results in the emergence of a steady-state pattern. Left image is the experimental result, in which brighter areas indicate a higher local intensity, which is correlated to a higher concentration of passive particles. Right image shows the result of Stokesian dynamics simulations, which reproduce the same pattern seen in the experiments.

169

6.2 **The length of the new structure is independent of the microroller's velocity (the rotational frequency) and the area fraction of the passive particles.** (a-b) Pattern length at two different actuation frequencies: (a) 5 Hz and (b) 13 Hz. We find that the pattern size, L_{pattern} , is independent of microroller velocity. (c-d) Similarly, altering the mean area fraction of passive particles has no effect on L_{pattern} . (c) $\phi = 0.02$ (d) $\phi = 0.19$. (e) To quantify L_{pattern} , we draw a box across the microroller along the x axis of the pattern and measure the average intensity in the y axis, as illustrated in the inset; the pink dashed line indicates the center of the box. Then, we find the peak of the intensity (the blue open circle) in front of the roller (the orange circle), and measure the distance from the peak to the microroller (the blue double arrow). (f) L_{pattern} is independent of both microroller velocity (actuation frequency f) and ϕ . We find the average L_{pattern} is $8.9 \pm 0.9 \mu\text{m}$ (the black dashed line in (f)). 170

6.3 **The pattern length is set only by the microroller's height above the floor.** We perform simulations at different microroller's heights h_{roller} at $T = 0\text{K}$ and $T = 293\text{K}$ to investigate L_{pattern} as a function of h_{roller} . We observe that L_{pattern} becomes smaller as h_{roller} decreases: (a) $h_{\text{roller}} = 1.4 \mu\text{m}$, (b) $h_{\text{roller}} = 1.05 \mu\text{m}$, and is identical at $T = 0 \text{ K}$ and $T = 293 \text{ K}$. 174

6.4 **The emergent pattern results from hydrodynamic interactions around a microroller.** Fluid streamlines in the microroller's frame

produced from a microroller (orange circle) at $z = 3h_r$ (a). The fluid velocity is normalized by the microroller’s translational speed. There are two characteristic sets of streamlines around the microroller, recirculating (blue) and bypassing (purple) streamlines. Additionally, we observe the presence of stagnation points (white x-crosses) in the front and back of the microroller. In a suspension of passive particles at $T = 0\text{ K}$, we extract passive particles that have residence times τ larger than background particles τ_p (b) and plot their trajectories (c). These trajectories are confined to the recirculating and bypassing regions. Using the average passive particle velocity profile in (d), we determined that particles in the recirculating region have long residence because they are trapped around the microroller. Meanwhile, particles in the bypassing region persist around the microroller due to their curved trajectories around the microroller. Finally, using simulation data of suspensions at $T = 293\text{ K}$, we show the passive particle streamlines around the microroller and overlay them on the simulation $\langle \rho_{\text{passive}}(\mathbf{r}) \rangle_t$ (top) and experimental emergent pattern (bottom)(e). This shows that the recirculating and bypassing streamlines span the emergent pattern.

176

6.5

The microroller’s hydrodynamic interactions extend in three dimensions and can be probed by passive particles at different heights. In the left panel, we plot the xz microroller streamlines at the $(x, 0, z)$ plane for a microroller height $h_{\text{roller}} = 1.34\ \mu\text{m}$, and

show that not all streamlines (grey curves) intersect the xy stagnation line or saddle line (dashed white curve). Additionally, the saddle line determines the x axis extension of the xy fluid recirculating streamlines at a given height (middle panel). Therefore, different average passive particle heights in suspensions will probe these different recirculating and bypassive streamlines and create different emergent patterns (right panel). We study suspensions with three different particle heights $1.01 \mu\text{m}$, $1.4 \mu\text{m}$, and $2.6 \mu\text{m}$ which we color code green, yellow and cyan, respectively. In the xz streamlines we bound regions that correspond to the average height of the passive particles and by the xz streamline far from the microroller at the average height of the passive particle. In the middle panel we plot the three different xy streamlines whose spatial extensions are mirrored in suspensions' emergent pattern. We find that the depletion region is present only in the suspensions with particle heights whose bound region near the saddle line is closed.

182

6.6

Tuning the pattern length by changing the microroller

height. We show that the pattern length L_{pattern} directly correlates to the distance between the microroller and its front saddle line $L_{\text{saddle}}(z; \langle h_{\text{roller}} \rangle)$ (blue region). As previously stated, the saddle line is a function of height, and multiple streamlines in the xz plane intersect a given height which complicates which height to choose to

calculate L_{saddle} . However, we bound the (blue) L_{saddle} region by using the bounds determined and shown in Fig. 6.5. 188

- 7.1 Training magnetoelastic sheets. Diagram of training protocol to train curvature into an initially flat sheet (a). Deflection of an experimental sheet during the training protocol (b). The analogous training curves for a simulated sheet (c). In both cases the upper curve shows the deflection of the free corner when the field is on, while the lower curve is the equilibrium deflection when the field has been turned off. Experimental training data is courtesy of Edward P. Esposito. 198
- 7.2 Theorized trainable system of a suspension of passive particles with a single driven particle. The red lines indicate pairwise interactions between particles which can be reconfigured due to the translation of the driven particle. Diagram courtesy of Shih-Yuan Chen. 200
- 7.3 Transporting passive particles. (a) Streamlines generated by a rotating particle above a plane. (b) Initial configuration of a driven rotating particle (red) and a passive particle (white), and the passive particle's pathline (golden curve). (c) Phase plot of passive particle pathlines for all initial configurations of the passive particle. 202
- A.1 Pair distribution function at the minimum and maximum temperatures at which BCC lattices were observed, for different numbers of small particle chains. 224
- A.2 Fits for ΔG as a function of number of small particle chains. 225

A.3	Lattice density as a function of temperature for different numbers of small particle chains.	226
A.4	Average number of large particles interacting with each small particle as a function of temperature for different numbers of small particle chains.	230
B.1	More detailed crystal phase diagrams for 3:1 and 4:1 systems.	236
B.2	Distances between nearest neighbors in a BCT lattice as a function of c/a .	241
B.3	Number of large particle neighbors of each small particle for all systems.	244
B.4	Lattice vibration components for different observed lattices.	245
B.5	Large particle number density for all systems.	246
B.6	Average small particle chain end-to-end distance for all systems.	247
B.7	Vibrational density of states for two different sublattice transitions.	248
B.8	Grain boundaries in a 7:1 system.	250
B.9	Velocity cross-correlation function for two different sublattice transitions.	252
B.10	Thermodynamic quantities for all 3:1 crystals systems as a function of temperature.	254
B.11	Thermodynamic quantities for all 4:1 crystals systems as a function of temperature.	255

- B.12 Thermodynamic quantities for all 6:1 crystals systems as a function of temperature. 256
- C.1 **Microroller speed is proportional to the applied frequency.**
 We make a microroller water suspension with low concentration (few microrollers within the field of view), and apply a rotational magnetic field with a constant field strength (80 Gs) in a range of frequencies. Then, we measure the average speed of the microrollers and fit a straight line across the whole data set. The black dashed line shows the fitting result; the slope of the line is $0.13 \mu\text{m}$. 259
- C.2 **Microroller speed is constant in the colloidal suspension.** We track the displacement of a microroller in a suspension ($\phi_{area} = 0.16\%$) that is driven by two different frequencies. We find that the speed is constant and is again proportional to the rotational frequency. 260
- C.3 **The depletion region is strongly affected by gravitational forces on the passive particles.** We performed two sets of simulations where we independently turn off near-field interactions and gravitational forces. In (a) we show the emergent pattern from simulations without near-field interactions between particles. The depletion region is unaffected by near-field interactions as it is still present in the pattern. Meanwhile, (b) is the emergent pattern from simulations with mass-less passive particles and observe that the depletion region is largely affected. 261

CHAPTER 1

Introduction

The line that separates the living and the not living is not fine at all. The manner in which the living can replicate, be autonomous, and continuously dissipate energy through processes which regulate their vitals, i.e. homeostasis, is a far cry from a piece of metal undergoing impact testing. Although this classification scheme describes very disparate objects, the living and non-living in fact can be conjoined by analyzing them in a more general lens using the paradigm of collective phenomena or emergent behavior [1, 2]. Here, eating and breathing are behaviors associated to a response of a collection of parts that regulate the amount of oxygen and nutrients in the interior of an organism. Meanwhile, in a simple inanimate object there is no real sense of regulation of its internal structure. The piece of metal in a stress test will respond by deforming or breaking, and depending on the amount of deformation, it may not relax back to its initial state, and much less heal after breaking. Meanwhile, living materials will activate internal processes to combat being taken away from the organism's "equilibrium" conditions, for example, animals and plants can heal when suffering a cut or a broken limb or branch. A piece of metal cannot because its internal degrees of freedom lack the complex internal structure of living matter. This brings us to the following questions we would like to address in this thesis: can we design inanimate matter to respond to external stimuli in specific ways by programming specific features into its internal degrees of freedom? If so, can inanimate matter be designed to replicate behavior largely associated to living systems such as training? Through the

study of self-assembled colloidal crystals, and non-equilibrium soft matter systems, we try to try to find answers to these questions and find empirical requirements for training in materials.

1.1. Colloidal matter and self-assembly

Creating materials using a bottom up approach from atoms is difficult as manipulating atoms requires large energy sources, and also due to the complexities of chemical bonding [3, 4]. An easier approach towards material synthesis is using colloids, suspensions comprised of particles, oligomers, and polymers. Due to their ease of synthesis, functionalization, and visualization [5, 6], colloids have been used to form crystals, gels, and other composite systems. The ability to finely design particles and their interactions in order to form materials has provided a window into the inner workings of nucleation and dislocation in not only colloidal solids but also atomic ones [7]. Moreover, being able to create crystals and colloidal material from a bottom up approach using tunable building blocks grants us the ability to answer one of the motivating questions of this thesis: can we design responses to external stimuli by programming features into a material's internal degrees of freedom? With colloidal matter we have the ability to imbue individual units with properties that may propagate and be reflected in the emergent properties of their resulting structure. This opens a path towards potentially programming features into an emergent's system internal degrees of freedom through the properties of their constituents. However, this is not as straightforward as it seems as the physical principles that describe the individual components of a material are not the same as those that describe its overall emergent structure. Rather, the properties and response to external stimuli of materials,

animate or inanimate, is the culmination of the correlations and dynamics of their internal degrees of freedom, and they are not the same as those that describe the individual units. Nonetheless, as already stated, colloids have been used to create colloidal matter, thus, as a starting point we must understand why they are capable of forming collective matter in the first place before entertaining the idea of designing the internal degrees of freedom of colloidal matter for targeted responses.

Of the different forms of colloidal matter, I shall be focusing on colloidal crystals, as different lattice symmetry groups will inform and impact a crystals emergent properties and responses to external perturbations. Thus, if one of our objectives is to obtain design principles for a bottom up approach to materials design, understanding features that control the formation of different colloidal crystal lattices is essential. In general, colloidal crystals are formed in solution using nanometer to micrometer sized particle cores with a grafted polymer shell. It is important to state that a characteristic energy scale in colloids is the thermal energy of the fluid $k_B T$ which drives the thermal fluctuations of the suspended particles, here k_B is the Boltzmann constant and T is the absolute temperature of the suspension. This thermal energy scale competes with the energetic interactions of the colloidal solid. Usually, the energetic contributions are sufficiently captured through pairwise interactions, thus, an important energy scale associated to the system is the magnitude of pairwise interactions ϵ between particles. The general principles that govern this are the ideas of ergodicity and energy minimization. Ergodicity assumes that the system is capable of visiting every state of its phase space, thereby permitting the system to reach a state that minimizes its total energy which is mostly driven by the particles' attractive interactions. Colloidal Using the machinery of thermodynamics, as

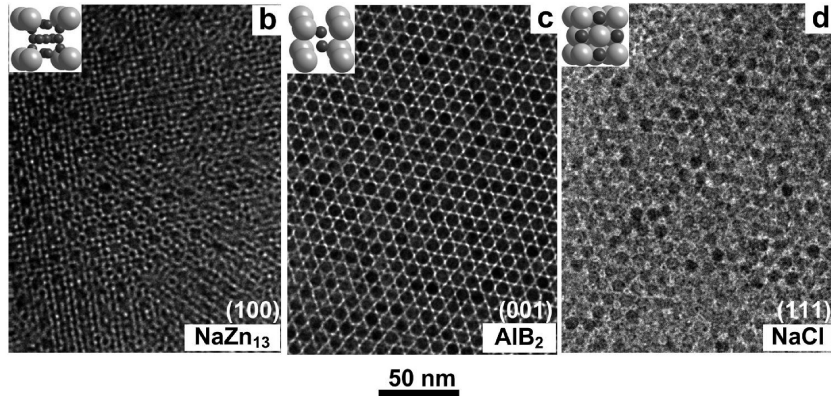


Figure 1.1. Different self-assembled colloidal crystals using a bidispersed set of particles of different sizes grafted with hydrocarbon chains. This is adapted from Bodnarchuk et al. [8].

colloidal crystals are comprised by hundreds of thousands of particles, we can determine the system's equilibrium configuration to be the state which minimizes its Helmholtz free energy F

$$F = U - TS,$$

where U is its internal energy, T is its temperature, and S is its entropy. Given the form of the function, we observe that F is a competition between the system's internal energy versus its entropy, which can be tuned by the system's temperature. The internal energy represents the sum of all possible interactions contained within the closed system, this can be further decomposed into the following pairwise interactions: particle core - particle core, particle core - polymer shell, and polymer shell - polymer shell. The interactions may be repulsive or attractive. Meanwhile, interactions that contribute to the system's entropy are less straightforward as they usually deal with the total configuration of the ensemble of particles, which for solids are usually vibrational and configurational (particle packing), and cannot be easily represented by pairwise interactions between particles.

Let us now analyze the internal energy contributions for the simple case of an ensemble of metallic particle cores. Naturally upon close proximity, particle cores polarize due to van der Waals interactions which will potentially drive particles to aggregate. We consider the interactions to be pairwise, and that the magnitude of this attractive energy between two particles $\epsilon(r)$ is dependent on the distance between the particle centers r . Particles will have the potential to form a bound pair only if they get close enough such that $|\epsilon(r)| \gtrsim k_B T$. But there is a Goldilocks problem here, if particles are able to come too close into contact then they will become trapped in whatever configuration they are in and the most likely configuration of the ensemble will be that of an amorphous solid as $|\epsilon(r)| \gg k_B T$. On the other hand, if particles are not able to come into close enough contact then $|\epsilon(r)| < k_B T$ and a dispersed state will most likely be the favored equilibrium configuration of the suspension. Thus, particles must be bound by interparticle interactions but not too strongly as they need to reconfigure to reach the energy minimizing equilibrium state. A common practice is to stabilize colloids through the addition of a hydrocarbon polymer shell their surfaces. This prevents colloids from aggregating randomly and forming an amorphous solid. As the polymer shell adds a lower bound to interparticle separations, particles cannot get close enough to randomly aggregate, therefore, they will be able to reconfigure into a free energy minimizing equilibrium state. The formation of crystals using this mechanism including nanodots has been summarized in the review article by Murray et al. [9]. Finally, the previous energetic analysis can also be applied to other types of attractive interactions among colloids. As we will see shortly, attractive interactions between the polymer shells of different particles will lead to the formation of self-assembled structures, equally motivated by the previous energetic principles.

Meanwhile, Bodnarchuk et al. [8] have reported the formation of a library of crystals using ensembles of particles comprised of metallic cores and polymer shells of hydrocarbon chains. However, they found that particles did not self-assemble due to the polarization of the particle cores or any other attractive interactions. Given their concentration of particles, and the length of the polymers in the polymer shell, it was entropic maximization that gave rise to the formation of the crystals. Their system showcases the complexity of crystal engineering and lays bare the competition between the system's internal energy with its entropy. In crystal lattices, particles are capable of vibrating around their equilibrium position unlike in a trapped amorphous state. Therefore, an ordered structure, counterintuitively, maximizes entropy as particle configurations have space to fluctuate around their lattice points [10, 11]. It is then apparent that what sets the symmetry of such ordered structures is then the geometrical properties of the particle cores, such as shape, size, and the ratio of particles of different sizes. In the same paper by Boles et al. [8], they explore the crystal lattice phase space by varying the ratio and size of a bicomponent system of particles, see Figure 1.1.

In order to expand the phase space of colloidal crystals and not be limited by the geometric properties of the suspended particles, we must enhance their degrees of freedom. One way of doing this is adding interparticle attractive interactions between colloids as evidenced by the form of the Helmholtz free energy. Currently, the addition of attractive potentials between colloids is mainly done by designing attractive particle core - particle core interactions or polymer shell - polymer shell interactions [12, 13]. Much success has been achieved by using the mutual attraction of particle cores by employing ionic particles to form crystals [14, 15]. But using this method relies on our ability to tune

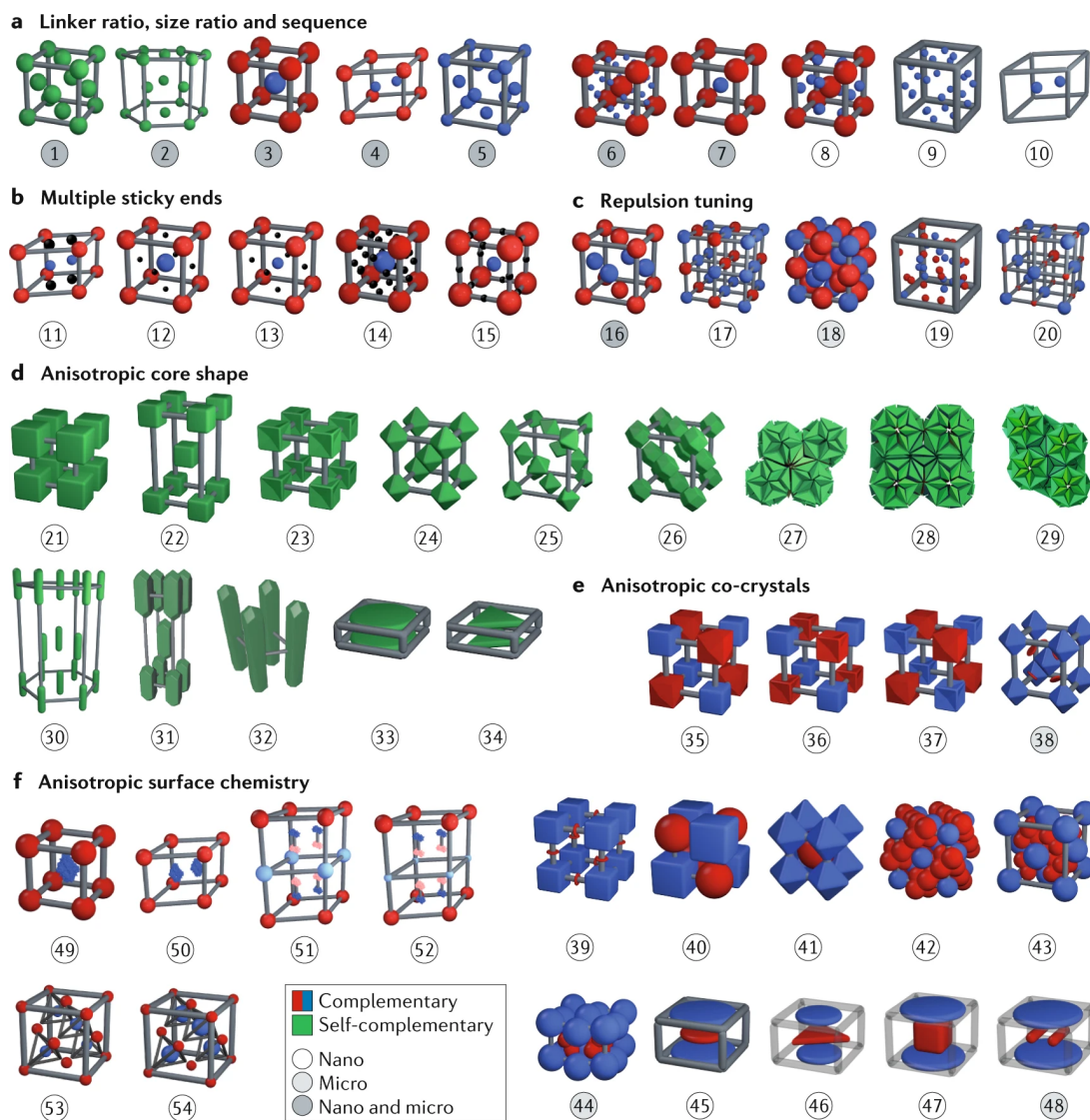


Figure 1.2. Library of colloidal crystal lattices obtained by varying the geometric properties of the particles and DNA strand length and strength of their grafted DNA chains. This is adapted from Laramy et al. [18].

the matter of which the cores are made of as opposed to the wide variety and tunability of polymers which can be grafted on the surfaces of particles. We focus then on the attractive interactions embedded in the particles' polymer shells, in particular, in the form of hydrogen bonding using single stranded deoxyribonucleic acid (DNA) [16, 17].

The use of DNA in colloidal crystal engineering is useful considering that the strength of the bond between complimentary strands can be tuned by adding or subtracting base pairs. This hinges on an inherent and unique property of DNA: its specificity of pairing between base pairs. Additionally, another advantage of using DNA is the weak and physical nature of hydrogen bonding between the base pairs. If single strands grafted on the surfaces of the particles are well designed, they will have many hybridization events (pair and unpairing) throughout the self-assembly process associated with the movement of the particle cores towards an energetically minimizing equilibrium state [19]. As shown by Laramy et al. [18], DNA self-assembled crystals not only span naturally occurring crystal lattices seen in hard condensed matter systems, but also can form unnatural crystals such as certain quasicrystals, see Fig. 1.2. The latter crystals are obtained by tuning both the particle's core shape and tailoring its DNA strands. Thus, colloidal collective structures prove to be not only an atomic analog of matter, but a playground for the study of emergent properties thanks to the high tunability of colloids.

In chapter 2, I present work that has contributed to the field of DNA self-assembled crystals. In this work, in collaboration with experimentalists, we show how we can aim for different crystal lattices by increasing the aspect ratio of highly anisotropic particle cores with grafted complimentary single stranded DNA chains. Interestingly, we found that by increasing the aspect ratio of the particles, we enhanced DNA hybridization within certain regions of the anisotropic particles, to the extent that these regions correlated with the symmetry of the resultant crystal lattices. Although we employed anisotropic particles in this work, we only studied systems of monodispersed particles. The bidispersed crystal lattices presented in Figure 1.2 demonstrate that particle size and number ratio of the

different particle sizes are other design knobs available for the formation of DNA self-assembled colloidal crystals. Motivated by this, Girard et al. [20] demonstrated that for particle number ratios of highly size-asymmetric particles with grafted DNA chains, they obtained crystals in which the larger particles are situated in crystal lattice sites while the smaller ones fill symmetric interstitial sites. They showed the appearance of different crystal lattices by tuning the number ratio of large to small particles. Under certain conditions, they found that the smaller particles are able to move in-between neighboring interstitial sites while the larger particles remained at their lattice points, see Figure 1.3. Girard et al. [20] suggested this to be analogous to the motion of electrons in simple metallic solids. In chapters 3 and 4, in collaboration with Ali Ehlen (my life partner), we create a simplified model of such size-asymmetric systems to further explore how far we can take the analogy of colloidal electrons. In our work, we find correlations between lattice vibrations and the enhancement of small particle diffusion. In our findings, we also show that large particles occupy crystal lattice points while the small particles inhabit symmetric interstitial sites. Additionally, we observe that small particle diffusion can discontinuously increase as a product of crystal lattice transitions driven by increasing the temperature of the system, similar to an insulator-to-metal transition in atomic systems. The latter is also evidence of diffusionless or displacive crystal phase transitions governed by the movement of the large and small particles upon variation the system's temperature.

The latter body of work demonstrates how designing a suspension of interacting particles can lead to the formation of self-assembled crystals. The process of self-assembly is simply the product of thermodynamic equilibrium, and it is beholden to events in which particles come together and, later, clusters grow to eventually form a final equilibrium

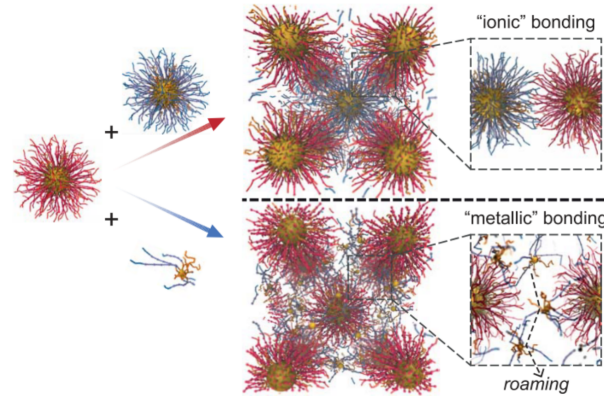


Figure 1.3. Size asymmetry matters in DNA self-assembled colloidal crystals. If the particles are of equal size, there is negligible particle diffusion. However, if there is strong size-asymmetry, the smaller particles will hold the colloidal crystal but also diffuse among the larger particles, similar to electrons in a simple metal. This is adapted from Girard et al. [20].

crystal structure. The information held by the suspending particles is constant or passive throughout the self-assembly process. In general, once a component has found its place in the crystal, it will likely remain there until perturbed by external stimuli. Lewis et al. [21] have shown that DNA colloidal crystals can still behave elastically when indented up to hundreds of kilopascals. But this still is far removed from polymeric solids and sheets that have Young's moduli of up to the tens of gigapascals [22, 23]. Although these self-assembled crystals are fascinating in their own right and have been useful as atomic analogs in order to gain a better understanding of hard condensed matter phenomena, they do not have much functionality once formed. This should not be surprising considering the passive nature of the components of DNA self-assembled colloidal crystals. In a sense, due to the lack of non-equilibrium phenomena based behavior of the components of the colloidal crystal, this passivity will also be reflected in the internal degrees of freedom of the crystal. There is then no reason to believe that these colloidal crystals will have

properties or dynamical responses associated to living systems – much like how we do not expect for a rock to talk. If we do want to imbue colloidal systems with a semblance of adaptable behavior similar to living systems, the colloidal collective must have dynamical internal degrees of freedom which can be manipulated and driven to different equilibrium states without eroding the solid’s internal structure. Thus we turn our attention to systems that can be driven out of equilibrium, and in particular, using external magnetic fields.

1.2. Driven colloidal systems, adaptability, and training

The current paradigm in materials science and engineering for materials design is based on four principles: Process, Structure, Properties, and Performance [24]. A material is processed or, rather, synthesized and will have a certain atomic structure. This structure will translate into specific material properties that can be employed for some use. The performance of this material will rely on its properties. The latter sequence of steps represents the bottom up approach for materials design but a top down approach can also be employed especially when designing a material for a particular performance [25]. This paradigm is not exclusive to atomic materials; we can easily see how this can be employed for colloidal materials we have previously discussed. In the case of DNA self-assembled colloidal crystals, the process involves both the synthesis of DNA functionalized particles and their self-assembly process. Afterwards, the self-assembled crystal will present properties based on its internal structure. Depending on the properties of these crystals they can potentially be applied for a certain task. Mainly they have been used in photonic devices [6, 26, 27]. However, using colloidal materials, or soft matter in general, we can

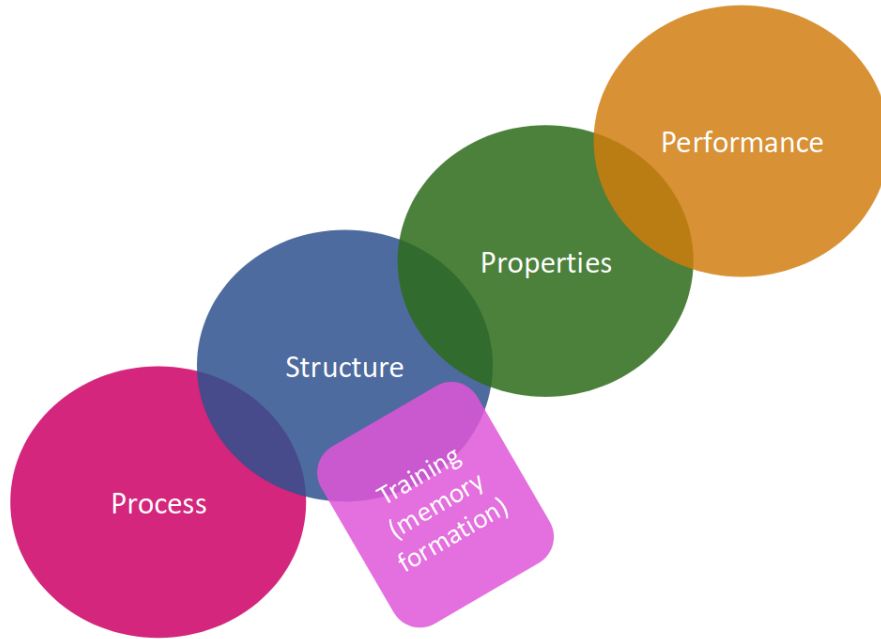


Figure 1.4. Modified material design paradigm with the inclusion of the concepts from training in materials. Training involves the reconfiguration of a material's internal degrees of freedom.

enhance the current paradigm of materials design by introducing the concept of training in materials [28], see Figure 1.4. This involves the reconfiguration of the material's internal structure or degrees of freedom by subjecting it to physically desired behavior. In this process the material adapts to the exposure of external stimuli by acquiring a new equilibrium state. This will be evidenced by an evolving response to the external perturbation, thus hinting at an answer of our second guiding question of this thesis. Usually, a material is trained by repeatedly being exposed to the external stimuli until its response is invariant to the training stimuli. In general, the concept of training had been reserved for animate matter, here we have described its analogous process for inanimate matter. But what are the requirements for a material to be trainable considering its lack of life?

Trainable materials need to have internal degrees of freedom that can evolve over different steady states, in this manner they can adapt to a training stimuli. Not only that, this new steady state of the internal degrees of freedom must persist even after the external perturbation is over. Therefore, for a material to be trainable it must be capable of forming memory with respect to the non-equilibrium state of the internal degrees of freedom when being stimulated. The evolution of the internal degrees of freedom are then governed by the training perturbation, and their degree of relaxation or reconfiguration after being driven out of equilibrium. The potential energy landscape of the degrees of freedom must then have energy wells into which they can settle when being driven out of equilibrium but not too deep nor too shallow such that they can be driven to different states only by the external stimuli. The dynamics of the degrees of freedom forces us to solve the system's dynamical equations [29, 30] and prevents us from using the theoretical machinery of equilibrium thermodynamics. Although we cannot solve for all of degrees of freedom (roughly six times Avogadro's number), we approximate and assume that only a subset of degrees of freedom are trained during a training period. For example, studies of non-Brownian granular systems have shown that only particle reconfigurability is essential for robust memory formation [31–33]. Similarly, it has been suggested that the brain's ability to reconfigure and decrease its threshold/firing potential in its connections among neurons reinforces and creates specific memories [34–36]. In both examples there is an implicit mention of time in the driving mechanism that is producing the configurational change. This I will call a training protocol. In glassy granular systems the training protocol is cyclic oscillatory shearing in which a target shear strain γ_{mem} is chosen and one cycle of the protocol is comprised of transitioning from γ_{mem} to $-\gamma_{\text{mem}}$ [37,

38]. The trained state or formed memory is then read out by measuring the mean squared displacement (MSD) of the particles as a function of the shear strain that is imposed on the system after training. As can be observed in Fig. 1.5, repeated training cycles will reinforce the presence of a minimum of MSD at γ_{mem} , be it for either one (see Fig. 1.5a) or two (see Fig. 1.5b) target shear strains. The mechanism that underlies the formation of memory in this system is the appearance of periodic orbits of the particles as a function of the training protocol for a given γ_{mem} [37, 38]. This indicates a reconfiguration of the glass's potential energy landscape by means of the training protocol. Motivated by these findings, in chapters 5 and 6 we explore systems that are potentially trainable given slight modifications. Both physical systems are driven out of equilibrium using external magnetic fields, but the dynamics of their internal degrees of freedom are mediated through different fields, elastic (chapter 5) and hydrodynamic (chapter 6). These systems offer different modes of relaxation with respect to their respective degrees of freedom which can potentially impact their trainability.

In chapter 5 we study, in collaboration with experimentalists, the magnetic actuation of magnetoelastic sheets. In experiments, nanometer sized magnetic particles are functionalized with oleic acid and later, through directed assembly, they are approximately hexagonally packed on a plane. These magnetic monolayers are then actuated using homogeneous external magnetic fields, where the elastic response arises from the van der Waals interactions among the strongly confined oleic acid chains. It is in the origin of elasticity in these sheets where there is a strong potential for trainability so long the chains can be reconfigured when actuated. In fact, I will briefly show this can be induced under the right conditions in chapter 7, using both experiments and simulations. Also,

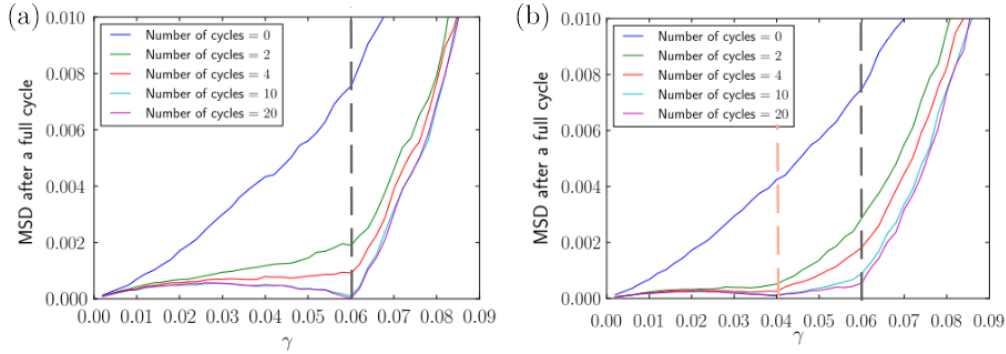


Figure 1.5. An example of reading out memory embedded in glassy granular matter. By shearing a trained system sequentially and in an increasing manner, a minimum is observed in the mean squared displacement (MSD) of the particles at the value of $\gamma_{\text{mem}} = 0.06$ in (a) and values $\gamma_{\text{mem}} = \{0.04, 0.06\}$ in (b). The formation of minimum values or memories are reinforced as a product of the number of cycles. This is due to the appearance of steady state particle periodic orbits due to the cyclic oscillatory shearing. These graphs were adapted from Fiocco D. *et al.* [37].

to even be capable of training these sheets we must understand their mechanics in the first place. For this, we turn to molecular dynamics and model the experimental sheets by studying a triangulated mesh with an overall shape of a square. All nodes of the mesh represent a single magnetic point dipole, while elastic interactions are imposed among the nodes. Through these approximations we arrive at the following expression for the sheets' internal energy U :

$$\begin{aligned}
 U &= U_{\text{elasticity}} + U_{\text{magnetism}}, \\
 U_{\text{elasticity}} &= \underbrace{\sum_{i,j} \frac{1}{2} k (r_{ij} - r_0)^2}_{\text{Stretching energy}} + \underbrace{\sum_i K (1 - \cos(\theta_i - \theta_{i,0}))}_{\text{bending energy}}, \\
 U_{\text{magnetism}} &= \sum_i \vec{\mu}_i \cdot \vec{B}_{\text{ext}} + \sum_{i,j} \frac{\mu_0}{4\pi r_{ij}^3} (\vec{\mu}_i \cdot \vec{\mu}_j - 3(\vec{\mu}_i \cdot \hat{r}_{ij})(\vec{\mu}_j \cdot \hat{r}_{ij})).
 \end{aligned}
 \tag{1.1}$$

Here, k is the spring constant between nearest neighboring nodes, r_{ij} is the distance between the i th and j th nodes, r_0 is the equilibrium distance between the nodes, K is the bending constant between two edge sharing triangular facets, θ is the angle between these two edges, and θ_0 is the equilibrium angle between the facets. Meanwhile for $U_{\text{magnetism}}$, $\vec{\mu}_i$ is the vector representing the magnitude and orientation of the i th point dipole, \vec{B}_{ext} is the external magnetic field vector, μ_0 is the vacuum magnetic permeability, and \hat{r}_{ij} is the unit vector between the i th and j th dipoles. Additionally, in order to simulate idealized versions of the experimental sheets, the model's elastic parameters k and K are calculated such that they are respectively proportional to the sheet's Young's and bending moduli. As for the magnetic properties of the dipoles, we consider that all point dipoles are described by identical Langevin magnetization curves which are free of hysteresis. This is motivated by the nanometric size of the experimental magnetic particles. Using this model we are able to replicate experimental results and achieve a master curve that correlates the amount of deflection in a sheet with the magnitude of a vertical external magnetic field for both experimental and model sheets. This indicates that our model accurately describes the experimental system. We then continue on to use this model to explore training in these sheets. Relevant degrees of freedom for training in our system would arise from its elastic parameters $\theta_{i,0}$, as I will later show in chapter 7. Surprisingly, this is analogous to findings reported on biological systems, particularly in cell division processes [39, 40] where the elastic parameters of a vertex model evolved over time in order to avoid the cell from becoming fluid during mitosis.

Meanwhile in chapter 6, I present how a suspension of passive particles in water can be reconfigured by a single driven particle even in the presence of thermal fluctuations.

As I have previously stated, this ability to reconfigure is essential for trainability. Here the interactions among all particles are entirely hydrodynamic, and because they are all of micrometer size, the dynamics of the fluid are well described by the Stokes equation:

$$-\nabla p + \mu \nabla^2 \vec{u} = \vec{F},$$

where p is the fluid's pressure, μ is the fluid's viscosity, \vec{u} is the fluid's velocity, and \vec{F} is the force acting on the fluid. This equation lacks the non-linear term characteristic of the full Navier-Stokes equation. The lack of this non-linearity has enabled some semi-analytical approaches to the Stokes equation to be feasible, specifically, the formulation of a Green's function. Under this approach, the solution for a point force can be obtained from solving

$$-\nabla p^{\text{PF}} + \mu \nabla^2 \vec{u}^{\text{PF}} = -\vec{F}^e \delta(\vec{x}).$$

The solution to this equation describes the perturbation of the fluid if a force point is located at the origin, the Green's function $\mathbf{G}(\vec{x})$ propagates this perturbation throughout the fluid to a point described by \vec{x}

$$\vec{u}^{\text{PF}}(\vec{x}) = \underbrace{\frac{1}{8\pi\mu} \left(\mathbf{I} + \frac{\mathbf{x} \otimes \mathbf{x}}{r^3} \right)}_{\mathbf{G}(\vec{x})} \cdot \mathbf{F}^e$$

Using this solution we use $\mathbf{G}(\vec{x} - \vec{y})$ to propagate the the stress σ_{jk} on the fluid emanating from a continuous and smooth surface $S(\vec{y})$, representing a boundary or movable particle, with the following integral

$$u_i(\vec{x}) - u_i^\infty(\vec{x}) = \int_S G_{ij}(\vec{x} - \vec{y}) (-\sigma_{jk} n_k)(\vec{y}) dS(\vec{y})$$

The solution of this integral thus provides the vector component i of the perturbative flow $u_i(\vec{x})$ at \vec{x} , relative to a background flow $u_i^\infty(\vec{x})$, due to the stresses arising from the body of surface S . However, this integral is usually difficult to effectuate. A common approximation that is taken for perfectly spherical bodies is a multipole expansion with respect to $\mathbf{G}(\vec{x} - \vec{y})$ in which $|\vec{x}| \gg |\vec{y}|$. Different moments of this expansion are identified with body forces, torques, and stresses of the spherical body. In essence, the latter serves as the basis of the Stokesian dynamics method [41] for the simulation of spherical particles through pairwise interactions. Using this method, and in collaboration with experimentalists, we observed the appearance of an emergent pattern of particles when a driven particle continuously translated through a suspension of passive particles suspended in water at room temperature. The emergent pattern is a manifestation of the hydrodynamic interactions stemming from the translating particle. This opens pathway for trainability in this system which so long an attractive interaction can be realized between particles such that thermal fluctuations do not destroy the emergent pattern. I will discuss this further in chapter 7, and look at manipulation of single passive particles with sizes that differ from that of the driven particle.

It is surprising that something as commonplace in complex animate systems as training can be applied to inanimate systems. In materials, it is straightforward to track the amount of training or adaptation by the change in the system's internal energy over a specified training period. This is unlike in animate systems where quantifying learning has involved exams or presentations. Can quantifying and understanding training in synthetic systems transcend inanimate systems and increase our understanding of memory formation in living or biological systems [42]? And if we are being provocative, can

trainable materials then become model systems for biological systems similar to how colloidal materials are model systems to atomic matter? Time will only tell... In the meantime, I present most of the work I have realized during PhD.

CHAPTER 2

Self assembly of colloidal crystals using anisotropic particle cores

This work was a collaboration between members of Chad Mirkin's and Monica Olvera de la Cruz's group. In this work I performed the simulations and contributed the theory associated with this study. I was guided by Martin Girard and Monica Olvera de la Cruz. The objective of this work was to quantify the impact of particle shape on DNA self assembled crystal lattices as was initially put forth by O'Brian et al. [43]. Unlike atomic systems, particles in colloidal systems can be synthesized to have different body shapes. We exploit this feature and study, using experiments and simulations, how the geometrical properties of the crystal subunits impact the lattice's overall structure. Our system consists of rhombic dodecahedra particles with tunable aspect ratios, these particles are also grafted with DNA complimentary strands. We observe that different crystal lattices are obtained by varying the particle's aspect ratio. Subsequently, this is understood by the varying importance of different facets of the particle shape for DNA hybridization as the particles' aspect ratio is varied.

The following was originally published in the ACS Nano in 2018. It is reproduced here with permission of the PUBLISHER.

Controlled Symmetry Breaking in Colloidal Crystal Engineering with DNA

Christine R. Laramy, Hector Lopez-Rios, Matthew N. O'Brien, Martin Girard, Robert J. Stawicki, Byeongdu Lee, Monica Olvera de La Cruz, Chad. A. Mirkin

2019, 13, 1412 – 1420

Reprinted with permission from:

ACS Nano 2019, 13, 1412-1420, DOI: acsnano.8b07027. Copyright 2018 American Chemical Society.

<https://pubs.acs.org/doi/10.1021/acsnano.8b07027>

with modified details.

ABSTRACT: The programmed crystallization of particles into low symmetry lattices represents a major synthetic challenge in the field of colloidal crystal engineering. Herein, we report an approach to realizing such structures that relies on a library of low symmetry Au nanoparticles, with synthetically adjustable dimensions and tunable aspect ratios. When modified with DNA ligands, and used as building blocks for colloidal crystal engineering, these structures enable one to expand the types of accessible lattices and to answer mechanistic questions about phase transitions that break crystal symmetry. Indeed, crystals formed from a library of elongated rhombic dodecahedra yield a rich phase space, including low symmetry lattices (body-centered tetragonal and hexagonal planar). Molecular dynamics simulations corroborate and provide insight into the origin of these phase transitions. In particular, we identify unexpected asymmetry in the DNA shell, distinct from both the particle and lattice symmetries, which enables directional, non-close packed interactions.

2.1. Introduction

The ability to arrange colloidal particles into crystalline lattices with controlled spacing and symmetry enables the construction of next generation materials.[44] In these materials, particles represent tunable building blocks that can be engineered in composition and structure, and assembled into sophisticated architectures with functionalities relevant for fields ranging from optoelectronics to catalysis [44–47] One powerful strategy to imbue these building blocks with chemical crystallization instructions, and thereby “program” their organization, is to attach DNA molecules, as ligands, to their surfaces.[48–52] Over two decades of research have yielded an optimized DNA design for this purpose, comprised of a rigid, double-stranded region near the particle surface and a solution-exposed, single-stranded terminus (known as a “sticky end”).[53, 54] Watson-Crick base pairing between sticky ends on adjacent particles drives crystallization through collective interactions between particles, where the most favorable configuration often maximizes the total number of hybridization events (known as the complementary contact model).[54] Researchers have used this approach to program the formation of over 50 different crystal symmetries and more than 500 different structures (e.g. same symmetry, but different compositional building blocks or lattice parameters).[54–56] However, the majority of these structures are high symmetry, cubic lattices, with dense particle packings.[54, 56, 57] As the symmetry of the lattice is reduced, the constituent unit cells lose symmetry operators, typically through the introduction of new interaction modes, a decrease in nearest neighbor interactions, or a change in relative particle orientations.[44, 45, 47] Experimental realization of these lower symmetry structures can be challenging,[44, 58] due to the more complex set of crystallization instructions required to break the symmetry

of interparticle interactions.[59] If successful, approaches to systematically and controllably reduce symmetry can provide an avenue to explore poorly understood areas of phase diagrams and structure-function relationships, and can be used to engineer functional material responses. For example, reduced symmetries are fundamental to the observation of chiral optical responses, metamaterial behavior, and photonic band gaps in particle-based lattices.

Recent experimental and theoretical work suggests that anisotropic building blocks can be used to direct interactions and, when combined with the encoding capabilities of DNA, provide access to structures not attainable with isotropic building blocks.[55, 60–65] With this approach, the particle core acts as a template to arrange the DNA into a conforming shell.[55, 64] Anisotropic shapes can thus encode spatially discrete, collective DNA interactions localized along each facet or spatial region of the particle. The number, geometry, and relative strength (i.e. the number of DNA molecules within each collective interaction) of these “bonds” can be tuned to produce different symmetries.[54, 55, 64, 66] Furthermore, recent work shows that flexible DNA ligands can deform to enable symmetries beyond those predicted by particle shape alone.[64, 66]

Realization of low symmetry lattices via this approach is dependent on the availability of chemical syntheses that produce the desired shapes with sufficient uniformity and yield. This is a challenge even for some of the most studied nanomaterial systems (e.g. noble metals), due to the thermodynamic preference for highly symmetric products and the poor understanding of symmetry breaking events.[67–70] Successful examples often result from trial-and-error, where kinetic processes trap structures in local energetic minima that are prone to subtle fluctuations in reaction conditions.[43, 69, 71, 72] Although

significant advances have been made in the preparation of low symmetry particles,[44, 69] realization of their full potential in programmable assembly requires access to a larger library. In particular, it would be useful to have sets of structures, defined by general shape, but with tunable aspect ratios. Such structures would increase our understanding of symmetry breaking processes in colloidal crystallization and potentially access low symmetry colloidal crystals.

Herein, we report a general approach to synthesize highly anisotropic nanoparticles with tunable aspect ratios (ARs). Importantly, these particles can be modified with DNA to explore the role of particle anisotropy in directing colloidal crystallization. As a case study, a base shape of a rhombic dodecahedron is systematically elongated, which enables the realization of broken symmetry lattices, including a body-centered tetragonal (BCT) lattice and a hexagonal planar (HP) lattice. When paired with molecular dynamics simulations, this platform enables one to probe the key factors that underlie a series of anisotropy-driven phase transitions. Simulations accurately predict each phase and reveal a symmetry breaking in the DNA shell that leads to the formation of the non-close packed HP lattice.

2.2. Results

Robust syntheses for nanocrystals require precise control over the placement of millions of atoms.[73] One strategy to achieve this control is to spatiotemporally separate homogeneous particle nucleation from heterogeneous growth onto existing particles, and thereby improve control over each step.[73] In this “seed-mediated” approach, a pre-formed

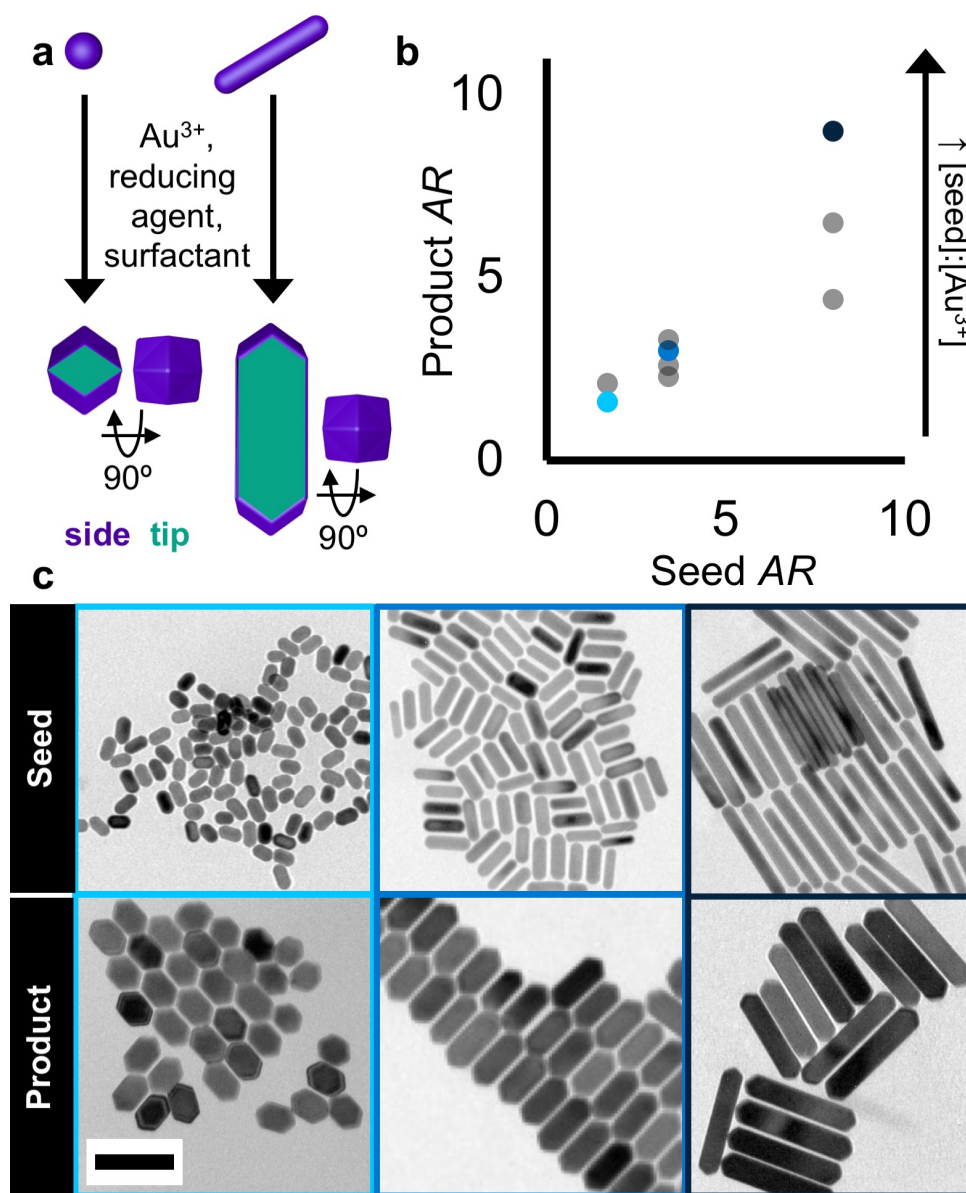


Figure 2.1. A rod-based seed-mediated synthesis can be used to generate elongated rhombic dodecahedra with tunable ARs. (a) Schematics show a seed-mediated synthesis with a sphere or a rod seed and their resultant products. Green indicates an elongated side facet, and purple indicates a tip facet. (b) Seed AR and different $[\text{seed}]:[\text{Au}^{3+}]$ ratios can be used to tune product AR. The algorithmic analysis of several hundred nanoparticles per sample from transmission electron microscopy (TEM) images can be used to quantitate this relationship. (c) Representative TEM images show seed and product particles that correspond to the colors in the plot in (b). The scale bar represents 100 nm.

particle surface (i.e. “seed”) is separately nucleated and added to finely tuned, mildly reducing growth solutions, such that the seed acts as a preferential site for heterogeneous nucleation.[43, 74–76] In many cases, this approach enables one to preferentially guide particles toward a single product with high uniformity and yield.[73] Furthermore, the structure of the nanoparticle seed can be used to direct the growth of the nanoparticle product.[77–79] Inspired by this work, one can envision a nanoparticle synthesis platform where the shape of a seed can be used to initiate symmetry breaking (rather than relying upon poorly understood and controlled nucleation events) and to manipulate the anisotropy of the nanoparticle product.

An ideal low-symmetry particle seed should be accessible in high yield with broadly tunable anisotropy (Figure 2.1a). For this purpose, we chose the well-studied syntheses for single crystalline Au rods, a particle in which symmetry is broken along a single axis.[71] The anisotropy of these particles can be defined by the ratio of the rod length divided by the rod diameter (i.e. AR), and directly measured via electron microscopy (EM). The shape and size of the particles (seeds and products) can be analytically determined for hundreds of particles per sample via algorithmic analysis of EM images in order to approximate population-level statistics.[79, 80] The electronic structure of these particles further enables structural changes to be measured via UV-Vis spectroscopy, where the broken symmetry manifests in two, spectrally separated localized surface plasmon resonances (LSPRs), which correspond to each dimension.[73, 75]

Several syntheses exist to control the AR of single crystalline Au rod seeds through the inclusion of different amounts of shape-directing additives (e.g. Ag^+). However, these syntheses simultaneously change both particle length and diameter.[79, 81, 82] An

ideal platform to control seed AR would permit control over length, while holding the diameter constant (or vice versa). One strategy to achieve such control could begin with high AR rods and selectively remove material from their tips; an approach previously demonstrated via the addition of an oxidizing agent (e.g. Au^{3+} salt).[79, 83] Importantly, EM of AR=8 rods etched to different extents enables access to rods of ARs down to 4.4, while maintaining the uniformity and diameter of the original particles. Starting the etching process with a lower AR rod (3.4) similarly afforded access to a range of low ARs down to 1.7.

To study the impact of seed anisotropy on product anisotropy, Au rods with the same diameter, but different ARs, were added to a seed-mediated synthesis that conventionally produces Au rhombic dodecahedra, a particle with twelve equal rhombus faces. While this synthesis has been shown to primarily yield a single product from single crystalline Au spherical seeds, it was uncertain whether the trace amount of Ag or the different faceting/surface curvature of the rod seeds would result in multiple products or impact the resultant shape. EM and UV-Vis revealed the formation of anisotropic products that resembled elongated rhombic dodecahedra. More specifically, facets adjacent to the axis of four-fold symmetry remained fixed in surface area and formed the “tips”, while the four remaining facets (at 90 degrees to this axis) elongated and increased in surface area (Figure 2.1a). Algorithmic image analysis of hundreds of particles confirmed the formation of this single product in > 95% yield by shape, as fit to an elongated hexagonal cross-section in EM image analysis (Figure 2.1b, c). The AR of the elongated rhombic dodecahedra directly correlated with the AR of the seeds (Figure 2.1b, c) and an EM image tilt series of products grown from the highest AR seeds revealed a consistent elongated rhombic

dodecahedron shape, with the preservation of a square cross-section along the four-fold symmetry axis. Importantly, the introduction of rod seeds into several other syntheses for anisotropic shapes (e.g. concave cubes, ditetragonal prisms) yielded similarly shifted LSPRs and elongated products, in support of this as a platform-type approach.

The anisotropy of elongated particles can be further tuned by varying the ratio of rod concentration to Au concentration in the growth solution, with higher ratios leading to more anisotropic products (Figure 2.1b). With this approach, products from a single rod seed can be tuned by up to a factor of two in AR (here defined as the longest edge length divided by the shortest) and a factor of 3 in minor edge length. In totality, both approaches enabled realization of a library of elongated rhombic dodecahedra that span from a regular rhombic dodecahedron with an AR, by definition, of 1.15 to the most anisotropic with an AR=9, with similar minor edge lengths.

Synthetic access to this library of elongated rhombic dodecahedra, with precise control of particle anisotropy, allows one to probe the effects of AR on colloidal crystallization with DNA. In principle, the ability to systematically manipulate AR allows one to probe the symmetries that form before, throughout, and after a phase transition. By mapping the boundaries of the transition, one can gain experimental insight into why particular phases occur in order to gain greater predictive power. Therefore, elongated Au rhombic dodecahedra with ARs spanning from 1.15 to 9 (1.1, 1.6, 2.0, 2.8, 3.5, 4.3, 5.0, 9.0), and minor edge lengths that differed by no more than 10 nm, were functionalized with thiol-modified DNA according to literature protocols (Figure 2.2a, b).[84, 85]

The extent to which an anisotropic building block displays directional interactions arises from an interplay between the shape of the particle core and the structure of the

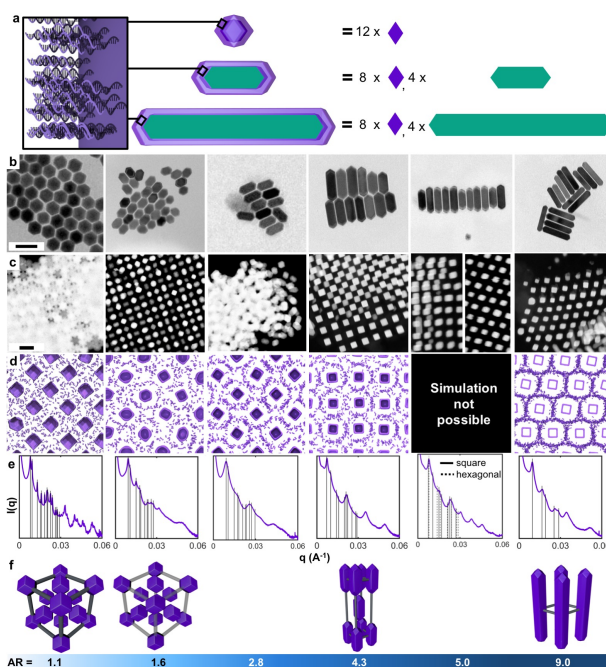


Figure 2.2. Elongated rhombic dodecahedra building blocks crystallized into multiple lattice symmetries. (a) As the AR of building blocks increases, the surface area (and thus number of DNA molecules) on elongated (green) facets increases, while the surface area of the tip (purple) facets remains the same. (b) TEM images show elongated rhombic dodecahedra before functionalization with DNA. From left to right these particles have a minor edge length and corresponding coefficient of variation (CV) and AR of: 30.4 ± 2.4 nm (8.0% CV) and 1.1; 20.9 ± 1.4 nm (6.6% CV) and 1.6; 22.3 ± 1.2 nm (5.4% CV) and 2.8; 26.2 ± 1.9 nm (7.2% CV) and 4.3; 21.5 ± 2.4 nm (11.3% CV) and 5.0; 16.2 ± 2.4 nm (14.6% CV) and 9.0, as determined by algorithmic analysis of TEM images. The scale bar represents 100 nm and corresponds to all images in (b). For a complete list of synthetic conditions and particle dimensions. (c) Z-contrast TEM images show crystals formed from the elongated rhombic dodecahedra in (b). Images corresponding to ARs of 1.6, 4.3, 5.0, and 9.0 were sectioned (section thicknesses of 200, 400, 400, and 400 nm, respectively) to facilitate imaging. The scale bar represents 100 nm and corresponds to all images in (c). (d) Simulations show crystals of elongated rhombic dodecahedra with ARs that correspond to those in (b, c) (left to right: ARs of 1.15, 1.65, 2.85, 4.5, infinite). Images are cut through particles along the closest-packed plane and include the DNA beads that represent the sticky ends. (e) Indexed SAXS patterns correspond to the crystals in (c). From left to right, patterns index to FCC, pFCC, disordered FCC-like, BCT, mixture of BCT and HP, and HP. (f) Unit cells were determined from the corresponding SAXS patterns and EM images. Transparent unit cell box (gray) indicates a plastic crystal. The color bar indicates the series of phase changes.

DNA. As the DNA increases in length, it can become more flexible, splay, and obscure particle anisotropy.[64] Therefore, the DNA was designed to be short and rigid enough to preserve the directional interactions templated by the underlying particle. This DNA design was kept constant for all particle cores in order to isolate the role of particle anisotropy (SI Table S5). A self-complementary DNA sticky end sequence was utilized, such that all particles could hybridize to each other. In order to remove kinetic traps and study the thermodynamically-preferred state of DNA-assembled particles, samples were heated above their collective DNA hybridization temperature and slowly cooled to room temperature (0.1°C/10 min).[86] Subsequently, the structure of these assemblies was directly visualized via EM and probed via small angle x-ray scattering (SAXS).[87] Since EM requires in vacuo conditions, aggregates were transferred to the solid state through a previously reported method shown to preserve the solution-phase structure.[88] Further embedding of these solid state aggregates in a polymer resin allowed the samples to be cut into 200 – 400 nm sections to visualize particles within lattices.[54]

Rhombic dodecahedra possess 12 facets of equal surface area and thus are capable of 12 equally strong, directional DNA interactions.[55, 64] Based on shape, at the lowest AR (1.15), one would thus expect a face-centered cubic (FCC) crystal symmetry, where the 12 directional interactions enable hybridization to 12 nearest neighbors.[55, 64] An increased facet surface area, as seen for the elongated rhombic dodecahedra, should contain a proportionally greater number of DNA molecules (assuming that each facet can be functionalized with a comparable DNA density). Consequently, the DNA along elongated side facets should be able to engage in a greater number of total DNA hybridization events and thereby exhibit an increased collective DNA “bond strength.”[55] Thus, elongated

rhombic dodecahedra should be capable of four equal, directional DNA interactions on each tip and four directional interactions that increase in strength as the AR increases.

EM and SAXS of crystals formed from this library of elongated rhombic dodecahedra revealed the formation of several phase transitions (Figure 2.2). Both techniques confirm that the control sample, a rhombic dodecahedron, formed the expected FCC lattice (Figure 2.2b, c, e, f). As the symmetry of the rhombic dodecahedron breaks and particles begin to elongate (AR of 1.6), the SAXS peaks broaden, but their positions remain correlated with a FCC symmetry (Figure 2.2e). If all of the particles were uniformly oriented along their long axes, it would not be possible to maintain a cubic unit cell. Thus, particles must orient irregularly to maintain face-to-face alignment with neighboring particles (i.e. the long axes of each particle differ in orientation throughout the crystal, but are randomly rotated in 90° increments to align facets; Figure 2.2f). EM images confirm this plastic FCC (pFCC) lattice (Figure 2.2c; plasticity here refers to the irregular orientation of the particles). The loss of orientational order likely causes the increased SAXS peak breadth (Figure 2.2e). As the AR of the particles continues to increase (AR of 2.0 to 2.8), particles further lose order in the formation of a disordered FCC-like structure. Above this AR (AR of 3.5 to 4.3), SAXS indicates the formation of 2D lattices with square in-plane arrangements (indexed peaks in Figure 2.2e), and EM images reveal BCT lattices where up to 5 planes are in registry (Figure 2.2c, f). The absence of the expected 00l reflections for a BCT lattice likely results from the limited extent of three-dimensional growth. For crystals with few “layers”, these SAXS peaks would be broad and have a significantly lower intensity than peaks that correspond to in-plane ordering (Figure 2.2e). Most interestingly, a phase transition is observed as AR increases further (AR of 5.0 to

9.0), from the expected BCT lattice, to a mixture of BCT and HP lattices (AR of 5.0), and then to solely a HP lattice (ARs of 5.0 to 9.0; Figure 2.2b, d, e, f). Throughout this phase transition, particles consistently orient in a face-to-face fashion with respect to their neighbors, but the angle of this orientation shifts from 90° to 60° .

Under the hypothesis that anisotropic particles create directional interactions perpendicular to their facets, these phase transitions, and notably, the formation of a HP lattice are not intuitive. At higher ARs, one might expect that particles would crystallize similarly to rods, which form primarily planar lattices.[55] In particular, one would expect the square cross-section of elongated rhombic dodecahedra to dictate only four in-plane neighbors (i.e. square in-plane symmetry) and the potential for inter-plane registry due to face-to-face interactions of the tips (i.e. a BCT symmetry if planes are in registry). However, there are limited experiments, simulations, or models in the literature that can be used to predict (or explain) the expected crystallization behavior of the elongated rhombic dodecahedron shape. Indeed, the closest example simulates the densest packing of rectangular prism-shaped particles (without any ligands) and finds that the four-fold symmetry of the particle's long axis should drive square in-plane arrangements, in line with current understanding.[89, 90] The divergent behavior observed in our system suggests that the exact shape of the particle, or the nature of the attached DNA shell, causes deviations from this densest packing behavior. Thus, we turned to molecular dynamics (MD) simulations to provide more insight into the origin of the BCT to HP phase transition.

MD simulations can aid in understanding phase transitions in colloidal crystal engineering with DNA through the explicit simulation of DNA interactions between particles.[54, 91, 92] Each particle can be modeled based on experimental inputs for both particle shape and DNA density.[64] DNA can be similarly modeled based on experimental inputs, as a chain of beads with mechanical properties analogous to regions of single- or double-stranded DNA, with a terminal region of beads programmed to act as sticky ends.⁴⁹ Due to computational limitations, particle size and DNA length were proportionally scaled down relative to experimental inputs to enable simulation. MD simulations use these models to evaluate the stability of different crystal symmetries by initializing particles in positions that correspond to a particular lattice and then allowing them to relax to their lowest energy state. This modeling strategy has been used previously to accurately predict the DNA-driven crystallization behavior of anisotropic building blocks.[64, 91]

Simulations with these particle models predicted all experimentally observed phase transitions at corresponding ARs up to an AR of 4.5, with the exception of the disordered region (Figure 2.2d). Prediction of disordered regions can be particularly challenging for this type of simulation. Since particles begin in an ordered lattice, simulations mitigate the formation of any kinetic traps that may prevent the experimental realization of ordered structures. Despite this disparity, simulations show a phase transition occurring near an AR of 2.5, analogous to experimental results. Particles with ARs between 3.5-4.5 were initialized in either BCT or FCC lattice positions and allowed to equilibrate. FCC lattices represent three-dimensional analogs of the experimentally observed HP lattice. Within this AR range, all particles initialized in a FCC lattice rearranged into a BCT lattice upon

relaxation. Conversely, those initialized in a BCT lattice remained stable upon relaxation, as expected.

Above an AR of 4.5, explicit modeling of building blocks exceeded computational capabilities due to the large number of DNA molecules required for an accurate representation. As a result, particles with an $AR > 4.5$ were modeled as infinite square prisms (i.e. without the tip facets, Figure 2.2d). This representation reduces computational requirements, because it allows for the simulation of only a single layer of particles, and is reflective of experimental observations, where predominantly planar crystals are observed. Interestingly, infinite square prisms (approximations for $AR > 4.5$) initialized in square, analogous to a single layer along the (001) of the experimentally observed BCT structure, or hexagonal arrangements both remained stable. To understand the thermodynamic preference between BCT or HP lattices for high AR, we analyzed the number of DNA hybridization events between particles in each lattice and used this to calculate a potential energy per particle, with lower energies suggestive of more stable arrangements. Particles initialized in a HP lattice resulted in lower potential energies per particle than those in a square lattice, as seen in experiments.

To explain the phase transition from BCT to HP lattices, we used MD simulations to analyze the number and location of DNA hybridization events between particles (i.e. on an elongated side or tip facet) for different AR particles (Figure 2.3a, b). As the AR increases, the ratio of hybridization events on elongated side facets relative to tip facets increases (Figure 2.3a). In other words, in-plane particle interactions become increasingly dominant over out-of-plane interactions, likely due to the greater surface area, and thus number of DNA molecules per facet. If only in-plane hybridization events are considered

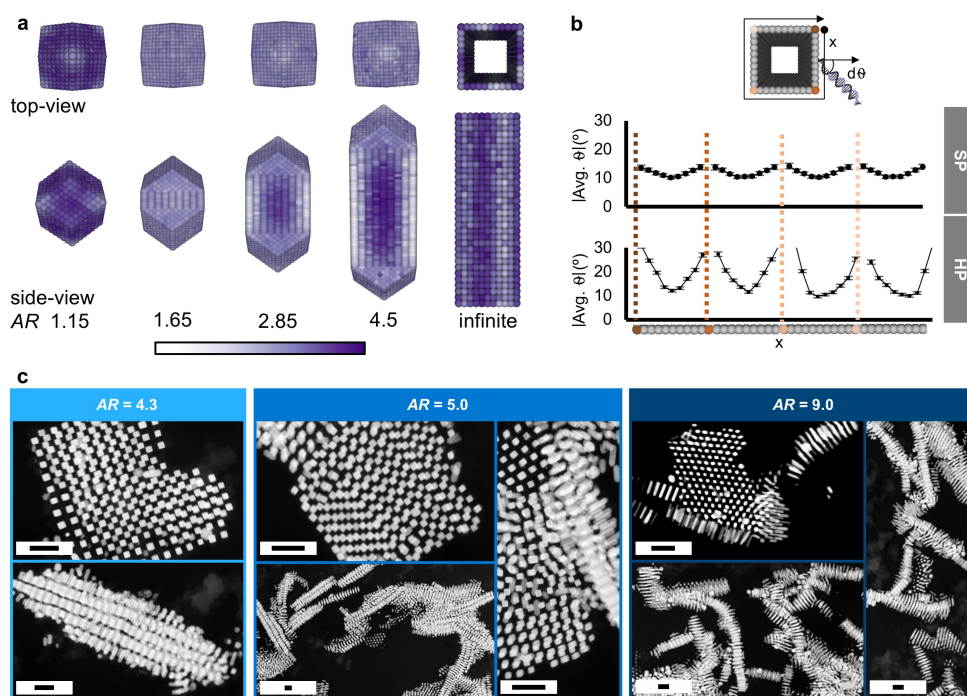


Figure 2.3. Analysis of the number and location of DNA hybridization events for high AR particles. **a** Models show the DNA hybridization probability mapped to the particle surface based on simulations initialized in their most stable lattice (FCC, FCC, BCT, BCT, HP lattices, respectively). Each point on the particle represents a bead that may have DNA attached. The darkest color indicates the maximum (0.84) and the lightest color indicates the minimum (0.17) probability that the DNA attached to the bead hybridizes to DNA on an adjacent particle. The color scale corresponds to all models. **b** Analysis of the average DNA angle with respect to the surface normal vector is shown for an infinite rectangular prism initialized in a square planar (SP) vs. HP lattice. The HP plot corresponds to the model in **a** for the infinite rectangular prism. Dashed lines indicate the location of corners. Error bars represent the standard error determined from the angle of DNA with respect to the reference vector for strands attached to 32 different beads in the same position along x over 80 discrete time steps (at equilibrium). **c** Sectioned EM images (section thicknesses of 400 nm) show BCT and HP lattices. (top) EM images show sections cut across the square cross-section of the particles (approximately parallel to the lattice plane). (bottom and right) EM images show sections cut approximately perpendicular to the lattice plane. EM images for particles with $AR=4.3$ show lattices with multiple layers in registry, while images for particles with $AR=5.0$ show multi-layer and single-layer lattices, and images of lattices formed from $AR=9.0$ particles show primarily single layers. Scale bars represent 200 nm.

for the same particle, the HP symmetry enables more hybridization events per particle than the BCT lattice. Indeed, simulations of infinite square prisms (an extreme case where tip, or out-of-plane, interactions are completely removed) verify this hypothesis. Furthermore, the four-fold symmetry of the particle tips matches the symmetry of inter-plane interactions within a BCT lattice, thereby enabling face-to-face interactions and likely a greater number of DNA hybridization events. In contrast, the symmetry mismatch between the particle tips and the HP lattice would disrupt such interactions. Therefore, tip interactions are likely key to the stabilization of the BCT lattice. These results suggest that once particles exceed a threshold AR, the energetic benefits of DNA hybridization on elongated side facets in the HP lattice begin to dominate the benefits of DNA hybridization on both elongated side and tip facets in the BCT symmetry. Sectioned EM images cut along different lattice planes support this conclusion (Figure 2.3c). For AR=4.3, these images reveal registry between multiple layers, while for AR=5.0 the number of layers decreases, and for AR=9.0 the images show primarily single layer structures.

To understand how a particle with a square cross-section breaks symmetry to engage in six nearest neighbor interactions while remaining oriented, we used MD simulations to examine the spatial distribution of sticky ends between particles (Figure 2.3a, b). Interestingly, along each elongated side facet, the DNA shell breaks symmetry to form two directional interactions – a primary face-to-face interaction comprising the majority of the DNA and a secondary face-to-face interaction involving the near-edge DNA (Figure 2.3a, b). This secondary interaction enables 66% of the simulated edge DNA to hybridize for a HP lattice, compared to only 17% for a SP lattice. Symmetry breaking of a DNA shell along a facet has been observed once previously, for cubes, where the DNA on a

single facet split into four equal face-to-face interactions as the DNA length increased.[64] In the work reported here, the symmetry breaking is distinct in the following respects: 1) the DNA shell is asymmetrically split along the facet different from both the particle (i.e. four-fold symmetry) and the lattice symmetries (i.e. six-fold symmetry), 2) a face-to-face interaction comprised of near-edge DNA is stabilized, and 3) the phase transition arises from an increase in particle AR, rather than in DNA length. This asymmetric split increases the number of DNA hybridization events between particles and likely decreases the repulsion between adjacent DNA molecules by increasing the separation distance. As a result, DNA ligands are able to drive the formation of a non-close packed hexagonal lattice that may not be predicted by densest packing simulations that account only for particle shape.

2.3. Conclusions

The ability to tune the anisotropy of nanoparticles represents a strategy to access lower symmetry lattices and to stabilize non-standard directional interactions (i.e. near-edge face-to-face). Exploration of this phase space reveals a phase transition driven by symmetry breaking of the DNA shell, which is induced by particle anisotropy. Importantly, this insight would not have been possible without precise, systematic control of a particle structure library. Going forward, the synthetic approach used here could be similarly applied to other broken symmetry particles, based on seeds comprised of one-dimensional rods (as shown here), two-dimensional plate-like particles (e.g. circular disks, triangular prisms), or three-dimensional polyhedra, or used in multi-step syntheses to create branched structures. These approaches should enable access to structures that have

yet to be synthesized or modeled and can be used as building blocks in crystal engineering with DNA. Such libraries of building blocks would offer insight into phase transitions that lead to low-symmetry lattices and would continue to push the boundaries of accessible lattice symmetries. The resulting low-symmetry lattices could be used to study and unlock access to additional metamaterial properties or afford control over optoelectronic functionality.

2.4. Methods

2.4.1. experiments

Materials. The following reagents were purchased from Sigma Aldrich and used as received: sodium borohydride (NaBH_4 , > 99%), tetrachloroauric acid trihydrate ($\text{HAuCl}_4 \times 3\text{H}_2\text{O}$, > 99%), L-ascorbic acid (AA, > 99%), silver nitrate (AgNO_3 , > 99%), potassium bromide (KBr , > 99%), dithiothreitol (DTT), concentrated hydrochloric acid (HCl , 37%), potassium cyanide (KCN , > 96%), and sodium chloride (NaCl , > 99%). The following reagents were purchased from bioWorld and used as received: cetyltrimethylammonium bromide (CTAB, > 99%) and cetylpyridinium chloride monohydrate (CPC, > 99%). The following reagents were purchased from TCI America and used as received: sodium oleate (> 97%).

Au Seed Synthesis. Au seeds (spheres and rods) with aspect ratios of 1, 3.4, and 8 were synthesized as previously reported.[81] The aspect ratio of rod seeds was tuned via addition of different amounts of $[\text{Au}^{3+}]$ and subsequent etching over 4 h at 40°C. See Supporting Information for amounts and resultant aspect ratios.

Au Elongated Nanoparticle Synthesis. Au products were synthesized through modifications to previously reported syntheses to incorporate seeds of different sizes and aspect ratios.[79] See Supporting Information for seed and reagent quantities and resultant particle statistics.

EM Image Analysis. Particle structure was analyzed through algorithmic analysis of EM images to directly measure particle edge length, aspect ratio, corner rounding, and shape yield as previously reported.[80] For structural measurements, at least 100 nanoparticles were analyzed in images taken from diverse areas of the EM grid. For yield calculations 1,000 nanoparticles were analyzed. See Supporting Information for statistical measurements of particle structure, representative EM images, and post analysis EM images where the structure of particles has been fit.

DNA Synthesis. All DNA sequences were synthesized on a solid-support MM48 synthesizer (BioAutomation) with reagents purchased from Glen Research. The resultant DNA, synthesized with a 5' trityl group, were cleaved from the support according to Glen Research procedures. DNA was purified using reverse-phase high-performance liquid chromatography (RP-HPLC; Agilent) and subsequently deprotected following standard procedures. The molecular weight of the DNA was confirmed with matrix-assisted laser desorption ionization time-of-flight mass spectrometry (MALDI-TOF-MS). Extinction coefficients for DNA were determined using IDT's "Oligonucleotide Analyzer" tool and UV-Vis spectroscopy measurements were used to determine DNA concentration. DNA was aliquoted in small volumes, dried, and kept at 2-8°C until use. See Supporting Information for DNA sequences.

DNA Functionalization. Nanoparticles were functionalized with 3' thiolated DNA according to previously reported procedures.[85, 93] After washing via three rounds of centrifugation and replacement with fresh buffer (0.5M NaCl, 0.01M phosphate buffer, 0.01 wt. % sodium dodecyl sulfate), DNA functionalization density was confirmed by liberating DNA strands through dissolution of the Au nanoparticle core with 150 mM KCN for 1 h at 40°C. Serial dilution of a solution of fresh DNA and KCN was used to create a standard curve from UV-Vis spectroscopy measurements to determine an extinction coefficient. After dissolution, each sample was measured with UV-Vis to determine the concentration of DNA. Comparison of this with an estimate of particle concentration and surface area yielded a surface density. See Supporting Information for details of these estimations and resultant DNA ligand density.

Superlattice Assembly. Nanoparticle superlattices were synthesized following previously reported methods with final nanoparticle to DNA linker ratios of 25,000 DNA molecules per particle or 50,000 molecules per particle and 0.5 M NaCl or 0.35 M NaCl.²¹ See Supporting Information for data not included in the text.

Transfer of Superlattices to Solid State. Superlattices were encapsulated in silica following previously reported procedures.[88] In order to prepare superlattices for sectioning, silica-encapsulated samples were further embedded in a polymeric resin (Embed 812, Electron Microscopy Sciences) following previously reported procedures.¹¹ Resin-embedded samples were then microtomed into 200 nm (lattices comprised of particles with an aspect ratio of 1.6) or 400 nm (all other lattices) thick sections in order to visualize particles within the lattice with electron microscopy.

Electron Microscopy. Transmission electron microscopy images of Au nanoparticles were collected using a Hitachi 8100. Scanning electron (SE) and Z-contrast mode images of superlattices were collected using a Hitachi HD2300 STEM.

SAXS Measurements. Solution phase samples were transferred to a 1.5mm quartz capillary tube. SAXS measurements were collected at the Dupont-Northwestern Dow Collaborative Access Team (DND-CAT) following previously reported methods.[94]

2.4.2. simulations

DNA-Nanoparticle Models. All nanoparticles were comprised of spherical beads, which remained bare, had an “anchor” DNA attached, or had a “linker” DNA strand attached. The DNA surface density was constant across all systems and consistent with experimental values. Moreover, effective interaction parameters, developed by Li et al.[91] and later modified by O’Brien and Girard et al.[64] were used to establish interactions between particles, including an attractive pairwise force between DNA sticky ends.

MD Simulations. All particle models were initialized in an ordered lattice and allowed to relax and equilibrate. The equilibration period was implemented using NPT integration as in HOOMD-blue.[95, 96] Particle models with ARs < 4.5 were initialized in both FCC and BCT lattices. Infinite rectangular prism models were initialized in both SP and HP lattices. A detailed description of the infinite rectangular prism model is included in the Supporting Information. Every simulation contained the same number of periods of Bravais lattices. See Supporting Information for additional simulation results.

Acknowledgements: This material is based upon work supported by the Air Force Office of Scientific Research under award FA9550-17-1-0348. This work made use of the EPIC facility of Northwestern University's NUANCE Center, which has received support from the Soft and Hybrid Nanotechnology Experimental (SHyNE) Resource (NSF ECCS-1542205); the MRSEC program (NSF DMR-1720139) at the Materials Research Center; the International Institute for Nanotechnology (IIN); the Keck Foundation; and the State of Illinois, through the IIN. This research used resources of the Advanced Photon Source, a U.S. Department of Energy (DOE) Office of Science User Facility operated for the DOE Office of Science by Argonne National Laboratory under Contract No. DE-AC02-06CH11357. M.G. was supported by the Center for Bio-Inspired Energy Science, an Energy Frontier Research Center funded by the U.S. Department of Energy, Office of Science, Basic Energy Sciences Award DE-SC0000989 (simulations and theory). H.L.R. and M.O. thank the computational support of the Sherman Fairchild Foundation. C.R.L. and M.N.O. are grateful to the National Science Foundation for a Graduate Research Fellowship.

CHAPTER 3

The nature of colloidal crystal delocalization in a size-asymmetric system

This work was a collaboration between Ali Ehlen and I. We both performed and analyzed simulations and wrote the paper. In this paper we further explore how size asymmetric particles within DNA self assembled crystals may become delocalized and still be capable of stabilizing the crystal structure. This system was introduced by [20] where he posited particle behavior to that of electrons in simple metallic solids – nuclear cores among a sea of electrons. Here we create a simplified model of such systems to study what is the nature of particle delocalization within these colloidal crystals. The crystals are comprised of a bidispersed mixture of small and large particles. Here, we only focus on a 1:6 particle number ratio of large to small particles, and tune the attractive strength of the particles to observe how small particle delocalization is affected by the system’s temperature. This leads us to study the competition between the internal energy and entropy in a direct manner.

The following was originally published in the Journal of Physical Chemistry C in 2021. It is reproduced here with permission of AUTHORS, and the PUBLISHER.

Supplementary material associated with this chapter can be found in Appendix A.

Delocalization Transition in Colloidal Crystals

Hector Lopez-Rios,* Ali Ehlen,* Monica Olvera de la Cruz

* equally contributing first authors

Reprinted with permission from:

Journal of Physical Chemistry C 2021, **125**, 1, 1096-1106, DOI:

10.1021/acs.jpcc.0c09730. Copyright 2021 American Chemical Society.

<http://pubs.acs.org/articlesonrequest/AOR-8UNXPU6QS5KATYESGAJA>

ABSTRACT: Sublattice melting is the loss of order of one lattice component in binary or ternary ionic crystals upon increase in temperature. A related transition has been predicted in colloidal crystals. To understand the nature of this transition, we study delocalization in self-assembled, size asymmetric binary colloidal crystals using a generalized molecular dynamics model. Focusing on BCC lattices, we observe a smooth change from localized-to-delocalized interstitial particles for a variety of interaction strengths. Thermodynamic arguments, mainly the absence of a discontinuity in the heat capacity, suggest that the passage from localization-to-delocalization is continuous and not a phase transition. This change is enhanced by lattice vibrations, and the temperature of the onset of delocalization can be tuned by the strength of the interaction between the colloid species. Therefore, the localized and delocalized regimes of the sublattice are dominated by enthalpic and entropic driving forces, respectively. This work sets the stage for future studies of sublattice melting in colloidal systems with different stoichiometries and lattice types, and it provides insights into superionic materials, which have potential for application in energy storage technologies.

3.1. Introduction

Binary colloidal systems, which have interspecies attraction and intraspecies repulsion, have been shown to self-assemble into a wide variety of binary lattices [8, 15, 97–99]. Generally, if the two colloid species are of sufficiently different sizes, the larger colloids will form a lattice while the smaller colloids occupy interstitial sites [14, 20, 100, 101]. In these size asymmetric colloidal systems, many cubic and non-cubic crystals have been detected, including a Frank-Kasper phase [20]. However, under certain conditions, the small particles may delocalize and roam around the crystal while the large particles remain in lattice sites; this is called sublattice melting. Previously, this behavior had been seen primarily in atomic systems, in materials termed superionics [102–104], where one ionic species delocalizes while the other stays fixed in a lattice. However, recent work has demonstrated sublattice melting in assemblies of hard spheres under pressure [100, 101], oppositely charged colloids with a Debye-Hückel potential [105], and colloids functionalized with sticky DNA chains [20]. The surprising loss of order of only the sublattice also resembles behavior found in metals. In this analogy, the small particles map to delocalized electrons and the large particles to fixed nuclei. Given the unique physical nature of this phenomenon in colloidal systems and the seeming generality of the colloidal crystals that exhibit it, we seek to understand the origin of colloidal sublattice melting using a simplified molecular dynamics (MD) model, which can provide insight into a range of systems.

To calculate reliable thermodynamic and physical quantities of delocalized systems, we developed a scalable MD model. This simplified model enables us to generalize previous work that predicted delocalization in systems of DNA-functionalized gold nanoparticles [20], where the interactions between colloid species were due to DNA hybridization, which is directional and specific. However, the experimental design also included additional free DNA chains that may have acted as depletants. To avoid complications related to DNA hybridization and to explore the generality of the phenomenon, the pairwise interactions in our model are isotropic and short-range.

The generality of this model also enables us to apply it to a wide variety of systems. This encompasses, for example, nanodots with thiols and end terminal attractive groups [106, 107], functionalized nanoparticles with light activated interactions [108, 109], and nanocomposite tectons [110–112]. In fact, nanocomposite tectons would be an ideal system for experimental verification of this study, because the parameters of the system reported in the present work can correspond to metallic nanoparticles functionalized with hydrocarbon chains with short ranged and strong complementary molecular binding pairs. Lastly, with this model, we can start to address questions that have been posed about sublattice melting in superionic materials [113, 114] such as the origin of the sublattice melting transition. However, superionic materials are constrained by the requirement of charge neutrality per unit cell, but colloidal crystals (and this model) have no such constraint.

In this paper, we study the localized-to-delocalized transition in functionalized, size asymmetric colloidal crystals. We explore the order of this transition with respect to temperature and by varying the number of chains per small particle (4, 6, 8, and 10

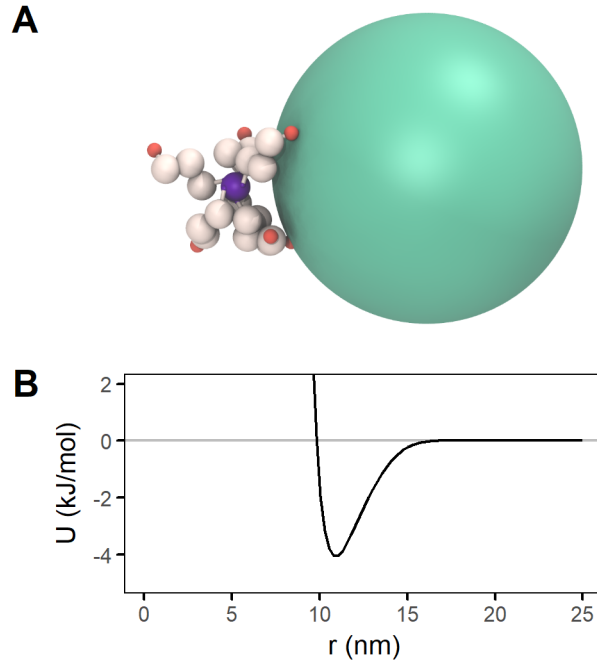


Figure 3.1. The simplified model. **(A)** The smaller colloid (purple) functionalized with chains (white) and larger colloid (turquoise) in our system, to scale. All beads have excluded volume based on their radii, and there is an attractive interaction between the large particles and the interactive ends of the small particle chains (orange). **(B)** Pair potential $U(r)$ between the centers of the large particles and the interactive chain ends. The high-energy region $r < 10$ nm represents excluded volume interactions, and the small potential well accounts for the attractive interaction. The value of U at the minimum is -4.1 kJ/mol.

chains per small particle). We focus on a system composition of 6 small particles per large particle ("6:1 ratio"), because at this composition, the large particles form a stable body centered cubic (BCC) lattice over a wide temperature range. Though other compositions exhibit interesting symmetry changes with temperature and number of chains, we use the 6:1 ratio to study the nature of the localized-to-delocalized transition without the added complexity of a change in the large particle lattice.

An image of the model is shown in Figure 3.1A. The larger colloidal species is represented by a single sphere (shown in turquoise). The smaller species is represented by a small sphere (shown in purple) grafted with a variable number of self-avoiding chains (shown in white). The only interactions in the system are excluded volume between all beads, using a Weeks-Chandler-Andersen (WCA) potential, and a generalized, attractive potential between the large particles and the interactive ends of the chains (shown in orange, referred to here as "interactive ends"); see Figure 3.1B. There is asymmetry in the interaction potential, as the range of the attractive potential is half of the diameter of the large particles. We chose to further simplify the system by representing the large species as spheres without explicit functionalized chains. This choice is consistent with colloidal systems that have previously shown sublattice melting, because these systems' large particles were either spherical [100, 105] or densely enough grafted with polymer chains [20] that a spherical potential is a reasonable approximation. However, the small particles cannot be modeled as spheres due to their higher curvature and therefore lower packing density of grafted chains. When chains are omitted and the interaction potential between small and large particles is modelled with spherical potentials, mostly FCC crystals are obtained [100, 105]. This may be because explicitly representing grafted chains on the small particles also enables spatially anisotropic interactions between the small and large particles. These can occur when chains bundle together in configurations analogous to hybridization electron orbitals present in covalent bonding called skyrmions [111, 115]. The concept of skyrmions has proved useful in explaining the appearance of non-close packed functionalized colloidal crystal structures.

With this model, we find that both size and interaction range asymmetries are needed for delocalization to occur. The passage from localized-to-delocalized small particles is fully continuous, closely related to diffusion of the small particles, and enhanced by the vibrational entropy of the large particle lattice. This continuous behavior arises from a competition between enthalpic and entropic driving forces. Here enthalpic contributions can be understood through analysis of the interaction energy landscape between the large particles and interactive beads of the small particles. Entropic contributions arise from the vibrations of the large particle lattice.

The rest of the paper is organized as follows. We begin by describing the MD simulations, as well as a theoretical model used for the free energy analysis of these crystals. We continue with a symmetry and energy analysis of relevant aspects of the BCC sublattice and its energy landscape. We then describe an analysis of the temperature-dependent thermodynamic and physical properties such as lattice parameter and specific heat per particle. We conclude by analyzing the importance of lattice vibrations as the driving force for both delocalization and lattice expansion for these crystals.

3.2. Methods

3.2.1. General description of the MD model

There are two types of pair interactions between the beads in the system. First, all beads have excluded volume interactions with each other through the WCA potential. Second, there is an attractive interaction between the interactive end of the chain and the large particles. That interaction is in the form of a Gaussian potential and is shown graphically

in Figure 3.1B and mathematically here:

$$(3.1) \quad U_{\text{pair}}(r) = \begin{cases} U_{\text{WCA}}(r) + U_{\text{Gaussian}}(r) & r \leq r_{\text{cutoff}} \\ 0 & \text{otherwise} \end{cases}$$

where

$$(3.2) \quad U_{\text{WCA}}(r) = 4 \left(\left(\frac{\sigma}{r} \right)^{12} - \left(\frac{\sigma}{r} \right)^6 \right) - 4 \left(\left(\frac{\sigma}{2^{1/6}\sigma} \right)^{12} - \left(\frac{\sigma}{2^{1/6}\sigma} \right)^6 \right) \quad \text{for } r \leq 2^{1/6}\sigma$$

$$(3.3) \quad U_{\text{Gauss}}(r) = -\varepsilon e^{-\frac{1}{2} \left(\frac{r}{\sigma_{\text{gauss}}} \right)^2} \quad \text{for } r \leq r_{\text{cutoff}}$$

where r is the distance between the centers of the large particle and the interactive end bead of the small particle chains; $\sigma = \sigma_{\text{large}} + \sigma_{\text{int. bead}}$, the sum of the radii of the large particle and the interactive bead; ε is a (positive valued) parameter that determines the strength of an individual large particle-interactive bead interaction; and σ_{gauss} is a parameter that determines the range of $U_{\text{Gauss}}(r)$. As usual, the WCA potential is cut off at $2^{1/6}\sigma$ and shifted such that U_{WCA} is zero at the cutoff, that is $U_{\text{WCA}}(r = 2^{1/6}\sigma) = 0$. The value for r_{cutoff} was selected such that $U_{\text{Gauss}}(r)$ has safely decayed to near zero by $r = r_{\text{cutoff}}$. We also used the HOOMD-blue `xplor` option which adds a subtle smoothing near r_{cutoff} such that the U_{Gaussian} decays smoothly to zero.¹

These parameters can be adjusted such that the system resembles interactions between two colloid species of choice. Additional parameters may vary are: particle size, number of chains on each small particle, temperature, system composition (ratio of small:large

¹See `md.pair.pair` documentation:

<https://hoomd-blue.readthedocs.io/en/stable/module-md-pair.html>

(a)

Parameter	Value
$\sigma_{\text{large particle}}$	10.5 nm
$\sigma_{\text{small particle center}}$	1.0 nm
$\sigma_{\text{chain bead}}$	1.0 nm
$\sigma_{\text{interactive chain end bead}}$	0.5 nm
ε	70 kJ/mol
σ_{gauss}	4.8 nm
r_{cutoff}	8.4 nm
# non-interactive beads/chain	3

(b)

Parameter	Value
small:large particle ratio	6:1
temperature	$k_B T = 0.8 - 2$ kJ/mol
# chains/small particle	4, 6, 8, 10

Table 3.1. Parameters used in the present study. **(a)** Fixed parameters (σ is radius). With these, the system resembles a binary system of weakly interacting chain-grafted colloids. **(b)** Variable parameters. Changing these allows us to explore properties of the system.

colloids in the simulation box), and length and stiffness of the chains on the small particles.

The properties chosen for the study in this paper are listed in the next section.

3.2.2. Parameters and simulation scheme

We chose parameters for the interaction of our particles to generalize the short ranged attractive potential found in self-assembled DNA functionalized colloidal crystals[19, 116–118]. DNA functionalized colloids interact by forming hydrogen bonds between the single stranded DNA at the ends of the grafted chains. Using the parameters in Table 3.1A, at $T^* = 1$, the potential well shown in Figure 3.1B has a depth of $-4.1 k_B T$, which is approximately the binding energy of hydrogen bonding in single-stranded DNA ($3 - 6 k_B T$ [117, 118]). However, given the general nature of our model, other forms of interactions found in functionalized colloidal crystals, such as dispersion interactions, can be represented with this model. Additionally, we fixed a particle size asymmetry that is in the regime in which binary solids form interstitial solid solutions (ISSs), where the smaller species occupies interstitial sites of the large species lattice. For example, in metallic binary alloys, one of the Hume-Rothery rules[119] require atomic size asymmetries where the smaller species size is ≤ 0.4 the size of the larger species in order to form ISSs. For functionalized binary colloidal particles, it was experimentally demonstrated[20] that ISSs were formed only for particle diameter ratios of 10 to 1.4 nm, while they were not formed when the smaller particles were larger.

For this study, we ran simulations of colloidal systems at different temperatures and number of grafted chains per small particle, as detailed in Table 3.1B. Varying both temperature and number of chains allows us to explore a wide range of system states. Changing the number of chains per small particle changes the total attraction strength between small and large particles, as well as the symmetry of available chain configurations. Additionally, because the attractive interaction is simple (Equation (3.3)), the

system's behavior is determined by the ratio $\varepsilon/k_B T$. Therefore, by varying temperature, we are also effectively examining the range of behavior that would appear if we instead varied interaction strength.

All simulations were run using HOOMD-blue version 2.5.1[120, 121] in the NPT ensemble with periodic boundary conditions at near-zero pressure (207 Pa, which is $\sim 2\%$ of atmospheric pressure). Using a pressure very close to zero enables us to attribute the observed crystal assembly to the interactions between colloids, rather than an external pressure [20]. Additionally, during the NPT portion of the run, the box was allowed to fluctuate in size and shape, which enabled lattices that were initialized in one crystal structure to relax into another if it was favorable to do so.

The full simulation scheme is as follows: we started the simulations in various initial lattice configurations (BCC, SC, FCC, BCT) with 6x6x6 unit cells in the simulation box. The simulations were then equilibrated, thermalized, and depressurized to their final pressure. This initial sequence lasted 312 ns. Then, the simulations were run in the NPT ensemble for an additional 8.44 μ s. For analysis, the first 1.38 μ s were considered to be an equilibration period and not included in calculation of properties. Therefore, analysis of the simulations was conducted on the last 7.37 μ s.

System topology for the simulation was built using Hoobas, [122] analysis was done in Python using MDAnalysis [123, 124] and R, visualization of the simulation was done in VMD [125] with the GSD plugin² using the internal Tachyon ray-tracing library [126] (see Figure 3.1A), and scientific plotting and calculation of isosurfaces and 3-dimensional densities (see Figures 3.3 and 3.6) was done in Mayavi [127].

²See HOOMD-blue GSD plugin for VMD at <https://github.com/mphoward/gsd-vmd>

3.2.3. Theoretical free energy of the exact soluble model

The theoretical model described in Section *Vibrational entropy drives lattice expansion* is derived by calculating the energetic environment of one interactive bead in one unit cell of a fixed BCC lattice of large particles. That is:

$$\begin{aligned}
 Z(a, T) &= \int \int e^{-U_{\text{end}}(\vec{r}, \vec{p}; a)/k_B T} d\vec{r} d\vec{p} \\
 (3.4) \quad Z(a, T) &= (2\pi m k_B T)^{3/2} \int e^{-U_{\text{potential}}(\vec{r}; a)/k_B T} d\vec{r}
 \end{aligned}$$

where $U_{\text{end}}(\vec{r}, \vec{p}; a)$ is the energy associated with the particles in one unit cell with lattice parameter a and an interactive end with position \vec{r} and momentum \vec{p} . The position of the interactive bead \vec{r} is integrated over one unit cell and its momentum $d\vec{p}$ is integrated over all real numbers (this Gaussian integral is known from the ideal gas partition function). The integral has been simplified using the definition of energy U_{end} as:

$$\begin{aligned}
 U_{\text{end}}(\vec{r}, \vec{p}; a) &= \frac{\vec{p}^2}{2m} + U_{\text{potential}}(\vec{r}; a) \\
 U_{\text{potential}}(\vec{r}; a) &= \sum_n U_{\text{pair}}(|\vec{r} - \vec{R}_n|; a) + \sum_{j < k} U_{\text{WCA}}(|\vec{R}_j - \vec{R}_k|)
 \end{aligned}$$

where $U_{\text{pair}}(\vec{r}; a)$ is the pair potential between a large particle and an interactive bead, as defined in Equation 3.1, and the sum is taken over all large particles that could influence the energy of an interactive bead at \vec{r} (\vec{R}_n indicates the position of the n th large particle). In this case, we include 15 large particles: all 9 pictured in the BCC cell in Figure 3.2A, plus the large particles in the center of all 6 non-diagonal adjacent unit cells. The range over which $U_{\text{pair}}(r; a)$ is nonzero in this model is short enough such that this captures all

interactions. $U_{\text{WCA}}(r)$ is the WCA potential between large particles; this term becomes important when a approaches the diameter of the large particles.

We then numerically integrate Equation 3.4 to find the partition function, and we can set up equations to calculate any statistical mechanical quantity that can be found with that result. For example, to calculate the average interaction energy between small and large particles, we numerically evaluate the following (assuming a is large enough that $U_{\text{WCA}}(r)$ can be neglected):

$$(3.5) \quad \langle U_{\text{potential}}(a, T) \rangle = \frac{1}{Z(a, T)} (2\pi m k_B T)^{3/2} \int \left(\sum_n U_{\text{pair}}(|\vec{r} - \vec{R}_n|; a) \right) e^{-U_{\text{potential}}(\vec{r}; a)/k_B T} d\vec{r}$$

The partition function is also used to calculate free energy using:

$$F(a, T) = -k_B T \ln(Z(a, T))$$

This model enables us to understand how the BCC energy landscape impacts system behavior, despite its simplicity. For example, it does not include lattice fluctuations. However, the lack of lattice fluctuations impacts the variance but not the mean of predicted energy values (we have seen this trend when comparing the mean and variance of the interaction energy between the fixed and fluctuating lattice cases).

Additionally, this model does not include particles other than the lattice and a single interactive bead. This is a sufficient approximation because the interaction between the small and large particles is more significant than the interaction between small particles. That is particularly true when small particles have fewer chains, because the small particles interact with 4 large particles when they sit at BCC tetrahedral sites. When there

are 4-6 chains on each small particle, each chain is, on average, attracted to one of the 4 nearby but physically separated potential wells (see Figures 3.2B and 3.2C). Therefore, their excluded volume interactions don't substantially impact their average energy values, and agreement between theory and simulation is stronger for systems with fewer chains per small particle. However, as described later, the theory's lack of bond constraints does matter. In simulation, the bonds in small particle chains don't allow interactive beads to access the lowest-energy part of the unit cell's potential wells. However, this appears to simply scale the average energy of the interactive beads, especially, as noted, for systems with fewer chains.

Lastly, note that the lattice parameter and temperature are both inputs to this partition function. It is possible that this formulation could predict some lattice expansion as a function of temperature. However, because of the differences in average location of the interactive bead between theory and simulation (due to bond constraints), we do not believe that this will be a quantitative prediction for properties of a fluctuating lattice simulation. Despite this, this theory can provide a sense of how much the lattice vibrations contribute to certain properties of a system where they are present.

3.3. Results and Discussion

3.3.1. 6:1 systems form BCC lattices with small particles localized at tetrahedral sites

For each value of chains per small particle, 6:1 systems form BCC lattices over a wide temperature range. This is consistent with findings of Girdard, et al. [20] with respect to their 6:1 systems. At temperatures below this range, we observe formation of other crystal

lattice types, and at higher temperatures, we observe liquid or gas phases; see SI for more information on determining BCC stability. At lower temperatures within the BCC range, the large particles sit at BCC lattice points and the small particles localize at the BCC tetrahedral sites, also known as 12d Wyckoff positions; these are shown in Figure 3.2A. The location of the tetrahedral sites means that each small particle can interact with four large particles simultaneously.

An analysis of the symmetry and energy associated with the tetrahedral sites reveals why small particles localize there. The potential energy of interaction between large particles and the interactive bead at the end of each chain can be seen in Figure 3.2B. Dark red indicates negative interaction energy and defines the areas most favorable for the interactive ends to occupy. Conversely, the lighter areas indicate an interaction energy of approximately zero. There are four nearly zero energy sites per face, visible in the (001) plane image in Figure 3.2B. These are the tetrahedral sites. This suggests that the small particle centers localize at the tetrahedral sites because this enables the interactive ends to access the most energetically favorable regions of the unit cell. Tetrahedral structures have also been observed experimentally. The formation of distorted tetrahedral structures between size asymmetric colloids has been reported within a specific size asymmetry range (which does not include the dimensions of our system)[128]. The experimental tetrahedral clusters, mediated by short ranged but strong potentials (both electrostatic and DNA hybridization), were explained using entropic principles. Here, enthalpy seems to be the predominant driving force for the formation of these BCC crystals.

The energy landscape shown in Figure 3.2B is a good predictor of the locations of particles in simulation. Figure 3.3A shows the probability density of the small particle

centers in a single BCC unit cell at low temperature. The small particles are clearly localized at the tetrahedral sites. Additionally, Figure 3.2C shows the probability density of the interactive ends in a low temperature simulation. The location of the highest density regions aligns well with the lowest energy positions in Figure 3.2B. A notable exception is that the limited reach of the chains in simulation does not allow the interactive beads to reach the bottom of each potential well.

Lastly, the 6:1 number ratio between small and large particles allows the tetrahedral sites to be exactly filled. This is because there are 2 lattice points (large particles) and 12 tetrahedral sites (small particles) per BCC unit cell. A lower ratio would produce vacancies in tetrahedral sites; in those cases, we observe hopping of small particles between sites. A larger ratio results in more small particles than available tetrahedral sites; in those cases, interstitial defects are prominent and full localization is not possible. Studying the 6:1 system allows us to focus on the properties of the localized-to-delocalized transition by avoid confounding factors introduced by vacancy hopping or symmetry change.

3.3.2. The localized-to-delocalized transition is smooth and its onset depends on interaction strength

Figure 3.3 shows the average visitation frequency of the small particle centers in one BCC unit cell, when localized and when delocalized. Though the system pictured has 6 chains per small particle, we see similar behavior for all values of chains per small particle: when localized, small particles occupy the tetrahedral sites, and when delocalized, they occupy a much larger volume. Even when delocalized, the small particles concentrate around the tetrahedral sites and form a pattern in which the additional volume occupied by the small

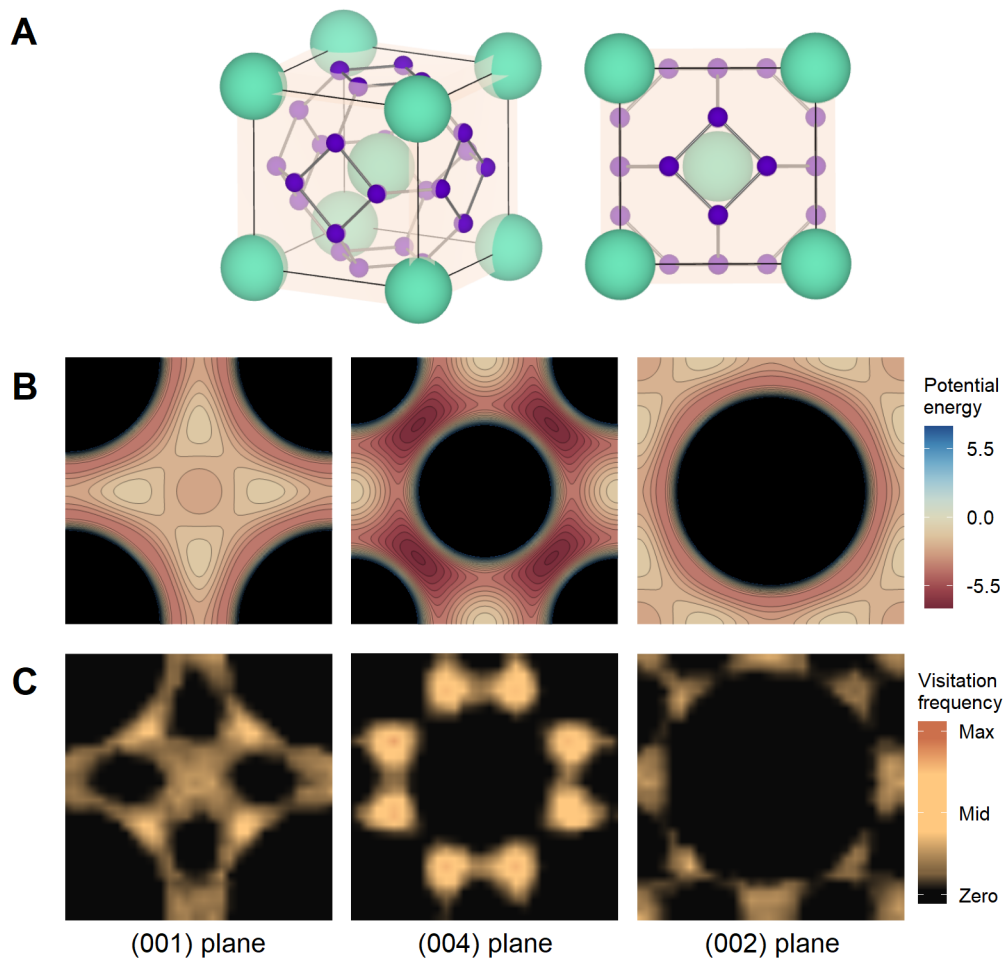


Figure 3.2. **(A)** BCC lattice sites (turquoise) and tetrahedral interstitial sites (purple) of an ideal BCC lattice. Connections between nearest-neighbor tetrahedral sites are shown as visual guides. **(B)** The potential energy landscape in different planes of one interactive end, based on its interaction potential with the large particles, in one BCC unit cell. Deeper red indicates negative values (more favorable energetic interaction), yellow indicates values around zero, and dark blue indicates positive values (unfavorable interactions; the location of large particles is shown in black). **(C)** The probability distribution of the interactive beads on different planes for the case of 6 chains at $T^* = 0.9$. Comparing this to (B), interactive bead probability is highest in areas with the most favorable energetic interactions.

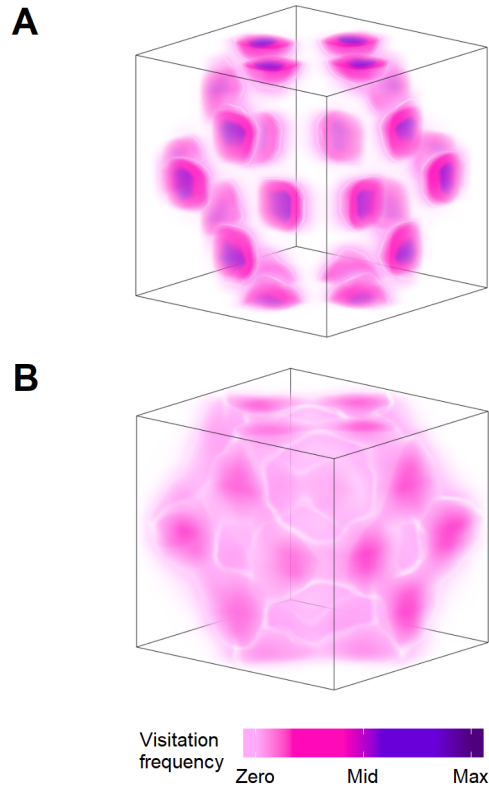


Figure 3.3. Visitation frequency of (centers of) small particles in one unit cell of localized and delocalized systems. Small particles have 6 chains, and the maximum of the visitation frequency is 0.0115. **(A)** $T^* = 0.9$. Small particles are localized on the tetrahedral sites of the BCC lattice. **(B)** $T^* = 1.6$. Small particles are delocalized. They favor the tetrahedral sites of the BCC lattice but also roam around the crystal.

particles is roughly along the edges of the BCC's Wigner-Seitz cell. This permits the small particles to move between nearest tetrahedral sites along an energetically-favorable path, equidistant to multiple neighboring lattice points.

We observe a smooth change from localized-to-delocalized behavior in all cases. Both the onset of delocalization T_{deloc} and the overall melting temperature of the lattice T_{melt} are higher with more grafted chains per small particle; see Table S1. In these systems,

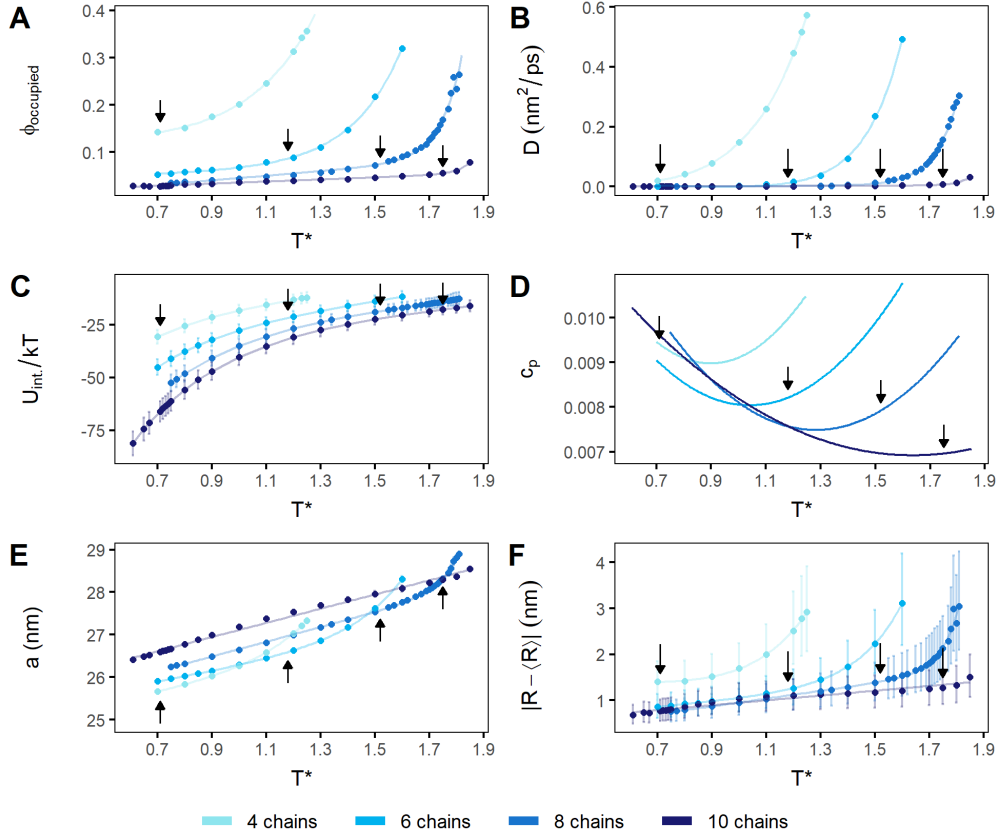


Figure 3.4. Lattice properties as a function of temperature, for all systems studied. Fits are included as visual guides. Black arrows indicate T_{deloc} , the onset of delocalization for each system; see SI for how these are identified. Note that all properties change linearly with temperature below and exponentially above T_{deloc} , with the exception of U_{int} . **(A)** Approximate volume fraction occupied by 70% of the small particles' probability ϕ_{occupied} . This is a qualitative measure of delocalization. **(B)** Diffusion constant D of the small particles. **(C)** Average interaction energy between small and large particles U_{int} , per small particle. **(D)** Specific heat at constant pressure $c_p = C_p/N$ (N is the total number of particles) of the system. These curves were calculated by fitting spline curves to mean values of enthalpy and differentiating those curves with temperature. **(E)** Average BCC lattice parameter a . **(F)** Lattice fluctuations, measured by the median displacement of large particles from their average positions. Uncertainty bars here indicate first and third quartiles, rather than standard deviation, due to the skewed nature of the underlying distribution.

the total strength of interaction between the small and large particles scales with the number of grafted chains. Therefore, we use the number of grafted chains per small particle and interaction strength interchangeably throughout this paper. Additionally, T_{deloc} approaches T_{melt} with increasing interaction strength, which means that we observe a range of behavior. In systems with 4 chains per small particle, T_{deloc} is very low, and the sublattice is delocalized at almost every reported temperature. For 6 and 8 chains per small particle, T_{deloc} is higher and the system is localized at low temperatures and delocalized at high temperatures. For 10 chains per small particle, T_{deloc} is almost equal to T_{melt} , and the small particles exhibit almost no sublattice delocalization until just before crystal melting.

In Figure 3.4, we plot structural and thermodynamic properties of the crystals to characterize their transition. These properties and their importance are listed below.

- Occupied volume fraction of the small particles, ϕ_{occupied} (Figure 3.4A), is a qualitative metric that directly measures delocalization. It represents the approximate volume occupied by 70% of the small particles' probability, as a fraction of the total available volume (see Supplementary Information for more information). In a previous study [20], delocalization was quantified using metallicity, a parameter associated to the Shannon entropy of the sublattice. Here we use a more direct parameter to measure the filling of space by small particles in the sublattice.
- Diffusion coefficient of the small particles, D (Figure 3.4B), has been used to categorize the order of superionic transitions [102]. We have observed that the localized-to-delocalized change is associated with both static properties like ϕ_{occupied} and dynamic properties like D .

- Average interaction energy of a small particle, U_{int} (Figure 3.4C), is capable of reflecting structural changes.
- Specific heat capacity, c_p (Figure 3.4D), provides insight into the order of phase transitions.
- Lattice parameter, a (Figure 3.4E), had been shown to reflect a first order phase transition in previous work in charged colloidal systems [105].
- Median lattice fluctuations (Figure 3.4F) are essential for quantifying melting through the Lindemann criterion.

All properties are plotted as a function of reduced temperature T^* , which is the value of $k_B T$ in energy units. In each panel in Figure 3.4, a black arrow indicates the approximate T_{deloc} for each system. This temperature is estimated from the diffusion properties of the sublattice; see SI for more information about how this was calculated.

Many of the properties in Figure 3.4 exhibit two trends, one during and another before delocalization. The occupied volume fraction ϕ_{occupied} , diffusion coefficient of the small particles D , the lattice parameter a , and the lattice fluctuations (Figures 3.4A, 3.4B, 3.4E, and 3.4F) all increase linearly below T_{deloc} and exponentially above, until the lattice melts. These phenomena appear correlated; particles begin to both diffuse and occupy a larger volume at the same temperatures, which is also the point at which lattice expansion and lattice fluctuations begin to increase dramatically. These ties will be explored in later sections.

The smooth increase in ϕ_{occupied} , a , and other properties suggests that the change from localized-to-delocalized small particles is not a phase transition. This is corroborated by the behavior of the specific heat of the system, c_p , shown in Figure 3.4D. We observe that c_p

of all systems is continuous and convex, indicating that no phase transition occurs during the process of delocalization. This is expected because the change from localization-to-delocalization does not reflect a change in the BCC symmetry imposed by the large particles and so the small particles' energy landscape is not qualitatively impacted.

Even though the c_p curves do not exhibit evidence of a phase transition, they provide information about the underlying energy landscape of the system. We explain the convexity of the c_p curves with the deactivation and activation of degrees of freedom into which energy can be distributed. The low temperature negative slope of these curves relates to the flattening of the local minima of the energy landscape. This flattening decreases the interactive ends' available configurational phase space, decreasing c_p . This is also why the slope is more negative for systems with higher interaction strength. At higher temperatures, new energy modes are enabled in the form of diffusion of the small particles and lattice vibrations. This eventually leads to delocalization, and c_p continues to increase until the lattice fully melts.

Notably, while the ϕ_{occupied} and a change rapidly above T_{deloc} , the interaction energy does not. Figure 3.4C shows the average "binding energy" (the energy of interaction between the large particles and interactive ends, relative to when they are infinitely far apart) per small particle in the system as a function of temperature. That this quantity increases only linearly even above T_{deloc} indicates that entropy plays an important role in delocalization. This will be discussed in Section *Vibrational entropy drives lattice expansion*.

3.3.3. Lattice fluctuations are essential for delocalization

To determine the importance of lattice fluctuations to delocalization, we ran additional simulations in which the large particles were fixed on their lattice points and not allowed to vibrate. The lattice parameter used for a given "fixed lattice" run was the mean value calculated from the unconstrained simulation with the same temperature and number of chains per small particle (Figure 3.4E). We found that without lattice vibrations, the small particles are not able to fully delocalize. This can be seen in the average visitation frequency plots in Figure 3.6. This is quantified by a large reduction in occupied volume fraction and a slight decrease of the diffusion coefficients relative to the unconstrained cases. This is similar to the finding by Schommers [103], who saw diffusion in molecular dynamics models of superionic α -AgI only when the iodine ion lattice was allowed to vibrate.

Based on these results, delocalization is driven by both lattice vibrations and diffusion. We posit that vibration-driven delocalization occurs when lattice deformation either shifts the energy landscape sufficiently such that small particles can more easily diffuse, or that large particles pull small particles between tetrahedral sites while vibrating. Vibration-driven delocalization is fully suppressed in the fixed lattice simulations; this can be seen in Figure 3.5A. However, some delocalization remains due to small particle diffusion. As can be seen in Figure 3.5B, diffusion is still present in the fixed lattice simulations and appears to primarily depend on temperature and the lattice parameter, because they determine the flatness of the energy landscape.

Analysis of the fixed lattice simulations demonstrates that delocalization is fully achieved only when both lattice vibrations and diffusion are present. The similarity

between c_p curves for the fixed and fluctuating lattice runs, shown in Figure 3.5D for the 4 chain system, underscores the importance of diffusion. With or without lattice vibrations, c_p is continuous. Both c_p curves exhibit an initial decrease characteristic of the flattening of the energy landscape but differ at higher temperatures. This is due to the lack of lattice vibrations in the fixed lattice simulations. As stated in the previous section, energy modes associated to the lattice vibrations are what drive the increase of c_p after the flattening of the energy landscape. Therefore, c_p for the fixed lattice simulations continues to decrease, whereas, the unconstrained simulations' c_p increases.

3.3.4. Vibrational entropy drives lattice expansion

Having established that lattice vibrations are crucial for delocalization, we turn to address the exponential expansion shown in Figure 3.4E. The exponential lattice expansion appears to be highly correlated with delocalization, but the reason that it occurs is unclear. To gain a better understanding, we performed a free energy analysis of our system using the same simplified theoretical model that predicted the energy landscape of a BCC unit cell in Figure 3.2B, and which is described in Section *Methods*. This theoretical model describes one interactive end in a fixed (non-fluctuating) BCC unit cell of large particles. The energy of one lattice configuration based on the temperature, lattice parameter, and position of the interactive end $U_{\text{end}}(\vec{r}, \vec{p}; a)$ is found in Equation 3.5, and is based on Equation 3.1 and Figure 3.1A. Using these definitions and a and T from simulation, we calculated the partition function $Z(a, T) = \int e^{-U_{\text{end}}(\vec{r}, \vec{p}; a)/k_B T} d\vec{r} d\vec{p}$ by numerically integrating over a unit cell. From this, we could calculate all relevant thermodynamic properties. See Section *Methods* for more information.

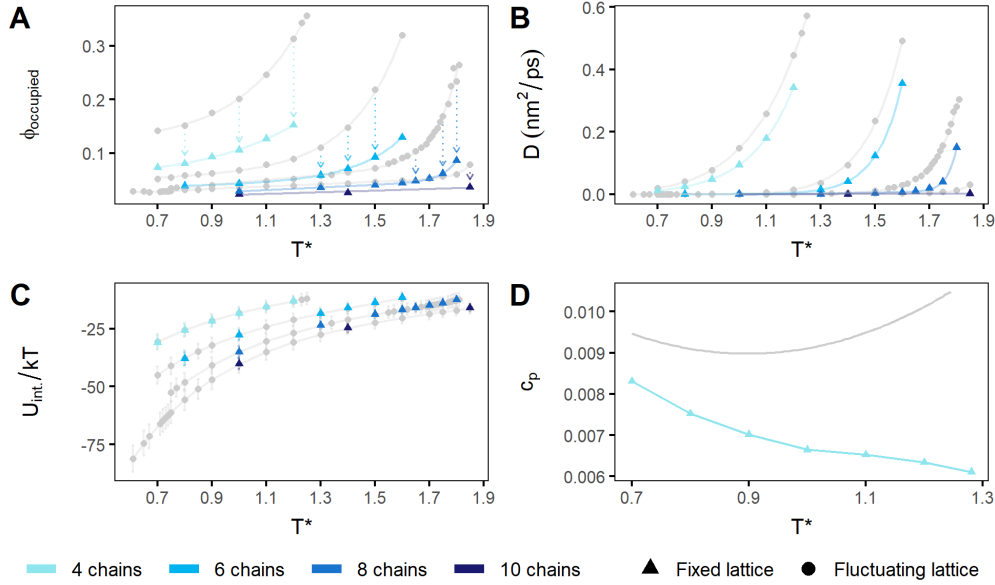


Figure 3.5. Lattice properties as a function of temperature, for fixed lattice runs (compared to unconstrained runs). Data from the main runs (also in Figure 3.4) is shown in grey circles, and data from the fixed lattice runs is shown in blue triangles. Removing lattice fluctuations substantially suppresses delocalization and minorly suppresses diffusion. **(A)** Approximate occupied volume fraction ϕ_{occupied} . Arrows connect fixed and fluctuating lattice simulations with the same number of chains per small particle as a visual guide. **(B)** Diffusion constant D of small particles. **(C)** Average interaction energy U_{int} of small particles with large particles. Because corresponding fixed and fluctuating lattice runs have the same average lattice constant, the average interaction energy of the small particles does not change, though the fluctuations of U_{int} do. **(D)** The specific heat at constant pressure c_p of the system with 4 chains per small particle.

We employed this model to explain why the lattice expands so rapidly at the onset of delocalization. To do this, we compared two cases: *(i)* exponential expansion, which is the observed behavior of the lattice, and *(ii)* linear expansion, in which the lattice expands only linearly over the entire temperature range. We ran fixed lattice simulations of both cases and compared those to theory.

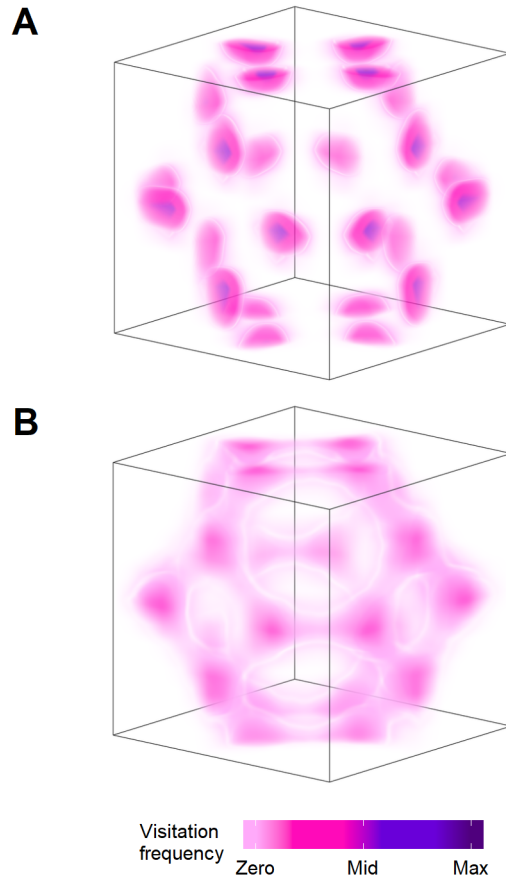


Figure 3.6. The average visitation frequency of the small particle centers in a fixed lattice system with 6 chains per small particle. The maximum of the visitation frequency is 0.0250. Without lattice fluctuations, the small particles in the delocalized case occupy less volume than when lattice fluctuations are present. Note that the unit cells of these lattices are actually different sizes, but the images have been scaled such that the two are comparable. **(A)** $T^* = 0.9$. Small particles are localized on the tetrahedral sites of the BCC lattice. This is similar to the unconstrained lattice case. **(B)** $T^* = 1.6$. Small particles are delocalized. Again, they favor tetrahedral sites but also diffuse between sites.

Figure 3.7A shows the average interaction energy per small particle in the exponentially and linearly expanding cases, for simulation (points) and theory (solid line). We

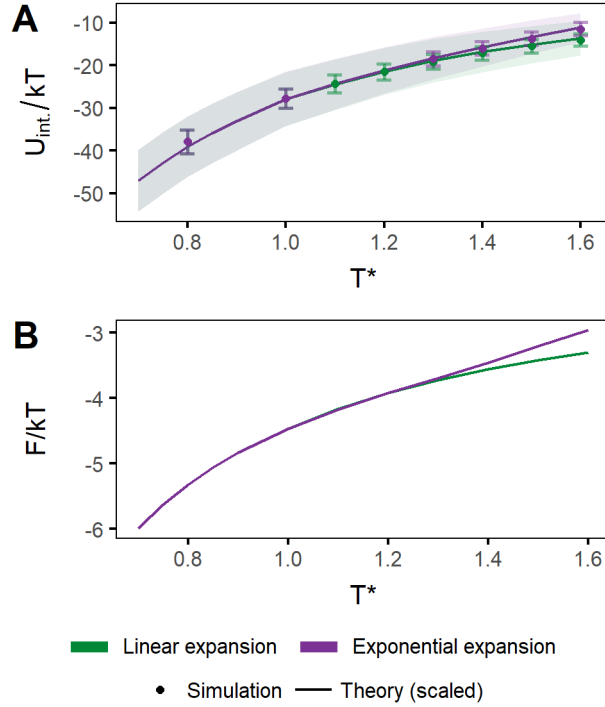


Figure 3.7. Comparison between theory and simulation (6 chain system). **(A)** Interaction energy between small and large particles. Line represents scaled theory results; points represent simulation results. **(B)** Theoretical prediction of the free energy of the systems with exponentially expanding lattice (main cases) and linearly expanding lattice. The free energy of the linear case is lower, indicating that something outside the theory must explain why the lattice expands exponentially.

find that the theoretical model accurately predicts the energy in both cases up to a multiplicative factor. In the theoretical model, the interactive energy of a single interactive end is $\langle U_{\text{potential}} \rangle = \frac{1}{Z(a,T)} \int U_{\text{potential}}(\vec{r}; a) e^{-U_{\text{end}}(\vec{r}, \vec{p}; a)/k_B T} d\vec{r} d\vec{p}$ (a summary of Equation 3.5). Because the result of this integral is the potential energy of one interactive end, we multiply $\langle U_{\text{potential}} \rangle$ by the number of chains per small particle to estimate the total energy of a small particle. For example, Figure 3.7 shows simulation results for runs with 6 chains per small particle. If the theoretical model were exact, we would multiply $\langle U_{\text{potential}} \rangle$ by

6. However, the theoretical model overestimates the average energy per small particle relative to simulation. This is due to the fact that, in simulation, the limited reach of the chains does not allow the interactive end to fully explore the lowest energy portions of the cell's potential wells (this can be seen in the comparison between Figures 3.2B and 3.2C). The result is that the interactive end's energy is about 20% lower in simulation than in theory. Therefore, the theoretical results shown in Figure 3.7A are scaled by a factor of 0.82 (this factor differs by a few percent for the case of 4 chains per small particle). Additionally, excluded volume interactions of more densely grafted chains can impact the possible configurations of the interactive ends. This effect is not observed for small particles with 4 and 6 chains, because the average energy per chain is independent of the number of chains. Meanwhile, excluded volume interactions affect particle energy to a minor extent in systems with 8 and 10 chains per small particle.

The close correspondence between small particle potential energy in simulation and that predicted by theory indicates that the theoretical model can predict differences in properties between the exponentially and linearly expanding cases. Therefore, we used this model to compare the free energies of the two cases, to understand why one is favorable. Using the partition function, we calculated the Helmholtz free energy, $F = -k_B T \ln Z$, which is plotted in Figure 3.7B. According to the theoretical model, the free energy of the linearly expanding lattice should be *lower* than the free energy of the exponentially expanding lattice, so exponential expansion should be not favorable. We conclude, therefore, that at least one of the few interactions missing from the theoretical model must be what drives the observed exponential expansion. There are three pieces missing from the

theoretical model: *(i)* excluded volume interactions due to the presence of the other particle types, *(ii)* bond constraints, and *(iii)* lattice vibrations. We have already established that excluded volume interactions do not greatly impact the average energy of the small particles. Therefore, excluded volume should not contribute to the difference between the exponentially and linearly expanding cases, especially with 4 and 6 chains per small particle. We also can account for the bond constraints by scaling the potential energy by about 0.8, as mentioned above. Additionally, bond constraints limit the reach of the interactive ends and therefore are likely to make rapid lattice expansion less energetically favorable. Therefore, it must be vibrational entropy that drives the exponential lattice expansion. Additionally, large lattice fluctuations have already been seen to stabilize BCC crystals around their melting temperatures [129], which is possible due to BCC crystals' non-close packed structure and low coordination number. Vibrational entropy becomes dominant only above a certain temperature that depends on the number of chains per small particle. This is why we see exponential expansion and delocalization at different temperatures depending on the interaction strength. Based on this analysis, we can see that lattice vibrations determine both the degree of delocalization and the thermal expansion of the lattice.

3.4. Conclusion

In summary, we have seen that the localized-to-delocalized transition in 6:1 (BCC) binary colloidal systems is continuous, dominated by lattice vibrations, and tunable by number of chains per small particle. Our results suggest that the delocalization of the sublattice in this system is not a phase transition. This is supported by the fact that

the symmetry of neither particle type changes during the transition; at all temperatures, the large particles form a BCC lattice and the small particles favor the BCC tetrahedral sites, even when delocalized. The lack of a phase transition is also evidenced by the fact that c_p is continuous for all systems. Moreover, delocalization is highly tied to vibrational entropy. Using simulations in which lattice vibrations were prohibited, as well as a free energy analysis with a simplified theoretical model, we conclude that most delocalization is driven by lattice vibrations, and that vibrational entropy is what causes the lattice to expand so rapidly above T_{deloc} . We can also see that the temperature range associated with the localized-to-delocalized transition is dependent on the number of chains per small particle, a proxy for interaction strength. The nature of the transition does not change as the number of chains per small particle does, but the presence of many chains suppresses delocalization almost entirely. Additionally, the validation between the theoretical model and simulation results reveals that the potential energy landscape of a single interactive end within a BCC unit cell is a faithful representation of the simulated system, even though we have not included other particles within the theoretical model. This is accurate because of the asymmetry of range of interactions imposed by the size asymmetry of the particles.

Based on our analysis, we can identify additional conditions that appear to be favorable for sublattice delocalization. Our findings show that delocalization tends to occur at temperatures such that the small-large particle binding energy per chain is $\sim 3 - 5 k_B T$. Per Figure 3.4C, delocalization occurs when the total interaction energy is around $22 k_B T$ /particle, distributed between all chains. This can be tuned by the number of chains

grafted to the small particles. Additionally, we posit that, for the possibility of delocalization, the small particle size must be comparable to the fluctuations of the lattice and an asymmetry of interaction ranges must exist. The attraction range between small and large particles must be greater than the repulsion range between small particles because small particles must sit at and travel between interstitial sites that are closer together than lattice points. This asymmetry is present in our model, and it can also be achieved with charged colloids given a disparity in charge magnitudes between the small and large particles [105, 130]. Note that increasing the range of repulsion between small particles may change the nature of the transition by adding correlations between small particles; however, we have not tested that here.

Under those conditions, similar analysis and conclusions may be generalized to other colloidal systems, with or without chains, but with certain caveats. For example, a more complex energy landscape with local energy minima at different interstitial symmetry points could change the nature of the transition. This could enable the small particles to transition through different symmetry points at different temperatures [113], which would be reflected in the order of the transition. This may be why previous work on charged colloidal systems [105] found a discontinuity in certain physical parameters like the lattice constant. Additionally, other compositions produce different crystal types, and a phase transition between two crystal lattices can occur as a function of temperature. This can also impact the order of the localized-to-delocalized transition. Finally, the scaling of interaction strength with number of chains per small particle may not hold at system compositions that form non-BCC crystals, because the symmetry of collective

chain configurations (impacted by the number of chains present) can affect the favorability of different interstitial points and crystal structures.

Concerning the comparison between superionics and delocalized colloidal crystals, a continuous transition has also been reported between ionic and superionic states for some superionic crystals [131]. Therefore, drawing on the superionics literature can help us understand colloidal crystal delocalization and vice versa. For example, soft vibrational modes, which are high amplitude vibrations, are reported to be important for the presence of superionic conduction, most commonly a mobile cationic interstitial within an anionic lattice. Soft vibrational modes are stabilized by non-close packed crystals already seen in superionics [113, 114] as well as in these BCC colloidal crystals. The mechanism of this phenomenon is still not fully understood in superionic materials. However, it may be possible to use results reported here by drawing an analogy between the electron density's role in the stability of the crystal and that of the potential energy landscape of our system. The two may be compared by assuming polar covalent bonding between the static and mobile species. If true, then our findings using these colloidal systems would translate to superionic materials which are relevant to applications for the improved design of solid-state batteries for energy storage [132–134].

3.5. Supporting Information

Supporting information contains: the pair distribution functions over the studied temperature range; details of the determination of T_{deloc} ; the calculation method for occupied volume and the heat capacity; and an analysis of nearest neighbor interactions (PDF).

Videos of rotating unit cells of a localized and delocalized sublattice for both unconstrained and fixed lattice simulations are also available (.mp4 videos).

Acknowledgements: This work was supported by the Center for Bio-Inspired Energy Science, an Energy Frontier Research Center funded by the US Department of Energy, Office of Science, Basic Energy Sciences under Award DE-SC0000989. H.L.-R. thanks a fellowship from Fulbright-Garcia Robles and A.E. thanks a fellowship from the National Science Foundation under grant DGE-1450006. M.O.d.l.C. thanks the computational support of the Sherman Fairchild Foundation.

CHAPTER 4

Insulator-to-metal transitions in colloidal crystals

This work was a collaboration between Ali Ehlen and I. We both performed and analyzed simulations and wrote the paper. This paper continues ideas presented in [20, 135], however we explore other number ratios not previously studied in [135]. This is with the objective of gaining a broader understanding of particle delocalization in different crystal lattices. It is in this paper that we find how delocalization sometimes drives crystal lattice transitions. We can control particle delocalization by tuning the temperature of the system or its attractive strength.

The following was originally published in Physical Review Materials in 2021. It is reproduced here with permission of INTRO, and PUBLISHER.

Supplementary material associated with this chapter can be found in Appendix B.

Metallization of colloidal crystals

Ali Ehlen,* Hector Lopez-Rios,* Monica Olvera de la Cruz

* equally contributing first authors

Reprinted with permission from:

Physical Review Materials 2021, **5**, 115601, DOI: 10.1103/PhysRevMaterials.5.115601

[https://journals.aps.org/prmaterials/abstract/10.1103/](https://journals.aps.org/prmaterials/abstract/10.1103/PhysRevMaterials.5.115601)

PhysRevMaterials. 5. 115601

ABSTRACT: Colloidal crystals formed by size-asymmetric binary particles co-assemble into a wide variety of colloidal compounds with lattices akin to ionic crystals. Recently, a transition from a compound phase with a sublattice of small particles to a metal-like phase in which the small particles are delocalized has been predicted computationally and observed experimentally. In this colloidal metallic phase, the small particles roam the crystal maintaining the integrity of the lattice of large particles, as electrons do in metals. A similar transition also occurs in superionic crystals, termed sublattice melting. Here, we use energetic principles and a generalized molecular dynamics (MD) model of a binary system of functionalized nanoparticles (NPs) to analyze the transition to sublattice delocalization in different co-assembled crystal phases as a function of temperature (T), number of grafted chains on the small particles, and number ratio between the small and large particles $n_s:n_l$. We find that $n_s:n_l$ is the primary determinant of crystal type due to energetic interactions and interstitial site filling, while the number of grafted chains per small particle determines the stability of these crystals. We observe first-order sublattice delocalization transitions as T increases, in which the host lattice transforms from low-

to high-symmetry crystal structures, including $A20 \rightarrow BCT \rightarrow BCC$, $A_d \rightarrow BCT \rightarrow BCC$, and $BCC \rightarrow BCC/FCC \rightarrow FCC$ transitions and lattices. Analogous sublattice transitions driven primarily by lattice vibrations have been seen in some atomic materials exhibiting an insulator-metal transition also referred to as metallization. We also find minima in the lattice vibrations and diffusion coefficient of small particles as a function of $n_s:n_l$, indicating enhanced stability of certain crystal structures for $n_s:n_l$ values that form compounds.

4.1. Introduction

Binary colloids of size-asymmetric particles have been shown to co-assemble into a diverse set of binary crystals [10, 14, 97, 136–140]. These crystals are compounds akin to atomic ionic crystals because the smaller particles occupy interstitial sites of a lattice formed by the large particles. Recently the exploration of binary colloidal crystals with highly size-asymmetric functionalized NPs has yielded the observation of crystal assemblies where the small NPs delocalize, rather than remaining fixed at interstitial sublattice sites [20, 135, 141]. This phenomenon was also observed in simulations of colloidal crystals of oppositely charged, highly size-asymmetric, and highly charge-asymmetric nanoparticles with screened Coulomb interactions [105, 142]. In all these systems, the delocalized and diffusive small particles keep the large particles in fixed lattice positions, as electrons do in crystalline metals. The result is a metal-like colloidal crystal.

The degree of sublattice delocalization was quantified using a normalized Shannon entropy, termed metallicity, by Girard and Olvera de la Cruz [20, 143]. They used simulations of co-assembled DNA-functionalized NPs that were highly asymmetric in size and

grafting density of complementary linkers. These showed that sublattice delocalization, and consequently metallicity, increased with T , changing the crystal from ionic to metallic. Furthermore, Girard and Olvera de la Cruz discovered a minimum in metallicity as a function of the ratio of the number of small NPs (n_s) to the number of large NPs (n_l) in the crystal. They used simple band structure construction concepts from solid state physics to explain the observed minimum in metallicity and equated metallicity to conductivity in metals [143]. In this analogy, the value n_s/n_l is the "valency," and the metallicity, akin to conductivity, decreases with increasing n_s/n_l as interstitial sites are filled until it reaches a minimum at the compound values of the lattice, when the interstitial sites are saturated (*i.e.*, $n_s/n_l = 6$ for a body-centered cubic (BCC) crystal). Upon further increase of n_s/n_l , the metallicity increases as the conductivity does in atomic systems with increasing number of electrons in the conduction band. They also highlighted that the minimum in metallicity becomes sharper with an increase in the interaction energy between the small and large NPs, achieved by increasing the number of linkers on the small NPs. They also suggested that the localization-delocalization transition in colloidal crystals can be described as a classical analog to a Mott-like insulator-metal transition (IMT) in atomic systems.

Interestingly, sublattice delocalization is also observed in non-metallic atomic systems, specifically superionic materials [102], and the transition to superionic sublattice delocalization is often termed "sublattice melting." A canonical superionic material is AgI, in which the larger atomic species I forms a BCC host lattice through which Ag ions diffuse. The Ag ions have been identified as diffusing between neighboring BCC tetrahedral

sites [103, 144], and diffusion has been seen to be strongly coupled to the dynamics of the host lattice [131, 145].

Recently, we have observed similar behavior in colloidal systems by using a generalized MD model of a binary, size-asymmetric system of functionalized NPs with $n_s:n_l = 6:1$. We reported the formation of stable colloidal BCC crystals with a diffusive sublattice of small particles translating between neighboring tetrahedral sites [135]. Similar to AgI, we observed a strong correlation between diffusion and lattice vibrations as a function of T , but we noted that the transition to sublattice delocalization is described by a smooth change, rather than a true phase transition. This suggests that phonons play an important role in the delocalization transition, and that an atomic analog to this classical localization-delocalization transition should include the effect of the interactions of the phonons with metallic electrons as in the Peierls IMT.

Here, we study the transition to sublattice delocalization at different values of the number ratio $n_s:n_l$, as a function of T and the number of grafted chains per small particle, and we examine the origin of the delocalization transition. We highlight the similarities with the IMT and with superionic sublattice melting and analyze the effect of the phonons in the localization-delocalization transition. We use the MD model established in [135] in the NPT ensemble at near zero pressure to ensure that the resulting assemblies are due to interactions between small and large particles alone. The model, consisting of mutually attractive and size-asymmetric NPs, is visually depicted in Fig. 4.1. The turquoise sphere is a coarse-grained representation of a large particle with either densely grafted chains or a functionalized surface. The small particle is represented by a central sphere (purple) and explicitly modeled grafted chains (white), each of which has an interactive terminus

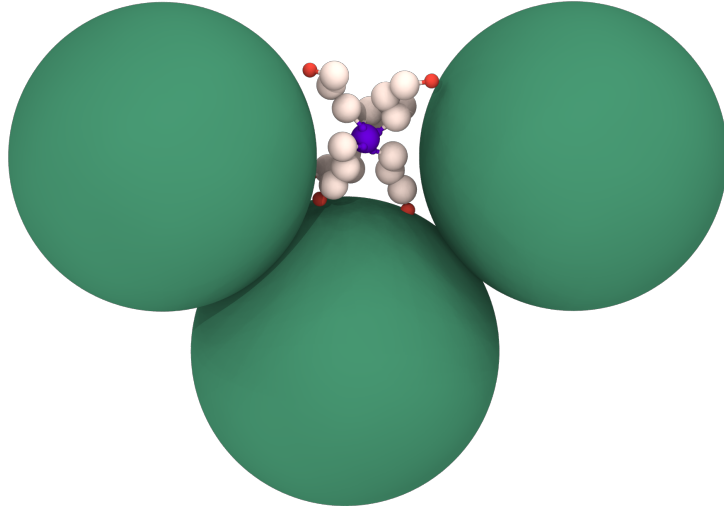


Figure 4.1. Graphical representation of the MD model. All beads have excluded volume interactions with each other, and there is an attractive interaction between the large particles (turquoise) and the interactive end of each chain (orange), as described in [135]. Note that there is no attractive interaction between large particles. Therefore, assemblies of these particles are held together exclusively by the attraction between the small particles' interactive beads and the large particles. Because the large particles represent densely grafted large particles, some overlap is permitted.

(orange) that is radially attractive only to large particles. The generality of the model implies that we can represent a variety of experimental systems [137, 138, 146–149], and the tunability of NPs enables us to find a rich variety of lattices and multiple types of delocalization transitions.

Using this model, we find that the crystal structure is determined by $n_s:n_l$ and the lattice stability is determined by the number of grafted chains per small particle. We observe a variety of crystals, including A20 and body-centered tetragonal (BCT) lattices, and we confirm that the low T (localized sublattice) positions of the small particles can be understood by analyzing their potential energy landscape. Almost all studied systems undergo a transition to sublattice delocalization with increasing T , and the type

of transition is also determined by $n_s:n_l$ based on energetic interactions and interstitial site filling. For some $n_s:n_l$ ratios, the sublattice smoothly delocalizes without undergoing a phase transition. This occurs for cubic lattices with nearly or completely full sublattice sites, near 6:1 and 10:1. For other number ratios, we observe a first-order sublattice delocalization transition accompanied by a first-order host lattice transition to a crystal of higher symmetry with inherent sublattice vacancies. This is seen in transitions from A20 to BCT, BCT to BCC, and BCC to face-centered cubic (FCC), which all occur upon increasing T . We present evidence that these transitions are entropic and driven by lattice vibrations, similar to the metallization of atomic materials driven by phonons, as in the Peierls IMT [150]. Finally, we identify minima in the lattice vibrations and diffusion coefficient of the small particles as a function of $n_s:n_l$. Crystals at the minima are those whose interstitial sites are saturated with small particles, except the high- $n_s:n_l$ FCC crystals.

This article is organized as follows. In the next section, we will describe the range of crystal lattices observed in our parameter space of 4, 6, 8, and 10 grafted chains per small particle and number ratios $n_s:n_l$ between 3:1 and 10:1, over a wide range of temperatures. We will then further detail the three delocalization behaviors we observe and discuss the implications of the diffusion coefficient minima.

4.2. Results

4.2.1. Determining crystal structure by number ratio $n_s:n_l$

At low temperatures, the large particles form a variety of lattices with the small particles localized at interstitial sites. These sites are always Wyckoff positions, which have a unique set of symmetry operators associated with the host lattice. The location of the

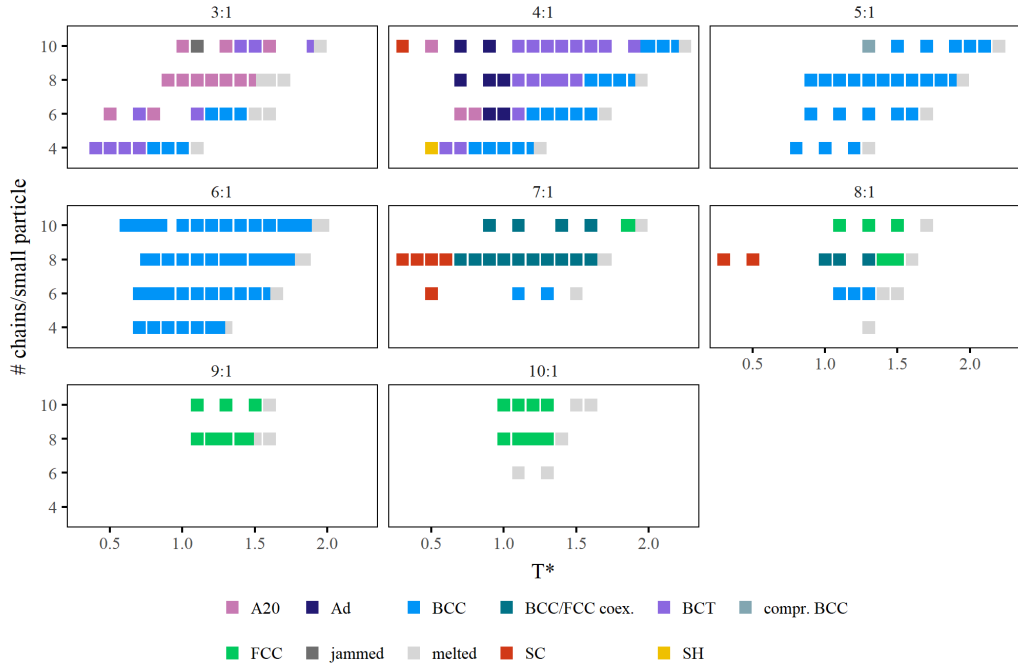


Figure 4.2. Phase diagrams of different $n_s:n_l$ values, as a function of reduced temperature T (see 4.4) and number of chains per small particle. “Coex.” stands for “coexistence” and 129a is an unknown crystal type in space group 129 defined in the Supplemental Material, Section B.2.1. The crystal structures observed only once are not analyzed in detail here. For the higher ratios where no data is shown for 4 or 6 chains, it is because no stable lattices were found. All data plotted in this paper is taken from simulations represented in these phase diagrams.

small particles at these interstitial sites is dependent only on crystal type. We find that the symmetry of the resulting lattices depends on $n_s:n_l$, and the stability of the lattice depends on the number of chains per small particle.

Table 4.1 shows the most common crystals observed in our systems and the number ratios $n_s:n_l$ that produce them, and Figure 4.2 shows a phase diagram of all simulations studied in this work. The phase diagrams demonstrate visually that $n_s:n_l$ determines crystal structure, and the crystal properties in Table 4.1 help explain trends present in

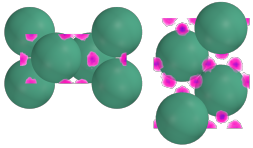
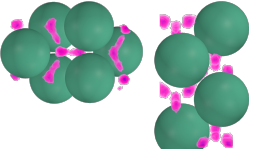
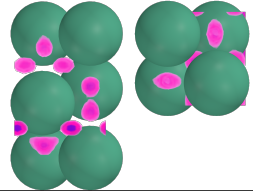
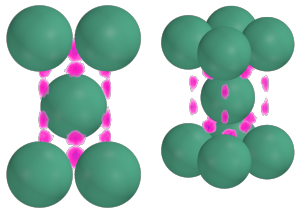
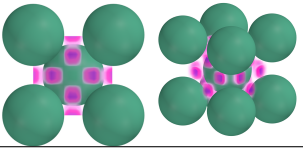
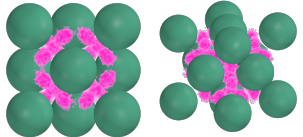
Lattice type, space group		# lattice pts/unit cell	Wyckoff position (# NNs/site)	$n_s:n_l$ ratios that result in this lattice
A20 63 Cmc _m	(3:1)  (4:1) 	4	16h, 4c (3:1 systems) or 16h, 8g ($\times 2$) (4:1 systems) (all 5 NNs)	3:1 and 4:1, resulting in different parameter ratios
A _d 129 P4/nmm		4	2c ($\times 2$), 4f, 8j (4-5 NNs)	4:1
BCT 139 I4/mmm		2	4d (4 NNs) 4e (5 NNs)	4:1 (with $c/a = 2$, as shown here)
BCC 229 $\text{Im}\bar{3}\text{m}$		2	12d* (4 NNs)	5:1, 6:1
FCC 225 $\text{Fm}\bar{3}\text{m}$		4	32f (3 NNs), 8c* (3 NNs)	9:1, 10:1

Table 4.1. Observed lattices, defined by large particles at lattice points and small particles at interstitial sites, and arranged by the $n_s:n_l$ at which they are observed with a localized sublattice. Lower symmetry lattices appear in lower $n_s:n_l$ systems, and the $n_s:n_l$ ratio at which we observe a crystal type corresponds to: #Wyckoff positions/#lattice points, on a per-unit cell basis (for example: $12/2 = 6$ for a BCC). In lower-symmetry lattices, small particles sit at Wyckoff positions with more nearest large particle neighbors (NNs) than those in higher-symmetry lattices. *12d positions in BCC crystals and 8c positions in FCC crystals are tetrahedral sites.

the phase diagrams. For example, the value of $n_s:n_l$ at which a crystal structure is observed is consistent with the ratio of the number of lattice points (large particles) to the number of interstitial points associated with Wyckoff positions (small particles) of the unit cell. Explicitly, column 4 = column 3 divided by column 2 (5:1 and 9:1 cases both contain interstitial vacancies). Note that some Wyckoff positions in A20 lattices are degenerate based on the observed lattice parameter ratios, so the A20 16h Wyckoff positions map onto 8 unique points instead of 16 and one 8g set maps onto 4 points. Table 4.1 also demonstrates that the number of large particle nearest neighbors (NNs) interacting with each small particle decreases with increasing lattice symmetry and $n_s:n_l$ ratio. This is also an important approximation to the average potential energy interactions U_{int} between the two species. In summary, the findings demonstrated in Table 4.1 and Fig. 4.2 show that decreasing $n_s:n_l$ results in lower-symmetry lattices with small particles sitting at lower-energy interstitial points.

The most common lattices are A20, A_d , high symmetry BCTs, BCC, and FCC, though simple hexagonal (SH) and simple cubic (SC) are also observed. The non-cubic nature of BCT, A_d , and A20 requires a larger set of defining lattice parameters than the cubic crystals, and we observe multiple parameter ratios for each structure. For example, most BCT lattices with $n_s:n_l = 4:1$ shown in Fig. 4.2 have the lattice parameter ratio $c/a = 2$. This is the configuration shown in Table 4.1, and it creates favorable conditions for 8 small particles in the unit cell, each of which interacts with 4 or 5 large particles depending on the site. However, some 3:1 and 4:1 BCT crystals in which the small particles have only 4 chains have $c/a = \sqrt{\frac{2}{3}}$ (not shown in Table 4.1 for simplicity). We hypothesize that the interstitial sites in the more elongated BCT structure that allow for interactions with

5 large particle nearest neighbors require the small particles to have at least 5 chains. Therefore, small particles with only 4 grafted chains cannot stabilize those elongated structures. This is supported by a Fig. B.3 in the Supplemental Material, which shows that small particles with 4 chains rarely interact with 5 large particles at once. Generally, BCT crystals only take discrete c/a ratios corresponding to lattices of higher symmetry. For more details, see the Supplemental Materials, Section B.2.1 and Section B.2.2.

A_d lattices are also tetragonal and can be visually compared to BCT lattices in which an additional symmetry is broken because the conventional unit cell's central particle is not body-centered. The A_d unit cell is defined by parameters a and c (similar to BCT) and z , which determines the offset of the central particles. When $z = 0.5$, BCT symmetry is recovered. For all observed A_d crystals $c/a = 2$. However, there is a continuous increase of the z parameter with T , from $z \sim 0.4$ at low T to $z = 0.5$ at the transition to BCT lattice with $c/a = 2$. These local spatial changes as a function of temperature indicate the capacity for these colloidal crystals to be used as reconfigurable materials.

A20 crystals are orthorhombic and yet lower symmetry and more complex than the BCT or A_d crystals. Their unit cells are defined by the ratios between a , b , and c , as well as a parameter y that determines the lattice point placement within the unit cell. We observe two A20 crystal types with different lattice parameter ratios as a function of $n_s:n_l$. All 3:1 A20s have a consistent set of parameters c/a , c/b , and y , while the 4:1 A20 have another. Each parameter set results in different numbers of interstitial sites for the small particles. Additionally, due to the low symmetry of the A20 lattice, its parameters can be tuned to produce other lattices of higher symmetry. These include those observed at

other values of $n_s:n_l$ and temperatures in this study, such as BCC and FCC. More details on all common lattices found in this study can be found in the Supplemental Material.

For almost all crystals listed in Table 4.1, a simple analysis of the potential energy landscape of a unit cell demonstrates why each lattice type is favorable at a given $n_s:n_l$ ratio. The landscapes were calculated with pairwise potentials between the large particles and one interactive chain bead, using the same method as described in [135]. The potential energy of a given point in a unit cell is the sum of the pairwise potential energy between a test particle (one interactive bead) located at that point within the unit cell and all large particles in the current and surrounding unit cells that contribute to the test particle's energy. This method only accounts for interactions between the large particle lattice and one interactive bead, and therefore does not take into account any small particle-small particle interactions or lattice vibration. However, even with these simplifications, the calculated energy landscapes can shed light on the spatial distribution of the particles. Each energy landscape shows potential energy wells (the most favorable locations for the interactive beads) and potential energy plateaus near zero (the least favorable locations for the interactive beads). For almost every lattice, the simulation results show that when the sublattice is localized, the interactive ends spend the most time in the energy wells, and the centers of the small particles spend the most time on the energy plateaus. This means we can predict the location of small particles once we know the unit cell of the large particle crystal, by identifying the location of the energy plateaus. The existence of these energy wells and their non-spherically symmetric distribution around the energy plateaus also highlights the importance of separation between the attractive component of the small particles and their cores, which in this case is due to the grafted chains.

The fact that an analysis of a static energy landscape calculated with only small particle-large particle interactions can accurately identify the locations of the small particle centers indicates that the small particles do not substantially interfere with each other. A more detailed analysis of the BCC case can be found in Lopez-Rios *et al.* [135], and a visual comparison between the energy landscape of a unit cell and the location of small particles can be found in the Supplemental Material. There is one important exception: the FCC energy landscape shows plateaus at the octahedral and tetrahedral sites (Wyckoff positions 4b and 8c, respectively). However, we observe the small particles localizing at the 32f sites, where the energy plateaus are much smaller. In our systems that result in FCC crystals, small particles never localize at the octahedral sites, and they localize at the tetrahedral sites only once the 32f sites are full (at ratios higher than $n_s:n_l = 8:1$). We hypothesize that this is because the distance from the 32f sites to the large particles is shorter than the other sites which is needed to maintain a stable crystal with our system of short-range interactions. Additionally, there are fewer 4b and 8c sites in an FCC, and for the $n_s:n_l$ ratio that would have filled those sites (3:1), there are more energetically favorable crystals available.

Finally, as the number of small particles in the lattice increases (larger $n_s:n_l$ ratios), the energetic interaction between each small particle and the surrounding large particles becomes weaker and the packing density of large particles decreases. This can be seen in Fig. 4.3, which shows the average small particle-large particle interaction energy and system density for each of the common crystal lattices observed in our system. Almost all simulations shown in Fig. 4.2 are included. The number of large particles with which

each small particle can interact decreases with increasing lattice symmetry; see the Supplemental Materials for corresponding simulation data. For example, a BCT lattice with $c/a = 2$ has 8 interstitial sites, at which the small particles can interact with 4 or 5 large particles. Meanwhile, a BCC unit cell contains 12 interstitial sites, and a small particle at any of those sites can interact with 4 large particles. Because BCT and BCC unit cells each contain 2 lattice sites, the favorable sublattice sites are fully occupied at a 4:1 number ratio for a BCT and at 6:1 for a BCC. If there are more small particles than can fit in the BCT interstitial sites, then the system's equilibrium lattice cannot be a BCT and it will instead form a BCC. This pattern holds across all number ratios: systems with larger $n_s:n_l$ ratios form crystals containing interstitial sites that are greater in number but less energetically favorable.

4.2.2. Sublattice delocalization transition entropy and dependence on interstitial site filling

We observe a transition to sublattice delocalization with increased T for almost all assembled crystals. For some values of $n_s:n_l$, the transition to sublattice delocalization is a phase transition accompanied by a change in symmetry of the large particle lattice. For others, sublattice delocalization occurs as a smooth change rather than a phase transition. In the subsequent subsections, we detail the signatures of each observed transition behavior and corresponding lattice properties.

For all values of $n_s:n_l$, we see two overarching trends. First, there is strong evidence that the transition to sublattice delocalization is driven by entropy. This is expected based on the form of the Gibbs free energy $\Delta G = \Delta H - T\Delta S$, the minimization of which

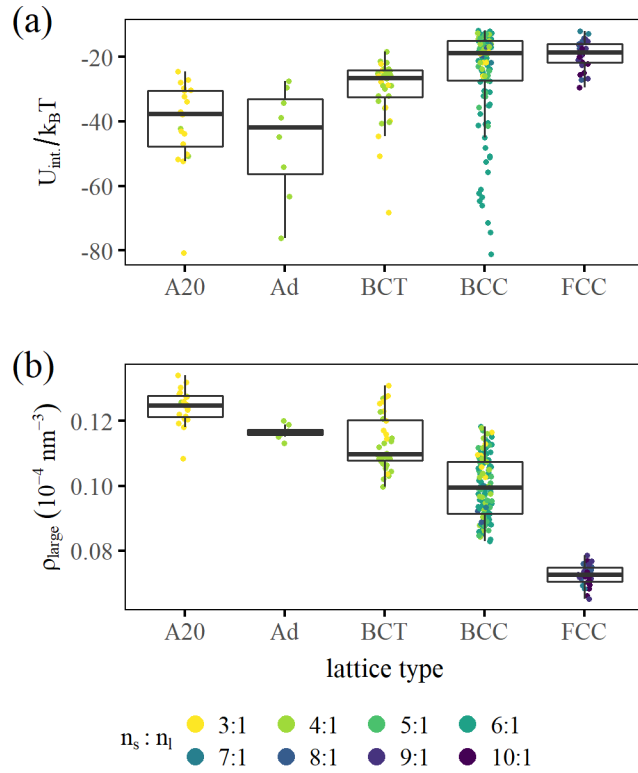


Figure 4.3. (a) Average interaction energy $U_{\text{int.}}/k_B T$ per small particle, which quantifies the potential energy due to small particle-large particle interactions, and (b) number density of the large particles ρ_{large} for each simulation that resulted in the most common crystals (A20, A_d, BCT, BCC, and FCC), arranged by crystal lattice type and colored by the value of $n_s:n_l$ to emphasize the effect of number ratio on lattice structure. Each data point represents a simulation under different conditions (temperature, number of chains, $n_s:n_l$), and the data shown comes from nearly all simulations in Fig. 4.2 that resulted in these common crystals. One very low temperature simulation with an A20 structure ($U_{\text{int.}}/k_B T < -100$) has been removed for clarity. Values of temperature and number of chains per small particle are not distinguished here.

determines the equilibrium crystal phase. ΔG is dominated by enthalpy ΔH at low T and entropy ΔS at high T . Entropic effects have also been experimentally shown to induce phase transitions of binary size-asymmetric colloidal crystals from energetically to

entropically favored phases [8]. In our systems, we see this for all types of transition to sublattice localization.

Second, increasing the chains per small particle increases the temperature at which the entropic transition occurs, effectively increasing the stability of the lattice. Crystal transition and melting temperatures increase approximately linearly with the number of chains per small particle for each value of $n_s:n_l$. Therefore, the addition of chains in most cases simply scales up the magnitude of the interaction between the large and small particles. There are a few exceptions to this rule, which will be discussed in following sections.

Note that the phenomenon of sublattice delocalization has been quantified using metallicity [20] and occupied volume fraction [135]. However, these metrics are difficult to use for comparison between crystal phases due to convergence and normalization issues. We have previously found that sublattice delocalization is highly tied to small particle diffusion and lattice vibrations quantified as median lattice displacement [135], both of which can be calculated more easily and are experimentally measurable. Therefore, we use these properties as measures of the degree of sublattice delocalization.

4.2.2.1. Phase transitions driven by lattice vibrations. For systems at low values of $n_s:n_l$, we observe a phase transition with increasing T from a localized, low-symmetry lattice to a delocalized, higher-symmetry one, specifically $\text{BCT} \rightarrow \text{BCC}$ and $\text{A20} \rightarrow \text{BCT}$. This is illustrated by a sharp increase in our two descriptors of sublattice delocalization, the diffusion coefficient (Fig. 4.4(a)) and lattice vibrations (Fig. 4.4(b)). The diffusion constant D is calculated as the slope of the mean squared displacement of the small particles, which increases linearly at long time scales. Lattice vibrations $|R - \langle R \rangle|$ are

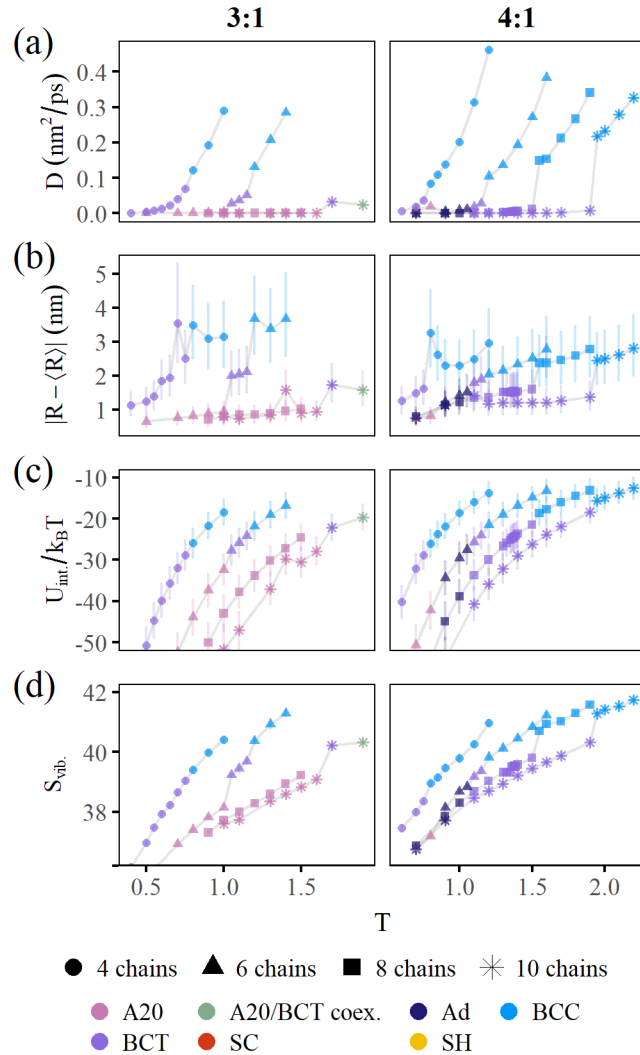


Figure 4.4. Lattice properties of 3:1 and 4:1 systems with 4, 6, 8, and 10 chains per small particle as a function of reduced temperature T (see Section 4.4). All BCT crystals shown have lattice parameters $\frac{c}{a} = 2$ except when the small particles have 4 grafted chains. (a) Diffusion constant, calculated as the slope of the mean squared displacement of the small particles in their linear (diffusive) regime. (b) Lattice fluctuations, quantified as the median displacement of large particles from their mean positions. *Post-publication note: the error bars show the fluctuations' first and third quartile. The fluctuations are not only larger, but have a larger spread, once the crystals have transitioned to BCC.* (c) Average interaction energy $U_{\text{int.}}/k_B T$ per small particle. (d) Average lattice vibrational entropy of the large particles (as they occupy the crystal's lattice points). All quantities show a jump around the phase transition to BCC crystals. Some vary low- T points not relevant to the transition have been removed for clarity.

quantified as the median of the magnitude of the displacement of large particles from their mean positions. Both of these properties increase suddenly at the temperature of a crystal lattice transition, particularly a change to BCC. It is also interesting to note that increasing the number of chains per small particle affects only the temperature at which this change occurs and does not impact the nature of the transition. That indicates that the addition of chains effectively increases the energetic interaction between the small and large particles, stabilizing the lattice against sublattice delocalization and melting. The exception to this is some systems with 4 grafted chains per small particle, which will be discussed later in this section.

The observed transitions appear to be driven by entropy, and this is consistent with the observation that crystals lose energetic interactions while gaining entropy when transitioning to a BCC with a delocalized sublattice. Fig. 4.4(c) shows the average interaction energy per small particle in each system, as a function of T . As temperature increases, the interaction energy tends closer to zero, meaning that energetic interactions become weaker and less favorable. There is also a small jump at the transition to BCC to weaker energetic interactions. This may occur for two reasons. First, the high-temperature BCC lattice is generally less dense and therefore contains weaker interactions than the low-temperature BCT lattice. Additionally, all BCTs shown in Fig. 4.4 with more than 4 grafted chains per small particle have the lattice parameter ratio $\frac{c}{a} = 2$. As indicated in Table 4.1, small particles interact with 4 or 5 neighboring large particles in this type of BCT crystal, but with only 4 in a BCC, so some lose favorable interactions transitioning to a BCC. Finally, delocalized small particles also occupy regions between interstitials

which also decreases the number of interactions with neighboring large particles, as seen in Supplemental Material, Fig. B.3.

Vibrational entropy shows a similar signature. Fig. 4.4(d) shows the lattice (large particle) vibrational entropy per large particle S_{vib} , as a function of T , with clear jumps at the transition temperature. The vibrations of the large particles in a BCT with $\frac{c}{a} = 2$ are more constrained parallel to the (001) planes due to denser packing in those planes. When the crystal transitions to a BCC, the overall density of the system decreases and vibrations can be larger and more isotropic and contribute more to the entropy of the crystal (see the Supplemental Material, Section B.3.2., for details). Other forms of entropy are larger in the BCC phase, as well. Delocalized small particles can occupy a larger volume than localized ones and therefore contribute to a larger entropy. Finally, BCCs with $n_s:n_l = 3:1$ or $4:1$ contain an average of 6 and 4 interstitial vacancies per unit cell, respectively, and therefore their sublattices also have more configurational entropy as not all sublattice sites are filled. This is because, as indicated in Table 4.1, the sublattice of a BCC is filled at $n_s:n_l = 6:1$. However, having more interstitial vacancies should increase the lattice entropy, and the stability of the crystal will be negatively impacted as the melting temperature will be decreased.

The nature of the transition can be further characterized by examining the behavior of the entropy of the system. Here, we consider S_{vib} to be representative of the total system entropy, as we know from previous work that lattice vibrations are highly tied to the other significant contributor to entropy, small particle delocalization, and it is more straightforward to calculate following [151], see the Supplemental Material, Section B.3.6. A first order phase transition occurs at a discontinuity in the first derivative of the free

energy, such as entropy. In Fig. 4.4(d), there is a sharp jump in S_{vib} at the transition to sublattice delocalization when the number of grafted chains per small particle is greater than 4, strongly hinting at a discontinuity that would indicate the presence of a first order phase transition between a localized BCT and a delocalized BCC. This is consistent with Landau *et al.* [152], who state that a first order phase transition is expected between crystal phases when the curve of an appropriate order parameter connecting two phases of differing symmetry is not continuous. While the large particles of a BCT with $\frac{c}{a} = 2$ can change continuously into a BCC, this does not appear to be possible for the small particles, based on their interstitial positions. Therefore, it appears that the transition from BCT with $\frac{c}{a} = 2$ and a localized sublattice to a BCC with a delocalized sublattice is first order. Additionally, estimates of the specific heat capacity corroborate these conclusions and are given in the Supplemental Material, Section B.3.1.

To further confirm the nature of this transition, we look to the phonon-driven IMT in vanadium dioxide (VO_2). The sudden change from an insulating to a conducting state in VO_2 as a function of T is enabled by a phase transition to a more symmetric and entropic crystal phase, in which a strong metallic electron-phonon correlation was detected consistent with a Peierls IMT [150]. Budai *et al.* identified the electron-phonon correlations using the phonon density of states, which narrows towards lower vibrational frequencies in the metallic phase, and anharmonic vibrational modes impeding the filling of lower energy orbitals only in the metallic phase. In our systems that appear to exhibit a first-order sublattice transition, we also find a bias towards lower vibrational modes in crystals with a delocalized sublattice. There is also evidence of anharmonic modes due the expanding lattice parameter of the metallic BCC crystals as a function of temperature. Finally, we

calculate a greater momentum exchange in crystals with a delocalized sublattice, which is most likely due to small particles being more homogeneously distributed throughout the crystal. See the Supplemental Materials for the vibrational density of states (following Dickey *et al.* [153]) and the momentum cross-correlation (following Verdaguer *et al.* and Ishida [154–156]) for the case of a system that exhibits a first-order sublattice transition.

The exception to this discussion is the cases in which the small particles have 4 grafted chains. In those cases, the entropy in Fig. 4.4(d) appears to be continuous but with a change in slope at the transition, indicating a discontinuity in the specific heat capacity, rather than entropy. According to Landau *et al.* [152], a discontinuity in the specific heat is to be expected for continuous phase transitions, specifically between crystal types that can continuously change into one another. While we would need more data to confidently determine the classification of this phase transition, it is also consistent with our intuition that the phase transition for 4 grafted chains per small particle be continuous. This is because the low temperature BCT crystals have $\frac{c}{a} = \sqrt{\frac{2}{3}}$ when the small particles have only 4 grafted chains. As discussed in Section 4.2.1, we believe that small particles with only 4 grafted chains cannot stabilize a BCT with $\frac{c}{a} = 2$. However, for BCT with $\frac{c}{a} = \sqrt{\frac{2}{3}}$, the interstitial sites appear to be such that it is possible for both the small and large particles to continuously change to their BCC lattice sites. Note that the 3:1 system with 4 chains per small particle also transitions through an unclassified BCT; see Fig. B.1 in the Supplemental Material for more information.

Finally, other low-temperature transitions between crystal types are shown in Fig. 4.4, for example $A_{20} \rightarrow \text{BCT}$ and $A_d \rightarrow \text{BCT}$. These transitions exhibit interesting changes in

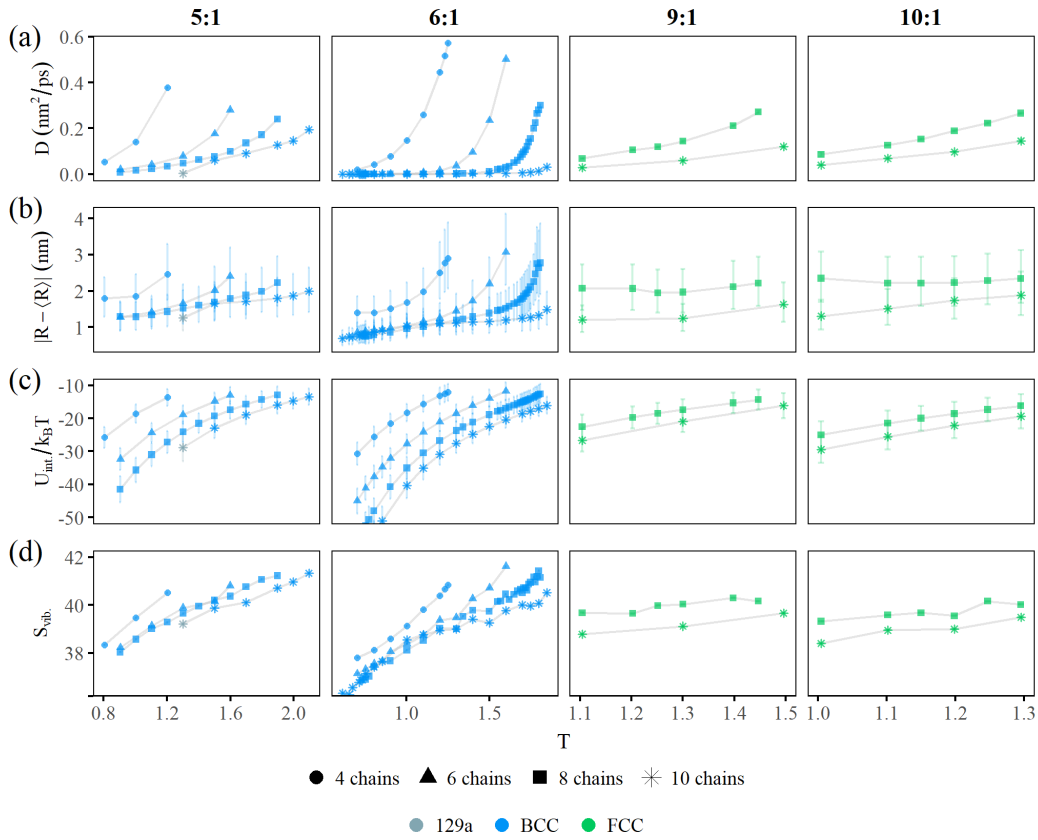


Figure 4.5. Lattice properties of 5:1, 6:1, 9:1, and 10:1 systems with 4, 6, 8, and 10 chains per small particle as a function of reduced temperature T (see 4.4). Data from the 6:1 system is taken from [135] and included for comparison. (a) Diffusion constant. (b) Lattice fluctuations. (c) Average interaction energy $U_{\text{int.}}/k_B T$ per small particle. (d) Average lattice vibrational entropy of the large particles. All show a smooth increase in diffusion and lattice vibrations, indicating a change to delocalization similar to that explored in the 6:1 system.

symmetry; however, we do not study those changes here because they are not accompanied by a change in sublattice delocalization.

4.2.2.2. Smooth change to sublattice delocalization driven by stoichiometry.

At $n_s:n_l$ near the stoichiometric values for BCC crystals (6:1) or FCC crystals (10:1), the transition to delocalization of the small particles is gradual and not a true phase

transition. In these cases, the sublattice delocalizes slowly over a range of temperatures and the large particle lattice never changes structure. This can be seen in Fig. 4.5. Note that, again, as T increases, diffusion and vibrational entropy of the large particles increase at the expense of the magnitude of the interaction energy. We hypothesize that this is because the BCC and FCC lattices are the most symmetric and stable crystals available to systems at lower and higher $n_s:n_l$ ratios, respectively. Specifically, BCC lattices are entropically stabilized at high T [129, 157], so we do not expect a BCC to transition to another crystal with increasing T as long as the number of small particles does not exceed the number of interstitial sites (*i.e.* a number ratio greater than 6:1). At higher number ratios, which would otherwise result in BCC lattices with interstitial defects, FCC crystals are stable simply based on stoichiometry. This will be discussed further in the next subsection.

The 6:1 system is an exemplar of this behavior and has been studied in detail by Lopez-Rios *et al.* [135]. The conclusions of that study were that lattice vibrations and sublattice delocalization are strongly tied, and the temperature of the onset of both is dependent on the number of chains per small particle. We have found this to be true in general for systems that do not exhibit a lattice transition with temperature.

4.2.2.3. Phase transition driven by interstitial defects. For systems with $n_s:n_l = 7:1$ and $8:1$, between the stoichiometric number ratios for BCC and FCC, we observe a stable two-phase coexistence between a localized BCC and delocalized FCC. Coexistence is an indication of a first-order transition between the two phases, and an example is in Fig. 4.6. Experimental evidence of a BCC/FCC mixture in colloidal crystals was reported

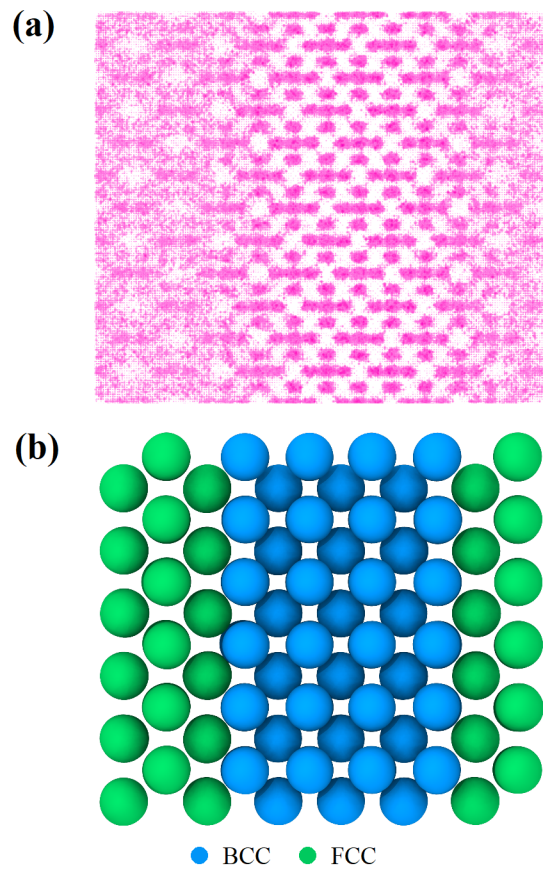


Figure 4.6. BCC/FCC coexistence in a simulation with $T = 1.6$, 8 chains per small particle, and $n_s:n_l = 7:1$. Stable localized BCC and delocalized FCC portions can be seen in (a) a snapshot of the locations of the small particle centers and (b) the averaged positions of the large particles, colored by crystal phase.

at a small particle-large particle number ratio between those required for fully BCC or fully FCC crystal structures [20].

FCC lattices in these systems appear only at high number ratios (7:1, 8:1, 9:1, 10:1), as can be seen in Table 4.1. This is also consistent with Girard *et al.* [20], who observed FCC lattices when the concentration of small particles in solution was high. In our 7:1 and 8:1 systems, the FCC phase appears to be the result of interstitial defect attraction. It has

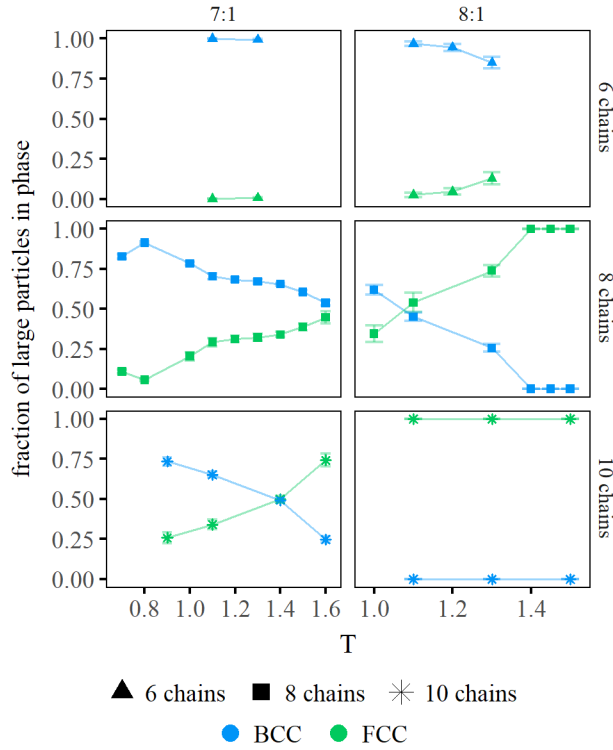


Figure 4.7. Fraction of large particles in the simulation in the BCC and FCC phases for 7:1 and 8:1 systems. The small portion of particles in neither phase is not shown. Increasing both reduced temperature T and number of chains per small particle increases the percentage of the delocalized FCC lattice. These compositions were tested for stability with annealing techniques and at multiple system sizes.

been established that BCC lattices with small particles localized at the usual tetrahedral sites ($n_s:n_l = 6:1$) are stable. At a $n_s:n_l$ of 7:1 or 8:1, however, a fully BCC system would contain 2-4 interstitial defects per unit cell, which is energetically unfavorable. As has been demonstrated by van der Meer *et al.* [101], interstitial defects in colloidal systems show long-range attraction. Therefore, the defects in the BCC system gather when there are strong small particle-large particle interactions (8 and 10 chains per small particle). At very low temperatures, they collect at a grain boundary; a snapshot of this is shown

in the Supplemental Material, Fig. B.8. At moderate and high temperatures, they collect and expand the lattice, resulting in a FCC phase with a delocalized sublattice coexisting with the BCC phase with a localized sublattice. This is consistent with Fig. 4.7, which shows that 8:1 systems have a higher FCC fraction at a given T and number of chains per small particle.

As can also be seen in Fig. 4.7, increasing T results in an increased fraction of the system in the FCC phase. This indicates that the transition between a localized BCC and delocalized FCC is at least in part driven by entropy. Each small particle interacts with 4 large particles in a BCC lattice when localized and only 3 in an FCC lattice (and even fewer when delocalized due to spending less time at energetically favorable sites). Therefore, the transition from the BCC phase to the FCC phase results in an energy penalty, which is compensated for by a gain in entropy in the form of small particle mobility and lattice vibrations in the FCC phase.

Lastly, increasing the number of chains per small particle results in a higher FCC fraction, which deviates from the general rule that adding chains simply increases lattice stability. We hypothesize that this is due to the difference in the unit cell energy landscape between the BCC and FCC lattices. The energy landscape of the FCC is overall shallower and more homogeneous than that of the BCC, as there is little overlap between the attractive regions around the large particles (see the Supplemental Material, Table B.1, for comparisons). In contrast, the BCC unit cell energy wells are deep and localized in spaces between large particles. Therefore, it may be that small particles interact favorably only with FCC energy landscapes when there are more chains and when those chains are configured more isotropically. This may explain why size-asymmetric binary colloidal

systems composed of spherical particles have only seen FCC lattices [100, 105] and why other crystals such as BCC have been observed only with the existence of flexible chains on the small particles [20, 135].

4.2.3. Stability as a function of number ratio $n_s:n_l$

Overall, crystals are more stable and have lower sublattice delocalization when small particles saturate their interstitial sites. This is highlighted in Fig. 4.8 and Fig. 4.9, which show diffusion and lattice vibrations as a function of $n_s:n_l$ for systems with different T -chain number combinations. For clarity, data is separated by whether there is a crystal phase transition as a function of $n_s:n_l$. A minimum in both quantities appears at 3:1, 4:1, and 6:1 (for the 3:1, 4:1 and 6:1 systems that form BCC, A20 and BCT lattices with a fully saturated sublattice). Meanwhile, the 5:1 (BCC crystals) and 9:1 (FCC crystals) ratios both contain inherent vacancies that diffuse, since BCC and FCC interstitials are fully occupied at 6:1 and 10:1 ratios, respectively. Additionally, according to Table 4.1, FCC lattices and their interstitials are less tightly bound than in BCC lattices and therefore should show more delocalization at a given T . It is not included, but lattice vibrations also show minima at 3:1 and 6:1 ratios.

The predominant appearance of BCC lattices over the entire phase space explored may be due to their stabilization by entropy [129]. Their lattice vibrations are isotropic and this garners them additional structural stability as a function of temperature that enables a larger degree of sublattice delocalization than other lattices. For similar reasons, BCC lattices have been suggested as optimal superionic conductors in atomic systems [113].

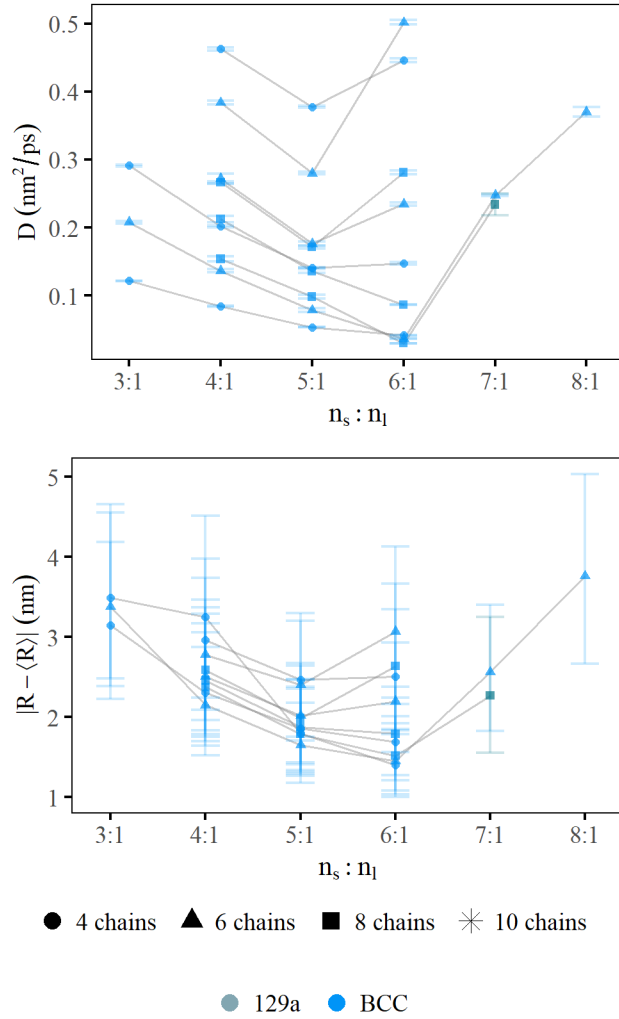


Figure 4.8. (a) Diffusion coefficients D and (b) lattice vibrations as a function of $n_s:n_l$ for simulation groups that do not exhibit a phase transition. Both D and lattice vibrations both show a minimum at 6:1, similar to the metallicity found by Girard *et al.* [20]. Lines connect points with the same value of T and number of chains, and lines are not drawn between non-adjacent points, or if any number of chain- T combination has fewer than 3 data points. Though it is not visually depicted, higher values of D and lattice vibrations for a given number of chains correspond to higher temperatures. *Post-publication note: The error bars here show the first and third quartiles of D and $|R - \langle R \rangle|$.*

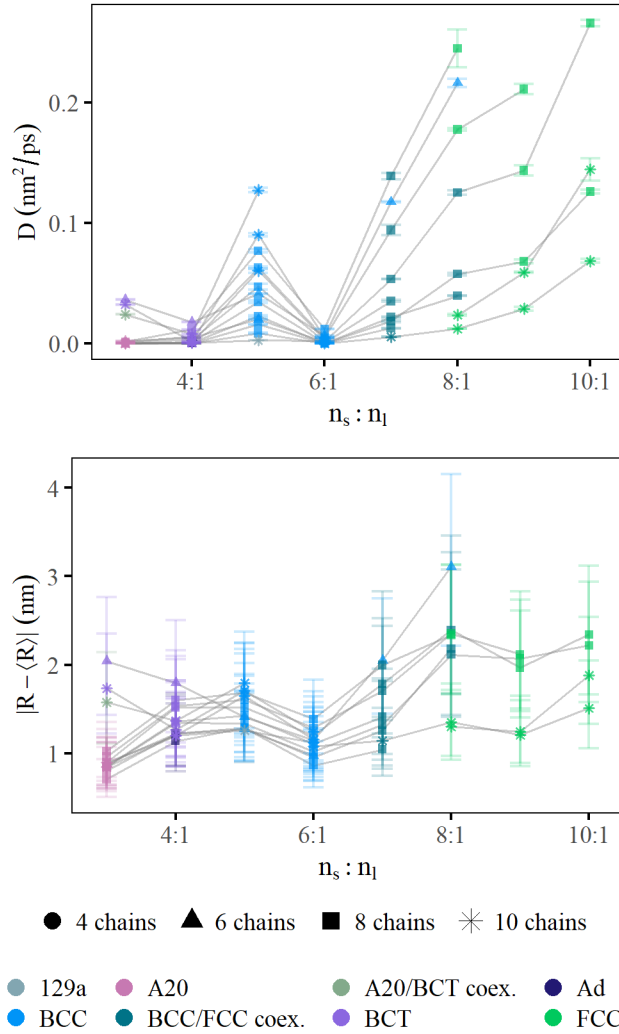


Figure 4.9. (a) Diffusion coefficients D and (b) lattice vibrations as a function of $n_s:n_l$ for simulation groups that do exhibit a phase transition. Both quantities show minima at number ratios corresponding to compound values for BCC and A20 crystals. Lines connect points with the same value of T and number of chains, and lines are not drawn between non-adjacent points, or if any number of chain- T combination has fewer than 3 data points. Though it is not visually depicted, higher values of D and lattice vibrations for a given number of chains correspond to higher temperatures. *Post-publication note: The error bars here show the first and third quartiles of D and $|R - \langle R \rangle|$.*

4.3. Discussion and conclusions

In summary, highly size-asymmetric binary colloids assemble into a variety of crystals that exhibit varying levels of sublattice delocalization. For temperatures at which the sublattice is localized, the crystal structure is determined by energetic interactions between the small and large particles. Crystals with a lower number ratio $n_s:n_l$ form lower-symmetry crystals whose unit cell potential energy landscapes contain many deep wells. As $n_s:n_l$ increases, crystals become more symmetric and the wells become shallower. As a function of T , we observe different types of entropically driven transitions to sublattice delocalization. In some cases, this transition occurs along with a symmetry change of the large particles, always from a lower-symmetry lattice to a higher-symmetry lattice containing more interstitial vacancies. In others, when the lattice is in a cubic configuration (these are entropically stabilized) or already contains inherent vacancies, there is not a phase transition to sublattice delocalization but rather a smooth change.

Additionally, we observe the appearance of different crystal lattices as a function of $n_s:n_l$ at constant T . This is consistent with experiments using DNA functionalized NPs [20, 141] even though hybridization DNA chemistry employed in those studies complicates experiments by including the presence of non-hybridized DNA chains that could act like depletant particles [20, 141]. In particular, the transition we found from BCT to BCC as $n_s:n_l$ increases agrees with Fig. 3 of Cheng *et al.* [141]; note that in [141], "valency" is the number of linkers per small particle and not the number ratio of small ("electron equivalent") particles to large particles as it was defined in [143] and in Fig. S29 in the SI of [20].

We report minima as a function of lattice vibrations and the diffusion constant of the small particles as a function of $n_s:n_l$ in Fig. 4.9 and Fig. 4.8. It is tempting to compare these minima to the minima in metallicity identified by Girard and Olvera de la Cruz [20], which were found for each crystal phase (BCC, FCC, and Frank-Kasper A15) and which correspond to the compound value of $n_s:n_l$ for that phase. The behavior of the lattice vibrations and diffusion constants is similar, indicating that these reflect the same underlying phenomenon. However, we found that it is difficult to compare metallicity values between phases due to normalization and numerical convergence issues; using the more physically measurable values resolves these problems. Plotting indicators of sublattice delocalization in multiple phases on the same axis allows us two additional insights. First, this enables us to compare behavior between phases. We find that there are still minima at the saturation values for some lattices (A20, BCT, and BCC), but that the minimum for FCC found in [20] does not appear because competition between BCC and FCC phases allows for a coexistence not seen in [20]. Second, we see that the studied assemblies are generally more stable in the form of a BCC lattice, whether their sublattice is localized or delocalized. Most of the low-symmetry crystal phases transition to BCC at high temperatures, and BCC only fully transitions to FCC when the number of interstitial defects is very high. BCC's greater structural stability is consistent with observations that BCC crystals are entropically stabilized near their melting point in colloidal assemblies [129] (even without a sublattice). For these systems, the result of BCC lattice stability is that these crystals can maintain a delocalized sublattice for a wider range of temperatures than other crystals. Additionally, Wang *et al.* predicted that superionic materials with a BCC structure should exhibit the highest conductivity [113],

which is of particular interest for applications in solid-state batteries. Our results agree with this for the case of NPs and confirm the stability of BCC colloidal crystals with delocalized sublattices.

It is intriguing to find similar behavior at multiple length scales, from sublattice melting in superionic materials to the insulator-metal transition (IMT) in inorganic materials to sublattice delocalization in colloidal binary crystals. Although colloidal systems are more flexible and tunable due to the lack of any sort of charge neutrality constraint on composition, they exhibit similarities to superionic materials in both structure and dependence on lattice vibrations, explored previously by Lopez-Rios, *et al.* [135]. There are also structural and delocalization transition analogs between colloidal crystals and materials exhibiting an IMT. For example, at low T and 4:1 number ratio, crystal phases resemble the actinide crystal structures, where increasing the number of chains per small particle is analogous to increasing the atomic number. Systems with 4, 6, and 8 chains per small particle assemble into BCT ($c/a = \sqrt{2/3}$), A20, and A_d lattices, which have the same symmetry as protactinium, α -uranium, and β -neptunium, respectively. Increasing T of these and other systems, we observe a transition to sublattice delocalization strongly driven by lattice vibrations. When accompanied by a change of lattice symmetry, this resembles a Peierls IMT, a transition driven by strong correlations between phonons and metallic electrons. For colloidal crystals, this can be thought of as a continuous pumping of momentum of the vibrating large particles to the diffusing small particles. As crystals become more symmetric, lower vibrational frequencies are available, which prolongs the exchange of momentum between the two species given their large vibrational wavelengths. Such tunability as a function of T makes these colloidal crystals possible candidates for

exploration as colloidal photonic crystals [158, 159]. There are other types of IMT, such as the Mott IMT, which is driven by the interactions and correlations between the smaller species. We observe stronger sublattice localization as a function of $n_s:n_l$ with a greater number of grafted chains, which is similar to the behavior of metallicity [143]. This may be seen as a Mott-like transition, where the delocalized lattice may be suppressed by the addition of grafted chains on the small particles as was alluded by Girard *et al.* [143]. However, in some cases, the addition of grafted chains may also change the crystal lattice structure, which complicates this analogy.

There is still more to explore. It is possible that by including the deformability of the large particles, one might increase the range of accessible phases such as the Frank Kasper A15 phase [20]. Furthermore, given that lattice vibrations drive the transition to sublattice delocalization and between host lattices, it would be interesting to consider how impinging acoustic waves or acoustic shock waves would affect the properties of these colloidal crystals for further applications.

4.4. Simulation methods

In the model, as described in Fig. 4.1 (and also in [135]), we change the temperature T , the number of chains per small particle, and the small particle-large particle number ratio $n_s:n_l$. Temperature T is expressed in reduced units, such that $T = \frac{k_B T'}{\varepsilon}$, where T' is the input temperature and ε is the energy unit of the simulation, in our case $T = 1 = 5/3$ kJ/mol.

All simulations were conducted at constant number of particles N , temperature T , and pressure P . The pressure P was the same in all simulations, $P = 2$ Pa (approximately

2% of atmospheric pressure). Simulations at low P simplify the possible contributions to the formation and stability of a crystal such that only two terms remain, energetic and entropic. The pair potential interactions within our model arise from an attractive Gaussian potential between large particles and the termini of the grafted chains $U_{\text{Gaussian}}(r)$ (Eq. 4.1), as well as excluded volume interactions amongst all particles, modeled using the Weeks-Chandler-Andersen (WCA) potential $U_{\text{WCA}}(r)$ (Eq. 4.2). The grafted chains are bonded with harmonic potentials, and no angle or dihedral potential is employed. We also used the HOOMD-blue `xplor` option which prevents artificial discontinuities in $U_{\text{Gaussian}}(r)$ as it decays to zero. Parameters used are shown in Table 4.2.

$$(4.1) \quad U_{\text{Gauss}}(r) = -\varepsilon e^{-\frac{1}{2}\left(\frac{r}{\sigma_{\text{gauss}}}\right)^2} \quad \text{for } r \leq r_{\text{cutoff}}$$

$$(4.2) \quad U_{\text{WCA}}(r) = 4 \left(\left(\frac{\sigma}{r} \right)^{12} - \left(\frac{\sigma}{r} \right)^6 \right) - 4 \left(\left(\frac{\sigma}{2^{1/6}\sigma} \right)^{12} - \left(\frac{\sigma}{2^{1/6}\sigma} \right)^6 \right) \quad \text{for } r \leq 2^{1/6}\sigma$$

where $\sigma = R_A + R_B$ is the sum of the radii of the interacting species.

All simulations were initiated with $6 \times 6 \times 6$ unit cells in the simulation box with either an FCC or BCC lattice with lattice parameter $a = 60$ nm. They were all energetically and thermally equilibrated using NVE integration and later Langevin integration, respectively, then depressurized to their final pressure. This sequence lasted 312 ns. Finally, the simulations were run at their final pressure $P = 2$ Pa for at least 8.44 μs , the first 1.38 μs of which was considered an equilibration period and not used for analysis. Simulation code is available upon request.

Parameter	Value
$R_{\text{large particle}}$	10.5 nm
$R_{\text{small particle center}}$	1.0 nm
$R_{\text{chain bead}}$	1.0 nm
$R_{\text{interactive chain end bead}}$	0.5 nm
ε	70 kJ/mol
σ_{gauss}	4.8 nm
R_{cutoff}	8.4 nm
# non-interactive beads/chain	3

Table 4.2. Parameters used in the present study.

To determine the crystal phase resulting from a simulation of a given set of parameters (T , $n_s:n_l$, number of grafted chains, and initial configuration), we analyzed the pair correlation function ($g(r)$) of the large particles. See the Supplemental Material, Section B.1.1. for details.

While exploring parameter space by changing $n_s:n_l$, it is important to ensure that the crystal configurations we are reporting are equilibrium configurations. To that end, we initialized many $n_s:n_l$ - T -chain parameter combinations in multiple ways, *i.e.* BCC and FCC with an unphysically large lattice parameter, about 3 – 5 times any lattice parameter from an equilibrated lattice structure of this study. If both simulations equilibrated to the same crystal configuration, we considered that configuration to be the lowest free energy state and selected only one to include for analysis in our final set. If the simulations had different results, we annealed both using various techniques described in the Supplemental

Material, Section B.1.1. until both equilibrated to the same configuration. Note that a simulation initialized as an FCC has twice as many particles as one initialized as a BCC (because the FCC unit cell contains twice as many particles), so this procedure of different initialization is also a test for finite size effects.

Sometimes, this annealing process resulted in one version of the simulation with a bulk monocrystal and another in a polycrystal with grain boundaries. It has been observed experimentally that annealing polycrystalline colloids does not always results in a monocrystalline phase, possibly because of the similarity between the melting temperature and the temperature required to remove grain boundaries (see the Supplementary Discussion of [160]). If, after a few rounds of annealing, the two did not converge to exactly the same configuration, we chose to use the simulation resulting in the monocrystal. This is because polycrystals are always higher energy than monocrystals, and the purpose of the current study is the understand bulk crystals based on different parameter sets. Including polycrystals and the added complexity of grain boundaries is outside of these bounds.

Finally, finite-size effects are often associated with seeing two-phase coexistence in an NPT simulation. To test whether simulation size played a role in the existence of two phase in our 7:1 and 8:1 systems, we ran and annealed all points of 7:1 and 8:1 systems in at least two initial configurations (usually BCC and FCC). Simulations of different sizes resulted in very similar BCC to FCC ratios, which are shown in Fig. 4.7. We tested one system (7:1, 8 chains per small particle, $T^* = 1.3$) with 432, 864, and 2000 large particles and saw roughly the same BCC to FCC ratio in all three simulations.

System topology for the simulation was built using Hoobas [122]. Simulations were run with Hoomd-blue [120, 161] and analyzed using MDAnalysis [123, 124]. Images were created with Mayavi [127] (Fig. 4.1 and 4.6(b)) and OvitoVIToteStukowski2010 (Fig. 4.1 and Fig. 4.6(a)). The $g(r)$ functions for determining crystal type were calculated using VMD [125], and some crystal structure determination was done using pymatgen [162] and the AFLOW database [163, 164].

See Supplemental Material at [URL] for all simulation details. An interactive version of the phase diagrams in Fig. 4.2 with pair correlation functions can be found at https://aliehlen.github.io/phase_diagrams/.

Acknowledgements: The authors would like to thank Martin Girard for useful discussions and review of the work. This work was supported by the Center for Bio-Inspired Energy Science, an Energy Frontier Research Center funded by the US Department of Energy, Office of Science, Basic Energy Sciences under Award DE-SC0000989. H.L.-R. thanks a fellowship from Fulbright-Garcia Robles and A.E. thanks a fellowship from the National Science Foundation under grant DGE-1450006. M.O.d.l.C. thanks the computational support of the Sherman Fairchild Foundation.

A.E. and H.L.-R. contributed equally to this work.

CHAPTER 5

Mechanics of monolayers of superparamagnetic particles

This work is a collaboration between Edward P. Esposito and I. He performed experiments, I performed the modeling and simulations, and we both contributed to the theory and topics of the paper. In this work we focused on the mechanics of superparamagnetic elastic sheets actuated with external homogeneous magnetic fields. In the presence of the field, the sheet will bend in its direction, therefore we show all the modes by which a square sheet can bend by tuning the strength and direction of the external field. Given the size of the particles that comprise the sheet, their magnetic response falls in the superparamagnetic regime which is affected by the local curvature of the sheet. This leads to an enhanced or diminished magnetization simultaneously controlled by local normal of the sheet and the orientation of the external magnetic field. Furthermore, this work sets up our on-going work of training curvature in these sheets through cyclic exposure to an external field and being scanned by a laser once actuated.

The following is a draft that will soon be submitted for review at PNAS. It is reproduced here with permission of AUTHORS.

Actuating monolayers of superparamagnetic particles

Edward P. Esposito,* Hector Manuel Lopez Rios,* Monica Olvera de la Cruz, Heinrich

M. Jaeger

* equally contributing first authors

This is paper is unpublished and will soon be submitted for review

ABSTRACT: Magnetically responsive, mechanically flexible microstructures are desirable for applications ranging from smart sensors to remote controlled actuation for surgery or robotics. Embedding magnetic nanoparticles into a thin matrix of elastic material enables high flexibility while exploiting the magnetic response of the individual particles. However, in the ultrathin limit of such nanocomposite materials the particles become too small to sustain a permanent dipole moment. This implies that now large magnetic field gradients are required for actuation, which are difficult to achieve with externally applied fields. Here we demonstrate through experiment and simulation that monolayer sheets of close-packed paramagnetic nanoparticles in a uniform applied field can generate large local field gradients through particle interactions. As a result, a strong collective magnetization is obtained that leads to large deflections of freestanding sheets already in moderate applied fields. Exploiting the vector nature of the applied field, we furthermore find that it is possible to induce more complex curvature and twist the sheets. Finally, we show that paramagnetic nanoparticle monolayers applied as coatings can generate sufficient force to deflect strips of non-magnetic material that is several orders of magnitude thicker.

5.1. Introduction

Since magnetic materials tend to be brittle and stiff [ref], recent work on magnetic actuation has focused on the bending of composites made of deformable non-magnetic materials with embedded magnetic particles [165–170]. The particles experience forces due to interactions with an applied field, and the forces induce the bending when the structure is sufficiently soft or flexible. For the largest bending, it is desirable to use ultra-thin materials to maximize their flexibility while at the same time using high particle density to generate the largest forces.

When the particles have permanent dipole moments, the behavior of such structures can be well-understood as the thin limit of hard-magnetic soft materials [171–175]. The mechanics are then straightforward because the permanent dipoles are independent of the applied magnetic field, so that material deformations involve direct relationships between the external field, the dipole positions, and the forces experienced by the material [172, 176]. However, once the nanoparticles are too small to retain a permanent dipole moment, they instead behave as paramagnets [177]. The behavior of such composite materials can now be best understood as the thin limit of soft-magnetic soft materials [173]. The mechanics are considerably more complex in this case because dipole moments are no longer independent of the external field or of each other [178, 179].

Correctly predicting the bending deformation of thin soft-magnetic soft materials requires accurate modelling of the magnetic forces, in turn requiring an accurate description of how the particle dipole moments align in the applied field. Prior work on large bending of soft magnetoelastic beams commonly assumes a completely in-material alignment of magnetic moments together with a linear magnetization response to the applied field [180–

182]. These assumptions, corresponding to magnetization dominated by dipole-dipole interactions in the small field regime, work well for sufficiently soft or flexible bulk magnetoelastic materials. However, the magnetic forces generated in the small field regime may be too small to bend many nano-scale systems which tend to have tensile stiffnesses on the order of 1 – 10 GPa [22, 23, 183]. It is also not clear whether in-material magnetization is a good assumption for quasi-2D systems. Indeed, some recent work on ultra-thin magnetoelastic systems assumes a magnetization that always follows the applied field [184–186], corresponding to an independent (or fixed) dipole model as commonly used in studies of colloidal magnetism [187–189].

In this work, we relax such assumptions about the field or the magnetization. We study paramagnetic nanoparticle (NP) monolayer sheets through experiments and simulations to understand their mechanics in the non-linear magnetization regime of large magnetic fields and forces. Experimental sheets consist of Fe_3O_4 NPs of diameter 12.25 nm self-assembled into the $20 \mu\text{m} \times 20 \mu\text{m}$ square NP sheets pictured by TEM and optical microscopy in Fig. 5.1*B*. Each NP’s surface is coated with a single layer of short oleic acid molecules. These ligand molecules act as spacers and provide the elastic matrix that holds the sheets together by van der Waals interactions between ligands on neighboring particles (1.75 nm around each particle; visible in the TEM image as the light gray region between the darker gray nanoparticle cores)[23, 190]. NP sheets that have torn partially free from the copper support, as highlighted in white in Fig. 5.1*B*, are subjected to uniform external magnetic fields \mathbf{B}_{ext} generated by permanent magnets as depicted in Fig. 5.1*C*. The sheets’ surface height $z(x, y)$, and especially the free corner deflection δ , is measured by confocal microscopy as the field is varied. Fig. 5.1*D* shows the initial and final state

of a NP sheet simulated by Molecular Dynamics (MD). Each NP is modeled directly in the simulation, having its own dipole moment vector \mathbf{m}_i , oriented at an angle $\theta_{m,i}$ from the vertical. Simulated NPs are separated from their immediate neighbors by a center-to-center rest distance of $r_0 = 15.75$ nm just as their counterparts in the experiments. We allow the dipole moments to evolve freely according to both the external magnetic field and the field generated by all other dipoles [187].

Using moderate-to-large fields in which NP magnetic moments approach saturation, we observe the NP sheets bending far into the non-linear regime. Although we apply uniform magnetic fields, the system nevertheless experiences large forces due to the high density of dipoles. We find that neither the dipole-dipole nor the Zeeman interactions dominate the induced magnetization, and the trade-off between them, especially with saturating particles, leads to non-trivial magnetization states not conforming to either limit. We show how the induced dipole moments depend on the local configuration of the sheet and use them to calculate the magnetic forces. By comparing deflections from experiments and simulations, we find a master curve that predicts the deflection of such a system for various magnetic and elastic parameters. We then extend these findings by demonstrating how dipole forces can generate not only bending deflections but also twist and, when applied in ultrathin coatings, how they can produce forces sufficiently strong to actuate much thicker non-magnetic sheets.

Theoretical Background

A magnetoelastic sheet composed of discrete magnetic particles embedded in an elastic medium can be characterized by its configuration, the set of all particle locations $\{\mathbf{r}_i\}$, and

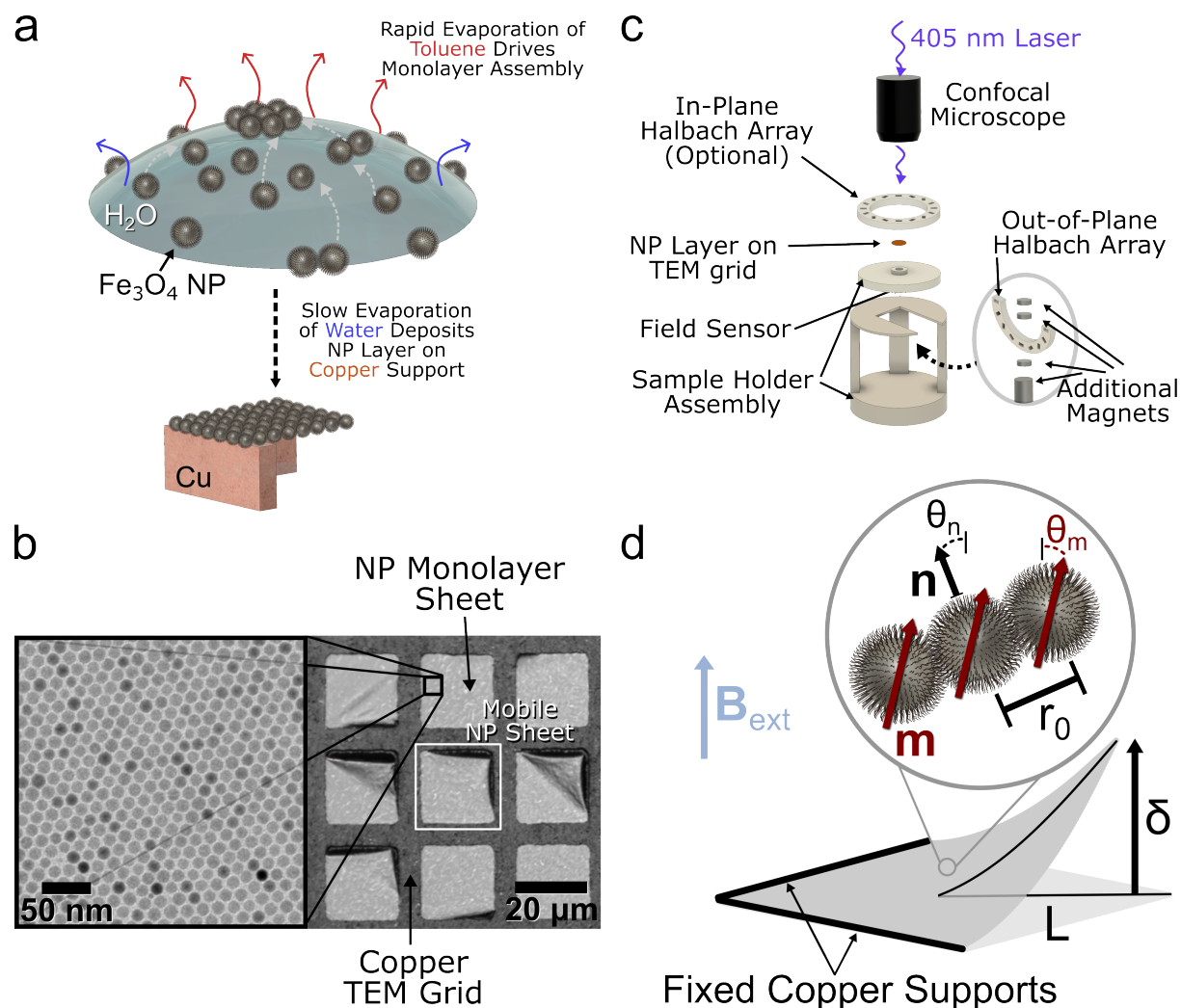


Figure 5.1. **NP Sheet formation and measurement.** (a) Self-assembly and deposition of nanoparticle sheets in schematic. (b) Characteristic TEM (left) and optical (right) micrographs of NP monolayer sheet on a copper TEM grid. Sheets that have torn partially free from the copper, as the one highlighted in the right image, are potentially mobile and are measured in subsequent experiments. (c) Experimental schematic. NP sheets on TEM grid are subjected to magnetic fields generated by permanent magnets in cylindrical Halbach arrays, with additional magnets added to control the field strength, measured with a linear Hall sensor. The surface is measured in each field by confocal reflectance microscopy. (d) NP sheet geometry and parameters.

its magnetization state, the set of all particle magnetizations $\{\mathbf{m}_i\}$. When subjected to an applied field \mathbf{B}_{ext} , the system responds by finding a configuration and magnetization state minimizing a total energy functional that may be separated into static elastic and magnetic functionals as $U(\{\mathbf{r}_i\}, \{\mathbf{m}_i\}, \mathbf{B}_{\text{ext}}) = U_{\text{el}}(\{\mathbf{r}_i\}) + U_{\text{mag}}(\{\mathbf{r}_i\}, \{\mathbf{m}_i\}, \mathbf{B}_{\text{ext}})$ [ref]. For a thin plate, the elastic energy generally separates further into functionals representing decoupled stretching and bending, $U_{\text{el}}(\{\mathbf{r}_i\}) = U_{\text{s}}(\{\mathbf{r}_i\}) + U_{\text{b}}(\{\mathbf{r}_i\})$ [191]. For a static micromagnetic system, the magnetic energy will generally separate into terms representing the coupling of particle magnetization with the external field and with the field generated by the other dipoles, $U_{\text{mag}}(\{\mathbf{r}_i\}, \{\mathbf{m}_i\}, \mathbf{B}_{\text{ext}}) = U_{\text{zee}}(\{\mathbf{m}_i\}, \mathbf{B}_{\text{ext}}) + U_{\text{dip}}(\{\mathbf{r}_i\}, \{\mathbf{m}_i\})$ [ref]. Since Fe_3O_4 has weak magnetocrystalline anisotropy[192], and since shape effects are minimal for our quasi-spherical particles, we disregard anisotropy energy. And we disregard exchange coupling between nanoparticles due to the ~ 2.7 nm core-core separation, since iron atoms on neighboring NPs are at least that far apart.

For a system of discrete paramagnets, the magnetizations are coupled to the configuration through some function $\mathbf{m}_i(\{\mathbf{r}_i\}, \mathbf{B}_{\text{ext}})$. We model the nanoparticles as point paramagnets using a mutual dipole model (MDM), standard in studies of magnetic colloids [ref] but uncommon in magnetoelasticity. In particular, we use a magnetization function

$$(5.1) \quad \mathbf{m}_i(\mathbf{B}_i) = m_{\text{sat}} \mathcal{L}(|\mathbf{B}_i|/B_{\text{sat}}) \frac{\mathbf{B}_i}{|\mathbf{B}_i|},$$

where $\mathcal{L}(x) = \coth(x) - 1/x$ is the Langevin function, $\mathbf{B}_i = \mathbf{B}(\mathbf{r}_i)$ is the total magnetic field experienced by particle i , m_{sat} is the saturation magnetization of the nanoparticles, and B_{sat} is a parameter measuring how strong a field will nearly saturate the particles

(related to their initial susceptibility as $\chi_0 = m_{\text{sat}}/B_{\text{sat}}$). Additionally, the total magnetic field $\mathbf{B}_i = \mathbf{B}_{\text{ext}} + \mathbf{B}_{i,\text{dip}}$ at particle i , includes both the external field and the field due to all of the other dipoles

$$(5.2) \quad \mathbf{B}_{i,\text{dip}} = \sum_{j \neq i} \frac{\mu_0}{4\pi r_{ij}^3} [3(\mathbf{m}_j \cdot \hat{\mathbf{r}}_{ij})\hat{\mathbf{r}}_{ij} - \mathbf{m}_j]$$

in which $\mathbf{r}_{ij} = \mathbf{r}_i - \mathbf{r}_j$, $r_{ij} = |\mathbf{r}_{ij}|$, and $\hat{\mathbf{r}}_{ij} = \mathbf{r}_{ij}/r_{ij}$. Once the magnetization has been calculated for a given configuration, the dipole forces can be evaluated through the relation $\mathbf{F}_i = (\mathbf{m}_i \cdot \nabla) \mathbf{B}_{i,\text{dip}}$ and then used to generate a new configuration (the magnetic force expression written exclusively in terms of the magnetization, after applying the gradient to Eq. 5.2, is given in the SI). New mechanical configurations and new sets of magnetic forces are calculated in alternation until the whole system reaches a steady mechanical configuration.

Results and discussion

Deflections in Uniform Fields

Fig. 5.2A shows the 3D confocal data for one experimental sheet with and without magnetic field. Scans are typically taken over a range of external magnetic field strengths from $B_{\text{ext}} = 0$ to 0.15 T, and Fig. 5.2B shows the surface height along the line trace of the diagonal depicted in the upper left corner for each strength. The deflection of the free corner traces a characteristic S-shaped curve as shown in the lower inset, initially curved for weak external fields, and seeming to saturate for large fields. Fig. 5.2C shows the

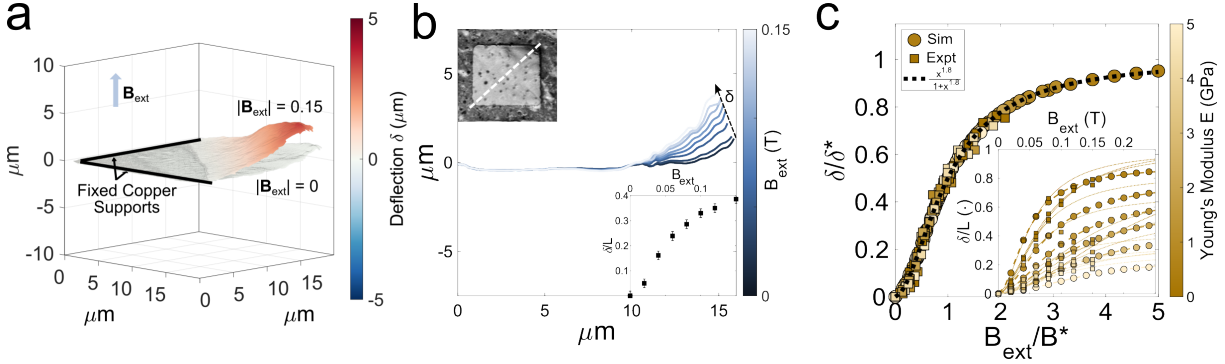


Figure 5.2. **Nanoparticle sheet deflection in applied external B -field.** (a) Confocal microscopy scans of a sheet without and with applied field. (b) Sheet deflection profiles for increasing B . Upper left inset: optical micrograph of the sheet. Dashed line indicates line scans for the deflection profiles. Lower right inset: Vertical deflection δ of the free corner of the sheet, normalized by the length L of the actuatable portion of the profile (in this case approximately half the diagonal of the square sheet). (c) Experimental and simulated deflections collapsed by the fitting function given by Eq. 5.3. Inset: Normalized deflection as a function of applied field from experiments on different sheets (squares) and simulations for Young's moduli from 0.5 to 5 GPa (circles).

results from many such experiments and simulations, collapsed by a fitting function

$$(5.3) \quad \delta(B_{\text{ext}}) = \delta^* \frac{B_{\text{ext}}^\alpha}{B^*{}^\alpha + B_{\text{ext}}^\alpha},$$

a generic class of sigmoid function that is 0 for $B_{\text{ext}} = 0$ and saturates to a value δ^* , attaining half saturation at $B_{\text{ext}} = B^*$ (generally different from B_{sat}). The curvature is controlled by the power α , found to be 1.8 from sheets simulated with different stiffnesses (see SI for why this particular fitting function was chosen). The inset of Fig. 5.2C shows the un-collapsed data, together with the fitting functions using $\alpha = 1.8$ as found in the simulations. The uncollapsed deflections are normalized by the linear scale L due to the difference in size between the experimental and simulated sheets.

Given the particle magnetization function Eq. 5.1, we can understand why some function like our Eq. 5.3 must fit well to the data. In our sheets with strong forces between densely-packed dipoles, we can think of the dipole-dipole forces per unit area as a type of pressure loading. For thin plates generically, at small pressures p the deflection will scale as $\delta \sim p$, while for larger pressures, the deflection will instead scale as $\delta \sim p^{1/3}$ [191]. The pressure here results from all of the induced magnetizations and are not related to the external field strength in a simple form. Well below saturation however, the induced dipole moments scale roughly linearly with the applied field, and since the forces scale as the product of the induced magnetic moments and the dipole field, itself scaling proportionally with the dipole moments, the pressures scale roughly quadratically with the dipole moments. If the induced dipole moments were strictly linear in the small field regime, we would then expect a quadratic scaling of the deflection with the external field strength and a power of $\alpha = 2$ in Eq. 5.3. The value found, $\alpha = 1.8$, is consistent with the sublinearity of the magnetization function Eq. 5.1. Once the particles begin to saturate and the induced magnetization stops increasing with the applied field (only reorienting closer to the external field, see Fig. 5.3 and the subsequent discussion), the forces will also stop increasing with the applied field. As the magnetic forces change less and less, the deflection saturates. The saturated value δ^* from Eq. 5.3 should then be a deflection corresponding to the largest balance between the magnetic energy (the maximal loading) and the elastic energy (the maximal deformation). From MD simulations of sheets with different Young's moduli, we find that

$$(5.4) \quad \frac{\delta^*}{L} \approx \exp \frac{-Et^3/12(1 - \nu^2)}{Nm_{\text{sat}}B_{\text{sat}}},$$

where the argument of the exponential is the ratio between the scales of magnetic energy and bending energy. If the magnetic scale far exceeds the bending scale, magnetic forces can be large enough to overcome the bending rigidity and produce deflections approaching the linear scale of the sheet. For the softest of our sheets, the largest measured deflections of $\delta/L \approx 0.75$ correspond to the free corner of the sheet bending through an angle of roughly 50° . In such cases, δ^*/t exceeds 1000, far into the non-linear plate bending regime. To test whether these fit values of δ^* correspond sensibly to the typical stiffnesses of the sheets, we used the saturation deflection values found from fitting our experimental curves together with other known or presumed material parameters to calculate a "measured" Young's modulus E . The distribution of moduli obtained in this way corresponds well to the distribution of moduli from direct measurements of similar sheets using AFM indentation tests, following the technique of [193] (See SI for details).

Non-Uniform Magnetization States

An isolated paramagnetic particle responds to an external field through Eq. 5.1 with only the applied field, as $\mathbf{m} = m_{\text{sat}} \mathcal{L}(|\mathbf{B}_{\text{ext}}|/B_{\text{sat}}) \mathbf{B}_{\text{ext}}/|\mathbf{B}_{\text{ext}}|$, since there is no field from other dipoles. In particular, its magnetic moment aligns fully with the applied field direction so that the angle between the moment and the field θ_m is zero, while the strength of the moment is $m = m_{\text{sat}} \mathcal{L}(|\mathbf{B}_{\text{ext}}|/B_{\text{sat}})$. When many such particles are packed closely together, the dipole field in Eq. 5.2 becomes appreciable relative to the applied field, so the total field experienced by the particles may be stronger or weaker than the applied field, and will generally not be in the same direction as the applied field. Since the dipole moment follows the total field direction, θ_m may no longer be zero, while m may also differ

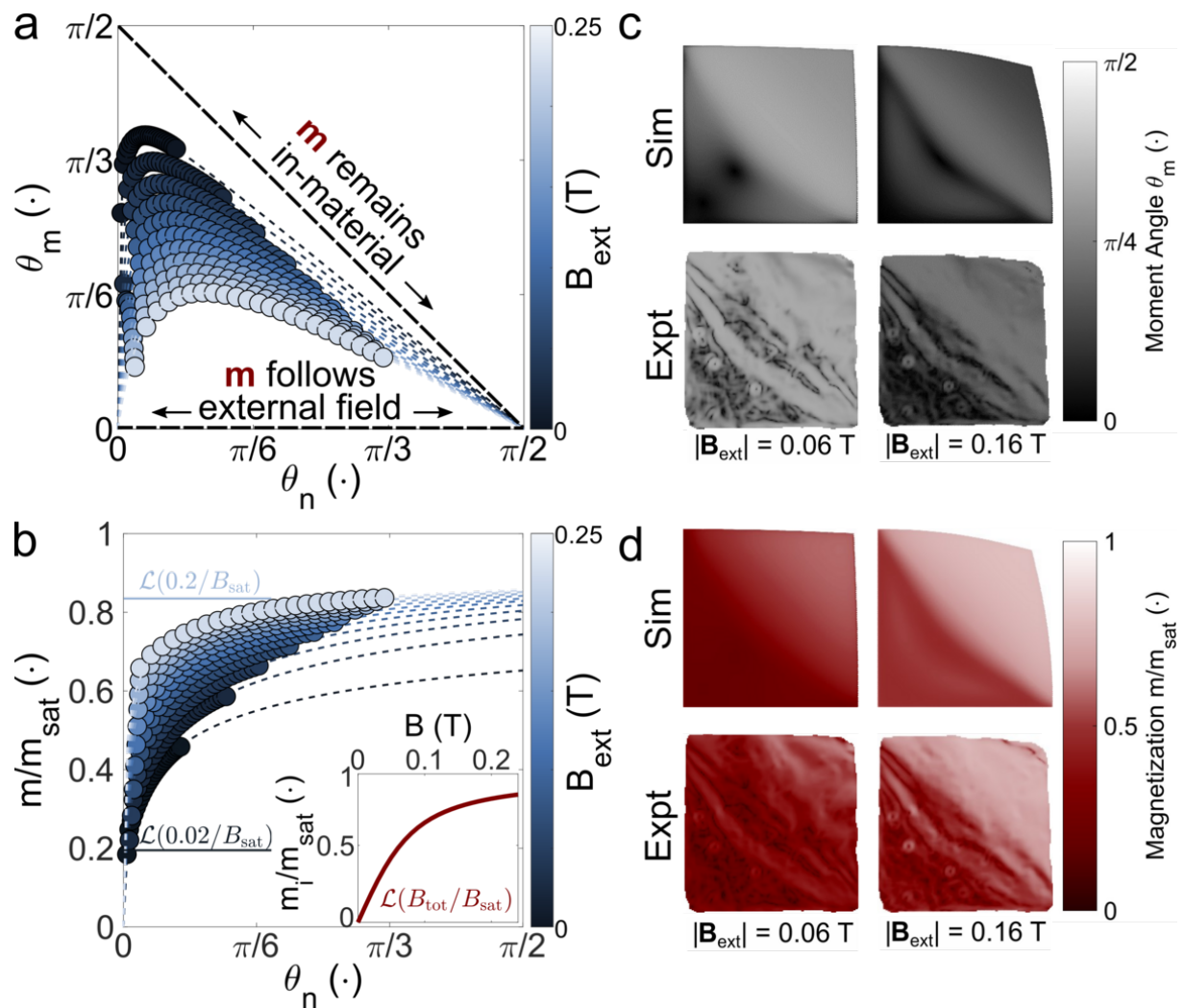


Figure 5.3. Magnetization direction and magnitude in nanoparticle sheets. (a) Single particle magnetization direction θ_m from molecular dynamics (MD) simulations, averaged over local surface orientations θ_n at different external field magnitudes. The angles θ_m and θ_n represent the deviations of the particle magnetic moments and of the local sheet normal from the direction of the applied field, respectively. If $\theta_m = \pi/2 - \theta_n$, then the magnetization remains in-plane. Dots: averages from simulation. Dashed lines: fitting function described in the text. (b) Magnetization as a function of local surface orientation for a range of external field strengths. Note how flat orientations of the sheet tend to suppress the magnetization due to stronger demagnetizing fields. Inset: Single particle Langevin magnetization function. (c) Low-field and high field moment angle, evaluated directly for the simulation, and using the fitting functions described in the text for the experiments. (d) Same as (c), but for the moment magnitude.

from $m_{\text{sat}}\mathcal{L}(|\mathbf{B}_{\text{ext}}|/B_{\text{sat}})$. The dipole field experienced by any particle depends strongly on the position and magnetization of neighboring particles, and the locations of neighboring particles contributing most to that dipole field can be characterized simply by the local surface normal. We therefore expect particle dipole moments to vary strongly with the angle θ_n between the local surface normal and the applied field. Fig. 5.3A demonstrates this variation with the local normal of the sheet of 1 GPa stiffness at various external field strengths (averaged over all particles in the simulated sheet with the various normal directions), while Fig. 5.3B shows how the magnitude of the magnetization varies. We find that the strength and direction of the particle moments are well described as functions of the local surface normal direction θ_n , irrespective of the sheet's stiffness (see Fig. S1), by

$$(5.5) \quad \begin{aligned} m(\theta_n) &= m^* \frac{\theta_n^{1/2}}{\theta_n^{*1/2} + \theta_n^{1/2}} \\ \theta_m(\theta_n) &= c_0 \frac{\theta_n(\frac{\pi}{2} - \theta_n)}{\theta_n - \theta_n^{**}}. \end{aligned}$$

Here m^* , θ_n^* , c_0 and θ_n^{**} are fit parameters that depend on the external field, as well as material properties like m_{sat} , B_{sat} and r_0 . As the sheet rotates into the applied field (i.e. as the sheet's normal rotates away from the applied field), the competition between the Zeeman and dipole energy terms reduces, and so the magnetization directions simultaneously approach both the tangent plane of the sheet and the applied field. As the external field strength is increased, the magnetization approaches the field direction more closely at all orientations of the local normal. This latter behavior is due to the fact that the particles saturate, limiting the magnitude of the dipole-dipole energy, whereas the Zeeman energy continues increasing linearly with the applied field. For saturated particles, increasing

the field strength increases the ratio of Zeeman to dipole-dipole energy, favoring closer alignment of the particle magnetization directions with the applied field.

Because of the variation of surface normals across the sheet, Fig. 5.3*C-D* display a distribution of magnetic moments strengths and orientations. In the free portion where deflections are large, the normal makes its largest angle with the applied field, and the strength of the magnetization is largest. The dipole-dipole and Zeeman interactions favor dipole orientations in similar directions. By contrast, in the fixed portion of the sheet, which remains relatively flat, dipole-dipole and Zeeman interactions favor magnetization orientations in competing directions, and the magnitude of the dipoles is reduced as a result. In all cases, we can understand variation of the magnetic moments in terms of the changing surface orientation as shown in Fig. 5.3*A-B*.

That dipole moment directions generally differ from both the applied field direction and the local tangent plane is a complexity not usually included in prior magnetoelastic studies. Some past works studying flexible paramagnetic rods assume magnetization always in the applied field direction [182, 194, 195]. Scherbakov and Winklhofer consider a beam with distributed paramagnetic material in which the magnetization is confined to the beam axis. Gerbal *et al.* consider beams embedded with superparamagnetic particles [181] and compare a model in which the beams magnetize in the applied field direction against a model in which they always magnetize along their axis. Their work demonstrated that only axial magnetization would reproduce their experimental results. The implicit assumption behind such models is that axial magnetization arises through the interdependent magnetization of the distributed superparamagnetic material. Although this could arise from the interactions of a high density of superparamagnetic material,

we point out that the superparamagnetic material in [181] consists of nanorods which themselves have a strong axial anisotropy and could be explained also on that basis. In our quasi-2D MDM system in which the superparamagnetic particles do not have a strong shape or magnetocrystalline anisotropy[192], despite the high density of particles, we find that the particle magnetization always lies somewhere between the applied field and the local tangent plane. The direction of the forces acting on the particles is therefore different from what either axial or in-field magnetization models would predict, so the deflections of our system are not well-described by those models.

Magnetic Forces without External B-Field Gradients

After calculating the particle magnetic moments, we may evaluate the magnetic forces between them. These dipole-dipole forces exist even in a uniform external field due to the finite size of the sheet. As discussed above, the magnitude of the dipole-dipole forces depends roughly quadratically on the magnitude of the magnetizations, having a scale of $\frac{\mu_0 m_{\text{sat}}^2}{4\pi r_0^4} \approx 2.7 \times 10^{-13}$ N. Experimental fields controlled by permanent magnets use Halbach cylinder arrays in order to reduce external gradients. The largest gradients in the experiments were roughly 200 T/m, which can produce forces only up to 1.45×10^{-16} N for fully saturated particles, orders of magnitude smaller than the forces between the dipoles themselves. We therefore neglect forces due to the gradients in the external field and assume that the only forces present are due to dipole-dipole interactions.

The direction of the forces depends on the directions of the particle dipole moments. We therefore expect variation in both the magnitude and directions of the dipole forces according to the variations in the dipole moments across the sheet. Fig. 5.4A demonstrates

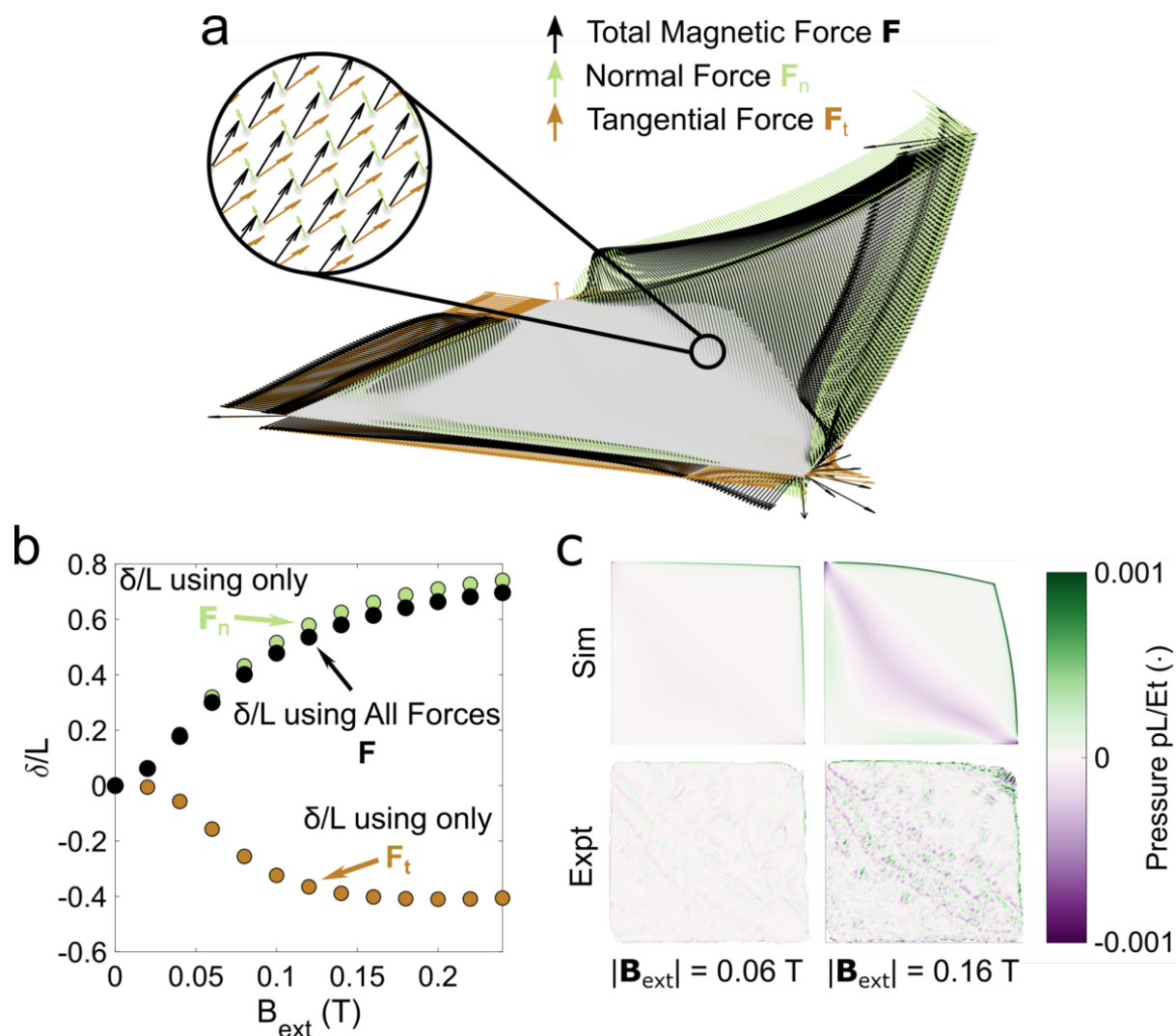


Figure 5.4. **Non-uniform magnetic pressures.** (a) Simulated sheet at large applied field, with force per particle depicted by arrows. Black arrows: total force. Green and brown arrows: normal and tangential force components, respectively. The forces vary across the sheet, the strongest are near and at the edges. The normal and tangential components are typically of similar magnitude, as seen from the zoomed-in view, where the tangential component even exceeds the normal component. (b) Deflection of an initially flat sheet using only the normal or only the tangential force components. Black circles: Data from full magnetoelastic simulation as in Fig. 5.2. Green and brown circles: Purely elastic simulation applying only the normal (green) or tangential (brown) force components found in the magnetoelastic simulation. (c) Normal force distribution at low and high fields for simulated and experimental sheets. These images show the non-uniform nature of the magnetic forces, with normal pressures even changing sign across the sheet.

this variability with an example of a sheet deflected at moderate field strength. Arrows representing the force per particle are superposed on the configuration of the sheet, with black arrows representing the full force while green and brown arrows represent the normal and tangential force components. It is most striking that the magnitude of forces on the edge particles is much larger than on particles within the bulk area, and also that the total force is significantly different from the normal force, since both the green and black arrows are visible. We show a zoomed view of one region of the bulk to emphasize that the tangential forces are a significant component of the total force, indeed even exceeding the normal force for the region chosen.

To test the importance of the normal and tangential force components, we performed purely elastic simulations using only one force component from the magnetoelastic simulation at each field strength and compared the deflections from these partial simulations with those from the full simulation. The results are presented in Fig. 5.4*B*. Despite the normal and tangential forces' being of similar magnitude, the normal forces alone very nearly reproduce the full magnetoelastic deflections, consistent with the analysis of magnetoelastic work and energy given by Brown [196]. Perhaps more surprisingly, the tangential forces alone produce sizable deflections of opposite sign, likely an indication of the buckling instability of the flat sheet under compressive forces. Note how the true deflection is not simply the sum of the two partial deflections in this non-linear deflection regime. Because they are the essential forces behind the measured sheet deflection, Fig. 5.4*C* shows the distribution of normal forces across the sheet, recast as a dimensionless normal pressure $\tilde{p} \equiv \frac{pL}{Et}$. The scaling used here accounts for the different sizes of the experimental and simulated sheets. Since the deflection scales cubically with the pressure

load as $\delta^3 \sim \frac{pL^4}{Et}$ according to the Föppl-von Kármán plate equations [191], the dimensionless deflection $\tilde{\delta} \equiv \frac{\delta}{L}$ therefore scales with the pressure as $\tilde{\delta}^3 \sim \frac{pL}{Et}$. The magnetic force distributions are visually striking because of their non-uniformity. The normal forces not only vary in magnitude but even change sign across the sheet.

Deflections under Different Field Orientations

One initially surprising observation in our experiments was that vertical magnetic fields cause the sheet to bend in the same direction regardless of the polarity of the field. This suggests that the nanoparticles do not retain their magnetic moments in the absence of the external field, or at the very least that all experimental fields were larger than the coercive field for the particles. Under the transformation $\mathbf{m}_j \rightarrow -\mathbf{m}_j$ in which all dipoles change their sign, the dipole field will also change its sign. The force on each dipole will then remain unchanged: $\mathbf{F}_i \rightarrow (-\mathbf{m}_i \cdot \nabla) (-\mathbf{B}_{i,\text{dip}}) = (\mathbf{m}_i \cdot \nabla) \mathbf{B}_{i,\text{dip}}$. We therefore expect that only the strength and the axis of the external field impact the deflection of the sheet.

To determine the effect of changing the direction of the applied field, we now fix the strength but allow the field to adopt any orientation in space in our simulations, with results as depicted in Fig. 5.5 for a 1 GPa sheet. The field is then described by $\mathbf{B}_{\text{ext}} = B_{\text{ext}}(\sin \theta \cos \phi \hat{\mathbf{x}} + \sin \theta \sin \phi \hat{\mathbf{y}} + \cos \theta \hat{\mathbf{z}})$. If we fix the field at some polar angle θ and allow the field to rotate around the vertical axis so that ϕ varies from 0 to 2π , we see that the free corner of the plate achieves its maximum deflection when the field points along the $\frac{\hat{\mathbf{x}}+\hat{\mathbf{y}}}{\sqrt{2}}$ axis ($\phi = \pi/4$), and that the deflection of the free corner tends to zero as the field approaches the $\frac{-\hat{\mathbf{x}}+\hat{\mathbf{y}}}{\sqrt{2}}$ axis ($\phi = 3\pi/4$). This effect is displayed in Fig. 5.5B. If instead we fix the azimuthal angle ϕ and vary the field's polar angle from $\theta = 0$ to $\theta = \pi$, the field

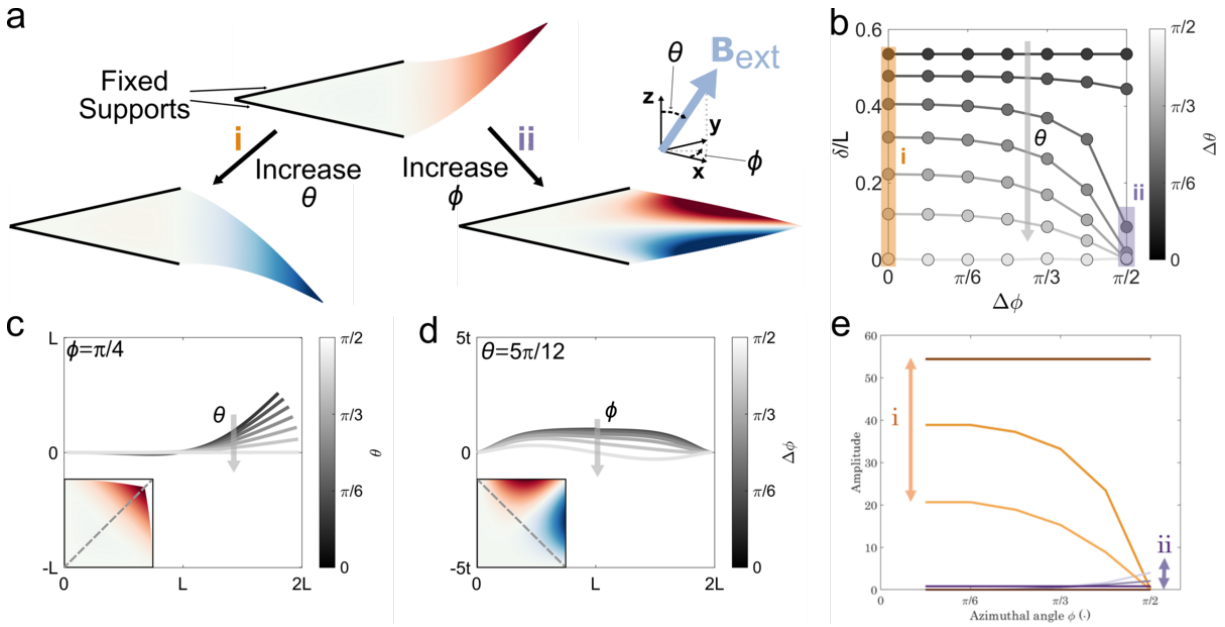


Figure 5.5. Twisting sheets by changing the applied field orientation (a) Deflections in fields with general direction are characterized by two modes: mode i corresponds to deflection along the free diagonal; mode ii corresponds to twisting around the mode i diagonal, leading to undulations in the perpendicular direction. Red, blue: positive and negative deflections respectively. (b) End deflection of 1 GPa sheet at constant field strength (here, $B_{\text{ext}} = 0.12$ T) but varying direction. At fixed ϕ and increasing θ , the field rotates away from the vertical and deflection decreases. At fixed θ but increasing ϕ , the field rotates around the vertical axis, and for fields with substantial components in the xy plane, end deflection vanishes abruptly as the field rotates away from the free corner. (c) Deflection profiles for different θ at $\phi = \frac{\pi}{4}$, corresponding to mode i. Inset: 2D projection of simulated sheet with $\theta = \frac{\pi}{2}$ and $\phi = \frac{\pi}{4}$; profiles evaluated along dashed line. (d) Deflection profiles for different ϕ at $\theta = \frac{5\pi}{12}$, corresponding to mode ii. As ϕ approaches $\frac{3\pi}{4}$, undulations indicate twisting of the sheet. Inset: 2D projection of simulated sheet with $\theta = \frac{5\pi}{12}$ and $\phi = \frac{3\pi}{4}$; profiles evaluated along dashed line. (e) Curves indicate amplitude of mode i (orange) or ii (purple) as a function of ϕ for fixed θ , where darker lines of either color correspond to lower θ . The contribution of modes i or ii can be tuned by re-orienting of the field.

rotates away from the vertical, passing through the diagonal of the sheet from the fixed corner to the free corner. The deflection of the free corner of the sheet follows the applied field as shown in Fig. 5.5*C*, achieving its maximum magnitude for fields fully normal to the flat sheet, and passing through zero when the field is in the plane of the flat sheet. For this field orientation (i.e. $\theta = \pi/2$ and $\phi = \pi/4$), the deformations are wholly confined to the plane of the sheet so that it remains flat everywhere. In this case however, since the field retains some component in the vertical direction, the sheet deforms out of the neutral plane by twisting about the $\frac{\hat{x}+\hat{y}}{\sqrt{2}}$ axis as much as possible in order simultaneously align the dipoles with each other and with the field. The free corner of the sheet remains at zero, and the maximum out-of-plane deflection of the sheet is attained along the free edges.

Since we find that the deflection of the free corner does not fully characterize the out-of-plane deformation of the plate, we therefore cast the sheet's configuration as a superposition of two deformation modes, a bending (i) and a twisting (ii) mode as demonstrated in Fig. 5.5*A*. Fig. 5.5*B* shows the profile of one of the free edges of the sheet. The two modes are well described by cubic and sinusoidal functions respectively, and the full shape by their superposition. Fig. 5.5*C* shows the amplitude of each of the two modes, either α or $1 - \alpha$ times the maximum deflection in each mode, as ϕ is rotated around the vertical axis. The different traces correspond to different values of the polar angle θ . Mode i dominates the deflection for most field orientations, but vanishes once the field approaches the fixed diagonal.

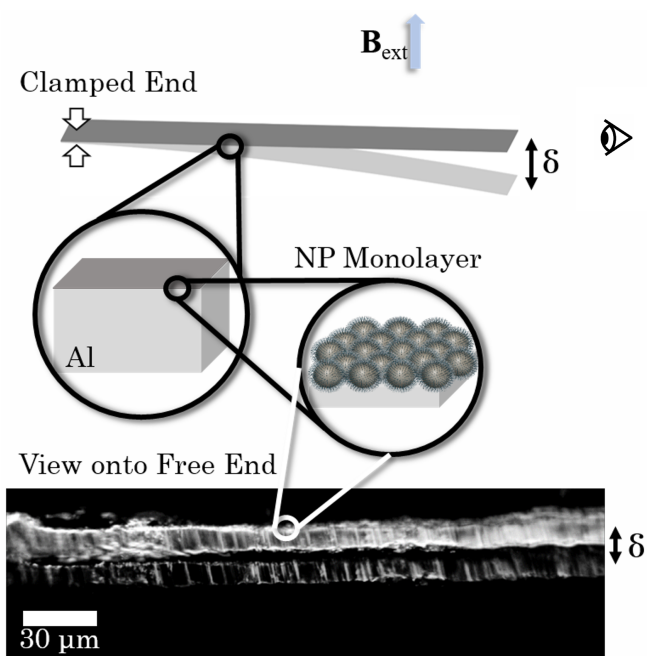


Figure 5.6. **Actuating NP coated Aluminum.** Fe_3O_4 NPs can be used as a surface coating to actuate non-magnetic structures. We demonstrate this by deflecting an aluminum sheet using a nanoparticle monolayer as depicted in the schematic. The bottom image is a composite micrograph (magnified 50x) of the free end before and after application of the field. The Al sheet is ~ 1000 times thicker than the monolayer and 50 – 100 times stiffer. Despite this, the NPs generate forces strong enough to deflect the Al sheet by $\delta/t_{\text{Al}} \sim 1$.

NP Sheets Coating Elastic Structures

NP sheets are able conform to high aspect ratio surface topographies [197], and could therefore find wide use as magnetically responsive coatings to actuate many other types of nanostructures. As a demonstration of the strength of field-induced forces that can be produced by self-assembled Fe_3O_4 NP sheets, we use them to coat much thicker sheets of non-magnetic material. Fig. 5.6 demonstrates this with an aluminum sheet of thickness $t_{\text{Al}} \sim 15 \mu\text{m}$ and Young's modulus $E_{\text{Al}} \sim 68 \text{ GPa}$ being deflected in a uniform external

magnetic field of strength 0.12 T due to the dipole pressures generated by a NP monolayer of thickness $t_{\text{NP}} \sim 12.25$ nm and typical stiffness of 0.5 – 1 GPa deposited on the Al surface. Being $t_{\text{Al}}/t_{\text{NP}} \sim 1000$ times thicker and $E_{\text{Al}}/E_{\text{NP}} \sim 50 - 100$ times stiffer than the NP sheet, the aluminum dominates the bending response of the combined structure. Nevertheless, the high areal density of NPs leads to dipole forces sufficient to deflect the aluminum sheet by $\delta/t_{\text{Al}} \sim 1$. This response can be further enhanced by sequentially depositing additional NP monolayers.

Conclusions

Our results demonstrate that thin elastic sheets comprising densely packed paramagnetic nanoparticles can exhibit large deflections deep into the non-linear plate bending regime even in uniform applied magnetic fields. We find that deflections follow a characteristic $\delta \sim B_{\text{ext}}^{1.8}$ curve for small fields while saturating for large fields, so that bending deflections measured for sheets with different magnetic and elastic parameters can be collapsed onto a single master curve (Fig. 5.2). We show how, as a result of strong interparticle dipole interactions, the magnetization response depends on the sheet's orientation with respect to the applied field (Fig. 5.3), and that the distribution of these magnetizations across the sheet leads to large non-uniform forces (Fig. 5.4). We also show how rotation of the applied field can generate more complex actuation, such as twisting (Fig. 5.5).

Constituting the ultrathin limit of self-assembled nanoparticle systems, the monolayer sheets discussed here are the thinnest nanoparticle based magnetoelastic composites with paramagnetic elements. Magnetic NP sheets allow external control and actuation of

nano-scale systems due to their thinness and bending flexibility, and they may be used independently or as coatings in a wide range of potential applications for magnetically controlled micro-mechanical or micro-robotic systems.

Materials and Methods

Experiments

12.25 nm Fe_3O_4 nanoparticles are synthesized according to the Sun protocol [198] (see SI for full description). With diameter substantially less than 25 – 30 nm, these particles are well into the superparamagnetic size regime for Fe_3O_4 [199]. Following the synthesis, the particles are dispersed in toluene. Quasi-2D nanoparticle sheets are then made through an evaporative self-assembly process adapted from earlier work involving sheets of thiol-coated gold nanoparticles [193]. Briefly, a support structure (typically a copper TEM grid with 20 μm square holes) is immersed in a 50 μL droplet of Ultrapure water on a PTFE substrate. A 1 μL droplet of the toluene/NP solution is gently contacted with the water droplet. The toluene coats the water droplet in a thin film, and as it evaporates the nanoparticles in the toluene film are trapped at the air-water interface. Following the rapid evaporation of the toluene and the formation of the NP monolayer at the air-water interface, the water evaporates slowly, gently draping the nanoparticle layer onto the support structure within the water droplet. Once the water completely evaporates, portions of the nanoparticle layer that have torn partially free from the support structure (typically a square with two adjacent free edges) are identified and scanned with a LEXT OLS-5000 confocal surface scanning microscope, with x-y resolution of 125 nm \times 125 nm per pixel and nominal z resolution of 10 nm. Since the interparticle separation is 15.75 nm, there

are roughly 80 NPs per pixel. Scans are performed with varying external magnetic field strengths and orientations using permanent magnets. Quasi-uniform magnetic fields are generated with arrays of NdFeB magnets in the dipolar cylindrical Halbach configuration, to which larger magnets can be added to generate stronger fields. To avoid contact with the microscope objective, half cylinders are used for generating vertical fields. Small and large half cylinders are used with additional magnets and in combination with each other to generate the different field strengths, which are measured with a linear Hall sensor. Gradients due to permanent magnets are measured with a pair of Hall sensors. The largest such gradients could lead to maximum per-particle forces, for fully saturated particles, that are still $\sim 100\times$ smaller than the typical dipole-dipole forces described in the main text. See SI for more on the production and measurement of the fields, and the potential impact of external gradients.

Simulations and Modelling

MD simulations are performed using ESPResSo v4.2 [200]. The simulated sheets consist of a triangular lattice of hard spheres making up a square of side length 180 particle diameters resulting in a total of 22680 particles. Simulated sheets correspond to a physical size of $2.2 \mu\text{m} \times 2.2 \mu\text{m}$. These sheets are initially flat and all particles along the \hat{x} and \hat{y} axes are held fixed to mimic the experimental boundary conditions. As in earlier work, particles interact elastically with their neighbors through a two-body stretching potential $u_s = \frac{\sqrt{3}}{4}Et(r - r_0)^2$, where r_0 is the inter-particle separation at rest, and through a four-body bending potential $u_b = \frac{Et^3}{6\sqrt{3}(1-\nu^2)}[1 - \cos(\theta)]$, penalizing angular deviations between the normal vectors of neighboring elements [201]. Particles are assumed to behave as

point paramagnets. We use a mutual dipole model in which the field due to all the other dipoles in the sheet is also included when determining the dipole magnitudes and directions [187, 202, 203]. To determine the particle magnetizations, we solve the set of N coupled non-linear equations $\mathbf{m}_i = m_{\text{sat}} \mathcal{L}(|\mathbf{B}^i|/B_{\text{sat}}) \hat{\mathbf{B}}^i$ directly. This last step sets the limit on computational speed by far. However, the MDM converges to the same configuration and magnetization regardless of whether the sheet is initially flat or bent, so to generate a relatively quick initial estimate of the final configuration and magnetic state we use an alternate model not previously seen in the literature, which we call the semi-Independent Dipole Model (sIDM). Whereas the MDM assumes $\mathbf{m}_i = m_{\text{sat}} \mathcal{L}(|\mathbf{B}^i|/B_{\text{sat}}) \hat{\mathbf{B}}^i$, the sIDM instead assumes $\mathbf{m}_i = m_{\text{sat}} \mathcal{L}(B_{\text{ext}}/B_{\text{sat}}) \hat{\mathbf{B}}^i$, indicating that the direction of the dipoles depends on the total field while the magnitude of the dipoles depends only on the external field. Because the sIDM avoids the nonlinearity connected with the Langevin function, this calculation is much faster. In practice, it can produce non-physical magnetization states however, and these are only resolved once we switch to the full MDM. Despite this, the final deflections from the sIDM are close to those from the MDM, and in this way the sIDM provides a good way to estimate the behavior of a very large system. As shown in Fig. 5.3 a mathematically flat sheet will not magnetize in a vertical field, so simulations begin with a slight offset to the vertical magnetic field for the first 200 time steps, before finally using a purely vertical field. See the SI for further

Acknowledgements: This work was primarily supported by the University of Chicago Materials Research Science and Engineering Center, which is funded by National Science

Foundation under award number DMR-2011854. HMLR acknowledges support from a MRSEC-funded Graduate Research Fellowship, DMR-2011854.

CHAPTER 6

Manipulating the medium to create patterns

This work is a collaboration between Shih-Yuan Chen and I. The experiments were performed by Shih-Yuan, while the simulations and theory were realized by me. We both wrote the paper. In this work we wanted to understand what was the range of the hydrodynamic interaction of a single driven particle within a suspension of passive particles. The motivation being that this system has the potential for training so long a single particle can manipulate the configuration of surrounding passive particles. However, for this system to truly be trainable, particle configurations would need not be erased by thermal fluctuations after being altered by the driven particle. Future work, would consist in adding attractive interactions among all particles to test whether this systems is indeed trainable.

The following was originally published in *Soft Matter* in 2024. It is reproduced here with permission of AUTHORS, and the PUBLISHER.

Supplementary material associated with this chapter can be found in Appendix C.

Restructuring a passive colloidal suspension using a rotationally driven particle

Shih-Yuan Chen,* Hector Manuel Lopez Rios,* Monica Olvera de la Cruz, Michelle M. Driscoll

* equally contributing first authors

Reproduced from [204] with permission from the Royal Society of Chemistry.

DOI: <https://doi.org/10.1039/D4SM00010B>

ABSTRACT: The interaction between passive and active/driven particles has introduced a new way to control colloidal suspension properties from particle aggregation to crystallization. Here, we focus on the hydrodynamic interaction between a single rotational driven particle and a suspension of passive particles near the floor. Using experiments and Stokesian dynamics simulations that account for near-field lubrication, we demonstrate that the flow induced by the driven particle can induce long-ranged rearrangement in a passive suspension. We observe an accumulation of passive particles in front of the driven particle and a depletion of passive particles behind the driven particle. This restructuring generates a pattern that can span a range more than 10 times of the driven particle's radius. We further show that size scale of the pattern is only a function of the particle's height above the floor.

6.1. Introduction

Colloids have been extensively used to explore the relation between structure and function of materials. Their structure is easily observable with a simple optical microscope

[205–207], and colloidal particles can be actuated to roll [208], spin [209], and oscillate [210]. Moreover, one can easily tune particle interactions in a colloidal system using straightforward modifications to particle size, shape, and surface chemistry, which allows for the design of exotic material properties such as tunable shear-jamming [211] and patterned wettability [212].

Generally, self-assembly is driven by interparticle forces and entropic forces. External applied fields, however, unlock self-assembly pathways that are otherwise inaccessible including avalanches [213] and configurations that encode memory [214, 215]; indeed, the soft matter community has established that self-propelling particles can tune self-assembly [216, 217]. Additional degrees of freedom, such as in mixtures of active and passive particles, enhance the phase space of microstructures [218–220]. The motion of self-propelling particles has been shown to enhance the diffusivity of passive particles [221, 222], create clusters of passive particles around self-propelling particles [223, 224], or induce phase separation between particle types [225–230]. Moreover, as the self-propelling particles exert forces on their surroundings, they continue reconfiguring the local structure already built [224, 231]. When active particles are added to an equilibrium passive crystal structure, their activity accelerates the annealing process, leading to large-scale single crystals [232]. Through active-passive interactions, active particles via self-diffusiophoresis [233] and driven particles via external fields have the potential to tune the aggregation of passive particles [216, 217], and ship cargo passive particles to desired locations [234, 235]. These examples demonstrate the complexity of active-passive and driven-passive interactions. To understand how these particles reshape material structure, it is crucial to understand how they interact with their surroundings in a colloidal suspension. In

many cases, hydrodynamics plays a significant role to explain the restructuring and the emergent patterns [224, 236, 237].

In this work, we examine how a driven particle, called a microroller [238, 239], immersed in a passive particle suspension can restructure its surroundings through experiments and Stokesian dynamics simulations with lubrication corrections (see Materials section). Here a microroller rearranges the passive particles through hydrodynamic interactions, creating an accumulation zone around itself and a depletion tail in its wake. We observe that a steady-state pattern emerges from these interactions, and this pattern is 10 times larger than the microroller radius and is three dimensional in nature. We note that in striking contrast to restructuring created by actively dragging a particle through a suspension [240], the highest concentration of passive particles in the accumulation area is roughly 10 microroller radii away from the microroller location. This underscores the mechanism of restructuring as the long-range flow field generated by the microroller. Due to the sensitive dependence of hydrodynamic interactions on the particle's height above the chamber floor, we find that the structure of the pattern is modified by changing the height of either the driven or passive particles.

6.2. Results

We experimentally study suspensions of passive particles in water doped with magnetically driven particles, named the microrollers, see Fig. 6.1(a). Both the microrollers and passive particles are denser than water, so they sediment to the floor of the suspension's container, forming a quasi-2D layer of particles. Both types of the particles share the

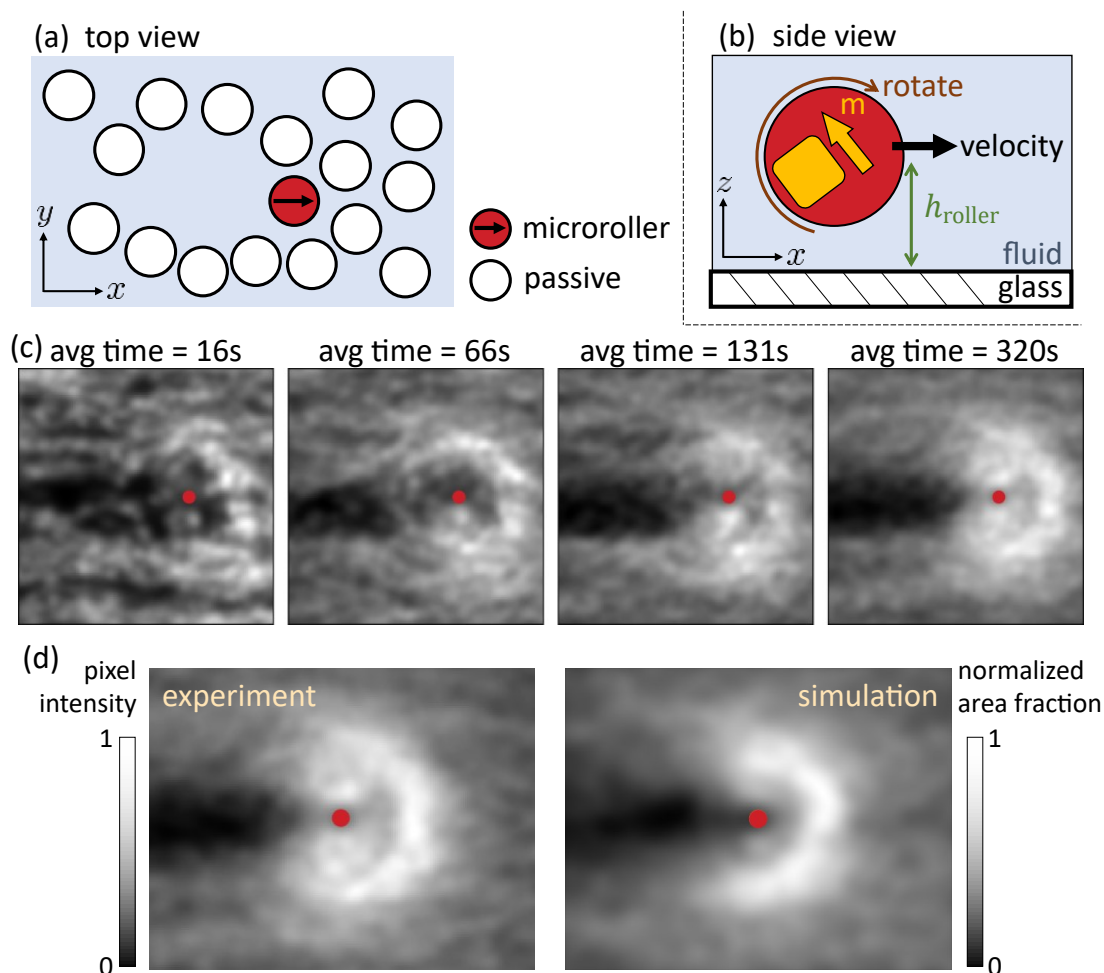


Figure 6.1. Microrollers alter microstructure in passive suspensions. We dope driven particles (microrollers) in a passive colloidal suspension, as demonstrated in the schematic (a) A small quantity of microrollers (driven particles) are added to a suspension of passive particles. (b) Microrollers contain a permanent magnetic moment, m , and are actuated by applying a uniform rotating magnetic field. This actuation generates strong advective flows, which scale with h_{roller} , the height of the particle above the surface; these flows are the driver for restructuring the passive suspension. (c) Microrollers restructure the passive suspension by modulating the mean local density; this restructuring becomes more and more apparent as we average over longer and longer times. (d) Restructuring of the passive suspensions results in the emergence of a steady-state pattern. Left image is the experimental result, in which brighter areas indicate a higher local intensity, which is correlated to a higher concentration of passive particles. Right image shows the result of Stokesian dynamics simulations, which reproduce the same pattern seen in the experiments.

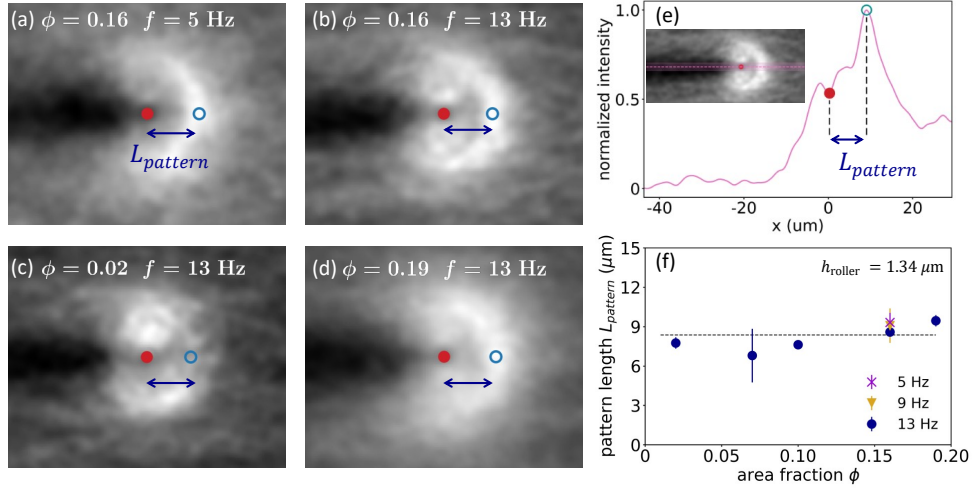


Figure 6.2. **The length of the new structure is independent of the microroller’s velocity (the rotational frequency) and the area fraction of the passive particles.** (a-b) Pattern length at two different actuation frequencies: (a) 5 Hz and (b) 13 Hz. We find that the pattern size, L_{pattern} , is independent of microroller velocity. (c-d) Similarly, altering the mean area fraction of passive particles has no effect on L_{pattern} . (c) $\phi = 0.02$ (d) $\phi = 0.19$. (e) To quantify L_{pattern} , we draw a box across the microroller along the x axis of the pattern and measure the average intensity in the y axis, as illustrated in the inset; the pink dashed line indicates the center of the box. Then, we find the peak of the intensity (the blue open circle) in front of the roller (the orange circle), and measure the distance from the peak to the microroller (the blue double arrow). (f) L_{pattern} is independent of both microroller velocity (actuation frequency f) and ϕ . We find the average L_{pattern} is 8.9 ± 0.9 μm (the black dashed line in (f)).

same size (2 μm in diameter). Due to the thermal fluctuation and electrostatic repulsion, both types of particles do not contact the floor but instead hover above the floor surface at an equilibrium height, h_{roller} and h_{passive} respectively, as shown in Fig. 6.1(b). The microroller’s translational velocity is determined by two parameters, the microroller’s height h_{roller} and its rotational frequency f . We select the rotational frequency to be between 5 Hz to 13 Hz in our experiments so that the speed of the microroller is linearly proportional to the rotating frequency (see SI.1).

In the driven-passive colloidal mixture, passive particles are initially distributed randomly around the microroller in the xy plane. When the external rotating magnetic field is on, the microroller is translating, and the flows generated by the microroller redistribute the passive particles (see Movie S1). We observe that the passive particles are restructured as follows: there is an accumulation of passive particles in the region of the direction of motion of the microroller (in the $+\hat{x}$ direction), while there is a depleted region opposite to the direction of translation (in the $-\hat{x}$ direction). We note that the average microroller speed is constant (see SI.2); the system is in a non-equilibrium steady state.

To quantify the restructuring, we calculate the time averaged number density of passive particles $\langle \rho_{\text{passive}}(\mathbf{r}) \rangle_t$ in the microroller's frame of reference. In the microroller's frame, the microroller is static, and it is the passive particles that move around the microroller (see Movie S2). A pattern in the passive particle distribution emerges around the microroller as we average more and more frames, as shown in Fig. 6.1(c). Brighter regions indicate a longer presence of passive particles while darker regions signal the opposite. The emergent pattern reveals a depletion of passive particles in the $-\hat{x}$ direction to the microroller, and a greater presence of passive particles in the vicinity of the microroller. Surprisingly, the peak of the accumulation (the brightest location) in the pattern in the $+\hat{x}$ direction to the microroller is much larger than the particle itself, approximately 10 times the radius of the microroller ($10 \mu\text{m}$).

To complement our experimental work, we study this system computationally using Stokesian dynamics with lubrication corrections (see Movie S3 for the microroller in the lab frame and S4 for the microroller in the microroller's frame). Therefore, near-field or lubrication corrections are included between particles in simulations. We also model

particles as perfectly rigid spheres to account for their finite size. Previous work has shown that a microroller rolls at constant angular velocity imposed by a rotating magnetic field rather than experiencing a constant torque [241]. Thus, to resemble experiments we study a rotating particle with constant angular velocity in a region where we have initially fixed the area fraction of passive particles. For suspensions at finite temperature we stochastically evolve the system to solve for Brownian dynamics and correctly account for thermal fluctuations. Importantly, the height of the microroller (h_{roller}) sets its velocity profile as a function of angular velocity. Obtaining h_{roller} from experiments is challenging, thus we use the velocity profile (the microroller's velocity as a function of rotational frequencies) to determine $\langle h_{\text{roller}} \rangle$ to use in simulations.

Moreover, we use Gaussian smoothing in all $\langle \rho_{\text{passive}}(\mathbf{r}) \rangle_t$ using a variance the size of the passive particle. This adds particle areal effects in $\langle \rho_{\text{passive}}(\mathbf{r}) \rangle_t$, and thus can be comparable to the experimental emergent pattern. In Fig. 6.1(d), we see that the simulation reproduces the same pattern as observed in experiments, and the areas of high intensity in experiments correspond to areas of high particle density in simulations.

In order to determine what parameters control the features and the size of the emergent pattern, we carry out experiments by varying the rotating frequency f from 5 Hz to 13 Hz, which linearly increases the microroller speed. We also perform experiments by varying the area fraction of passive particles ϕ_{passive} from 2% to 19%. As the temperature, particle density, and the electrostatic repulsions remain the same, h_{roller} is kept at $h_{\text{roller}} = 1.34 \mu\text{m}$ in all experiments. In no case do we observe that the pattern changes, see Fig. 6.2(a-d). To quantify our results, we compute a characteristic pattern length L_{pattern} by measuring the intensity across the pattern along the x axis and define L_{pattern} to be the distance

between the microroller center to the intensity peak, see Fig. 6.2(e). As expected from the experimental images, in Fig. 6.2(f), L_{pattern} is invariant with respect to ϕ_{passive} and f . The results demonstrate that the pattern length is independent of the microroller speed or the area fraction of passive particles at a given h_{roller} .

Using simulations, we also investigate the influence of changing h_{roller} . The simulations are carried out at $f = 10$ Hz and $\phi = 0.17$ at $T = 0\text{K}$ and $T = 293\text{K}$. The results are shown in Fig. 6.3. We measure the peak area fraction of the pattern to the microroller to extract L_{pattern} . As shown in Fig. 6.3(c), L_{pattern} is directly proportional to h_{roller} , even in the presence of thermal fluctuations. Both the flow field generated by the microroller and the microroller speed depend on both h_{roller} and f . As shown in Fig. 6.2, L_{pattern} is independent of f for a given h_{roller} . Therefore, the change of the flow field as a result of modifying h_{roller} must be the reason why the pattern changes. We will further elaborate the pattern mechanism in the Discussion section.

6.3. Discussion

To understand the origin of the emergent pattern from experiments we must determine the principle stresses at play in suspensions at finite temperature. Hydrodynamic forces between particles can be impacted by thermal fluctuations as they will disrupt particle's trajectories along streamlines. To estimate the relative influence of thermal fluctuations compared to the advective flows, we calculate the Péclet number, $\text{Pe} = \frac{R_{\text{passive}} u_{\text{fluid}}}{D_{\text{passive}}}$, where R_{passive} is the average passive particle radius, u_{fluid} is approximately the maximum velocity of the fluid due to a microroller, and D_{passive} is the passive particle diffusion coefficient. Using the values $R_{\text{passive}} = 1 \mu\text{m}$, $u_{\text{fluid}} = 50 \mu\text{m/s}$, and $D_{\text{passive}} = 0.15 \mu\text{m}^2/\text{s}$, we calculate

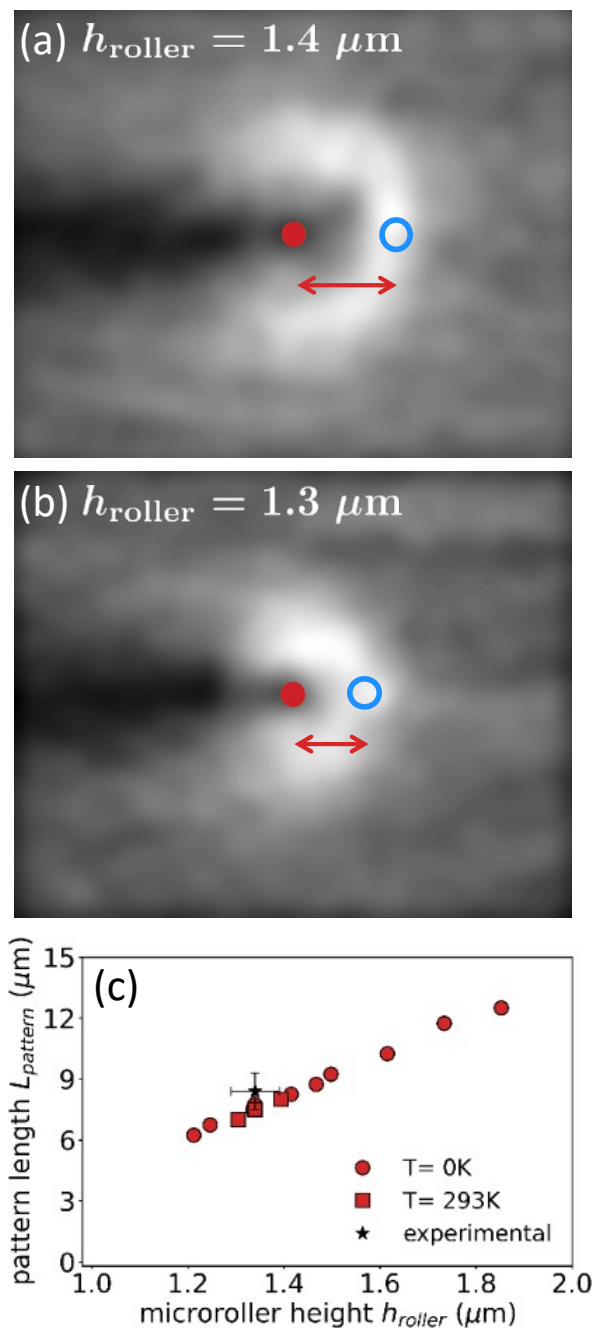


Figure 6.3. **The pattern length is set only by the microroller's height above the floor.** We perform simulations at different microroller's heights h_{roller} at $T = 0\text{K}$ and $T = 293\text{K}$ to investigate L_{pattern} as a function of h_{roller} . We observe that L_{pattern} becomes smaller as h_{roller} decreases: (a) $h_{\text{roller}} = 1.4 \mu\text{m}$, (b) $h_{\text{roller}} = 1.05 \mu\text{m}$, and is identical at $T = 0\text{K}$ and $T = 293\text{K}$.

that $Pe = 333 \gg 1$; and thus reveals that passive particle transport is dominated by microroller-generated advective flows rather than from thermal fluctuations. Therefore, computationally less expensive simulations at $T = 0K$ are sufficient to understand the origin of the pattern formation; Brownian motion does not alter the average size of the pattern.

As this is an advection-dominated system, we focus on the streamlines generated by the microroller to explain the formation of the emergent pattern. While these streamlines are three dimensional in nature we will show that it is sufficient to focus on streamlines in the xy plane to understand the formation of the emergent pattern. Moreover, the experimental measurements only capture the pattern extent in the xy plane.

We begin by calculating the flow velocity around the rotating microroller in the frame of the microroller, see Fig. 6.4(a). In the microroller frame, the microroller is stationary while the passive particles are the mobile species. In the flow profile in the microroller frame, two different sets of streamlines are observed in the fluid in the vicinity of the microroller: (1) a set that surrounds and recirculates around a pair of axial symmetric vortices alongside the microroller (light blue streamlines in Fig. 6.4(a)), and (2) a set that bounds and bypasses the recirculating region (light purple streamlines in Fig. 6.4(a)). An additional feature in the flow field is the appearance of two axially symmetric stagnation points in the front and back of the microroller. These stagnation points are saddle points, that is the fluid flow is convergent along one direction and divergent in the orthogonal direction. In our system, the microroller is always driven in the $+\hat{x}$ direction; this breaks the symmetry of the stagnation points. The front stagnation point focuses fluid along the x axis and ejects fluid in the $+\hat{y}$ and $-\hat{y}$ directions. Meanwhile, the opposite is true for

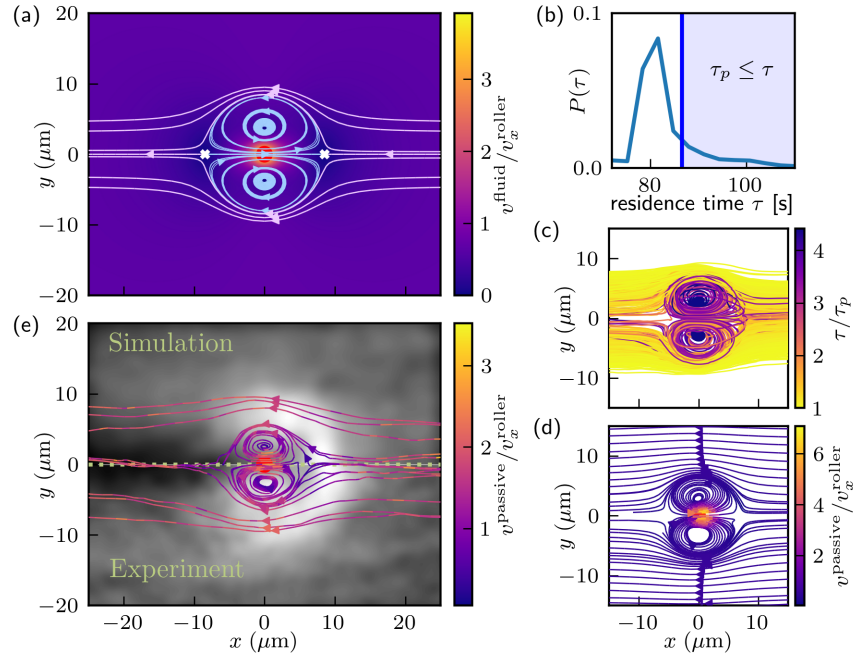


Figure 6.4. **The emergent pattern results from hydrodynamic interactions around a microroller.** Fluid streamlines in the microroller's frame produced from a microroller (orange circle) at $z = 3h_r$ (a). The fluid velocity is normalized by the microroller's translational speed. There are two characteristic sets of streamlines around the microroller, recirculating (blue) and bypassing (purple) streamlines. Additionally, we observe the presence of stagnation points (white x-crosses) in the front and back of the microroller. In a suspension of passive particles at $T = 0$ K, we extract passive particles that have residence times τ larger than background particles τ_p (b) and plot their trajectories (c). These trajectories are confined to the recirculating and bypassing regions. Using the average passive particle velocity profile in (d), we determined that particles in the recirculating region have long residence because they are trapped around the microroller. Meanwhile, particles in the bypassing region persist around the microroller due to their curved trajectories around the microroller. Finally, using simulation data of suspensions at $T = 293$ K, we show the passive particle streamlines around the microroller and overlay them on the simulation $\langle \rho_{\text{passive}}(\mathbf{r}) \rangle_t$ (top) and experimental emergent pattern (bottom)(e). This shows that the recirculating and bypassing streamlines span the emergent pattern.

the stagnation point behind the microroller; fluid is focused through streamlines in the y axis and expelled in the $+\hat{x}$ and $-\hat{x}$ directions.

To understand how a pattern emerges in the passive suspension, we first consider how a single passive particle interacts with the flow field generated by the microroller. To simplify our analysis, we assume that the passive particle does not perturb the microroller streamlines even though they are of finite size. We believe this is reasonable considering the dimensions of the emergent pattern as the distance between the microroller and the passive particles are a distance away where lubrication is negligible. We begin our analysis by considering a passive particle which remains in the plane of the xy streamlines (above the microroller) as seen in Fig. 6.4(a); a single passive particle approaching the microroller from the right and located around $y = 0$ will encounter the front stagnation point. Any slight perturbation will displace the particle in the $+\hat{y}$ or $-\hat{y}$ directions and direct the particle into the bypassing streamlines bounding the recirculating region. The particle would then be transported to the back stagnation point where once again a slight perturbation can either push the particle into the recirculating region or eject it in the $-\hat{x}$ direction. Sources of perturbations in the experimental system are thermal fluctuations and near field (lubrication) interactions from other particles. In dense passive particle suspension, near field interactions are prominent due to the proximity of particles in space. For equal sized spheres, this occurs when the distance between a pair of particles is equal to or less than two particle diameters. This interaction is largely associated to the squeezing of fluid out from between the narrowly separated particles. When two particles are close enough to each other in the stagnation region, where the fluid flow speed vanishes, near

field interactions will enable these particles to travel across streamlines away from the stagnation point and enter either the recirculating or bypassing streamlines.

To explain the emergent pattern observed in experiments, we note that $\langle \rho_{\text{passive}}(\mathbf{r}) \rangle_t$ is set by the residence time of the passive particles in the vicinity of the microroller. The emergent pattern arises from the contrast of residence times between the background passive particles and particles that spend more time near the microroller; passive particles that comprise the emergent pattern are those that remain in the vicinity of the microroller for an amount of time τ greater than the background passive particles. We calculate the background residence time, τ_p , which is the maximum time for background passive particles to spend within a square box that envelops the recirculating region of the fluid flow:

$$\tau_p = \frac{L_x}{\langle v_{\text{roller}} \rangle - \sigma_{v_{\text{roller}}}},$$

where L_x is the box length, and $\sigma_{v_{\text{roller}}}$ is the standard deviation of the microroller's speed in the \hat{x} direction. Interestingly, even in a suspension of passive particles at $T = 293$ K we observe deviations in the height of the microroller due to the near field interactions with passive particles. These height fluctuations result in fluctuations in the microroller's velocity. Here we choose $L_x = 20 \mu\text{m}$ as this is larger than the recirculation zone at this value of the microroller height. We note that the choice of L_x does not matter as long as the extension of the emergent pattern is contained within the box. This is because the variability of residence times only occurs in the regions of non-negligible hydrodynamic interactions near the microroller.

There are two possible mechanisms for passive particles to have residence times greater than the background time ($\tau > \tau_p$): (i) particles traverse the length L_x slower than the

microroller, or (ii) particles travel a distance greater than L_x within the square box with area L_x^2 . Using the passive particle trajectories from our simulations at $\phi_{\text{passive}} = 0.17$, $f = 5 \text{ Hz}$ and, $T = 0 \text{ K}$ we identify the set of passive particles where $\tau > \tau_p$. This set corresponds to the tail end of the distribution of residence times $P(\tau)$ as seen in Fig. 6.4(b), where the mean of $P(\tau)$ approximately corresponds to $\frac{L_x}{\langle v_{\text{roller}} \rangle}$. In Fig. 6.4(c) we plot the set of individual passive particle trajectories with $\tau \geq \tau_p$ colored by their residence time normalized by τ_p . Recalling that we are analyzing the particle trajectories in the microroller's frame, we observe that the trajectories with $\tau > \tau_p$ clearly replicate the microroller's streamlines as seen in Fig. 6.4(a). This shows that near field interactions between passive particles do not qualitatively affect the trajectories expected from the flow field of the microroller. There are two visible regions with contrasting residence times which directly correlate to the two sets of streamlines from Fig. 6.4(a), the recirculating and bypassing streamlines. Residence times within the recirculating region are on average 2.5 times greater than those that bypass it. This is further evidenced by Fig. 6.4(d) where we have calculated the average spatial velocity profile of the passive particles and observe that passive particles travel at the background speed and sometimes faster than the microroller. There is an additional set of particles with $\tau > \tau_p$; these are the particles whose trajectories correspond to the bypass region near the recirculation zone. As these curved trajectories are longer than the straight trajectories of the background particles, $\tau > \tau_p$ even though these particles move at the same velocity as the background particles. These results suggest that these two regions are responsible for the emergent pattern in experiments. To test this hypothesis, we perform simulations at finite temperature to more accurately replicate experimental conditions.

In order to produce simulation results that can be quantitatively compared to experiments, we carry out simulations at $T = 293$ K (see Fig. 6.1). From these simulations we calculate a pattern length of $8 \mu\text{m}$, similar to the experimental length ($8.4 \pm 0.9 \mu\text{m}$) and identical to the pattern length of suspensions at $T = 0$ K. This agreement is expected as thermal fluctuations are negligible in our system. To demonstrate the agreement between the experimental results and the Stokesian dynamics simulations we directly compare the pattern found in experiments with that found in the simulations; the top half of Fig. 6.4(e) is the passive particle distribution from the simulations, while the lower half is that obtained from experiments. We observe that the passive particle streamlines associated to the recirculating and bypassing region in Fig. 6.4(e) overlap with the emergent pattern. Moreover, these streamlines also reflect thermal fluctuations in the positions of the passive particles. Therefore, we have shown the emergent pattern from suspensions at finite temperature are well described by advective flows generated by the microroller.

In summary, we have established that the emergent pattern reveals regions of non-negligible hydrodynamic interactions. We have characterized this by demonstrating passive particle residence times around the microroller are extended due to the recirculating and bypassing streamlines produced by a microroller. Thus far it has been sufficient to only use information from the xy plane to explain the experimental results. This is due to the fact that the patterns obtained from the experiments are calculated from particle locations projected on the xy plane within the depth of field of the microscope. Experimentally, we lose information away from the focal plane, but particle fluctuations from their average height seem to be negligible. Thus, it is sufficient to only use information

from the xy flow plane to trace passive particle trajectories and explain the origin of the emergent pattern.

We now consider how the passive particle height, h_{passive} , influences the emergent pattern. By modulating the passive particle height, we will sample a different region of the microroller flow field, and, consequently, the emergent pattern will change. To illustrate this, we need to analyze the flow field in three dimensions, and understand how the recirculating and bypassing regions change as a function of passive particle height. Additionally, we need to consider how xz streamlines (Fig. 6.5 left panel) can lift particles above their average height. This will lead passive particles to interact with different sets of streamlines in the xy plane and lead to emergent patterns with different spatial features (Fig. 6.5 right panel).

Previously, we identified the existence of two stagnation points at the front and back of the microroller in the xy plane, see Fig. 6.4(a). The region bounded between both stagnation points is the recirculating region of the microroller streamlines in the xy plane and gives rise to the emergent pattern. To understand how the emergent pattern changes with respect to the z axis, it is sufficient to track the front stagnation point as a function of the height from the floor. In Fig. 6.5, we show the microroller's xz streamlines at $y = 0$ in the microroller's frame. We superimpose the calculated xy velocity component stagnation line (dashed white line) which correlates to the extension of the recirculating region on the xy plane. Note that the streamlines intersect the stagnation line, meaning the z component velocity is not zero. This curve is not a true stagnation line as not all velocity components are zero, therefore, it is a saddle line.

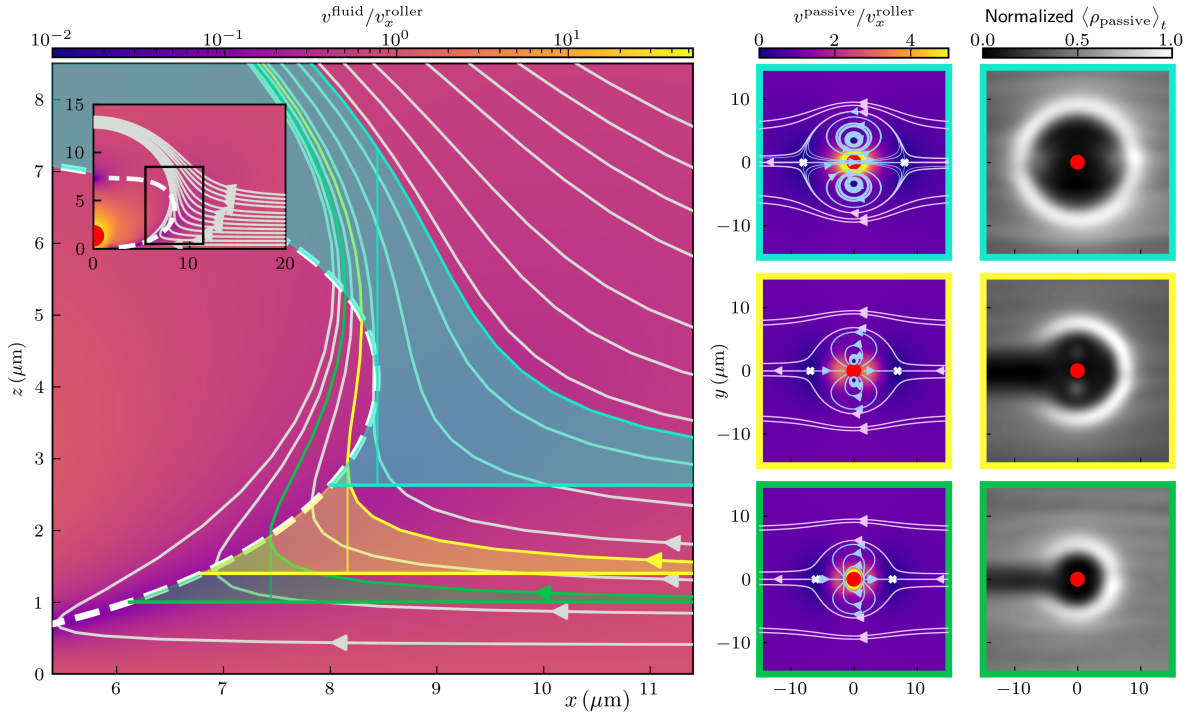


Figure 6.5. **The microroller’s hydrodynamic interactions extend in three dimensions and can be probed by passive particles at different heights.** In the left panel, we plot the xz microroller streamlines at the $(x, 0, z)$ plane for a microroller height $h_{\text{roller}} = 1.34 \mu\text{m}$, and show that not all streamlines (grey curves) intersect the xy stagnation line or saddle line (dashed white curve). Additionally, the saddle line determines the x axis extension of the xy fluid recirculating streamlines at a given height (middle panel). Therefore, different average passive particle heights in suspensions will probe these different recirculating and bypassive streamlines and create different emergent patterns (right panel). We study suspensions with three different particle heights $1.01 \mu\text{m}$, $1.4 \mu\text{m}$, and $2.6 \mu\text{m}$ which we color code green, yellow and cyan, respectively. In the xz streamlines we bound regions that correspond to the average height of the passive particles and by the xz streamline far from the microroller at the average height of the passive particle. In the middle panel we plot the three different xy streamlines whose spatial extensions are mirrored in suspensions’ emergent pattern. We find that the depletion region is present only in the suspensions with particle heights whose bound region near the saddle line is closed.

The saddle line's x axis extension varies as a function of z . This indicates that the spatial extension of the emergent pattern changes by tuning the height of the passive particles. This is because passive particles will sample different sections of the saddle line. We note that the saddle line is uniquely determined by h_{roller} . Here we continue to solely focus on passive particle suspensions in water with $h_{\text{roller}} = 1.34 \mu\text{m}$.

In order to demonstrate the degree of tuning of the emergent pattern's extent with respect to the height of the passive particles, we perform sets of simulations at $T = 0\text{K}$ with different average passive particle heights $\langle h_{\text{passive}} \rangle$ at constant $\langle h_{\text{roller}} \rangle$. In athermal suspensions, only hydrodynamic forces and the interplay between gravitational and charge repulsion from the floor will change particles' height. We tune $\langle h_{\text{passive}} \rangle$ by varying their excess mass m_{passive} with respect to water, and focus on three different $\langle h_{\text{passive}} \rangle$. In suspensions without the presence of a microroller, passive particles have an average height of $1.01 \mu\text{m}$, $1.4 \mu\text{m}$, and $2.6 \mu\text{m}$ for passive particle excess masses of $10m_{\text{passive}}$, m_{passive} , and with $1/100m_{\text{passive}}$, respectively.

As we have previously stated, suspensions with different h_{passive} will form distinct emergent patterns given the curvature of the saddle line. However, we must consider how the xz streamlines in Fig. 6.5 will impact where passive particles intersect the saddle line. Near the saddle line, xz streamlines can lift particles above their $\langle h_{\text{passive}} \rangle$ and lead to intersect at $z > h_{\text{passive}}$. In Fig. 6.5 left panel, we color regions green, yellow, and cyan, to indicate the range of heights where passive particles will most likely intersect the saddle line for $\langle h_{\text{passive}} \rangle = \{1.01, 1.4, 2.6\} \mu\text{m}$, respectively. The lower bound of the colored regions is defined by the particle's $\langle h_{\text{passive}} \rangle$, and the upper bound corresponds to the xz streamline far from the microroller at the respective $\langle h_{\text{passive}} \rangle$. At a distance far from

the microroller, $\sim 30 \mu\text{m}$, the microroller's hydrodynamic interactions have sufficiently decayed such that the xz streamlines are parallel to one another. This simply represents the background flow which in this reference frame corresponds to the microroller's velocity.

In general, all xz streamlines curve upwards as approaching the saddle line. This leads to multiple xz streamlines overlapping the different colored regions that passive particles will most likely intersect the saddle line for a given average height. Out of simplicity, we select to intersect the saddle line at the lower bound of this region, the average passive particle height, and plot the xy streamlines around the microroller at this height, see Fig. 6.5 middle panel (where we show and color the borders of the xy streamlines green, yellow, and cyan to indicate average passive particle heights $\langle h_{\text{passive}} \rangle = \{1.01, 1.4, 2.6\} \mu\text{m}$, respectively). As expected, the spatial extension of the recirculating streamlines at different z levels follow the saddle line x values for a given height. In order to show that the emergent patterns obtained from athermal suspensions at different passive particle heights mirror their respective xz streamlines, we plot their $\langle \rho_{\text{passive}}(\mathbf{r}) \rangle_t$ obtained from simulations at $T = 0 \text{ K}$, see Fig. 6.5 right panel. For all cases, emergent patterns mirror the L_{pattern} of their bypassing streamlines in the xy plane. However, we find a wide variety in the geometry of the emergent pattern. Only suspensions of passive particles with $\langle h_{\text{passive}} \rangle = \{1.01, 1.4\} \mu\text{m}$ have a depletion region behind the microroller. Meanwhile, suspensions composed of passive particles with $\langle h_{\text{passive}} \rangle = 2.6 \mu\text{m}$ produce an emergent pattern without a depletion region. This difference is produced by the nature of the xz streamlines and their ability to lift particles above their average height. Suspensions that produce emergent patterns with an inverted c-shape structure correspond to passive particle heights in which the majority of the particles will intersect with the saddle line.

This can be observed in the colored bounded regions in Fig. 6.5 left panel, where all xz streamlines in the green and yellow regions are also fully bounded by the saddle line. It is the cyan region which corresponds to passive particles with $\langle h_{\text{passive}} \rangle = 2.6 \mu\text{m}$ that contains xz streamlines that miss the saddle line. Thus, not all passive particles intersect with the saddle line and avoid interacting with the recirculating and bypassing streamlines. By not entering the recirculating region, the xz streamlines will transport passive particles above and around the microroller and occupy the region where the depletion region is seen at lower $\langle h_{\text{passive}} \rangle$.

Moreover, we briefly explore the origin of the depletion region of the emergent pattern by performing two sets of simulations at $T = 0 \text{ K}$. Each set of simulations isolates different interactions between particles. In one case, we remove the hydrodynamic near-field interaction, and the steric interaction that prevents particles from overlapping. In the second set, we leave all near-field interactions intact but simulate mass-less passive particles. We initialize their height at $z = 1.34 \mu\text{m}$. Interestingly, the depletion region is still present when near-field interactions are neglected but disappears in suspensions of mass-less passive particles, see Figure S3. This indicates the importance of sedimentation when particles are lifted above their equilibrium height. It has previously been reported[239] that the strength of gravity plays an important role in the dynamics of microroller systems.

Although this is out of the scope of this paper, we believe that the size of the passive particles should also play a role in the formation of the depletion region. Given that all particles in the suspension are of finite size, they simultaneously sample multiple sets of streamlines and experience shearing. Therefore, a competition between particle size and

the local gradients of the streamlines ensues where particles with sizes smaller than the local gradient will mostly be advected while larger particles will be more greatly sheared which will affect their dynamics.

Overall, no matter $\langle h_{\text{passive}} \rangle$, all emergent patterns mirror the extension of the recirculating and bypassing regions in the xy plane at their respective height. We should thus expect that for $\langle h_{\text{passive}} \rangle$ above the saddle line no emergent pattern will appear as there would be no region of non-negligible hydrodynamic interactions for the passive particles to sample. Importantly, we have shown that the emergent pattern can be controlled by modifying the height of the passive particles. As we move up from the floor, both recirculating and bypassing regions should increase until they begin to decay as we probe heights further away from the microroller.

As the saddle line correlates well with the extension of the emergent pattern, we propose L_{pattern} to be the distance between the microroller and the saddle line L_{saddle} . As previously quantified in Fig. 6.2(f), L_{pattern} does not change when varying the suspension's passive particle area fraction nor the microroller's velocity, it only changes with the height of the microroller, as does the saddle line. However, to compare L_{saddle} and L_{pattern} , one ambiguity persists, at which height to calculate L_{saddle} ? By analyzing the xz streamlines we have identified a set of bounds for a given $\langle h_{\text{passive}} \rangle$ that delimits the heights passive particles will be driven to by the microroller's xz streamlines. Using these bounds, and knowing both $\langle h_{\text{roller}} \rangle$ and $\langle h_{\text{passive}} \rangle$, we can provide an interval for L_{saddle} to compare with L_{pattern} obtained from simulations and experiments to show that these two quantities are equivalent.

We perform simulations with a microroller at different $\langle h_{\text{roller}} \rangle$ and calculate L_{pattern} . Furthermore, we compare and parameterize L_{pattern} by $L_{\text{saddle}}(z; \langle h_{\text{roller}} \rangle)$, where z is the height above the floor. As previously discussed, the pattern length has a strong dependency on passive particle height for a given microroller height due to the curvature of the saddle line. Therefore, in simulations at $T = 0\text{K}$ we keep the ratio between the passive particle and microroller height approximately constant, $\langle h_{\text{passive}} \rangle / \langle h_{\text{roller}} \rangle \approx 1.2$, to only focus on the effects of h_{roller} on the emergent pattern. Meanwhile, the average height of the passive particles in finite temperature suspensions is $\langle h_{\text{passive}} \rangle = 2.5 \mu\text{m}$. In Fig. 6.6, we plot L_{pattern} and the L_{saddle} region, and show that the L_{saddle} region is a good descriptor for the emergent pattern obtained from suspensions at $T = 0\text{K}$, and $T = 293\text{K}$. Additionally, the extension of the pattern length and L_{saddle} decreases as the microroller approaches the no-slip boundary. This is expected, as moving closer to the surface effectively screens the hydrodynamic interactions, reducing their extent. The opposite is true for a microroller further away from the surface. However, as the microroller's height is increased the coupling between the microroller's rotation and translation diminishes until the translation velocity becomes infinitesimally small. In a suspension at finite temperature, thermal fluctuations would then disrupt the pattern created by advective flows.

6.4. Conclusion

In conclusion, we have demonstrated the ability to use a driven particle to create a large-scale (10 times the particle radius), asymmetrical 3D pattern from a quasi-2D colloidal suspension. The pattern includes an accumulation region with its center being

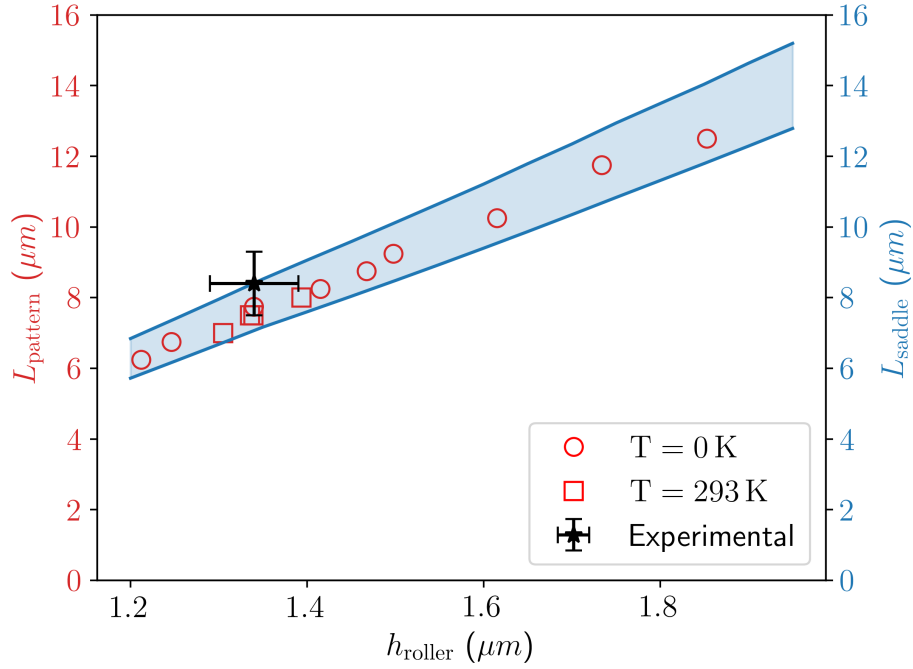


Figure 6.6. **Tuning the pattern length by changing the microroller height.** We show that the pattern length L_{pattern} directly correlates to the distance between the microroller and its front saddle line $L_{\text{saddle}}(z; \langle h_{\text{roller}} \rangle)$ (blue region). As previously stated, the saddle line is a function of height, and multiple streamlines in the xz plane intersect a given height which complicates which height to choose to calculate L_{saddle} . However, we bound the (blue) L_{saddle} region by using the bounds determined and shown in Fig. 6.5.

several particle sizes away from the microroller, and a depletion region along the microroller trajectory. This pattern is created via hydrodynamic interactions, and is unmodified by thermal fluctuations, passive particle area fraction, or driving velocity. We show two main pathways to modify the pattern by altering the hydrodynamic interactions between the microroller and the passive particles. This can be done by tuning the height of the passive particles in the suspension with respect to the microroller, or by modifying the

height of the microroller with respect to the floor. Our analysis of the microroller-driven advective flow that generates the pattern demonstrates that the extension of the emergent pattern is equivalent to the distance between the microroller and the flow's saddle line. Thus, modifying the average height of the microroller changes the pattern's size as it changes the features of its fluid velocity profile. Additionally, by modifying the passive particle height in a suspension at constant microroller height, the particles are able to sample other planes of non-negligible hydrodynamic regions and change the extension of the pattern, which demonstrates the three dimensional nature of the microroller's streamlines.

Our analysis reveals that the pattern scale is determined by equilibrium quantities: the microroller height and the height distribution of the passive particles. Thus, the size scale of the emergent pattern provides an alternative pathway to determine an approximate average passive particle height in a suspension if the h_{roller} is known. This analysis is straightforward, is not computationally demanding, and offers a new tool for studying fluid-mediated interactions of driven particles. If there are weak or transient interaction between the passive particles (for example in a colloidal gel), this pattern formation could be exploited for material restructuring. This system also offers an alternative way to do active microrheology [240]. For example, we observe that a microroller moves slower when it is in a colloidal suspension than when it is in a pure fluid. One can thus calculate the effective viscosity of the colloidal suspension by measuring the change of the microroller speed as a function of colloidal volume fraction, and measure density fluctuations by measuring roller velocity fluctuations. Additionally, similar principles of microroller streamlines can perhaps be used to explain how a mixture of passive particles

and biologically active swimmers lead to anomalous transport coefficients of the passive particles via hydrodynamic interactions [221, 222]. Finally, we note that when the passive particles enter the recirculating streamlines, they are trapped and move together with the microrollers. Therefore, microrollers that generate these streamlines, or microvortices, have the potential to transport micron-size particles.

Materials and Methods

Experiments

The passive particles are spherical and made of polystyrene (Bangs laboratory©, FSPP005) with a density of 1.06 g/cm^3 and a mean diameter of $= 2.07 \pm 0.15 \mu\text{m}$. The microrollers in the experiment are described in detail in [241] and [242]. The microroller has a mean diameter of $2.1 \pm 0.1 \mu\text{m}$ and a permanent magnetic dipole as it is comprised of a hematite cube within a spherical polymer matrix, see Fig. 6.1(b). The mean density of the microroller is 1.74 g/cm^3 . We clean the passive particles by replacing the solution with DI water for three times. Then we add a small amount of microroller solution to the passive particle solution, and mix the solution with a vortex followed by a sonicator. We withdraw the mixture solution with a capillary tube, and seal the tube entrance with glue. Then, we mount the sample on a microscope, and check the area fraction of passive particles after all particles sediment to the floor. Finally, we apply rotating magnetic fields and record the particle distribution with the fluorescent microscope. The microrollers and the passive particles have different fluorescent wavelength, giving us the ability to separate the two types of particles in two channels.

The system and the mechanism to drive a microroller is described in detail in [241]. In short, we use two pairs of Helmholtz coils to generate an external rotating magnetic field (100 G). The permanent dipole of a driven particle experiences the torque from the external field, causing the driven particle to rotate synchronously with the field. As the microroller is near the floor, the flow generated by the rotating driven particle becomes asymmetrical due to the non-slip boundary of the floor, which causes the microroller to translate. We trace the location of the microrollers using Python and the package Trackpy, which we use to generate a sequence of images around the microroller. We then use the position of the microroller to shift the coordinates of all images to the microroller frame.

Simulations

As we have shown, the predominant interaction between a microroller and passive particles in suspension are hydrodynamic in nature. To correctly quantify these interactions we simulate these systems using lubricated corrected Brownian dynamics [241]. In this method the position and orientation of a particle $\mathbf{q}_1 = \{\mathbf{x}, \theta\}$ are evolved by

$$(6.1) \quad \frac{d\mathbf{Q}}{dt} = \overline{\mathbf{M}}\mathbf{F} + k_B T \partial_{\mathbf{Q}} \cdot \overline{\mathbf{M}} + \sqrt{2k_B T \overline{\mathbf{M}}} \mathbf{W}(t)$$

where $\mathbf{Q} = [\mathbf{q}_1, \mathbf{q}_2, \dots, \mathbf{q}_n]$ is the vector containing the the individual positions and orientations of all particles. Here, pairwise hydrodynamic interactions between particles are determined by their configuration in space and contained in the lubrication corrected mobility matrix $\overline{\mathbf{M}}(\mathbf{Q})$. The magnitude of these interactions are weighted by deterministic properties governed by external forces \mathbf{f} and torques τ acting on particles in solution, and

stochastic properties arising from the presence of thermal fluctuations. The first term with respect to the right of Eq. 6.1 details its deterministic character, here $\overline{\mathbf{M}}$ is weighted by the vector comprised of individual external forces and torques on impinging on all particles $\mathbf{F} = [\mathbf{f}_1, \tau_1, \dots, \mathbf{f}_n, \tau_2,]$. The second and third terms of the equation deal with the thermal drift, and random walk nature of the of the thermal fluctuations, respectively. Here, k_B denotes the Boltzmann constant, T indicates the solvent temperature, and $\mathbf{W}(t)$ represents a Wiener process or a collection of independent white noise processes essential for the generation of Brownian velocities. Given that this is a stochastic differential equation, we temporally integrate this equation using a stochastic scheme, specifically the ‘Stochastic Trapezoidal Split’ (STS) scheme [241]. In this paper we perform simulations of Eq. 6.1 evolved by the STS scheme using a publicly accessible code found on github at RigidMultiblobsWall. More details including the accuracy of this scheme, and pre-conditioners employed in the solution for $\overline{\mathbf{M}}^{1/2}$ can be found in [241].

To simulate suspensions of passive particles with a microroller, we model passive particles and the microroller as spherical rigid particles with radii $R_{\text{passive}} = 1.0 \mu\text{m}$, and $R_{\text{roller}} = 1.0 \mu\text{m}$, respectively. The particles are immersed in water at $T = 293.15 \text{ K}$, and they have a buoyant mass of $m_{\text{passive}} = 2.5 \times 10^{-16} \text{ kg}$, and $m_{\text{roller}} = 3.1 \times 10^{-15} \text{ kg}$, respectively. We perform three dimensional simulations with an initial condition set by fixing the area fraction of passive particles and randomly populating passive particles in a two dimensional strip of $250 \mu\text{m}$ in length and $75 \mu\text{m}$ width at $z = 1.5 \mu\text{m}$. Finally, we place a non-rotating microroller to the left of the strip, and equilibrate particle positions by evolving the system for approximately 60s, after which we rotate the microroller at

constant angular velocity using the algorithm detailed in [241]. For all instances of the simulations we use a time step of $\Delta t = 0.05$ s.

In this paper, all particles experience gravitational forces given their excess mass, and electrostatic repulsion with the lower surface. We model the electrostatic repulsion using the Yukawa type potential:

$$(6.2) \quad U(h) = \begin{cases} \epsilon \exp\left(\frac{R-h}{\kappa}\right) & \text{if } h > R \\ \epsilon \left(1 - \frac{R-h}{\kappa}\right) & \text{if } h < R \end{cases},$$

where h is the particle center to floor distance, and R is the radius of the respective particle. For the microroller, we set the magnitude of the potential ϵ , and its screening factor κ that simultaneously matches the height that replicates its experimentally obtained velocity profile ($h_{\text{roller}} = 1.34 \mu\text{m}$), and its measured diffusion coefficient, $D_{\text{roller}} = 0.15 \mu\text{m}^2/\text{s}$. For the passive particles, we assume the same κ as the microroller, and instead fit ϵ to match its experimentally obtained diffusion coefficient, $D_{\text{roller}} = 0.015 \mu\text{m}^2/\text{s}$. The list of parameters used in the simulations can be found tabulated in the SI. Additionally, as the suspension is located above a no-slip wall, hydrodynamic interactions are calculated using Blake's solution of the Green's function solution to the Stokes equation above a no-slip wall generalized for spherical rigid particles [243, 244]. However, this Green's function only correctly describes far field hydrodynamic interactions between all pairs of surfaces, particle-particle and particle-wall. To include near field hydrodynamic interactions related to the squeezing of fluid between pairs of surfaces we use the previously mentioned lubrication corrected mobility matrix $\overline{\mathbf{M}}$ detailed in [241]. Moreover, we use two different cutoffs

that determines at which distance between surfaces at which to calculate either near field hydrodynamic interactions or far field hydrodynamic interactions. For particle-particle interactions the cutoff distance is $r \leq 5 \mu\text{m}$ where for distances greater than $5 \mu\text{m}$ we simply calculate interactions with the Green's function solution. Meanwhile, we calculate near field hydrodynamic interactions for particle-wall interactions for any distance above the wall. For more information about the implementation of the resistance scalars for near field interactions can be found in [241]. We additionally complement near field hydrodynamic interactions with a short-ranged steric repulsion potential $U_{\text{cut}}(r)$ with the Yukawa type potential of Eq. 6.2 for particle-particle and particle-wall interactions. In the case for particle-particle interactions we substitute $R = 2R(1 - \delta_{\text{cut}})$, while $R = R(1 - \delta_{\text{cut}})$ for particle-wall interactions, where $\delta_{\text{cut}} = 10^{-3} \mu\text{m}$. The complete set of parameters used in $U_{\text{cut}}(r)$ are also tabulated in the SI.

Additionally, we calculate $\langle \rho_{\text{passive}} \rangle_t$ averaging over at least 10 different simulation runs using a $30 \mu\text{m} \times 30 \mu\text{m}$ mesh with bin width $\Delta L = 0.25 \mu\text{m}$. We choose to average over frames 0.1 s apart and where the microroller is $L_x \in [20, 230] \mu\text{m}$. Under these bounds the microroller is within the region of passive particles with a given area fraction ϕ . We also use this implementation to avoid averaging over regions outside the bounds of the suspension which affects the formation and dimensional features of the emergent pattern. After calculating $\langle \rho_{\text{passive}} \rangle_t$ we use Gaussian smoothing with a variance the size of the passive particle radius to include particle areal size effects. This allows comparison between $\langle \rho_{\text{passive}} \rangle_t$ and experimental emergent patterns now that $\langle \rho_{\text{passive}} \rangle_t$ contains information of the passive particle size and loosens the constraints on the distributions obtained by using a homogeneous binning mesh of $0.25, \mu\text{m}$. We calculate all velocity distributions of

a microroller also using the Blake's solution to the Green's function of a stokeslet above a no-slip wall generalized for a spherical particle [244].

6.5. Supporting Information

Supporting information contains: the pair distribution functions over the studied temperature range; details of the determination of T_{deloc} ; the calculation method for occupied volume and the heat capacity; and an analysis of nearest neighbor interactions (PDF). Videos of rotating unit cells of a localized and delocalized sublattice for both unconstrained and fixed lattice simulations are also available (.mp4 videos).

Acknowledgements: We thank Brennan Sprinkle for fruitful discussions concerning Brownian motion of low density particles, and Bhargav Rallabandi for discussions on the Péclet number and tracers. H.L.-R. acknowledges support from a MRSEC-funded Graduate Research Fellowship, (DMR-2011854). This work was primarily supported by the University of Chicago Materials Research Science and Engineering Center, which is funded by National Science Foundation under award number DMR-2011854.

CHAPTER 7

Conclusions and Outlook

The impact that colloidal matter, and in general soft matter, has had on materials science has been vast. Colloidal matter has been found to be a model system for hard condensed matter systems to the extent that nucleation [7] and dislocation dynamics [6, 27] in colloidal systems has been used to gain a better understanding of their atomic counterparts. The latter was done by showing that dynamical behaviors in both systems, colloidal and atomic, are described by the same mathematical equations and thus follow identical dynamical scalings. This sense of universality between phenomena found in either type of matter, colloidal or atomic, I find fascinating as this can open other horizons by questioning what other functionalities can colloidal matter be imbued with such that it may also serve as a model for other systems. The body of work in this thesis strived to explore and further expand functionalities associated to colloidal matter such as an analogous form for the insulator-to-metal transition and their potential for training in materials.

In chapter 2, we found how tuning the shape anisotropy of particles grafted with complementary DNA chains affects the phase space of DNA self-assembled colloidal crystals. Unlike atoms in atomic matter, particles of colloidal suspensions can be synthesized to take many different shapes. The only sense of similarity to different particle shapes in atomic crystals is the different possible hybridization electronic states molecules can take dictated by their valence electrons. In either case, different particle shapes or different

molecule hybridization types enables an entire onslaught of different crystal structures. The applications for colloidal crystal lattices have been difficult to find considering how soft and fragile they are [245], but they have been found uses as photonic materials as certain lattices contain photonic band gaps useful for light sensing [159]. To enhance the applicability of these colloidal crystals one must further enhance their internal degrees of freedom. One path is to introduce a greater degree of symmetry breaking within the components of the colloidal crystal. This was the objective of the work presented in chapters 3 and 4, work which was also greatly motivated by the findings of [20]. By simply breaking the symmetry of the interacting components of the self-assembling crystal, we found that lattice vibrations controlled behavior akin to a insulator-to-metal type transition. The larger species are located at the lattice points of all self-assembled crystals, whereas the smaller species locate at their symmetric interstitial sites. When the larger particles begin to vibrate due to thermal fluctuations, this affects the potential energy landscape of the smaller particles and enables them to delocalize and diffuse throughout the crystal. In some cases, the enhanced small particle diffusion leads to a crystal lattice transition. Thus, this system shows a insulator-to-metal like behavior, which seems heavily tied the lattice vibrations. These size-asymmetric colloidal crystals can be further analyzed by exposing them to externally produced shockwaves with the idea of adding a new knob for controlling their crystal lattice type. Additionally, another pathway for enhancing these systems is the addition of some charge to the smaller particles for charge transport. Such systems could then be used as model systems for superionic materials [102].

Meanwhile, chapters 5 and 6 consisted of systems with dynamical internal degrees of freedom necessary for training in materials. Only through the repeated reconfiguration of a

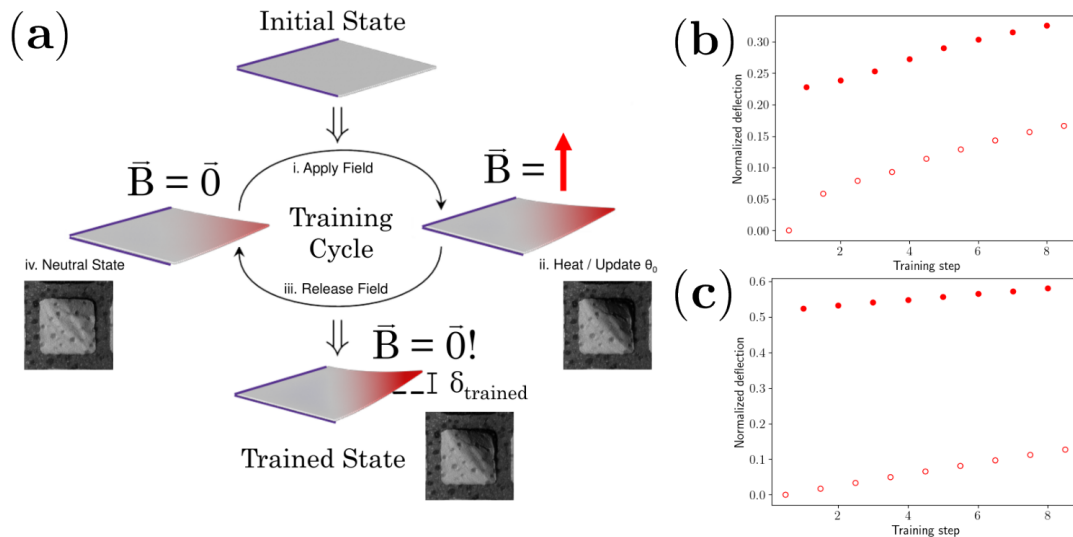


Figure 7.1. Training magnetoelastic sheets. Diagram of training protocol to train curvature into an initially flat sheet (a). Deflection of an experimental sheet during the training protocol (b). The analogous training curves for a simulated sheet (c). In both cases the upper curve shows the deflection of the free corner when the field is on, while the lower curve is the equilibrium deflection when the field has been turned off. Experimental training data is courtesy of Edward P. Esposito.

subset of a material's internal degrees of freedom have materials been shown to be trainable [28, 246]. We showed in chapter 5 how an elastic sheet of magnetic particles can bend out of plane in the direction of the external magnetic field due to arising magnetic dipole forces among all the particles. The origin of the sheet's elastic response is the van der Waals interactions arising from the confined grafted oleic acid chains on the particles surfaces. Simulations of these sheets assume that the equilibrium configuration of the sheet is a perfectly flat state. The actuation of these sheets is driven by the magnetic forces which are balanced with the sheet's elastic properties, which oppose out-of-plane configurations. However, sheet reconfigurability only fulfills half of the requirements for the sheet to be trainable. The sheets must elastically reconfigure towards a new equilibrium state during

being actuated. Preliminary experimental data has shown that under the presence of both a magnetic field and a laser, the sheet will retain some curvature proportional to its deflection after both the laser source and magnetic field are turned off. From the latter we construct our training protocol which consists of two steps: first, actuate the sheet until it has equilibrated and then scan the sheet with a laser, and second, turn the field off. We repeat this until the amount of deflection in the sheet saturates, see Figure 7.1(a). Figure 7.1(b) shows experimentally this is possible, where the upper curve is the maximally deflected state (the external field and laser are on), and the lower curve is the new equilibrium configuration of the sheet (the external field and laser are off). We believe that the mechanism for training of the sheets must consist of some reconfiguration of the grafted chains only when the sheet is being simultaneously bent and heated. We test this hypothesis using simulations where we locally update all the i th reference angles $\theta_{i,0}$ (see equation 1.1) between adjacent triangular facets. We choose the amount of curvature to be added to be proportional to the angle between the adjacent facets when the field is applied. In Figure 7.1(c) we see that our simulation results qualitatively reproduces the training seen in experiments. However, there is still much more to do. First, we must confirm that our simulation results are quantitatively similar to experiments. Second, once we have confirmed our simulation model, it would be of great interest to correlate training and its associated elastic energy. In this way we may extract information about the degree of chain reconfiguration after every training step and calculate parameters associated to the efficiency of learning in these sheets.

In chapter 6, we were similarly motivated to take advantage of the relaxation effects on motile particles due to an enveloping medium. But instead of using an elastic medium, we

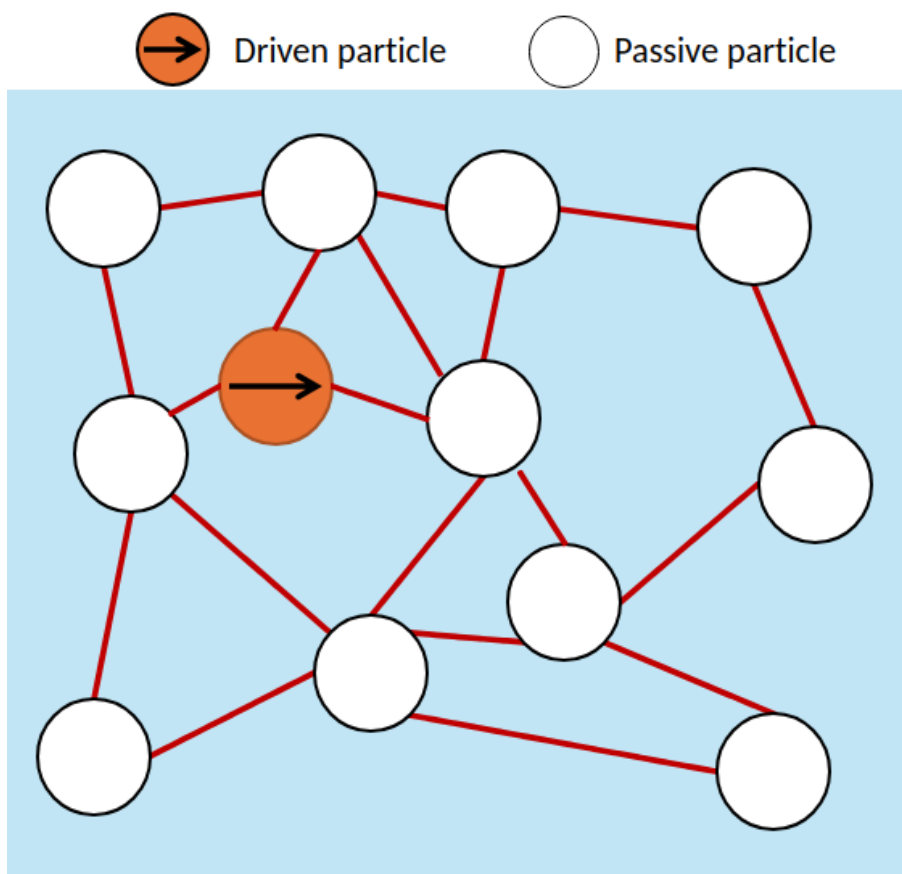


Figure 7.2. Theorized trainable system of a suspension of passive particles with a single driven particle. The red lines indicate pairwise interactions between particles which can be reconfigured due to the translation of the driven particle. Diagram courtesy of Shih-Yuan Chen.

use a hydrodynamic one through which particles can easily flow. Additionally, we wished to understand the reach of hydrodynamic forces of a single rolling and translating particle in a suspension of passive particles at finite temperature. All particles in this system are close to a horizontal and solid surface, thus a rolling particle will also translate given its proximity to the surface [243]. In general, by driving the rotation of a single particle we showed that the range of non-negligible hydrodynamic interactions emanating from this single rotating-translating particle is 10 times its radius. We found this range to be

Independent of external physical parameters such as passive particle concentration and the particle's rotation velocity. We identified this by analyzing an emergent pattern created by passive particles. However, once we stopped driving the rotation of the rolling-translating particle, the emergent pattern would disappear due to thermal fluctuations. Thus, we would need to enhance this system for it to be trainable. One idea is to induce attractive interactions among all particles, see Figure 7.2, such that they would be strong enough to oppose particle motion due to thermal fluctuations, but weak enough for particles to still be mobile due to hydrodynamic interactions. Interesting features of such a system would be how the number of interacting particles affects the suspension's viscosity as this would be tunable by the translating driven particle. A similar analysis on different acoustically trained suspensions has been shown to impact the strain rate for the onset of shear jammed states [246]. The latter was modulated by different training protocols where frequency amplitudes of the acoustic source was varied. Though it is difficult to tune the magnitude of the interactions in our theorized system, we can modify the range of the hydrodynamic forces. In chapter 6 we found that there are two ways of doing this: modifying the height of the rolling-translating particle or altering the height of the passive particles. But these two parameters are two faces of the same coin, they simply reveal the inhomogenous nature of the hydrodynamic flow around a rolling-translating particle. In Figure 7.3(a), we observe two distinguishable sets of streamlines, those that encapsulate a vortex, and others that avoid this encapsulating region. The interface of these two sets defines the range of the non-negligible hydrodynamic interactions between the driven particle and passive particles. Additionally, the appearance of a microvortex indicates the ability of this microroller to transport passive particles like cargo [247, 248]. This is striking because

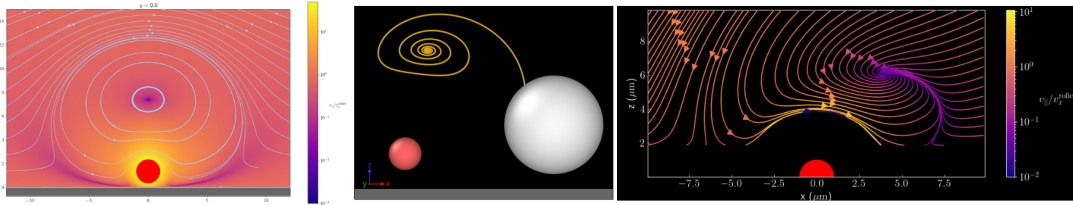


Figure 7.3. Transporting passive particles. (a) Streamlines generated by a rotating particle above a plane. (b) Initial configuration of a driven rotating particle (red) and a passive particle (white), and the passive particle's pathline (golden curve). (c) Phase plot of passive particle pathlines for all initial configurations of the passive particle.

spheres were once thought not to have this functionality [**chamolly2020irreversible**]. Inspired by our previous work that dealt with particle size asymmetry (chapters 3 and 4) we have preliminary results that suggest a smaller rolling-translating particle can carry a passive particle up to three times its size. In Figure 7.3(b) we show the initial configuration of a microroller and passive particle at rest (before we start driving its rotation) with the pathline of the passive particle in the reference frame of the rotating-translating particle when it is driven to rotate. However, this is but one of many initial configurations, Figure 7.3(c) shows the pathlines of the passive particle in the reference frame of the roller for any initial configuration. This opens up other questions concerning the parameters that control a microroller's capacity to carry particles larger than itself which we are continuing to explore.

In conclusion, the work presented in this thesis was highly motivated by the capacity to add complexity to a set of synthetic particles to create emergent structures with, in the eyes of this author, extraordinary emergent behavior. By simply adding attractive tethers to suspended particles we have enabled them to come together and form structures with excellent symmetry, all dictated by the laws of thermodynamics. But, if we wish to

free ourselves from the limitations of phenomena at thermal equilibrium set by ergodic principles, we do so by further enhancing the properties of the participating particles. By further functionalization or increase of complexity, we may go exploring into the realm that life is also a part of: non-equilibrium systems. In chemistry, there is saying: like dissolves like, referring to the fact that solutions of one type of polarity usually only dissolve compounds of similar polarity. Analogously, in physics, you can only probe phenomena of energy scales related to the energy scale of your perturbation. Thus, here, by adding more degrees of freedom to individual units, their collective structure will exhibit more complex behavior. So how far then are we from creating model systems for life comprised of entirely synthetic particles? We have already seen in this thesis that a concept usually associated to living systems has found a use in inanimate systems. The materials that are being trained are not living, not even close. But are there complex systems caught in the meso-scale of complexity between totally inanimate and animate behavior? No matter the case, the increasing use of synthetic systems to study life-like behavior can only mean it's only a matter of time before we understand what it means to be living from a physical perspective.

Bibliography

- [1] P. W. Anderson, “More is different: broken symmetry and the nature of the hierarchical structure of science.”, *Science* **177**, 393–396 (1972).
- [2] O. Artime and M. De Domenico, *From the origin of life to pandemics: emergent phenomena in complex systems*, 2022.
- [3] S. H. Kennedy, B. D. Dherange, K. J. Berger, and M. D. Levin, “Skeletal editing through direct nitrogen deletion of secondary amines”, *Nature* **593**, 223–227 (2021).
- [4] T. Shimajiri, S. Kawaguchi, T. Suzuki, and Y. Ishigaki, “Direct evidence for a carbon–carbon one-electron -bond”, *Nature*, 10.1038/s41586-024-07965-1 (2024).
- [5] T. Hueckel, G. M. Hocky, and S. Sacanna, “Total synthesis of colloidal matter”, *Nature Reviews Materials* **6**, 1053–1069 (2021).
- [6] S. Zang, A. W. Hauser, S. Paul, G. M. Hocky, and S. Sacanna, “Enabling three-dimensional real-space analysis of ionic colloidal crystallization”, *Nature Materials*, 1–7 (2024).
- [7] V. N. Manoharan, *Colloidal matter: Packing, geometry, and entropy*, 2015.
- [8] M. I. Bodnarchuk, M. V. Kovalenko, W. Heiss, and D. V. Talapin, “Energetic and entropic contributions to self-assembly of binary nanocrystal superlattices: Temperature as the structure-directing factor”, *J. Am. Chem. Soc.* **132**, 11967–11977 (2010).
- [9] C. B. Murray, C. R. Kagan, and M. G. Bawendi, “Synthesis and characterization of monodisperse nanocrystals and close-packed nanocrystal assemblies”, *Annual review of materials science* **30**, 545–610 (2000).
- [10] M. D. Eldridge, P. A. Madden, and D. Frenkel, “Entropy-driven formation of a superlattice in a hard-sphere binary mixture”, *Nature* **320**, 35–37 (1993).
- [11] D. Frenkel, *Order through entropy*, Jan. 2015.
- [12] M. A. Boles and D. V. Talapin, “Many-body effects in nanocrystal superlattices: Departure from sphere packing explains stability of binary phases”, *J. Am. Chem. Soc.* **137**, 4494–4502 (2015).
- [13] M. A. Boles, M. Engel, and D. V. Talapin, *Self-assembly of colloidal nanocrystals: From intricate structures to functional materials*, Sept. 2016.
- [14] M. E. Leunissen, C. G. Christova, A.-P. Hynninen, C. P. Royall, A. I. Campbell, A. Imhof, M. Dijkstra, R. van Roij, and A. van Blaaderen, “Ionic colloidal crystals of oppositely charged particles”, *Nature* **437**, 235–240 (2005).

- [15] T. Hueckel, G. M. Hocky, J. Palacci, and S. Sacanna, “Ionic solids from common colloids”, *Nature* **580**, 487–490 (2020).
- [16] A. P. Alivisatos, K. P. Johnsson, X. Peng, T. E. Wilson, C. J. Loweth, M. P. Bruchez Jr, and P. G. Schultz, “Organization of ‘nanocrystal molecules’ using dna”, *Nature* **382**, 609–611 (1996).
- [17] C. A. Mirkin, R. L. Letsinger, R. C. Mucic, and J. J. Storhoff, “A dna-based method for rationally assembling nanoparticles into macroscopic materials”, in *Spherical nucleic acids* (Jenny Stanford Publishing, 2020), pp. 3–11.
- [18] C. R. Laramy, M. N. O’Brien, and C. A. Mirkin, “Crystal engineering with DNA”, *Nat. Rev. Mater.*, 10.1038/s41578-019-0087-2 (2019).
- [19] T. I. Li, R. Sknepnek, R. J. MacFarlane, C. A. Mirkin, and M. Olvera de la Cruz, “Modeling the crystallization of spherical nucleic acid nanoparticle conjugates with molecular dynamics simulations”, *Nano Lett.* **12**, 2509–2514 (2012).
- [20] M. Girard, S. Wang, J. S. Du, A. Das, Z. Huang, V. P. Dravid, B. Lee, C. A. Mirkin, and M. Olvera de la Cruz, “Particle analogs of electrons in colloidal crystals”, *Science* **364**, 1174–1178 (2019).
- [21] D. J. Lewis, D. J. D. Carter, and R. J. Macfarlane, “Using dna to control the mechanical response of nanoparticle superlattices”, *Journal of the American Chemical Society* **142**, PMID: 33140957, 19181–19188 (2020).
- [22] J. Chang, K. B. Toga, J. D. Paulsen, N. Menon, and T. P. Russell, “Thickness dependence of the young’s modulus of polymer thin films”, *Macromolecules* **51**, 6764–6770 (2018).
- [23] G. Wang, F. Najafi, K. Ho, M. Hamidinejad, T. Cui, G. C. Walker, C. V. Singh, and T. Filleter, “Mechanical size effect of freestanding nanoconfined polymer films”, *Macromolecules* **55**, 1248–1259 (2022).
- [24] A. Jain, S. P. Ong, G. Hautier, W. Chen, W. D. Richards, S. Dacek, S. Cholia, D. Gunter, D. Skinner, G. Ceder, et al., “Commentary: the materials project: a materials genome approach to accelerating materials innovation”, *APL materials* **1** (2013).
- [25] A. Zunger, “Inverse design in search of materials with target functionalities”, *Nature Reviews Chemistry* **2**, 0121 (2018).
- [26] A. Hensley, T. E. Videbæk, H. Seyforth, W. M. Jacobs, and W. B. Rogers, “Macroscopic photonic single crystals via seeded growth of dna-coated colloids”, *Nature communications* **14**, 4237 (2023).
- [27] S. Kim, I. Svetlizky, D. A. Weitz, and F. Spaepen, “Work hardening in colloidal crystals”, *Nature*, 1–6 (2024).
- [28] H. M. Jaeger, A. Murugan, and S. R. Nagel, “Training physical matter to matter”, *Soft Matter* **20**, 6695–6701 (2024).
- [29] T. R. Gingrich, J. M. Horowitz, N. Perunov, and J. L. England, “Dissipation Bounds All Steady-State Current Fluctuations”, *Physical Review Letters* **116**, 10.1103/PhysRevLett.116.120601 (2016).

- [30] J. M. Horowitz and T. R. Gingrich, “Thermodynamic uncertainty relations constrain non-equilibrium fluctuations”, *Nature Physics* 2019 16:1 **16**, 15–20 (2019).
- [31] J. R. Royer and P. M. Chaikin, “Precisely cyclic sand: Self-organization of periodically sheared frictional grains”, *Proceedings of the National Academy of Sciences of the United States of America* **112**, 49–53 (2015).
- [32] M. O. Lavrentovich, A. J. Liu, and S. R. Nagel, “Period proliferation in periodic states in cyclically sheared jammed solids”, *Physical Review E* **96**, 10.1103/PhysRevE.96.020101 (2017).
- [33] K. A. Murphy, J. W. Kruppe, and H. M. Jaeger, “Memory in Nonmonotonic Stress Relaxation of a Granular System”, *Physical Review Letters* **124**, 168002 (2020).
- [34] J. J. Hopfield, “Neurons with graded response have collective computational properties like those of two-state neurons”, *Proceedings of the National Academy of Sciences of the United States of America* **81**, 3088–3092 (1984).
- [35] E. Montbrió, D. Pazó, and A. Roxin, “Macroscopic description for networks of spiking neurons”, *Physical Review X* **5**, 021028 (2015).
- [36] N. C. Keim, J. D. Paulsen, Z. Zeravcic, S. Sastry, and S. R. Nagel, “Memory formation in matter”, *Reviews of Modern Physics* **91**, 035002 (2019).
- [37] D. Fiocco, G. Foffi, and S. Sastry, “Encoding of memory in sheared amorphous solids”, *Physical Review Letters* **112**, 10.1103/PhysRevLett.112.025702 (2014).
- [38] D. Fiocco, G. Foffi, and S. Sastry, “Memory effects in schematic models of glasses subjected to oscillatory deformation”, *Journal of Physics: Condensed Matter*, 194130 (2015).
- [39] I. Tah, D. Haertter, J. M. Crawford, D. P. Kiehart, C. F. Schmidt, and A. J. Liu, *Minimal vertex model explains how the amnioserosa avoids fluidization during drosophila dorsal closure*, 2023.
- [40] S. Arzash, I. Tah, A. J. Liu, and M. L. Manning, *Rigidity of epithelial tissues as a double optimization problem*, 2024.
- [41] J. F. Brady, G. Bossis, et al., “Stokesian dynamics”, *Annual review of fluid mechanics* **20**, 111–157 (1988).
- [42] C. Floyd, A. R. Dinner, A. Murugan, and S. Vaikuntanathan, “Limits on the computational expressivity of non-equilibrium biophysical processes”, arXiv preprint arXiv:2409.05827 (2024).
- [43] Y. Xia, Y. Xiong, B. Lim, and S. E. Skrabalak, “Shape-controlled synthesis of metal nanocrystals: simple chemistry meets complex physics?”, *Angew. Chem., Int. Ed.* **48**, 60 (2009).
- [44] M. A. Boles, M. Engel, and D. V. Talapin, “Self-assembly of colloidal nanocrystals: from intricate structures to functional materials”, *Chem. Rev.* **116**, 11220 (2016).
- [45] D. V. Talapin, J.-S. Lee, M. V. Kovalenko, and E. V. Shevchenko, “Prospects of colloidal nanocrystals for electronic and optoelectronic applications”, *Chem. Rev.* **110**, 389 (2010).

- [46] J. F. Galisteo-López, M. Ibisate, R. Sapienza, L. S. Froufe-Pérez, Á. Blanco, and C. López, “Self-assembled photonic structures”, *Adv. Mater.* **23**, 30 (2011).
- [47] S. J. Tan, M. J. Campolongo, D. Luo, and W. Cheng, “Building plasmonic nanostructures with dna”, *Nat. Nanotechnol.* **6**, 268 (2011).
- [48] C. A. Mirkin, L. Letsinger, R. C. Mucic, and J. J. Storhoff, “A dna-based method for rationally assembling nanoparticles into macroscopic materials”, *Nature* **382**, 607 (1996).
- [49] R. J. Macfarlane, M. N. O’Brien, S. H. Petrosko, and C. A. Mirkin, “Nucleic acid-modified nanostructures as programmable atom equivalents: forging a new “table of elements”, *Angew. Chem., Int. Ed.* **52**, 5688 (2013).
- [50] M. R. Jones, N. C. Seeman, and C. A. Mirkin, “Nanomaterials. programmable materials and the nature of the dna bond”, *Science* **347**, 1260901 (2015).
- [51] W. B. Rogers, W. M. Shih, and V. N. Manoharan, “Using dna to program the self-assembly of colloidal nanoparticles and microparticles”, *Nat. Rev. Mater.* **1**, 16008 (2016).
- [52] N. C. Seeman and H. F. Sleiman, “Dna nanotechnology”, *Nat. Rev. Mater.* **3**, 17068 (2017).
- [53] S. Y. Park, A. K. R. Lytton-Jean, B. Lee, S. Weigand, G. C. Schatz, and C. A. Mirkin, “Dna-programmable nanoparticle crystallization”, *Nature* **451**, 553 (2008).
- [54] R. J. Macfarlane, B. Lee, M. R. Jones, N. Harris, G. C. Schatz, and C. A. Mirkin, “Nanoparticle superlattice engineering with dna”, *Science* **334**, 204 (2011).
- [55] M. R. Jones, R. J. Macfarlane, B. Lee, J. Zhang, K. L. Young, A. J. Senesi, and C. A. Mirkin, “Dna-nanoparticle superlattices formed from anisotropic building blocks”, *Nat. Mater.* **9**, 913 (2010).
- [56] W. Liu, M. Tagawa, H. L. Xin, T. Wang, H. Emamy, H. Li, K. G. Yager, F. W. Starr, A. V. Tkachenko, and O. Gang, “Diamond family of nanoparticle superlattices”, *Science* **351**, 582 (2016).
- [57] Y. Tian, Y. Zhang, T. Wang, H. L. Xin, H. Li, and O. Gang, “Lattice engineering through nanoparticle-dna frameworks”, *Nat. Mater.* **15**, 654 (2016).
- [58] C. A. Silvera Batista, R. G. Larson, and N. A. Kotov, “Nonadditivity of nanoparticle interactions”, *Science* **350**, 1242477 (2015).
- [59] L. Cademartiri and K. J. M. Bishop, “Programmable self-assembly”, *Nat. Mater.* **14**, 2 (2015).
- [60] S. Torquato and Y. Jiao, “Dense packings of the platonic and archimedean solids”, *Nature* **460**, 876 (2009).
- [61] U. Agarwal and F. A. Escobedo, “Mesophase behaviour of polyhedral particles”, *Nat. Mater.* **10**, 230 (2011).
- [62] J. de Graaf, R. van Roij, and M. Dijkstra, “Dense regular packings of irregular nonconvex particles”, *Phys. Rev. Lett.* **107**, 155501 (2011).
- [63] P. F. Damasceno, M. Engel, and S. C. Glotzer, “Predictive self-assembly of polyhedra into complex structures”, *Science* **337**, 453 (2012).

- [64] M. N. O'Brien, M. Girard, H.-X. Lin, J. A. Millan, M. Olvera de la Cruz, B. Lee, and C. A. Mirkin, "Exploring the zone of anisotropy and broken symmetries in dna-mediated nanoparticle crystallization", *Proc. Natl. Acad. Sci. U. S. A.* **113**, 10485 (2016).
- [65] E. Ducrot, M. He, G.-R. Yi, and D. J. Pine, "Colloidal alloys with preassembled clusters and spheres", *Nat. Mater.* **16**, 652 (2017).
- [66] A. Travesset, "Soft skyrmions, spontaneous valence and selection rules in nanoparticle superlattices", *ACS Nano* **11**, 5375 (2017).
- [67] C. Lofton and W. Sigmund, "Mechanisms controlling crystal habits of gold and silver colloids", *Adv. Funct. Mater.* **15**, 1197 (2005).
- [68] J. L. Elechiguerra, J. Reyes-Gasga, and M. J. Yacaman, "The role of twinning in shape evolution of anisotropic noble metal nanostructures", *J. Mater. Chem.* **16**, 3906 (2006).
- [69] K. D. Gilroy, H.-C. Peng, X. Yang, A. Ruditskiy, and Y. Xia, "Symmetry breaking during nanocrystal growth", *Chem. Commun.* **53**, 4521 (2017).
- [70] C. R. Laramy, L.-K. Fong, M. R. Jones, M. N. O'Brien, G. C. Schatz, and C. A. Mirkin, "Understanding nanoparticle-mediated nucleation pathways of anisotropic nanoparticles", *Chem. Phys. Lett.* **683**, 389 (2017).
- [71] S. E. Lohse and C. J. Murphy, "The quest for shape control: a history of gold nanorod synthesis", *Chem. Mater.* **25**, 1250 (2013).
- [72] M. L. Personick and C. A. Mirkin, "Making sense of the mayhem behind shape control in the synthesis of gold nanoparticles", *J. Am. Chem. Soc.* **135**, 18238 (2013).
- [73] M. N. O'Brien, M. R. Jones, and C. A. Mirkin, "The nature and implications of uniformity in the hierarchical organization of nanomaterials", *Proc. Natl. Acad. Sci. U. S. A.* **113**, 11717 (2016).
- [74] A. Gole and C. J. Murphy, "Seed-mediated synthesis of gold nanorods: role of the size and nature of the seed", *Chem. Mater.* **16**, 3633 (2004).
- [75] C. Burda, X. Chen, R. Narayanan, and M. A. El-Sayed, "Chemistry and properties of nanocrystals of different shapes", *Chem. Rev.* **105**, 1025 (2005).
- [76] M. Grzelczak, J. Perez-Juste, P. Mulvaney, and L. M. Liz-Marzan, "Shape control in gold nanoparticle synthesis", *Chem. Soc. Rev.* **37**, 1783 (2008).
- [77] J.-H. Lee, K. J. Gibson, G. Chen, and Y. Weizmann, "Bipyramid-templated synthesis of monodisperse anisotropic gold nanocrystals", *Nat. Commun.* **6**, 7571 (2015).
- [78] Q. Zhang, L. Han, H. Jing, D. A. Blom, Y. Lin, H. L. Xin, and H. Wang, "Facet control of gold nanorods", *ACS Nano* **10**, 2960 (2016).
- [79] M. N. O'Brien, M. R. Jones, K. A. Brown, and C. A. Mirkin, "Universal noble metal nanoparticle seeds realized through iterative reductive growth and oxidative dissolution reactions", *J. Am. Chem. Soc.* **136**, 7603 (2014).

- [80] C. R. Laramy, K. A. Brown, M. N. O'Brien, and C. A. Mirkin, "High-throughput, algorithmic determination of nanoparticle structure from electron microscopy images", *ACS Nano* **9**, 12488 (2015).
- [81] R. D. Near, S. C. Hayden, R. E. Hunter, D. Thackston, and M. A. El-Sayed, "Rapid and efficient prediction of optical extinction coefficients for gold nanospheres and gold nanorods", *J. Phys. Chem. C* **117**, 23950 (2013).
- [82] X. Ye, C. Zheng, J. Chen, Y. Gao, and C. B. Murray, "Using binary surfactant mixtures to simultaneously improve the dimensional tunability and monodispersity in the seeded growth of gold nanorods", *Nano Lett.* **13**, 765 (2013).
- [83] M. N. O'Brien, M. R. Jones, K. L. Kohlstedt, G. C. Schatz, and C. A. Mirkin, "Uniform circular disks with synthetically tailorable diameters: two-dimensional nanoparticles for plasmonics", *Nano Lett.* **15**, 1012 (2015).
- [84] S. J. Hurst, A. K. R. Lytton-Jean, and C. A. Mirkin, "Maximizing dna loading on a range of gold nanoparticle sizes", *Anal. Chem.* **78**, 8313 (2006).
- [85] M. N. O'Brien, B. Radha, K. A. Brown, M. R. Jones, and C. A. Mirkin, "Langmuir analysis of nanoparticle polyvalency in dna-mediated adsorption", *Angew. Chem., Int. Ed.* **53**, 9532 (2014).
- [86] E. Auyeung, T. I. N. G. Li, A. J. Senesi, A. L. Schmucker, B. C. Pals, M. O. de la Cruz, and C. A. Mirkin, "Dna-mediated nanoparticle crystallization into wulff polyhedra", *Nature* **505**, 73 (2014).
- [87] T. Li, A. J. Senesi, and B. Lee, "Small angle x-ray scattering for nanoparticle research", *Chem. Rev.* **116**, 11128 (2016).
- [88] E. Auyeung, R. J. Macfarlane, C. H. Choi, J. I. Cutler, and C. A. Mirkin, "Transitioning dna-engineered nanoparticle superlattices from solution to the solid state", *Adv. Mater.* **24**, 5181 (2012).
- [89] B. S. John and F. A. Escobedo, "Phase behavior of colloidal hard tetragonal parallelepipeds (cuboids): a monte carlo simulation study", *J. Phys. Chem. B* **109**, 23008 (2005).
- [90] J. Kundu and R. Rajesh, "Phase transitions in a system of hard rectangles on the square lattice", *Phys. Rev. E* **89**, 052124 (2014).
- [91] T. I. N. G. Li, R. Sknepnek, R. J. Macfarlane, C. A. Mirkin, and M. O. de la Cruz, "Modeling the crystallization of spherical nucleic acid nanoparticle conjugates with molecular dynamics simulations", *Nano Lett.* **12**, 2509 (2012).
- [92] M. Girard, J. A. Millan, and M. O. de la Cruz, "Dna-driven assembly: from polyhedral nanoparticles to proteins", *Annu. Rev. Mater. Res.* **47**, 33 (2017).
- [93] F. X. Redl, K. S. Cho, C. B. Murray, and S. O'Brien, "Three-dimensional binary superlattices of magnetic nanocrystals and semiconductor quantum dots", *Nature* **423**, 968 (2003).
- [94] J. A. Mason, C. R. Laramy, C.-T. Lai, M. N. O'Brien, Q.-Y. Lin, V. P. Dravid, G. C. Schatz, and C. A. Mirkin, "Contraction and expansion of stimuli-responsive dna bonds in flexible colloidal crystals", *J. Am. Chem. Soc.* **138**, 8722 (2016).

- [95] J. A. Anderson, C. D. Lorenz, and A. Travesset, “General purpose molecular dynamics simulations fully implemented on graphics processing units”, *J. Comput. Phys.* **227**, 5342 (2008).
- [96] J. Glaser, T. D. Nguyen, J. A. Anderson, P. Lui, F. Spiga, J. A. Millan, D. C. Morse, and S. C. Glotzer, “Strong scaling of general-purpose molecular dynamics simulations on gpus”, *Comput. Phys. Commun.* **192**, 97 (2015).
- [97] E. V. Shevchenko, D. V. Talapin, N. A. Kotov, S. O’Brien, and C. B. Murray, “Structural diversity in binary nanoparticle superlattices”, *Nature* **439**, 55–59 (2006).
- [98] A. P. Hynninen, C. G. Christova, R. van Roij, A. van Blaaderen, and M. Dijkstra, “Prediction and observation of crystal structures of oppositely charged colloids”, *Phys. Rev. Lett.* **96**, 138308 (2006).
- [99] J. S. Oh, G. R. Yi, and D. J. Pine, “Reconfigurable self-assembly and kinetic control of multi-programmed DNA-coated particles”, *ACS Nano* **14**, 4595–4600 (2020).
- [100] L. Filion, M. Hermes, R. Ni, E. C. Vermolen, A. Kuijk, C. G. Christova, J. C. Stiefelhagen, T. Vissers, A. van Blaaderen, and M. Dijkstra, “Self-assembly of a colloidal interstitial solid with tunable sublattice doping”, *Phys. Rev. Lett.* **107**, 168302 (2011).
- [101] B. van der Meer, E. Lathouwers, F. Smalenburg, and L. Filion, “Diffusion and interactions of interstitials in hard-sphere interstitial solid solutions”, *J. Chem. Phys.* **147**, 234903 (2017).
- [102] S. Hull, “Superionics: Crystal structures and conduction processes”, *Reports Prog. Phys.* **67**, 1233 (2004).
- [103] W. Schommers, “Correlations in the motion of particles in n-Agl: A molecular-dynamics study”, *Phys. Rev. Lett.* **38**, 1536–1539 (1977).
- [104] M. Tatsumisago, Y. Shinkuma, and T. Minami, “Stabilization of superionic α -Agl at room temperature in a glass matrix”, *Nature* **354**, 217–218 (1991).
- [105] Y. Lin and M. Olvera de la Cruz, “Sublattice melting in binary superionic colloidal crystals”, *Phys. Rev. E* **101**, 032603 (2020).
- [106] M. D. Donakowski, J. M. Godbe, R. Sknepnek, K. E. Knowles, M. Olvera de la Cruz, and E. A. Weiss, “A quantitative description of the binding equilibria of para-substituted aniline ligands and CdSe quantum dots”, *J. Phys. Chem. C* **114**, 22526–22534 (2010).
- [107] R. D. Harris, V. A. Amin, B. Lau, and E. A. Weiss, “Role of interligand coupling in determining the interfacial electronic structure of colloidal CDS quantum dots”, *ACS Nano* **10**, 1395–1403 (2016).
- [108] A. M. Kalsin, M. Fialkowski, M. Paszewski, S. K. Smoukov, K. J. Bishop, and B. A. Grzybowski, “Electrostatic self-assembly of binary nanoparticle crystals with a diamond-like lattice”, *Science* **312**, 420–424 (2006).

- [109] R. Klajn, K. J. Bishop, and B. A. Grzybowski, “Light-controlled self-assembly of reversible and irreversible nanoparticle suprastructures”, *Proc. Natl. Acad. Sci. U. S. A.* **104**, 10305–10309 (2007).
- [110] J. Zhang, P. J. Santos, P. A. Gabrys, S. Lee, C. Liu, and R. J. Macfarlane, “Self-assembling nanocomposite tectons”, *J. Am. Chem. Soc.* **138**, 16228–16231 (2016).
- [111] P. Santos, J., Z. Cao, J. Zhang, A. Alexander-Katz, and R. J. Macfarlane, “Dictating nanoparticle assembly via systems-level control of molecular multivalency”, *J. Am. Chem. Soc.* **141**, 14624–14632 (2019).
- [112] P. J. Santos, T. C. Cheung, and R. J. Macfarlane, “Assembling ordered crystals with disperse building blocks”, *Nano Lett.* **19**, 5774–5780 (2019).
- [113] Y. Wang, W. D. Richards, S. P. Ong, L. J. Miara, J. C. Kim, Y. Mo, and G. Ceder, “Design principles for solid-state lithium superionic conductors”, *Nat. Mater.* **14**, 1026–1031 (2015).
- [114] S. Muy, J. C. Bachman, L. Giordano, H. H. Chang, D. L. Abernathy, D. Bansal, O. Delaire, S. Hori, R. Kanno, F. Maglia, S. Lupart, P. Lamp, and Y. Shao-Horn, “Tuning mobility and stability of lithium ion conductors based on lattice dynamics”, *Energy Environ. Sci.* **11**, 850–859 (2018).
- [115] A. Travesset, “Soft skyrmions, spontaneous valence and selection rules in nanoparticle superlattices”, *ACS Nano* **11**, Publisher: American Chemical Society, 5375–5382 (2017).
- [116] C. Knorowski, S. Burleigh, and A. Travesset, “Dynamics and statics of DNA-programmable nanoparticle self-assembly and crystallization”, *Phys. Rev. Lett.* **106**, 215501 (2011).
- [117] P. L. Biancaniello, A. J. Kim, and J. C. Crocker, “Colloidal interactions and self-assembly using DNA hybridization”, *Phys. Rev. Lett.* **94**, 058302 (2005).
- [118] W. B. Rogers and J. C. Crocker, “Direct measurements of DNA-mediated colloidal interactions and their quantitative modeling”, *Proc. Natl. Acad. Sci. U. S. A.* **108**, 15687–15692 (2011).
- [119] W. Hume-Rothery, *The Structures of Alloys of Iron* (Elsevier, Amsterdam, 1966).
- [120] J. A. Anderson, C. D. Lorenz, and A. Travesset, “General purpose molecular dynamics simulations fully implemented on graphics processing units”, *J. Comput. Phys.* **227**, 5342–5359 (2008).
- [121] J. Glaser, T. D. Nguyen, J. A. Anderson, P. Lui, F. Spiga, J. A. Millan, D. C. Morse, and S. C. Glotzer, “Strong scaling of general-purpose molecular dynamics simulations on GPUs”, *Comput. Phys. Commun.* **192**, 97–107 (2015).
- [122] M. Girard, A. Ehlen, A. Shakya, T. Bereau, and M. Olvera de la Cruz, “Hoobas: A highly object-oriented builder for molecular dynamics”, *Comput. Mater. Sci.* **167**, 25–33 (2019).
- [123] N. Michaud-Agrawal, E. J. Denning, T. B. Woolf, and O. Beckstein, “MDAnalysis: A toolkit for the analysis of molecular dynamics simulations”, *J. Comput. Chem.* **32**, 2319–2327 (2011).

- [124] R. Gowers, M. Linke, J. Barnoud, T. Reddy, M. Melo, S. Seyler, J. Domański, D. Dotson, S. Buchoux, I. Kenney, and O. Beckstein, “MDAnalysis: A python package for the rapid analysis of molecular dynamics simulations”, Proc. 15th Python Sci. Conf., 98–105 (2016).
- [125] W. Humphrey, A. Dalke, and K. Schulten, “VMD: Visual molecular dynamics”, J. Mol. Graph. **14**, 33–38 (1996).
- [126] J. E. Stone, “An efficient library for parallel ray tracing and animation”, PhD thesis (Computer Science Department, University of Missouri-Rolla, 1998).
- [127] P. Ramachandran and G. Varoquaux, “Mayavi: 3D visualization of scientific data”, Comput. Sci. Eng. **13**, 40–51 (2011).
- [128] N. B. Schade, M. C. Holmes-Cerfon, E. R. Chen, D. Aronzon, J. W. Collins, J. A. Fan, F. Capasso, and V. N. Manoharan, “Tetrahedral colloidal clusters from random parking of bidisperse spheres”, Phys. Rev. Lett. **110**, 148303 (2013).
- [129] J. Sprakel, A. Zaccone, F. Spaepen, P. Schall, and D. A. Weitz, “Direct observation of entropic stabilization of BCC crystals near melting”, Phys. Rev. Lett. **118**, 088003 (2017).
- [130] R. Higler and J. Sprakel, “Doping colloidal BCC crystals-interstitial solids and meta-stable clusters”, Sci. Rep. **7**, 1–13 (2017).
- [131] M. Salamon, “Physics of Superionic Conductors”, in , Vol. 15, edited by M. Salamon (Springer-Verlag Berlin Heidelberg, Berlin, 1979), pp. 175–200.
- [132] J. B. Goodenough and K.-S. Park, “The Li-ion rechargeable battery: A perspective”, J. Am. Chem. Soc **29**, 1167–1176 (2013).
- [133] J. C. Bachman, S. Muy, A. Grimaud, H. H. Chang, N. Pour, S. F. Lux, O. Paschos, F. Maglia, S. Lupart, P. Lamp, L. Giordano, and Y. Shao-Horn, “Inorganic solid-state electrolytes for lithium batteries: Mechanisms and properties governing ion conduction”, Chem. Rev. **116**, 140–162 (2016).
- [134] T. Famprikis, P. Canepa, J. A. Dawson, M. S. Islam, and C. Masquelier, “Fundamentals of inorganic solid-state electrolytes for batteries”, Nat. Mater. **18**, 1278–1291 (2019).
- [135] H. Lopez-Rios, A. Ehlen, and M. Olvera de la Cruz, “Delocalization Transition in Colloidal Crystals”, The Journal of Physical Chemistry C **125**, 1096–1106 (2021).
- [136] G.-R. Yi, D. J. Pine, and S. Sacanna, “Recent progress on patchy colloids and their self-assembly”, Journal of Physics: Condensed Matter **25**, 193101 (2013).
- [137] I. Cherniukh, G. Rainò, T. Stöferle, M. Burian, A. Travasset, D. Naumenko, H. Amenitsch, R. Erni, R. F. Mahrt, M. I. Bodnarchuk, and M. V. Kovalenko, “Perovskite-type superlattices from lead halide perovskite nanocubes”, Nature **593**, 535–542 (2021).
- [138] A. D. Dinsmore, J. C. Crocker, and A. G. Yodh, “Self-assembly of colloidal crystals”, Current Opinion in Colloid and Interface Science **3**, 5–11 (1998).

- [139] L. Filion and M. Dijkstra, “Prediction of binary hard-sphere crystal structures”, *Phys. Rev. E - Stat. Nonlinear, Soft Matter Phys.* **79**, 10.1103/PhysRevE.79.046714 (2009).
- [140] A. Travesset, “Nanoparticle Superlattices as Quasi-Frank-Kasper Phases”, *Physical Review Letters* **119**, 115701 (2017).
- [141] H. F. Cheng, S. Wang, and C. A. Mirkin, “Electron-Equivalent Valency through Molecularly Well-Defined Multivalent DNA”, *Journal of the American Chemical Society* **143**, 33 (2021).
- [142] J. Tauber, R. Higler, and J. Sprakel, “Anomalous dynamics of interstitial dopants in soft crystals”, *Proc. Natl. Acad. Sci. U. S. A.* **113**, 13660–13665 (2016).
- [143] M. Girard, “Models and studies of self-assembled systems using high information polymer coated particles”, PhD thesis (Northwestern University, 2018) (available at <http://aztec.tech.northwestern.edu/Images/People%20slides/MartinPhDthesis.pdf>), <http://aztec.tech.northwestern.edu/Images/People%2>.
- [144] W. Schommers, “Structure and dynamics of superionic conductors”, *Phys. Rev. B* **21**, 847–851 (1980).
- [145] T. M. Brenner, C. Gehrman, R. Korobko, T. Livneh, D. A. Egger, and O. Yaffe, “Anharmonic host-lattice dynamics enable fast ion conduction in superionic AgI”, *Physical Review Materials* **4**, 115402 (2020).
- [146] A. F. Demirörs, P. P. Pillai, B. Kowalczyk, and B. A. Grzybowski, “Colloidal assembly directed by virtual magnetic moulds”, *Nature* **503**, 99–103 (2013).
- [147] S. Sacanna, W. T. Irvine, P. M. Chaikin, and D. J. Pine, “Lock and key colloids”, *Nature* **464**, 575–578 (2010).
- [148] Y. K. Lee, X. Li, P. Perdikaris, J. C. Crocker, C. Reina, and T. Sinno, “Hydrodynamic and frictional modulation of deformations in switchable colloidal crystallites”, *Proceedings of the National Academy of Sciences of the United States of America* **117**, 12700–12706 (2020).
- [149] F. Lu, K. G. Yager, Y. Zhang, H. Xin, and O. Gang, “Superlattices assembled through shape-induced directional binding”, *Nature Communications* 2015 6:1 **6**, 1–10 (2015).
- [150] J. D. Budai, J. Hong, M. E. Manley, E. D. Specht, C. W. Li, J. Z. Tischler, D. L. Abernathy, A. H. Said, B. M. Leu, L. A. Boatner, R. J. McQueeney, and O. Delaire, “Metallization of vanadium dioxide driven by large phonon entropy”, *Nature* **515**, 535–539 (2014).
- [151] U. Pinsook, “Molecular dynamics study of vibrational entropy in bcc and hcp zirconium”, *Physical Review B - Condensed Matter and Materials Physics* **66**, 024109–1–6 (2002).
- [152] L. Landau, E. Lifshitz, and M. Pitaevskii, *Statistical Physics. Part 1*, 3rd ed. (Pergamon Press, Oxford, Sept. 1980), pp. 446–516.
- [153] J. M. Dickey and A. Paskin, “Computer simulation of the lattice dynamics of solids”, *Physical Review* **188**, 1407–1418 (1969).

- [154] A. Verdaguer, J. A. Padró, and J. Trullàs, “Molecular dynamics study of the velocity cross-correlations in liquids”, *Journal of Chemical Physics* **109**, 228–234 (1998).
- [155] A. Verdaguer and J. A. Padró, “Computer simulation study of the velocity cross correlations between neighboring atoms in simple liquid binary mixtures”, *Journal of Chemical Physics* **114**, 2738–2744 (2001).
- [156] T. Ishida, “Molecular dynamics study of the dynamical behavior in ionic liquids through interionic interactions”, in *Journal of non-crystalline solids*, Vol. 357, 2 (Jan. 2011), pp. 454–462.
- [157] S. Alexander and J. McTague, “Should all crystals be BCC? Landau theory of solidification and crystal nucleation”, *Phys. Rev. Lett.* **41**, 702–705 (1978).
- [158] Z. Cai, Z. Li, S. Ravaine, M. He, Y. Song, Y. Yin, H. Zheng, J. Teng, and A. Zhang, “From colloidal particles to photonic crystals: advances in self-assembly and their emerging applications”, *Chemical Society Reviews* **50**, 5898–5951 (2021).
- [159] M. He, J. P. Gales, É. Ducrot, Z. Gong, G. R. Yi, S. Sacanna, and D. J. Pine, “Colloidal diamond”, *Nature* **585**, 524–529 (2020).
- [160] E. Auyeung, T. I. N. G. Li, A. J. Senesi, A. L. Schmucker, B. C. Pals, M. Olvera de la Cruz, and C. A. Mirkin, “DNA-mediated nanoparticle crystallization into Wulff polyhedra”, *Nature* **505**, 73–77 (2014).
- [161] J. A. Anderson, J. Glaser, and S. C. Glotzer, “HOOMD-blue: A Python package for high-performance molecular dynamics and hard particle Monte Carlo simulations”, *Computational Materials Science* **173**, 109363 (2020).
- [162] S. P. Ong, W. D. Richards, A. Jain, G. Hautier, M. Kocher, S. Cholia, D. Gunter, V. L. Chevrier, K. A. Persson, and G. Ceder, “Python Materials Genomics (pymatgen): A robust, open-source python library for materials analysis”, *Computational Materials Science* **68**, 314–319 (2013).
- [163] M. J. Mehl, D. Hicks, C. Toher, O. Levy, R. M. Hanson, G. Hart, and S. Curtarolo, “The AFLOW Library of Crystallographic Prototypes: Part 1”, *Computational Materials Science* **136**, S1–S828 (2017).
- [164] D. Hicks, M. J. Mehl, E. Gossett, C. Toher, O. Levy, R. M. Hanson, G. Hart, and S. Curtarolo, “The AFLOW Library of Crystallographic Prototypes: Part 2”, *Computational Materials Science* **161**, S1–S1011 (2019).
- [165] C. Li, G. C. Lau, H. Yuan, A. Aggarwal, V. L. Dominguez, S. Liu, H. Sai, L. C. Palmer, N. A. Sather, T. J. Pearson, D. E. Freedman, P. K. Amiri, M. O. de la Cruz, and S. I. Stupp, “Fast and programmable locomotion of hydrogel-metal hybrids under light and magnetic fields”, *Science Robotics* **5**, eabb9822 (2020).
- [166] Y. Zhou, X. Zhao, J. Xu, Y. Fang, G. Chen, Y. Song, S. Li, and J. Chen, “Giant magnetoelastic effect in soft systems for bioelectronics”, *Nature Materials* **20**, 1670–1676 (2021).
- [167] X. Wang, B. Sprinkle, H. K. Bisoyi, T. Yang, L. Chen, S. Huang, and Q. Li, “Colloidal tubular microrobots for cargo transport and compression”, *Proceedings of the National Academy of Sciences* **120**, e2304685120 (2023).

- [168] G. Hwang, A. J. Paula, E. E. Hunter, Y. Liu, A. Babeer, B. Karabucak, K. Stebe, V. Kumar, E. Steager, and H. Koo, “Catalytic antimicrobial robots for biofilm eradication”, *Science robotics* **4**, eaaw2388 (2019).
- [169] S. Ponomareva, M. Carriere, Y. Hou, R. Morel, B. Dieny, and H. Joisten, “Microstructured magnetoelastic membrane for magnetic bioactuators and soft artificial muscles applications”, *Advanced Intelligent Systems* **5**, 2300022 (2023).
- [170] Z. Qi, M. Zhou, Y. Li, Z. Xia, W. Huo, and X. Huang, “Reconfigurable flexible electronics driven by origami magnetic membranes”, *Advanced Materials Technologies* **6**, 2001124 (2021).
- [171] L. Lu, J. Sim, and R. R. Zhao, “Mechanics of hard-magnetic soft materials: A review”, *Mechanics of Materials* **189**, 104874 (2024).
- [172] L. Dorfmann and R. W. Ogden, “Hard-magnetic soft magnetoelastic materials: Energy considerations”, *International Journal of Solids and Structures* **294**, 112789 (2024).
- [173] Y. Kim and X. Zhao, “Magnetic Soft Materials and Robots”, *Chem. Rev.* **122**, 5317–5364 (2022).
- [174] R. Zhao, Y. Kim, S. A. Chester, P. Sharma, and X. Zhao, “Mechanics of hard-magnetic soft materials”, *Journal of the Mechanics and Physics of Solids* **124**, 244–263 (2019).
- [175] R. M. Erb, J. J. Martin, R. Soheilian, C. Pan, and J. R. Barber, “Actuating Soft Matter with Magnetic Torque”, *Adv Funct Materials* **26**, 3859–3880 (2016).
- [176] D. J. Steigmann, “Equilibrium theory for magnetic elastomers and magnetoelastic membranes”, *International Journal of Non-Linear Mechanics* **39**, 1193–1216 (2004).
- [177] C. P. Bean and J. D. Livingston, “Superparamagnetism”, *Journal of Applied Physics* **30**, S120–S129 (1959).
- [178] G. Maugin and C. Goudjo, “The equations of soft-ferromagnetic elastic plates”, *International Journal of Solids and Structures* **18**, 889–912 (1982).
- [179] Y.-H. Zhou and X. Zheng, “A general expression of magnetic force for soft ferromagnetic plates in complex magnetic fields”, *International Journal of Engineering Science* **35**, 1405–1417 (1997).
- [180] C. Li, G. C. Lau, H. Yuan, A. Aggarwal, V. L. Dominguez, S. Liu, H. Sai, L. C. Palmer, N. A. Sather, T. J. Pearson, et al., “Fast and programmable locomotion of hydrogel-metal hybrids under light and magnetic fields”, *Science robotics* **5**, eabb9822 (2020).
- [181] F. Gerbal, Y. Wang, F. Lyonnet, J.-C. Bacri, T. Hocquet, and M. Devaud, “A refined theory of magnetoelastic buckling matches experiments with ferromagnetic and superparamagnetic rods”, *Proc. Natl. Acad. Sci. U.S.A.* **112**, 7135–7140 (2015).
- [182] V. P. Shcherbakov and M. Winklhofer, “Bending of magnetic filaments under a magnetic field”, *Phys. Rev. E* **70**, 061803 (2004).

- [183] Y. Wang, P. Kanjanaboos, S. P. McBride, E. Barry, X.-M. Lin, and H. M. Jaeger, “Mechanical properties of self-assembled nanoparticle membranes: stretching and bending”, *Faraday Discuss.* **181**, 325–338 (2015).
- [184] P. Vázquez-Montejo and M. O. De La Cruz, “Flexible paramagnetic membranes in fast precessing fields”, *Phys. Rev. E* **98**, 032603 (2018).
- [185] C. A. Brisbois, M. Tasinkevych, P. Vázquez-Montejo, and M. Olvera De La Cruz, “Actuation of magnetoelastic membranes in precessing magnetic fields”, *Proc. Natl. Acad. Sci. U.S.A.* **116**, 2500–2505 (2019).
- [186] C. A. Brisbois and M. O. De La Cruz, “Locomotion of magnetoelastic membranes in viscous fluids”, *Phys. Rev. Research* **4**, 023166 (2022).
- [187] E. E. Keaveny and M. R. Maxey, “Modeling the magnetic interactions between paramagnetic beads in magnetorheological fluids”, *Journal of Computational Physics* **227**, 9554–9571 (2008).
- [188] J. Faraudo, J. S. Andreu, C. Calero, and J. Camacho, “Predicting the Self-Assembly of Superparamagnetic Colloids under Magnetic Fields”, *Adv Funct Materials* **26**, 3837–3858 (2016).
- [189] A. Spatafora-Salazar, D. M. Lobmeyer, L. H. P. Cunha, K. Joshi, and S. L. Biswal, “Hierarchical assemblies of superparamagnetic colloids in time-varying magnetic fields”, *Soft Matter* **17**, 1120–1155 (2021).
- [190] H. E. Meijer and L. E. Govaert, “Mechanical performance of polymer systems: the relation between structure and properties”, *Progress in Polymer Science* **30**, Plenary Lectures, 915–938 (2005).
- [191] L. D. Landau and E. M. Lifshitz, *Theory of elasticity: course of theoretical physics, volume 7*, Vol. 7 (Elsevier, 2012).
- [192] H. Mamiya, H. Fukumoto, J. L. Cuya Huaman, K. Suzuki, H. Miyamura, and J. Balachandran, “Estimation of magnetic anisotropy of individual magnetite nanoparticles for magnetic hyperthermia”, *ACS nano* **14**, 8421–8432 (2020).
- [193] Y. Wang, H. Chan, B. Narayanan, S. P. McBride, S. K. R. S. Sankaranarayanan, X.-M. Lin, and H. M. Jaeger, “Thermomechanical Response of Self-Assembled Nanoparticle Membranes”, *ACS Nano* **11**, 8026–8033 (2017).
- [194] A. Cēbers and I. Javaitis, “Bending of flexible magnetic rods”, *Phys. Rev. E* **70**, 021404 (2004).
- [195] A. Cēbers and I. Javaitis, “Dynamics of a flexible magnetic chain in a rotating magnetic field”, *Phys. Rev. E* **69**, 021404 (2004).
- [196] W. F. Brown, *Magnetoelastic interactions*, Vol. 9 (Springer, 1966).
- [197] N. Mitchell and N. Mitchell, “Conforming nanoparticle sheets to surfaces with gaussian curvature”, *Geometric Control of Fracture and Topological Metamaterials*, 31–51 (2020).
- [198] S. Sun, H. Zeng, D. B. Robinson, S. Raoux, P. M. Rice, S. X. Wang, and G. Li, “Monodisperse MFe_2O_4 ($M = Fe, Co, Mn$) Nanoparticles”, *J. Am. Chem. Soc.* **126**, 273–279 (2004).

- [199] Y. A. Koksharov, “Magnetism of nanoparticles: effects of size, shape, and interactions”, *Magnetic nanoparticles*, 197–254 (2009).
- [200] F. Weik, R. Weeber, K. Szuttor, K. Breitsprecher, J. De Graaf, M. Kuron, J. Landsgesell, H. Menke, D. Sean, and C. Holm, “ESPReso 4.0 – an extensible software package for simulating soft matter systems”, *Eur. Phys. J. Spec. Top.* **227**, 1789–1816 (2019).
- [201] H. S. Seung and D. R. Nelson, “Defects in flexible membranes with crystalline order”, *Phys. Rev. A* **38**, 1005–1018 (1988).
- [202] D. Du, F. Toffoletto, and S. L. Biswal, “Numerical calculation of interaction forces between paramagnetic colloids in two-dimensional systems”, *Phys. Rev. E* **89**, 043306 (2014).
- [203] Z. M. Sherman, D. Ghosh, and J. W. Swan, “Field-Directed Self-Assembly of Mutually Polarizable Nanoparticles”, *Langmuir* **34**, 7117–7134 (2018).
- [204] S.-Y. Chen, H. M. Lopez Rios, M. Olvera de la Cruz, and M. Driscoll, “Restructuring a passive colloidal suspension using a rotationally driven particle”, *Soft Matter* **20**, 2151–2161 (2024).
- [205] F. Li, D. P. Josephson, and A. Stein, “Colloidal Assembly: The Road from Particles to Colloidal Molecules and Crystals”, en, *Angewandte Chemie International Edition* **50**, 360–388 (2011).
- [206] J. Zhang, E. Luijten, and S. Granick, “Toward Design Rules of Directional Janus Colloidal Assembly”, *Annual Review of Physical Chemistry* **66**, 581–600 (2015).
- [207] V. N. Manoharan, “Colloidal matter: Packing, geometry, and entropy”, *Science* **349**, 1253751 (2015).
- [208] M. Driscoll, B. Delmotte, M. Youssef, S. Sacanna, A. Donev, and P. Chaikin, “Unstable fronts and motile structures formed by microrollers”, en, *Nature Phys* **13**, 375–379 (2017).
- [209] S. Sabrina, M. Tasinkevych, S. Ahmed, A. M. Brooks, M. Olvera de la Cruz, T. E. Mallouk, and K. J. M. Bishop, “Shape-Directed Microspinnners Powered by Ultrasound”, *ACS Nano* **12**, 2939–2947 (2018).
- [210] Z. Zhang, H. Yuan, Y. Dou, M. O. de la Cruz, and K. J. M. Bishop, “Quincke Oscillations of Colloids at Planar Electrodes”, *Phys. Rev. Lett.* **126**, 258001 (2021).
- [211] C. Chen, M. van der Naald, A. Singh, N. D. Dolinski, G. L. Jackson, H. M. Jaeger, S. J. Rowan, and J. J. de Pablo, “Leveraging the Polymer Glass Transition to Access Thermally Switchable Shear Jamming Suspensions”, *ACS Cent. Sci.* **9**, 639–647 (2023).
- [212] C. Shao, J. Chi, Z. Chen, L. Cai, and Y. Zhao, “Superwetable colloidal crystal micropatterns on butterfly wing surface for ultrasensitive detection”, *Journal of Colloid and Interface Science* **546**, 122–129 (2019).
- [213] M. Driscoll and B. Delmotte, “Leveraging collective effects in externally driven colloidal suspensions: experiments and simulations”, *Current Opinion in Colloid & Interface Science, Particle Systems* **40**, 42–57 (2019).

- [214] D. M. Kaz, R. McGorty, M. Mani, M. P. Brenner, and V. N. Manoharan, “Physical ageing of the contact line on colloidal particles at liquid interfaces”, en, *Nature Materials* **11**, 138–142 (2012).
- [215] B. Zhang, H. Yuan, A. Sokolov, M. O. de la Cruz, and A. Snezhko, “Polar state reversal in active fluids”, en, *Nat. Phys.* **18**, 154–159 (2022).
- [216] H. Massana-Cid, J. Codina, I. Pagonabarraga, and P. Tierno, “Active apolar doping determines routes to colloidal clusters and gels”, *Proceedings of the National Academy of Sciences* **115**, 10618–10623 (2018).
- [217] A. K. Omar, Y. Wu, Z.-G. Wang, and J. F. Brady, “Swimming to Stability: Structural and Dynamical Control via Active Doping”, *ACS Nano* **13**, 560–572 (2019).
- [218] X. Cheng, X. Xu, S. A. Rice, A. R. Dinner, and I. Cohen, “Assembly of vorticity-aligned hard-sphere colloidal strings in a simple shear flow”, en, *Proceedings of the National Academy of Sciences* **109**, 63–67 (2011).
- [219] S. A. Mallory, C. Valeriani, and A. Cacciuto, “An Active Approach to Colloidal Self-Assembly”, *Annual Review of Physical Chemistry* **69**, [_eprint: https://doi.org/10.1146/annurev-physchem-050317-021237](https://doi.org/10.1146/annurev-physchem-050317-021237), 59–79 (2018).
- [220] I. P. Madden, L. Wang, J. Simmchen, and E. Luijten, “Hydrodynamically Controlled Self-Organization in Mixtures of Active and Passive Colloids”, en, *Small* **18**, 2107023 (2022).
- [221] G. Miño, T. E. Mallouk, T. Darnige, M. Hoyos, J. Dauchet, J. Dunstan, R. Soto, Y. Wang, A. Rousselet, and E. Clement, “Enhanced Diffusion due to Active Swimmers at a Solid Surface”, *Phys. Rev. Lett.* **106**, 048102 (2011).
- [222] A. Jepsen, V. A. Martinez, J. Schwarz-Linek, A. Morozov, and W. C. K. Poon, “Enhanced diffusion of nonswimmers in a three-dimensional bath of motile bacteria”, *Phys. Rev. E* **88**, 041002 (2013).
- [223] J. Palacci, S. Sacanna, A. P. Steinberg, D. J. Pine, and P. M. Chaikin, “Living Crystals of Light-Activated Colloidal Surfers”, *Science* **339**, 936–940 (2013).
- [224] J. Katuri, W. E. Usual, M. N. Popescu, and S. Sánchez, “Inferring non-equilibrium interactions from tracer response near confined active Janus particles”, *Science Advances* **7**, eabd0719 (2021).
- [225] S. R. McCandlish, A. Baskaran, and M. F. Hagan, “Spontaneous segregation of self-propelled particles with different motilities”, en, *Soft Matter* **8**, 2527–2534 (2012).
- [226] M. E. Cates and J. Tailleur, “Motility-Induced Phase Separation”, *Annual Review of Condensed Matter Physics* **6**, 219–244 (2015).
- [227] J. Stenhammar, R. Wittkowski, D. Marenduzzo, and M. E. Cates, “Activity-Induced Phase Separation and Self-Assembly in Mixtures of Active and Passive Particles”, *Phys. Rev. Lett.* **114**, 018301 (2015).
- [228] A. Wysocki, R. G. Winkler, and G. Gompper, “Propagating interfaces in mixtures of active and passive Brownian particles”, en, *New J. Phys.* **18**, 123030 (2016).
- [229] J. Smrek and K. Kremer, “Small Activity Differences Drive Phase Separation in Active-Passive Polymer Mixtures”, *Phys. Rev. Lett.* **118**, 098002 (2017).

- [230] P. Dolai, A. Simha, and S. Mishra, “Phase separation in binary mixtures of active and passive particles”, en, *Soft Matter* **14**, 6137–6145 (2018).
- [231] K. Singh, A. Yadav, P. Dwivedi, and R. Mangal, “Interaction of Active Janus Colloids with Tracers”, *Langmuir* **38**, 2686–2698 (2022).
- [232] S. Ramananarivo, E. Ducrot, and J. Palacci, “Activity-controlled annealing of colloidal monolayers”, en, *Nat Commun* **10**, 3380 (2019).
- [233] P. Illien, R. Golestanian, and A. Sen, “‘Fuelled’ motion: phoretic motility and collective behaviour of active colloids”, en, *Chem. Soc. Rev.* **46**, 5508–5518 (2017).
- [234] T. Petit, L. Zhang, K. E. Peyer, B. E. Kratochvil, and B. J. Nelson, “Selective Trapping and Manipulation of Microscale Objects Using Mobile Microvortices”, *Nano Lett.* **12**, 156–160 (2012).
- [235] L. Zhang, T. Petit, K. E. Peyer, and B. J. Nelson, “Targeted cargo delivery using a rotating nickel nanowire”, *Nanomedicine: Nanotechnology, Biology and Medicine* **8**, 1074–1080 (2012).
- [236] M. C. Marchetti, J. F. Joanny, S. Ramaswamy, T. B. Liverpool, J. Prost, M. Rao, and R. A. Simha, “Hydrodynamics of soft active matter”, *Rev. Mod. Phys.* **85**, 1143–1189 (2013).
- [237] D. Boniface, S. G. Leyva, I. Pagonabarraga, and P. Tierno, *Hydrodynamics is Needed to Explain Propulsion in Chemophoretic Colloidal Rafts*, arXiv:2309.11084 [cond-mat], Sept. 2023.
- [238] B. Delmotte, M. Driscoll, P. Chaikin, and A. Donev, “Hydrodynamic shocks in microroller suspensions”, *Phys. Rev. Fluids* **2**, 092301 (2017).
- [239] B. Delmotte, “Hydrodynamically bound states of a pair of microrollers: a dynamical system insight”, *Phys. Rev. Fluids* **4**, 044302 (2019).
- [240] R. N. Zia, “Active and Passive Microrheology: Theory and Simulation”, *Annual Review of Fluid Mechanics* **50**, 371–405 (2018).
- [241] B. Sprinkle, E. B. v. d. Wee, Y. Luo, M. M. Driscoll, and A. Donev, “Driven dynamics in dense suspensions of microrollers”, en, *Soft Matter* **16**, 7982–8001 (2020).
- [242] E. B. van der Wee, B. C. Blackwell, F. Balboa Usabiaga, A. Sokolov, I. T. Katz, B. Delmotte, and M. M. Driscoll, “A simple catch: Fluctuations enable hydrodynamic trapping of microrollers by obstacles”, *Science Advances* **9**, eade0320 (2023).
- [243] J. R. Blake, “A note on the image system for a stokeslet in a no-slip boundary”, *Mathematical Proceedings of the Cambridge Philosophical Society* **70**, 303–310 (1971).
- [244] J. W. Swan and J. F. Brady, “Simulation of hydrodynamically interacting particles near a no-slip boundary”, *Physics of Fluids* **19**, 113306 (2007).
- [245] D. J. Lewis, D. J. D. Carter, and R. J. Macfarlane, “Using DNA to control the mechanical response of nanoparticle superlattices”, *J. Am. Chem. Soc.*, jacs.0c08790 (2020).

- [246] E. Y. Ong, A. R. Barth, N. Singh, M. Ramaswamy, A. Shetty, B. Chakraborty, J. P. Sethna, and I. Cohen, “Jamming memory into acoustically trained dense suspensions under shear”, *Physical Review X* **14**, 021027 (2024).
- [247] L. Zhang, T. Petit, Y. Lu, B. E. Kratochvil, K. E. Peyer, R. Pei, J. Lou, and B. J. Nelson, “Controlled propulsion and cargo transport of rotating nickel nanowires near a patterned solid surface”, *ACS nano* **4**, 6228–6234 (2010).
- [248] T. Petit, L. Zhang, K. E. Peyer, B. E. Kratochvil, and B. J. Nelson, “Selective trapping and manipulation of microscale objects using mobile microvortices”, *Nano letters* **12**, 156–160 (2012).
- [249] W. Cai and W. D. Nix, “Imperfections in Crystalline Solids”, in *Imperfections in crystalline solids* (Cambridge University Press, Cambridge, Sept. 2016), pp. 271–318.
- [250] F. H. Stillinger, “A topographic view of supercooled liquids and glass formation”, *Science* **267**, 1935–1939 (1995).
- [251] P. G. Debenedetti and F. H. Stillinger, “Supercooled liquids and the glass transition”, *Nature* **410**, 259 (2001).
- [252] V. Ramasubramani, B. D. Dice, E. S. Harper, M. P. Spellings, J. A. Anderson, and S. C. Glotzer, “freud: A software suite for high throughput analysis of particle simulation data”, *Computer Physics Communications* **254**, 107275 (2020).
- [253] P. M. Larsen, S. Schmidt, and J. Schiøtz, “Robust structural identification via polyhedral template matching”, *Modelling and Simulation in Materials Science and Engineering* **24**, 055007 (2016).
- [254] A. Stukowski, “Visualization and analysis of atomistic simulation data with OVITO—the Open Visualization Tool”, *Modelling and Simulation in Materials Science and Engineering* **18**, 015012 (2010).

APPENDIX A

Supplementary information for Chapter 3

This appendix contains the supplementary information associated with Chapter 3.

The following was originally published in the Journal of Physical Chemistry C in 2021.
It is reproduced here with permission of AUTHORS, and the PUBLISHER.

Delocalization Transition in Colloidal Crystals: Supplementary Information

Hector Lopez-Rios,* Ali Ehlen,* Monica Olvera de la Cruz

* equally contributing first authors

Reprinted with permission from:

Journal of Physical Chemistry C 2021, **125**, 1, 1096-1106, DOI:

10.1021/acs.jpcc.0c09730. Copyright 2021 American Chemical Society.

<http://pubs.acs.org/articlesonrequest/AOR-8UNXPU6QS5KATYESGAJA>

A.0.1. BCC Crystal Stability

# chains	T_{\min}	T_{deloc}	T_{\max}	T_{melt}
4	0.7	0.7	1.25	1.28
6	0.7	1.2	1.6	1.65
8	0.75	1.5	1.81	1.82
10	0.61	1.75	1.85	1.9

Table A.1. The (reduced) temperatures of the onset of delocalization (T_{deloc}) and the melting temperature of the crystal (T_{melt}). T_{deloc} is a qualitative measure and roughly corresponds to when the diffusion constant of the small particles is significantly greater than zero. T_{\min} and T_{\max} are the lowest and highest simulation temperatures that produced BCC lattices. T_{melt} is the lowest temperature at which the system is melted.

The thermodynamic stability of the BCC lattice is supported by several trial simulations in which we initialized the 6:1 system with the large particles in different lattice configurations (BCC, FCC, SC, BCT). In those simulations, almost all systems within this temperature range converged to a BCC lattice in equilibrium; this is possible because the simulation box was able to change size and shape during our NPT simulations (see Section *Parameters and simulation scheme*). The range of temperatures used in our simulations for each number of chains per small particle is listed in Table A.1 in columns T_{\min} and T_{\max} . Above the temperature range we report, the simulations show a melted lattice, starting at T_{melt} . Below that temperature range, we see the large particles form other lattices, most of which are SC; this regime requires further study. The values of T_{\max} also demonstrate that crystals are stronger when the small particles have more grafted chains: more chains on the small particles leads to higher melting temperatures. Additionally, in Figure A.1 we show the pair distribution functions, $g(r)$, for all simulations. We observe an ordinary coarsening of BCC peaks as the temperature is increased, without any hallmark for the onset of delocalization.

A.0.2. Determining T_{deloc}

We estimated T_{deloc} for each system as the temperature at which its diffusion increases over a threshold (0.1). Qualitatively, this represents when noticeable diffusion begins. The diffusion coefficient, D , of interstitials can be related to the free energy barrier between interstitial sites as follows [249]:

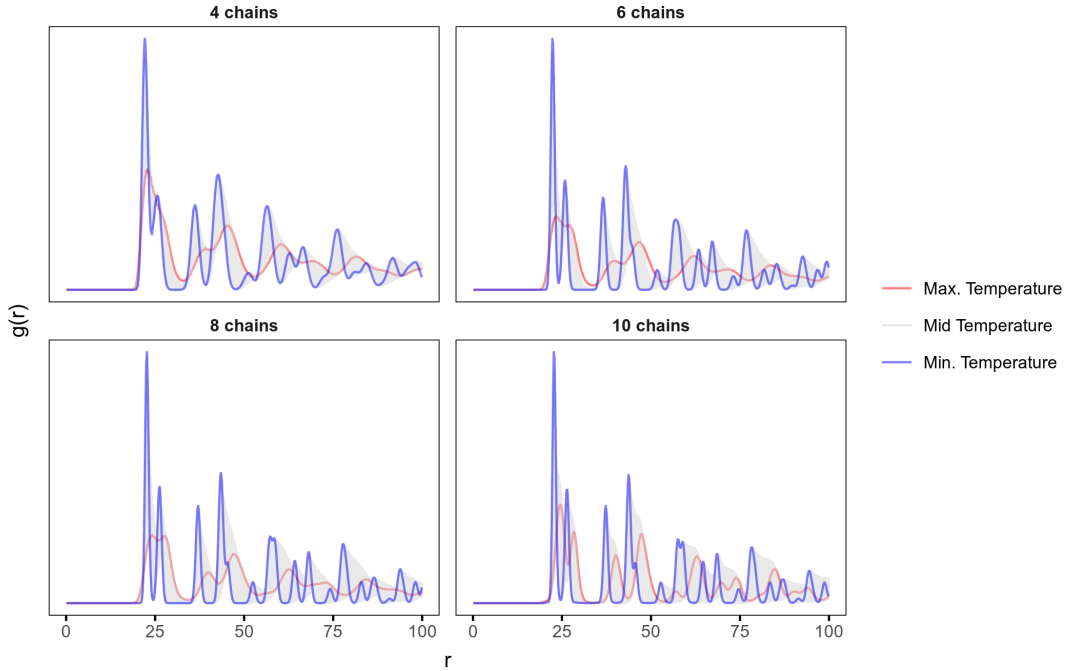


Figure A.1. The pair distribution functions, $g(r)$, for all interaction strengths over their respective temperature range, from T_{\min} to T_{\max} . The pair distribution curves at different temperatures have been color coded. Blue corresponds to T_{\min} , red corresponds to T_{\max} , and all other intermediate temperatures are grey. The coarsening of the BCC peaks is observable over increasing temperature, which is expected.

$$(A.1) \quad D \propto e^{-\Delta G/k_B T}$$

Using this relation, we can fit an exponential curve to the diffusion coefficients in Figure 4B and find the Gibbs activation free energy, ΔG . The resulting fitting parameters, ΔG , are shown in Figure A.2. We can see that the free energy barrier to diffusion increases linearly with the number of chains on the small particles, with a slope of roughly 6.4 kJ/mol-linker. This energy is approximately the enthalpy associated with one interactive

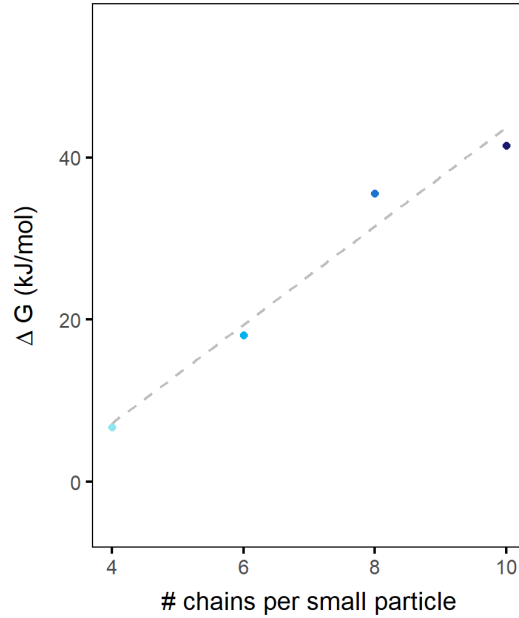


Figure A.2. The fitting parameter ΔG in Equation (A.1). This increases linearly with the number of chains per small particle.

bead localizing in its most energetically favorable volume (darkest red regions in the 004 plane in Figure 2B). This might mean that the contribution of each additional chain is generally enthalpic.

The smooth transition of the diffusing small particles is reminiscent of that of the glass transition curves of enthalpy and volume [250, 251] around the material's glass transition temperature, T_g . Because of the smoothness of the transition, T_g has many definitions. One is the temperature at which the viscosity of the material surpasses a particular value (10^{12} Pa · s). In a similar manner, we defined T_{deloc} as the temperature at which the diffusion coefficient passes a small but specific threshold.

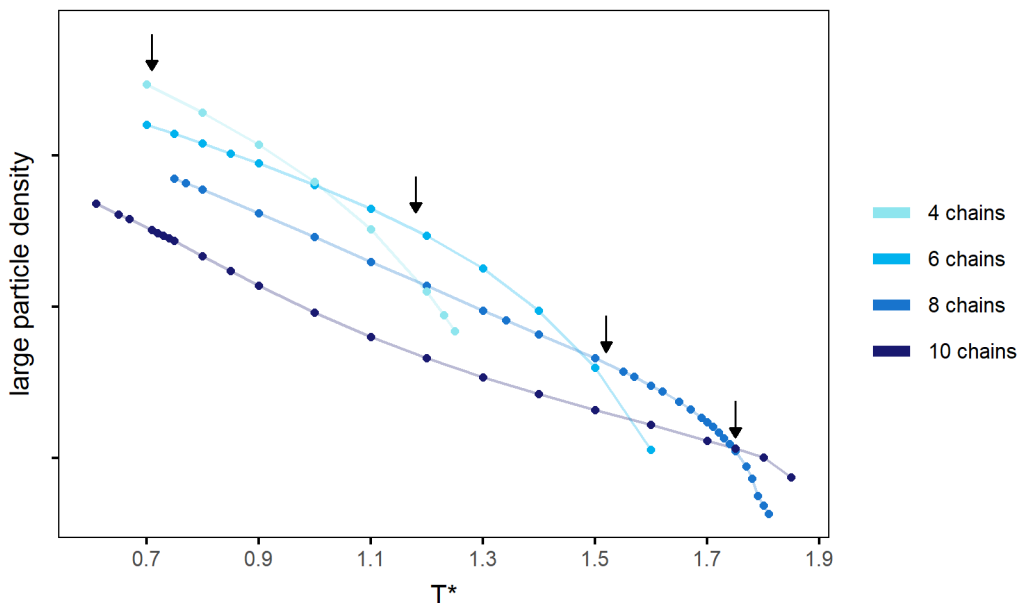


Figure A.3. Lattice density ($1/a^3$) for different cases, as a function of temperature.

This version of T_{deloc} has consistently shown to correlate well with the onset of non-linear behavior of physical and thermodynamical properties as seen in Figure 4 and Figure A.3.

A.0.3. Calculation of occupied volume

The parameter ϕ_{occupied} was inspired by an attribute of delocalization given by the spatial extent of π electrons in aromatic compounds. In these molecules, atomic orbitals conjoin to form hybrid orbitals that span over a carbon based ring backbone. We calculated the volume occupied by the top 70% of small particles' probability in the entire crystal for every simulation, as a fraction of the volume available to the small particles. To do so, we used voxels with side length equal to the diameter of the small particle centers and calculated the small particle centers' probability density distribution (normalized

visitation frequency) for each voxel over all production simulation frames. Then, we ordered the voxels by that probability and summed the probability associated with the first (highest probability) voxels until we reached 0.7. Then, we totaled the volume of all those voxels. Finally, we divided the resulting volume by the available volume, which is the total simulation box volume minus the total volume of the large particles. The resulting fraction is ϕ_{occupied} .

To determine the stability of this metric, we calculated ϕ_{occupied} using different voxel sizes and cutoff values. Occupied volume values using voxel sizes smaller than the diameter of the small particle did not converge with number of frames while the others did. It is understandable for smaller voxels to converge slower than larger ones given that sampling is greatly reduced (by $\sim \delta l^3$, where δl is the difference of side length between different size voxels). This can be corrected with longer simulation times for increased sampling but, that would likely not change the trend obtained with slightly larger voxels. However, it is important to note that using different voxel sizes gives different occupied volume values that vary proportional to the voxel size; bigger voxels equal greater occupied volume values. Thus, this method of calculating ϕ_{occupied} is qualitative, rather than quantitative: changing voxel size does not change the behavior of ϕ_{occupied} with temperature, but it does change the overall value. Larger voxels greatly coarsen space and thus we chose to use voxels that reflect the dimensions of the species under question, meaning side lengths close to the diameter of the small particle. Any value approximating the latter length should all give occupied volume values with similar exponential behavior upon the onset of delocalization.

A.0.4. Calculation of the specific heat c_p

We calculated the specific heat per particle using:

$$(A.2) \quad c_p = \frac{1}{N} \frac{\langle H^2 \rangle - \langle H \rangle^2}{k_B T^2} \quad \text{where, } \langle H \rangle = \langle U \rangle + P \langle V \rangle.$$

The $\langle \cdot \rangle$ operator signifies an ensemble average. In order to calculate the average internal energy, $\langle U \rangle$, of a system, we took into account all known energy contributions of all particles within it, *i.e.* all forms of potential energy (excluded volume interactions and Gaussian bond potentials) and kinetic energy, both translational and rotational. We also calculated c_p employing thermodynamic principles, which should result in the same values if the system is sufficiently large:

$$(A.3) \quad c_p = \frac{1}{N} \left(\frac{\partial \langle H \rangle}{\partial T} \right)_{N,P}.$$

We used cubic spline fitting for $\langle H \rangle$ and calculated its derivative. Both methods give similar results for the unconstrained simulations but they are not identical. A large amount of data is needed to obtain smooth curves from Equation A.2 but they appear to be converging to those values obtained by Equation A.3 for the unconstrained simulations. Additionally, given that the kinetic energy scales linearly with temperature and particle velocity distributions follow that of Maxwell-Boltzmann, we neglected kinetic energy contributions to the internal energy and observed no qualitative change in c_p curves. Therefore, we report c_p curves obtained by Equation A.3 without the kinetic energy contribution to the internal energy for the unconstrained simulations. For the fixed lattice simulations we only employed Equation A.2 to calculate c_p because $\langle H \rangle$ for both sets of

simulations are almost identical and Equation A.3 will not reflect the reduction in energy modes due to fixing the lattice.

A.0.5. Evolution of the number of interacting particles as a function of temperature

Here we show the average number of unique large particles interacting with each the small particle as a function of temperature. The small particles occupy the BCC tetrahedral sites and are functionalized with identically sized chains. Therefore, they must interact with at most four unique large particles at any temperature even when delocalized. Figure A.4 shows that indeed the maximum number of unique large particles interacting with a small one is four for every system. But at temperatures above T_{deloc} , there is a non-negligible fraction of small particles interacting with a lesser amount. This is expected as this parameter is closely related to delocalization. The close relation between delocalization and the ratio of unique interacting large particles to small particles is heightened by both showing continuous behaviour during delocalization. Additionally, Figure A.4 evidences the seeping of probability between nearest neighbor tetrahedral sites without the visitation to other sublattice sites, *e.g.* octahedral (6b Wyckoff positions) sites, which is also clear from Figure 3 and Figure 6.

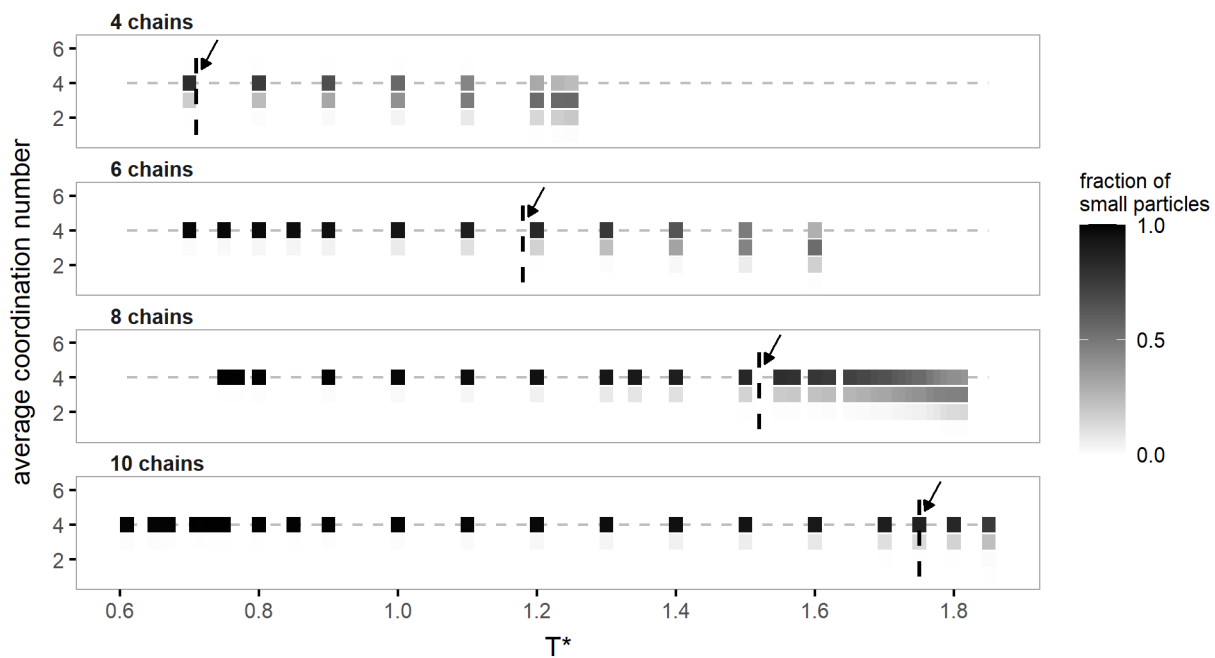


Figure A.4. Distribution of number of large particles interacting with each small particle. The horizontal grey dotted lines indicate interactions with 4 large particles, which is expected for a small particle that is localized at a BCC tetrahedral site. An estimate of T_{deloc} , the onset of delocalization, is marked with an arrow and black dotted line for each system.

APPENDIX B

Supplementary information for Chapter 4

This appendix contains the supplementary information associated with Chapter 4.

The following was originally published in Physical Review Materials in 2021. It is reproduced here with permission of AUTHORS, and PUBLISHER.

Phase transitions in colloidal crystals with sublattice delocalization:

Supplementary Material

Ali Ehlen,* Hector Lopez-Rios,* Monica Olvera de la Cruz

* equally contributing first authors

Reprinted with permission from:

Physical Review Materials 2021, **5**, 115601, DOI: 10.1103/PhysRevMaterials.5.115601

[https://journals.aps.org/prmaterials/abstract/10.1103/](https://journals.aps.org/prmaterials/abstract/10.1103/PhysRevMaterials.5.115601)

PhysRevMaterials. 5. 115601

B.1. Supplementary details on phase diagrams and simulation methods

B.1.1. More detailed simulation methods

More details on annealing, initializing with different configurations and system sizes, and determining crystal type

The majority of points on the phase diagram were simulated using more than one initial configuration. This was done to ascertain the system configuration for production which was later analyzed. Two main initial configurations were used, FCC and BCC. Both configurations began with a lattice parameter of 70σ which is always at least 3 times larger than any stable crystal lattice parameter obtained. With such a large initial lattice parameter, we expect that the equilibrium configuration of each simulation should not be affected or limited given their initial configuration. Therefore, we can assume simulations with different initial configurations, but same physical parameters, are effectively simulations of different system sizes, for example, simulations initialized as a FCC crystal will have two times the number of particles as those initialized as a BCC.

We implemented an annealing protocol for certain kinetically jammed simulations, and for situations in which multiple runs with the same parameter set resulted in different crystals (*i.e.* one initialized as an BCC and the other initialized as an FCC). In the cases where there was initial conflicting information about what the equilibrium lattice was, we annealed both until both simulations resulted in the same lattice. This was also true for systems exhibiting two-phase coexistence. If the percent of the box identified as BCC and FCC (using techniques described in the next section) were vastly different for runs, we also annealed both simulations to test whether they would converge to similar values. They did, and we did not use final values unless all simulations run under the same temperature, $n_s:n_l$, and number of chains per small particle agreed.

Most simulations that required annealing were systems with low composition. As described in the main text, the small particles interact with more large particles at lower small to large particle number ratios. This consequently drives the formation of denser crystals which are prone to kinetically trapped configurations. Different flavors of annealing protocols were employed, but all consisted in raising and lowering the heat bath's temperature albeit in different manners. The temperature ramps followed either an exponentially decaying sinusoidal, a square wave or a sequence of step functions of decreasing value. Additionally, larger simulation systems required higher maximum temperatures for their temperature ramp than smaller simulation sizes. In very unusual cases, only three points of the phase diagram, a barostat ramp was employed followed by a temperature ramp to verify the crystal's stability.

To determine crystal type resulting from a simulation, we analyzed the pair correlation function $g(r)$ of the large particles. The ratios of distances to peaks and relative peak

heights are unique for different crystal types (SC, BCC, FCC, *etc.*). Pair correlation functions were calculated using VMD [125] (without periodic boundary conditions because VMD's tool does not calculate $g(r)$ with periodic boundary conditions in simulation boxes that do not have right angles) and compiled in an online tool we built ¹. If $g(r)$ peak ratios and relative heights matched a known crystal (for example, BCC), we classified the crystal. If not, we used the Python package `pymatgen` [162] to identify the symmetry of the lattice, then compared to online databases such as AFLOW ² [163, 164], and verified by independently reproducing the $g(r)$ using AFLOW parameters and the python package `freud`. For example, this is how we identified A20 and A_d crystals. Finally, if the lattice visually resembled a BCT, we used calculations in Mathematica to predict the most likely $g(r)$ peak ratios as a function of c/a (see the Supplementary Materials section on BCT lattice parameters). If peak ratios from simulation matched any predicted value of c/a , we verified by reproducing the $g(r)$ with these parameters using the `freud` library [252].

B.1.2. Calculations of compositions in the systems exhibiting two-phase co-existence

Polyhedral template matching (PTM) [253] as implemented in OVITO [254] version 3.4 was used to identify which phase particles belonged to. This identification method relies on comparing the distances and graph symmetries of neighboring particles of a central particle with those of a perfect candidate crystal called template. Given the lack of a cut-off distance to identify neighboring particles and the nature of the graph analysis between template and simulation points, this method is more robust against thermal

¹available at [aliehlen.github.io/phase_diagrams](https://github.com/aliehlen/phase_diagrams)

²<http://www.aflowlib.org/>

fluctuations than other lattice identification algorithms like adaptive common neighbor analysis. Although, like any identification algorithm, the minimization and low value of an objective function is what determines the likelihood of whether or not a set of points corresponds to a given phase. It is here where some uncertainty enters this scheme of identification because a bounding value must be considered for the objective function. Here the objective function is a root-mean-square-deviation (RMSD) between two sets of points. One set is obtained from simulation coordinates and the other corresponds to lattice points from a perfect crystal. Here we used a maximum RMSD value of 0.5.

Using PTM we calculated the arithmetic mean of the number of particles in a certain phase over at least 100 uncorrelated frames. We compared data between simulations of different sizes (systems initialized as BCCs and FCCs) and average phase values seemed to be statistically equivalent. This indicates that the average phase values reported are not entirely dependent on system size and physically meaningful.

B.2. Full structure detail: phase diagrams and comparison of energy landscapes and simulations

B.2.1. Full phase diagrams and lattice specification

Here, we include full information about the plotted phase diagrams, including lattice parameters of the various lower-symmetry crystals reported in this paper. This is shown in Fig. B.1. Note that one BCT parameter ratio is still undefined. Below are listed the lattice points and parameter sets for all types of lattice reported.

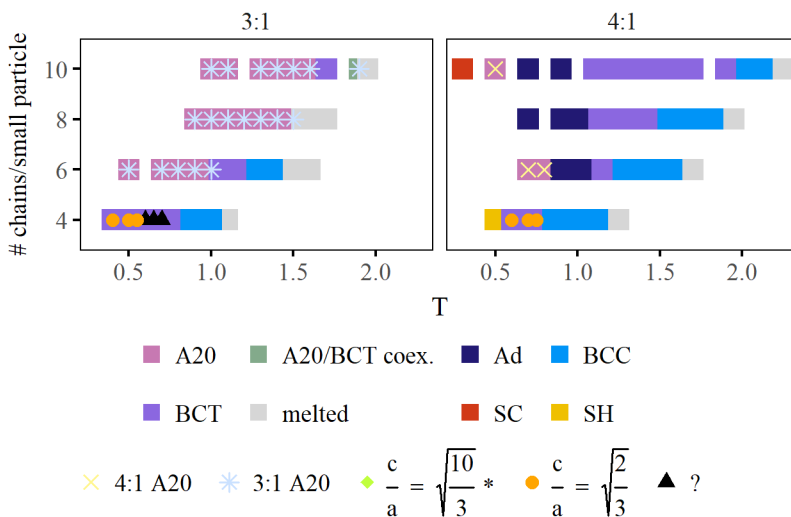


Figure B.1. Phase diagrams for the 3:1 and 4:1 composition systems, also shown in the main paper. These are superimposed with additional detail about the A20 and BCT crystal lattice parameters. Note that all unlabeled BCT points have $\frac{c}{a} = 2$. The parameters differentiating 3:1 A20 and 4:1 A20 crystals are defined in this section.

An interactive version of the phase diagrams, including plots of the pair correlation function of the large colloids in each lattice, can be found at https://aliehlen.github.io/phase_diagrams/.

A20: Orthorhombic, space group 63 (Cmcm)

Parameters: $a \neq b \neq c, y$

Parameter ratios observed: For A20 crystals observed in 3:1 systems, $b/a \sim 2.36$, $c/a \sim 1.44$, $y = 0.14$. For those in 4:1 systems, $b/a \sim 2.5$, $c/a \sim 1.4$ $y = 0.3613$

Basis points in $(\hat{x}, \hat{y}, \hat{z})$ basis:

$$\vec{a}_1 = (a, 0, 0)$$

$$\vec{a}_2 = (0, b, 0)$$

$$\vec{a}_3 = (0, 0, c)$$

Lattice points in $(\vec{a}_1, \vec{a}_2, \vec{a}_3)$ basis:

$$(0, y, 0.25)$$

$$(0, -y, 0.75)$$

$$(0.5, y - 0.5, 0.25)$$

$$(0.5, 0.5 - y, 0.75)$$

Primitive cell convention:

Basis points in $(\hat{x}, \hat{y}, \hat{z})$ basis:

$$\vec{a}_1 = (\frac{1}{2}, -\frac{1}{2}b, 0)$$

$$\vec{a}_2 = (\frac{1}{2}a, \frac{1}{2}b, 0)$$

$$\vec{a}_3 = (0, 0, c)$$

Lattice points in $(\vec{a}_1, \vec{a}_2, \vec{a}_3)$ basis:

$$(-y, y, 0.25)$$

$$(y, -y, 0.75)$$

A_d: Tetragonal, space group 129 (P4/nmm)

Parameters: $a = b \neq c, z$

Parameter ratios observed: $a = \sqrt{c}$. Various values of z between 0.4 and 0.5, increasing with higher temperature. When $z = 0.5$, this becomes identical to a BCT with $c'/a' = 2$.

Basis points in $(\hat{x}, \hat{y}, \hat{z})$ basis:

$$\vec{a}_1 = (a, 0, 0)$$

$$\vec{a}_2 = (0, a, 0)$$

$$\vec{a}_3 = (0, 0, c)$$

Lattice points in $(\vec{a}_1, \vec{a}_2, \vec{a}_3)$ basis:

$$\left(\frac{3}{4}, \frac{1}{4}, 0\right)$$

$$\left(\frac{1}{4}, \frac{3}{4}, 0\right)$$

$$\left(\frac{1}{4}, \frac{1}{4}, z\right)$$

$$\left(\frac{3}{4}, \frac{3}{4}, -z\right)$$

129a: Tetragonal, space group 129 (P4/nmm)

Parameters: $a = b \neq c, z$

Parameter ratios observed: $a = 0.94c, z = 0.3$. Note that this lattice is observed only once in our simulations, and this is in a low-temperature 5:1 system. It is visually similar to a BCC, but compressed in one direction in such a way that there are 10 interstitial sites instead of 12. It is also equivalent to an A_d without the first two lattice points.

Basis points in $(\hat{x}, \hat{y}, \hat{z})$ basis:

$$\vec{a}_1 = (a, 0, 0)$$

$$\vec{a}_2 = (0, a, 0)$$

$$\vec{a}_3 = (0, 0, c)$$

Lattice points in $(\vec{a}_1, \vec{a}_2, \vec{a}_3)$ basis:

$$\left(\frac{1}{4}, \frac{1}{4}, z\right)$$

$$\left(\frac{3}{4}, \frac{3}{4}, -z\right)$$

BCT: Tetragonal, space group 139 (I4/mmm)

Parameters: $a = b \neq c$

Parameter ratios observed: $c/a = 2$ (most common), $c/a = \sqrt{2/3}$, and one unclassified parameter set.

Basis points in $(\hat{x}, \hat{y}, \hat{z})$ basis:

$$\vec{a}_1 = (a, 0, 0)$$

$$\vec{a}_2 = (0, a, 0)$$

$$\vec{a}_3 = (0, 0, c)$$

Lattice points in $(\vec{a}_1, \vec{a}_2, \vec{a}_3)$ basis:

$$(0, 0, 0)$$

$$(0.5, 0.5, 0.5)$$

BCC: Cubic, space group 229 ($\text{Im}\bar{3}\text{m}$)

Parameters: $a = b = c$

Parameter ratios observed: N/A

Basis points in $(\hat{x}, \hat{y}, \hat{z})$ basis:

$$\vec{a}_1 = (a, 0, 0)$$

$$\vec{a}_2 = (0, a, 0)$$

$$\vec{a}_3 = (0, 0, a)$$

Lattice points in $(\vec{a}_1, \vec{a}_2, \vec{a}_3)$ basis:

$$(0, 0, 0)$$

$$(0.5, 0.5, 0.5)$$

FCC: Cubic, space group 225 ($\text{Fm}\bar{3}\text{m}$)

Parameters: $a = b = c$

Parameter ratios observed: N/A

Basis points in $(\hat{x}, \hat{y}, \hat{z})$ basis:

$$\vec{a}_1 = (a, 0, 0)$$

$$\vec{a}_2 = (0, a, 0)$$

$$\vec{a}_3 = (0, 0, a)$$

Lattice points in $(\vec{a}_1, \vec{a}_2, \vec{a}_3)$ basis:

$$(0, 0, 0)$$

$$(0.5, 0.5, 0)$$

$$(0.5, 0, 0.5)$$

$$(0, 0.5, 0.5)$$

B.2.2. Types of BCT lattices

The BCT crystals that we have observed have c/a ratios that lead to higher-symmetry arrangements. This can be seen in Fig. B.2. This means that the distance between distinct lattice points are equal. For example, for $c/a = \sqrt{2}$ (when a BCT structure is equivalent to an FCC structure), the distance from the $(0,0,0)$ point in a BCT unit cell to the adjacent corner (a) is equal to the distance to the point at the center of the unit cell ($\frac{1}{2}\sqrt{c^2 + 2a^2}$).

B.2.3. Identification of interstitial sites using unit cell energy landscape

We found that, with the exception of the FCC crystal, the potential energy landscape is a good predictor of the location of the small colloid species. The small particle cores localize at the near-neutral points in the energy landscape, while the interactive beads at the ends of their chains localize at or on the border of the energy wells (this is dependent on the reach of the chains). Here, we show direct comparisons between calculated energy

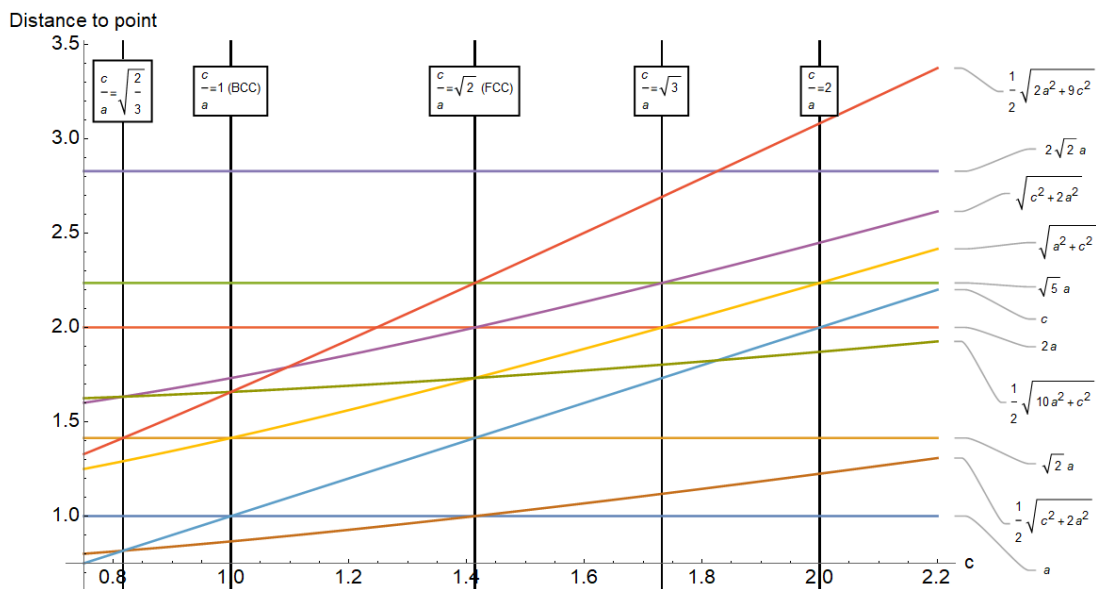


Figure B.2. For a value of $a = 1$, the distance from the point $(0, 0, 0)$ of a BCT unit cell to the 11 nearest points in the lattice, as a function of the value of c . Each line on the plot represents one lattice point. Higher symmetry points (where the lines cross *i.e.* where distances to multiple distinct lattice sites are equal) are highlighted with vertical black lines. These correspond to the c/a ratios seen in BCT lattices observed in this study.

landscapes and simulations results. It is difficult to adequately compare three dimensional structures in two dimensions, so we have included representative two-dimensional slices for each crystal type as an example in Table B.1. Mathematica notebooks showing three dimensional plots of the energy landscapes are available upon request.

B.3. Supplementary simulation results

B.3.1. Nearest neighbor plots for identifying lattices

As we have seen, the local spatial symmetry of the small particles varies as a function of the crystal phase, see Table B.1, this is to be expected. But if the sublattice is delocalized,

A20 (3:1): $\perp \vec{a}_3$		A20 (3:1): $\perp \frac{1}{2}\vec{a}_3$		A20 (4:1): $\perp \vec{a}_3$		A20 (4:1): $\perp \frac{1}{2}\vec{a}_3$	
Sim.	Theory	Sim.	Theory	Sim.	Theory	Sim.	Theory
A_d : $\perp \vec{a}_3$		A_d : $\perp \frac{1}{4}\vec{a}_3$		BCT: $\perp \vec{a}_3$		BCT: $\perp \frac{1}{2}\vec{a}_3$	
Sim.	Theory	Sim.	Theory	Sim.	Theory	Sim.	Theory
FCC: $\perp \frac{1}{8}\vec{a}_3$		FCC: $\perp \frac{3}{8}\vec{a}_3$		FCC: $\perp \frac{1}{4}\vec{a}_3^*$		Sim.	Theory
Sim.	Theory	Sim.	Theory	Sim.	Theory	<i>prob.</i>	$U_{pot.}$

Table B.1. Comparison between simulation results and theoretically calculated energy landscapes. Simulation: visitation frequency of the small particle centers from various simulations in a given slice of the unit cell. Theory: potential energy landscape of a single interactive chain end in the same slice of a unit cell of large particles, calculated using an average lattice parameter from simulation. All slices are taken parallel to the plane formed by \vec{a}_2 and \vec{a}_3 , and at the intersection with \vec{a}_3 indicated by \perp . Note the similarity between the regions of high probability in simulation to regions of near-zero potential energy. The 6:1 case can be found in [135]. *The tetrahedral sites shown here are only filled when the $n_s:n_l > 8:1$, *i.e.* once the 32f sites are full. The other FCC images depict 8:1 systems.

the small particles' coordination number to large particles must be different than when localized. This is due to their exploration of regions that are between their interstitial sites and should be smaller compared to when localized. Therefore, observing the coordination number distribution of the small particles is indicative of the crystal phase, see Figure B.3. Additionally, if there is a large percentage of coordination numbers that is smaller than for a localized sublattice of the same crystal phase, this is a good indication of sublattice delocalization. For example, we know that four is the coordination number of the small particles to large particles in a BCC lattice (hence, the tetrahedral interstitial site nomenclature), therefore, a significant percentage of lower coordination numbers would be indicative of a delocalized sublattice.

B.3.2. Anisotropy of vibrations in BCT lattices

The vibrations of BCT lattices are anisotropic, which can be seen in Fig. B.4. The x , y , and z directions are based on simulation and do not necessarily correspond to lattice directions. The important differences between BCT and other lattice types is that the majority of BCT lattices show vibrations that are not equal in all directions. We hypothesize that the vibrations in the BCT lattices are perpendicular to the (001) planes (direction of \vec{a}_3), because of the spacing in the BCT unit cell. Modeling a BCT ($c/a = 2$) with thermal noise that is larger in the \vec{a}_3 direction produces a pair correlation function that matches that of simulation.

According to the combination of Fig. B.4 and Fig. 4, when a crystal transforms from BCT to BCC, lattice vibrations become more isotropic and greater in magnitude, which is a component of the entropic favorability of the BCC lattice.

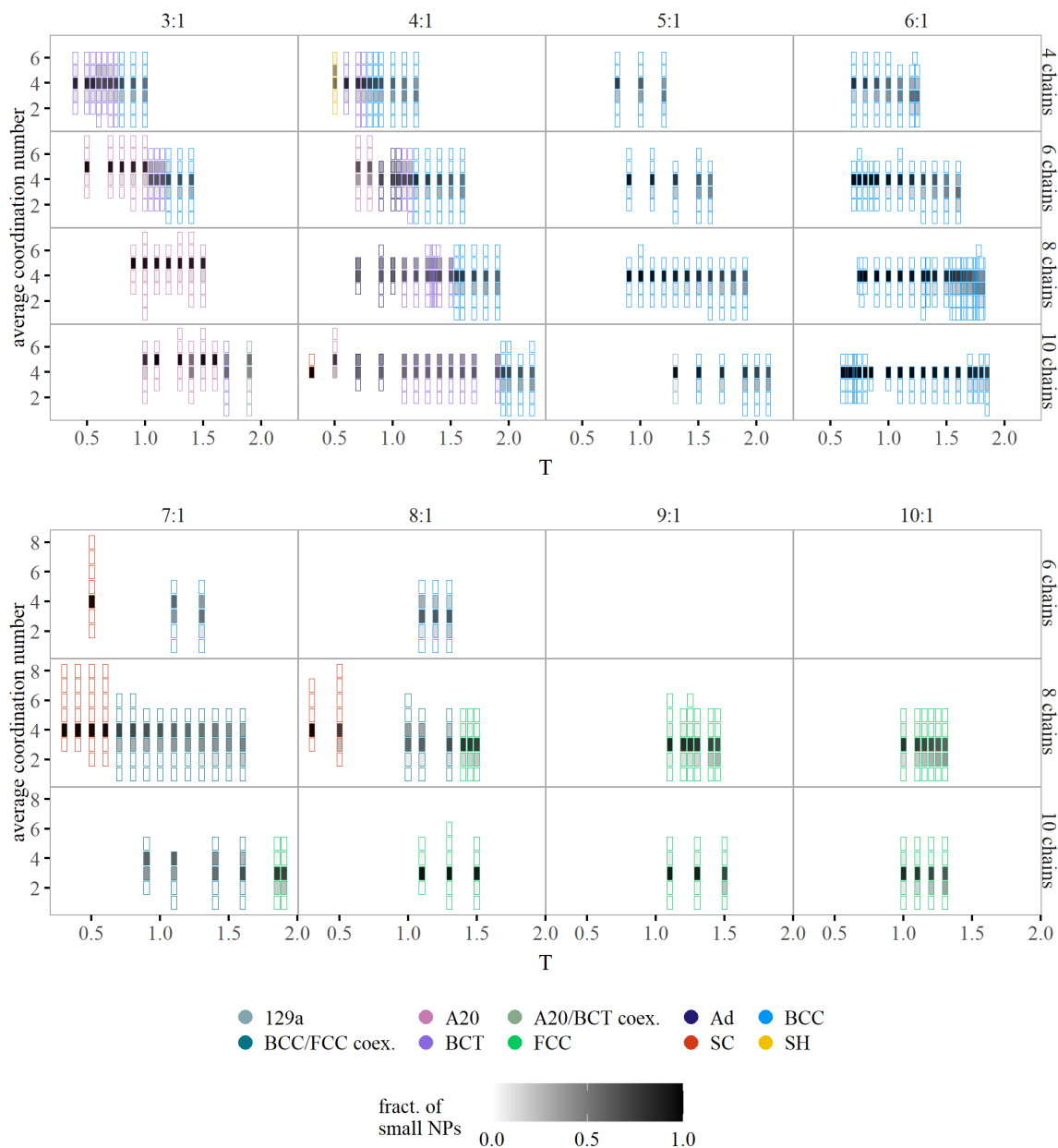


Figure B.3. Histograms of how many large particles each small particle is interacting with as a function of T , for all (non-melted) simulations used in this work. Colors indicate the lattice type. Each lattice type had a unique distribution, which tends toward lower numbers with increasing T . 6:1 data taken from [135] and included for comparison.

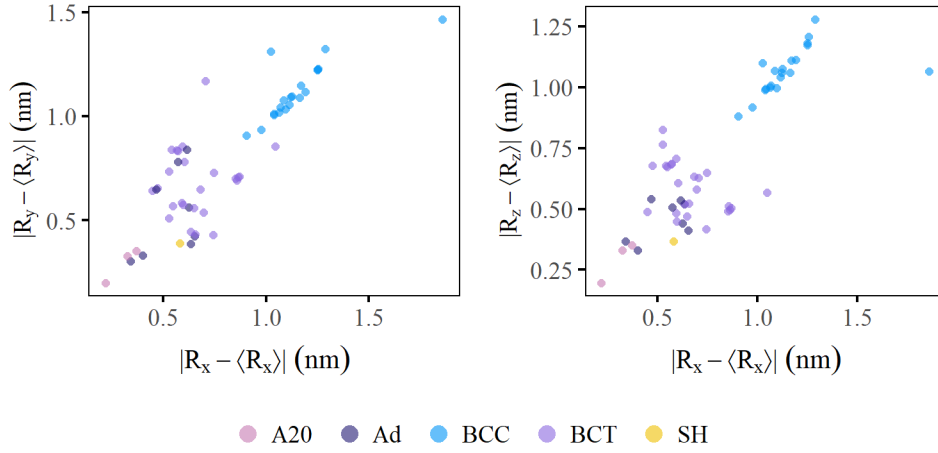


Figure B.4. Lattice vibration components for different types of lattices. Vibrations in BCC and A20 lattices are isotropic because all components are approximately equal. Vibration components of BCT crystals are not equal, indicating anisotropy. Different points correspond to different $n_s:n_l$ ratios, number of chains per small particle, and T .

B.3.3. Lattice density as a function of temperature

Plot of large particle number density (# large particles per volume) as a function of T , $n_s:n_l$, and number of chains per small particle. Density is a more useful metric for comparison than lattice parameter, because some crystal types are characterized by multiple lattice parameters.

B.3.4. Small particle chain end-to-end distance

End-to-end distance of the chains attached to the small particles. This decreases with temperature as chains explore more configurational space, and increases with number of chains per small particle because of excluded volume effects. The crystal lattice configuration also impacts the chain end-to-end distance, as can be seen in the small but consistent change in values between different crystal types.

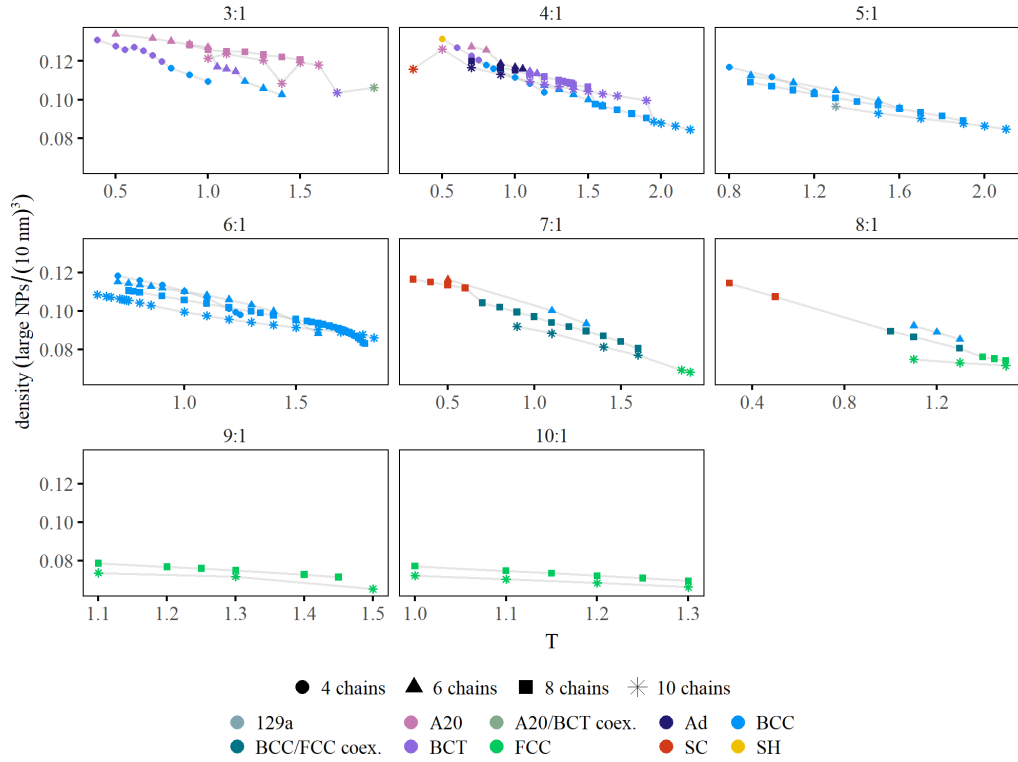


Figure B.5. Large particle number density of all (non-melted) simulations used in this work.

B.3.5. Vibrational Density of States

The vibrational density of states $D(\omega)$ is calculated by normalizing the real part of the Fourier transform of the velocity auto-correlation function (VACF) of the large particles [153]:

$$(B.1) \quad \text{VACF} = \frac{\langle \vec{v}(t) \cdot \vec{v}(0) \rangle}{\langle v^2(0) \rangle}$$

An approximate resolution of 37 ps is used for sampling data points for the construction of the VACF. In the left panel of Fig. B.7 we observe $D(\omega)$ for two different crystals. The left panel shows data for a 4:1 system with 8 grafted chains per small particle at

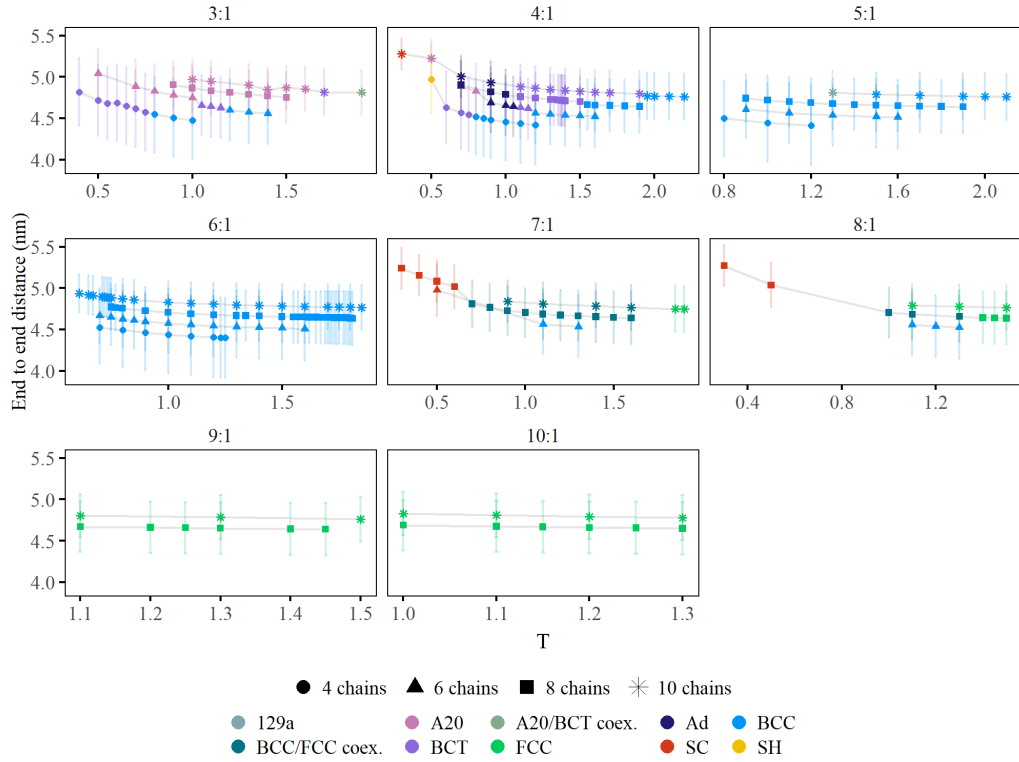


Figure B.6. Average end-to-end distance of the chains grafted on the small particles for all (non-melted) simulations used in this work.

$T = 1.3$ (blue curve, forms a BCT with a localized sublattice) and $T=1.7$ (red curve, forms a BCC with a delocalized sublattice). The lower temperature system has a more complex $D(\omega)$ than the higher temperature one. This is relevant given that a bias towards lower vibrational frequencies at higher T is also observed in the Peierls metallic-insulator transition of VO_2 [150].

The right panel of Fig. B.7 shows $D(\omega)$ for a 6:1 system with 8 grafted chains per small particle at $T = 1.3$ (blue curve, forms a BCC with a localized sublattice) and $T = 1.7$ (red curve, forms a BCC with a delocalized sublattice). There is little qualitative difference in the shape of $D(\omega)$ between two crystals with the same structure but different

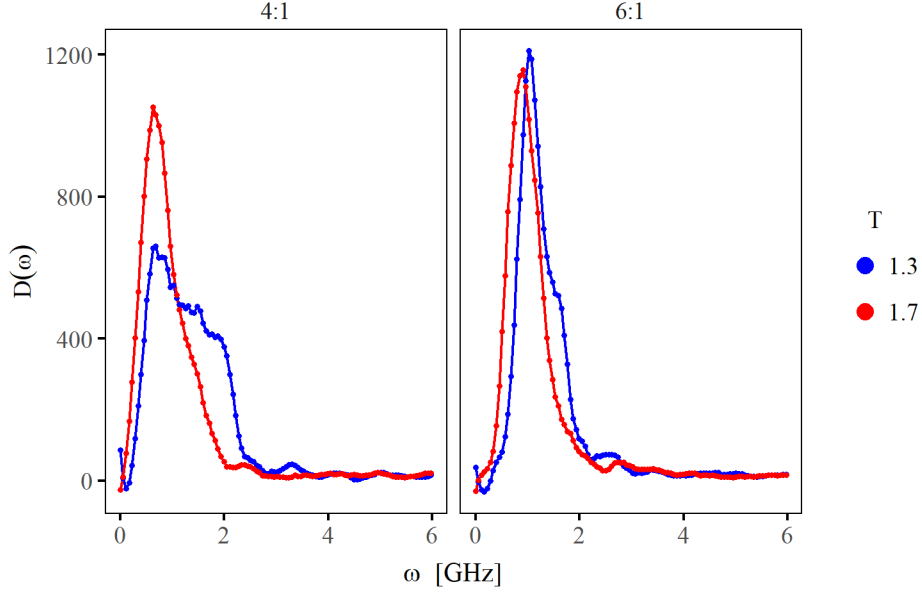


Figure B.7. Vibrational density of states for two systems that exhibit different sublattice transitions. The 4:1 system (left panel) with 8 grafted chains per small particle exhibits a first order sublattice phase transition at which it forms a BCT lattice with a fixed sublattice at $T = 1.3$ and forms a BCC phase with a delocalized lattice at $T = 1.7$. A similar system but with a 6:1 ratio (right panel) remains a BCC lattice when its sublattice is localized at $T = 1.3$ (blue curve) and delocalized $T = 1.7$ (red curve)

degrees of sublattice delocalization, though there is a slight shift toward lower frequencies at higher temperature.

B.3.6. Vibrational Entropy

We calculate vibrational entropy S_{vib} using

$$(B.2) \quad S_{\text{vib}} = 3 \int_0^{\omega_{\text{max}}} d\omega D(\omega) [(n(\omega) + 1) \ln(n(\omega) + 1) - n(\omega) \ln(n(\omega))]$$

where $D(\omega)$ is the vibrational density of states and $n(\omega) = \frac{1}{e^{\frac{\hbar\omega}{k_B T}} - 1}$ is the Bose-Einstein occupation factor. We use a cutoff frequency of $\omega_{\text{max}} = 6$ GHz. This expression for S_{vib}

has been employed with a $D(\omega)$ obtained from either experimental measurements [150] or simulations [151].

B.3.7. Existence of crystals with grain boundaries at 7:1 $n_s : n_l$

As discussed in Section 4.2.2.3 of the main text, we observe the existence of grain boundaries in mostly BCC lattices for 7:1 systems with 8 and 10 grafted chains per small particle at low T . This is shown in Fig. B.8 where the left image corresponds to a mostly BCC lattice with a grain boundary in its diagonal, while the right image corresponds to its sublattice composed of small particles. Interestingly, we do not see the appearance of stable grain boundaries in 7:1 systems with 6 grafted chains per small particles, we posit this is due to the lower enthalpic effects of the small particles that prevents the growth of a stable grain boundary.

B.3.8. Momentum transfer of the lattice to neighboring small particles

In order to quantify the momentum coupling between the lattice and small particles for systems that exhibit a first order crystal phase transition, we calculated the velocity-cross correlation function [154–156]

$$\gamma(t) = \frac{\langle \vec{v}_{s,i}(t) \cdot \vec{v}_{l,j}(0) \rangle_R}{\sqrt{v_s^2(0)v_l^2(0)}}$$

where $\vec{v}_{s,i}$ is the velocity of the i -th small particle, $\vec{v}_{l,j}$ is the velocity of the j -th large particle and $\langle \cdot \rangle_R$ is a restricted ensemble average over pairs whose distance $r = \sqrt{\|\vec{r}_{s,i} - \vec{r}_{l,j}\|^2}$ is within a range R . In this work, we choose $R \in (0, 15.75)\sigma$ where σ is the simulation length unit. $\gamma(t)$ is then interpreted as the momentum imparted by a large particle to

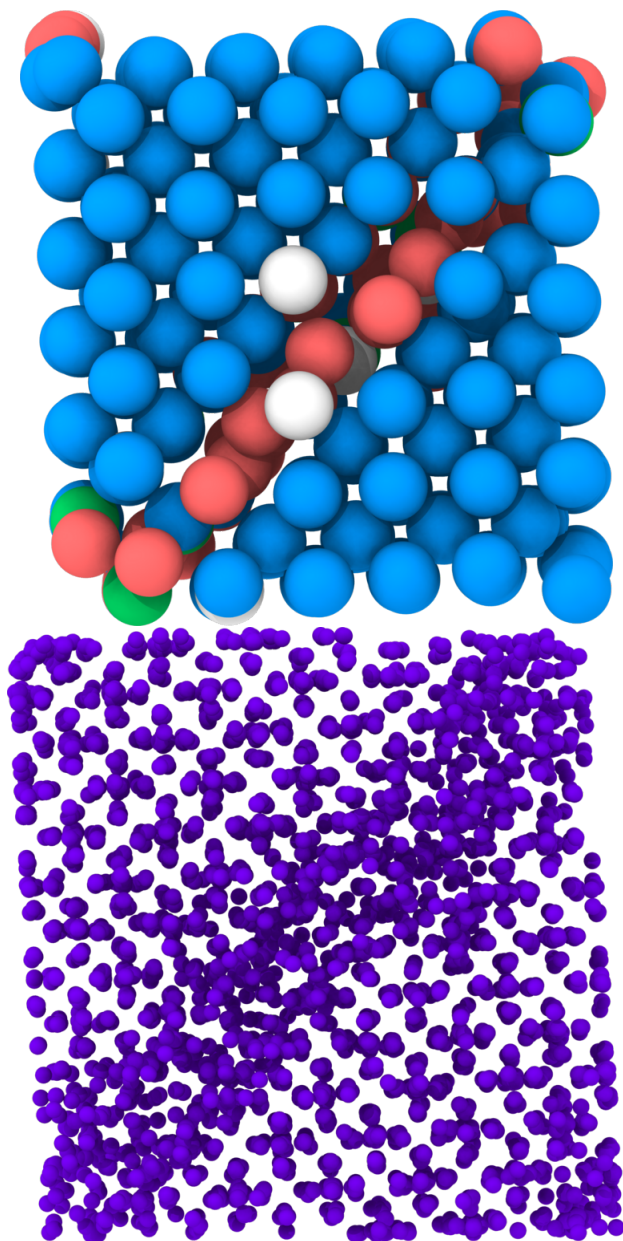


Figure B.8. Formation of grain boundaries in 7:1 systems with mostly a BCC lattice and 8 and 10 grafted chains per small particles at low T . The left image represents a snapshot of only the large particles where the color blue denotes a BCC lattice. The colors green, red, and white represent the HCP, FCC, and no lattice, respectively. The right image is the sublattice of the left image.

small particles within a sphere with radius 15.75σ , and a slower decay of the oscillations of $\gamma(t)$ signify a greater momentum exchange. In the left panel of Fig. B.9, we plot $\gamma(t)$ for a 4:1 mixture with 8 grafted chains on the small particles at two different temperatures. The system at $T = 1.3$ (blue curve) forms a BCT lattice with a localized sublattice, while at $T = 1.7$ (red curve) it has transitioned to a BCC crystal with a delocalized sublattice. Here we see a greater momentum exchange from the large particles to the small particles when the 4:1 system in the sublattice delocalized BCC phase, consistent with a Peierls insulator-metal transition. Meanwhile, for comparison to a system that does not exhibit a Peierls-like transition, the right panel shows $\gamma(t)$ for a 6:1 system with 8 grafted chains per small particles and for the same temperatures as the systems on the left. These crystals are both BCC lattices, but the sublattice is localized at lower T (blue curve) and delocalized at higher T (red curve). We observe no clear difference between the system with a localized sublattice and that with a delocalized one. This is contrasting to the 4:1 case, which had a first order sublattice transition.

B.3.9. Heat capacity c_P

We calculate the heat capacity c_P of all crystal phases using

$$(B.3) \quad c_P = \frac{1}{N} \left(\frac{\partial \langle H \rangle}{\partial T} \right)_{N,P} \approx \frac{1}{N} \frac{\Delta \langle H \rangle_{N,P}}{\Delta T}$$

Where N is the total number of particles in the system, H is the enthalpy of the system, T is the simulation temperature, and P is the simulation pressure. As indicated in Equation 3, we approximate the partial derivative of H with respect to T by calculating the ratio

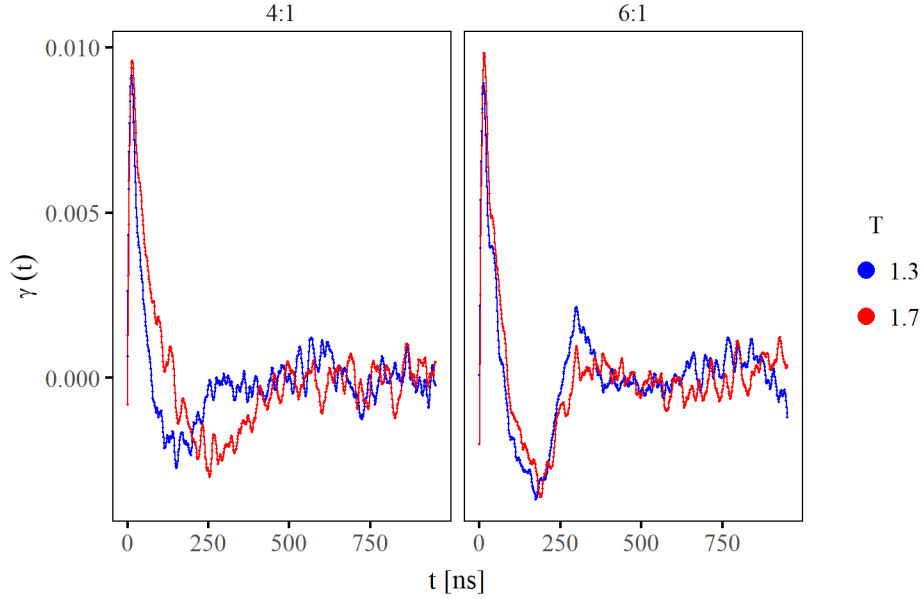


Figure B.9. Velocity cross-correlation function $\gamma(t)$ for a system that has a first order sublattice phase transition and another system that exhibits a continuous change from a localized to delocalized sublattice. The 4:1 system (right panel) with 8 grafted chains per small particle exhibits a first order sublattice phase transition at which it forms a BCT lattice with a fixed sublattice at $T = 1.3$ and forms a BCC phase with a delocalized lattice at $T = 1.7$. A similar system but with a 6:1 ratio (right panel) remains a BCC lattice when its sublattice is localized at $T = 1.3$ (blue curve) and delocalized $T = 1.7$ (red curve)

of differences of H and T between neighboring simulation points of identical physical parameters ordered sequentially by ascending simulation temperatures.

As indicated in the main text, a discontinuity in S indicates a first order phase transition, while the existence of an inflection point could indicate a continuous phase transition. We observe likely signatures of both behaviors in our system, as discussed in Section 4.2.2. of the main text. However, particularly since we are only estimating entropy using $S_{\text{vib.}}$, it is necessary to observe additional signatures within c_P to conclude which type of phase transition if any is present in these systems. To confirm the existence of a first order phase

transition, there must be an undefined point within c_P (corresponding to the discontinuity in S), while a discontinuity or divergence in c_P would be expected for a continuous phase transition. In simulations and in experiments, properly identifying a phase transition is a difficult task due to finite size effects and the amount of data needed to confirm such mathematical points. Our case is no different and thus we can only suggest the presence of these points given a combination of a qualitative understanding of our system, physical arguments by those such as Landau *et al.* [152], and observations in Fig. B.10 and Fig. B.11.

Fig. B.10(b) and Fig. B.11(b) show $S_{\text{vib.}}$, which appears to show a discontinuity at any transition from a non-cubic, localized lattice to a delocalized BCC lattice for systems with more than 4 chains per small particle, and a possible kink for systems with 4 chains per small particle. Fig. B.12 shows no change in lattice type and no such discontinuity in $S_{\text{vib.}}$. The plotted values of c_P show a spike at points of structural transition, indicated by a black circle. This indicates a first order phase transition, and by comparing interstitial and lattice sites and the argument of Landau *et al.*, we expect that for the transition BCT ($\frac{c}{a} = 2$) \rightarrow BCC. If this is the case, this spike should become an undefined point for larger system sizes and with much more dense data.

There are indications of small peaks or discontinuities at other transitions (BCT ($\frac{c}{a} = \sqrt{\frac{2}{3}}$) \rightarrow BCC, $A_d \rightarrow$ BCT ($\frac{c}{a} = 2$)). This may indicate the presence of a continuous phase transition, and with more data and by varying system size, we would be able to distinguish more precisely the behavior of c_P there.

In contrast, Fig. B.12 shows no crystal lattice transition at any temperature, and no peak in c_P . The change in slope of $S_{\text{vib.}}$ for the system with 10 chains per small particle

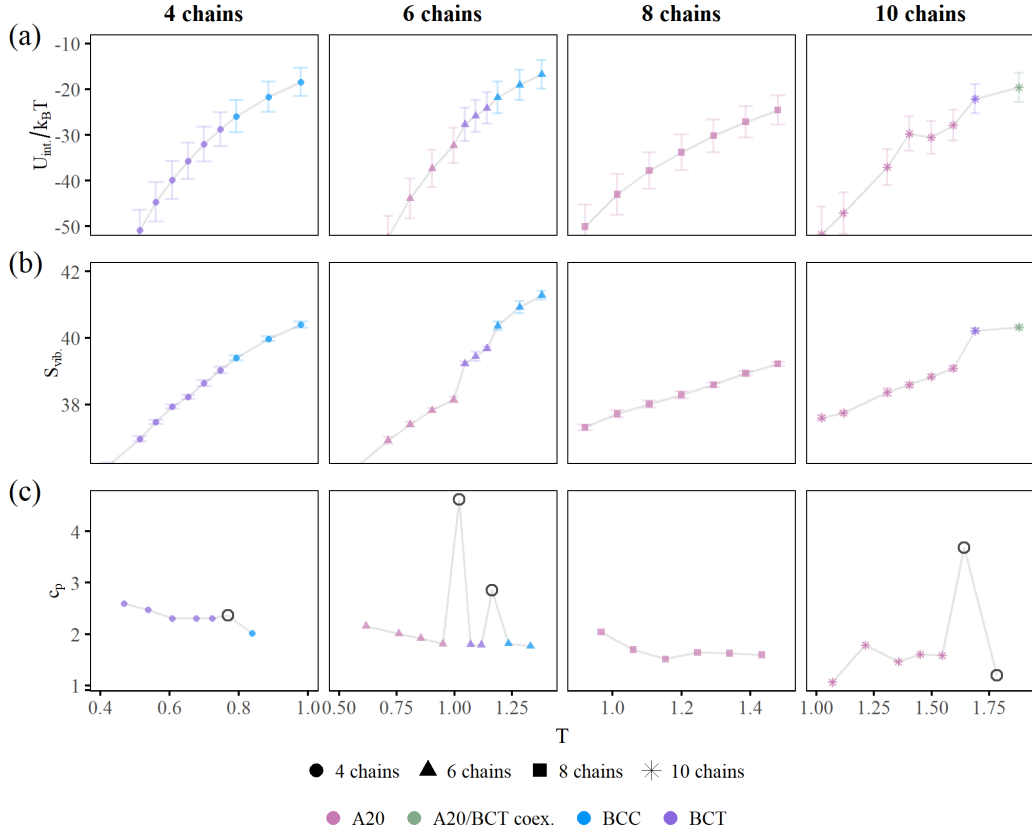


Figure B.10. Thermodynamic quantities of all stable crystal phases for particle number ratio 3:1 ($n_s : n_l$) as a function of simulation temperature. We plot the (a) average interaction energy per small particle $U_{\text{int}}/k_B T$, (b) lattice entropy S_{vib} , and (c) c_P , calculated as the slope between simulation points $j, j+1$ using $\frac{1}{N} \frac{H_{j+1} - H_j}{T_{j+1} - T_j}$, per Eq. (B.3). Hollow circles indicate points for which simulations j and $j+1$ resulted in different crystal types. We can see evidence for a first order phase transition for systems with greater than 4 chains. At region where there is a crystal phase transition, we see evidence for a discontinuity in the average interaction energy and lattice entropy, along with a peak in their c_P , indicative of a possible undefined point. For systems with 4 chains, we see evidence for a continuous phase transition in c_P , namely, a possible discontinuity between different crystal structures.

may indicate interesting behavior, but because this does not correspond to a transition to delocalization of the sublattice, it is out of the scope of this paper to explore this further.

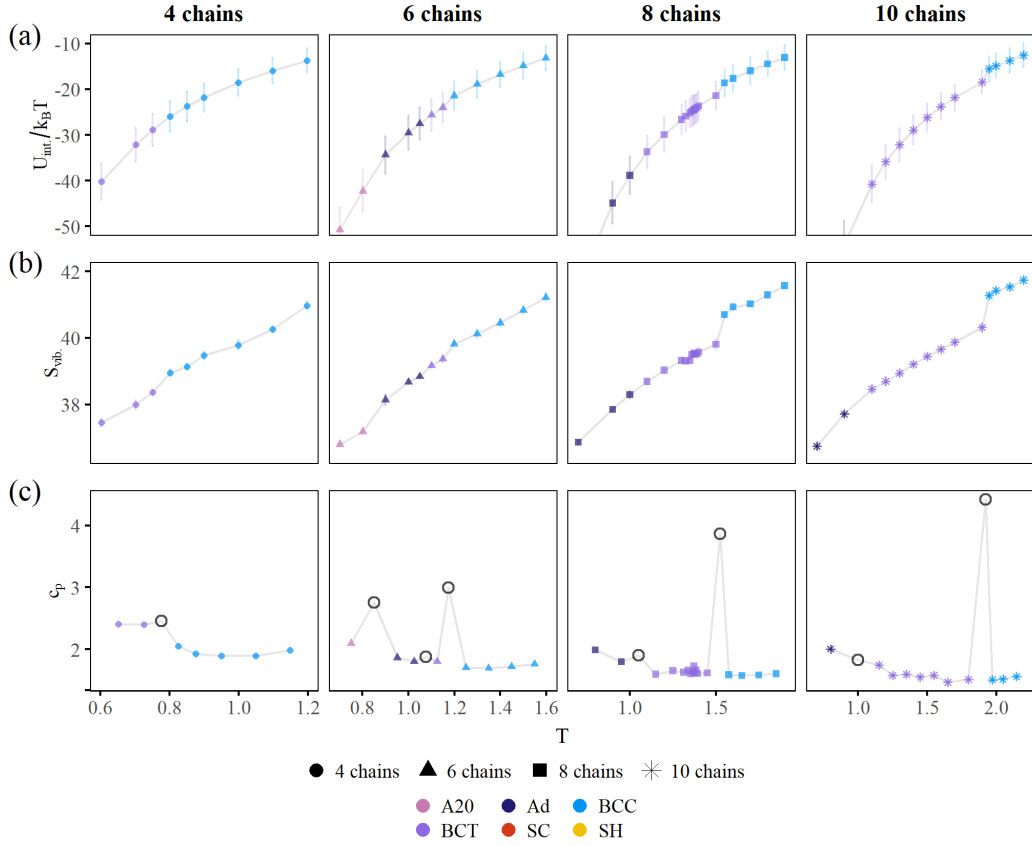


Figure B.11. Thermodynamic quantities of all stable crystal phases for particle number ratio 4:1 as a function of simulation temperature. We plot the (a) average interaction energy per small particle $U_{\text{int.}}/k_{\text{B}}T$, (b) lattice entropy $S_{\text{vib.}}$, and (c) c_P , calculated as the slope between simulation points $j, j + 1$ using $\frac{1}{N} \frac{H_{j+1} - H_j}{T_{j+1} - T_j}$, per Eq. (B.3). Hollow circles indicate points for which simulations j and $j + 1$ resulted in different crystal types. We can see evidence for a first order phase transition for systems with greater than 4 chains. At region where there is a crystal phase transition, we see evidence for a discontinuity in the average interaction energy and lattice entropy, along with a peak in their c_P , indicative of a possible divergence. For systems with 4 chains and for the $A_{\text{d}} \rightarrow \text{BCT}$ transitions, we see evidence for a continuous phase transition, namely, a possible discontinuity in c_P between different crystal structures.

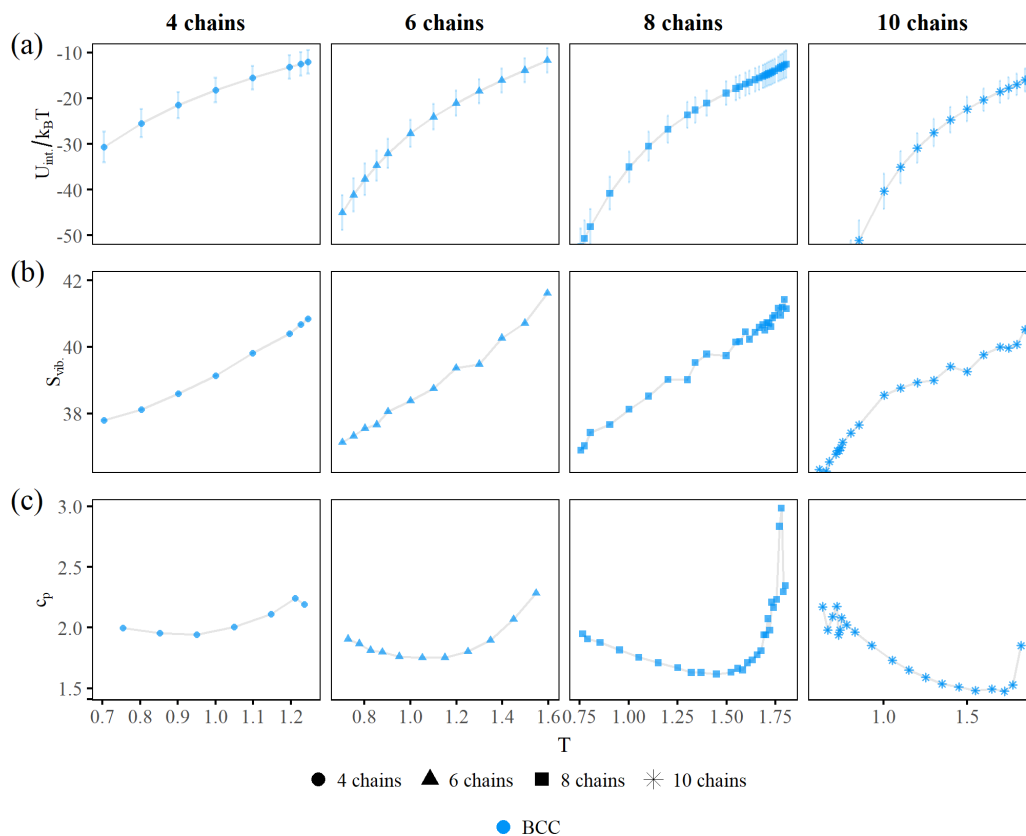


Figure B.12. Thermodynamic quantities of all stable crystal phases for particle number ratio 6:1 as a function of simulation temperature. We plot the (a) average interaction energy per small particle $U_{\text{int.}}/k_B T$, (b) lattice entropy $S_{\text{vib.}}$, and (c) c_P . Invariant of number of chains, we see no evidence for a any type of phase transition due to the continuous nature of all thermodynamic parameters plotted. The lack of hollow circles in c_P is also indicative of a lack of any phase transition occurring in these 6:1 systems.

APPENDIX C

Supplementary information for Chapter 6

This appendix contains the supplementary information associated with Chapter 6.

The following was originally published in Soft Matter in 2024. It is reproduced here with permission of AUTHORS, and PUBLISHER.

Restructuring a passive colloidal suspension using a rotationally driven particle

Shih-Yuan Chen,* Hector Manuel Lopez Rios,* Monica Olvera de la Cruz, Michelle M. Driscoll

* equally contributing first authors

Reproduced from [204] with permission from the Royal Society of Chemistry.

DOI: <https://doi.org/10.1039/D4SM00010B>

Supplementary Information

C.1. Microroller speed against rotational frequencies

We measure the microroller speed as a function of the applied rotational frequency. We carry the pattern experiments in the frequency range to which the speed is proportional to make sure that the applied torque is the dominant mechanism of the microroller translation.

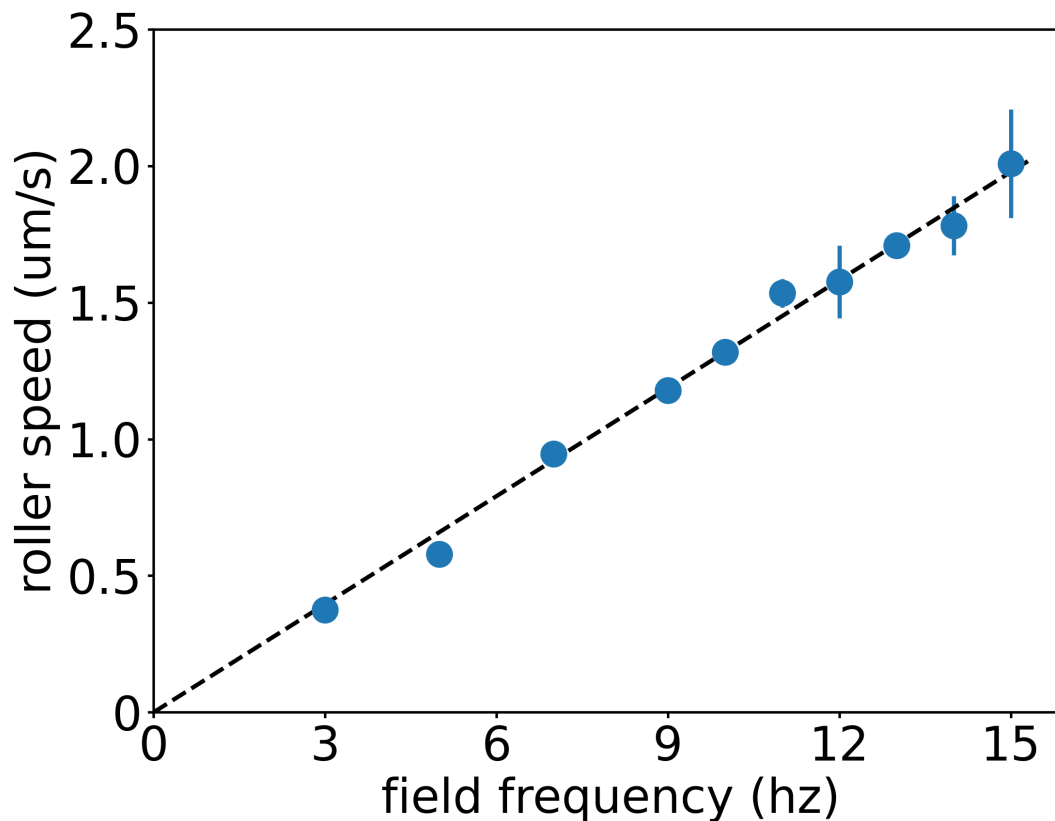


Figure C.1. **Microroller speed is proportional to the applied frequency.** We make a microroller water suspension with low concentration (few microrollers within the field of view), and apply a rotational magnetic field with a constant field strength (80 Gs) in a range of frequencies. Then, we measure the average speed of the microrollers and fit a straight line across the whole data set. The black dashed line shows the fitting result; the slope of the line is $0.13 \mu\text{m}$.

C.2. Microroller displacement in a passive suspension

Fig. C.2 shows the microroller displacement in a passive colloidal suspension with two rotational frequencies.

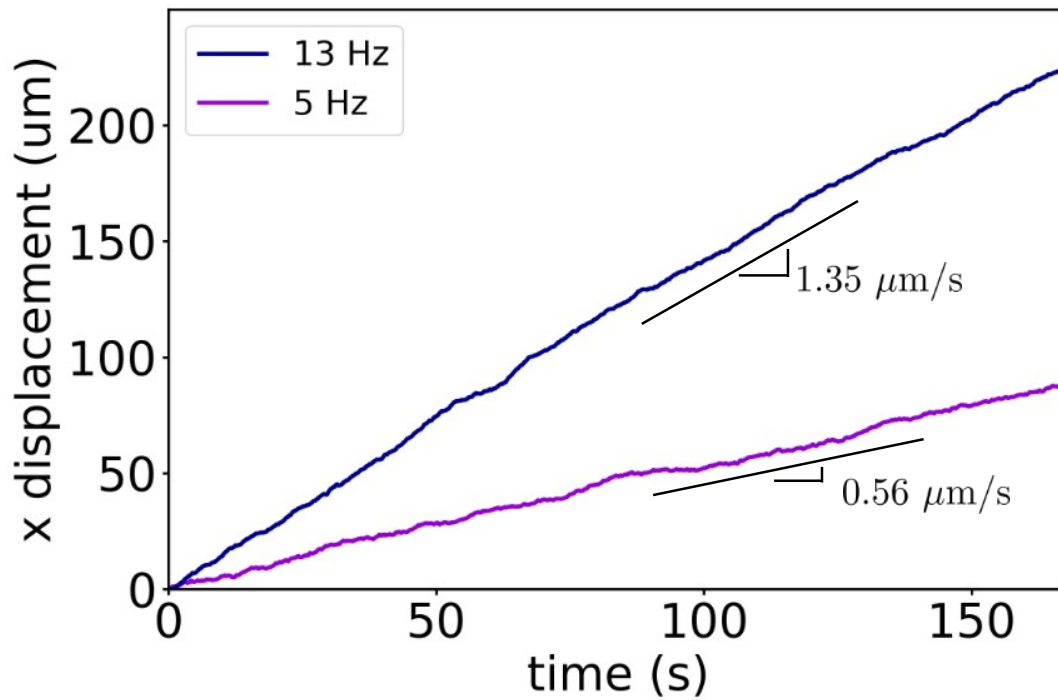


Figure C.2. **Microroller speed is constant in the colloidal suspension.** We track the displacement of a microroller in a suspension ($\phi_{area} = 0.16\%$) that is driven by two different frequencies. We find that the speed is constant and is again proportional to the rotational frequency.

C.3. Depletion region is affected by the mass of the passive particles

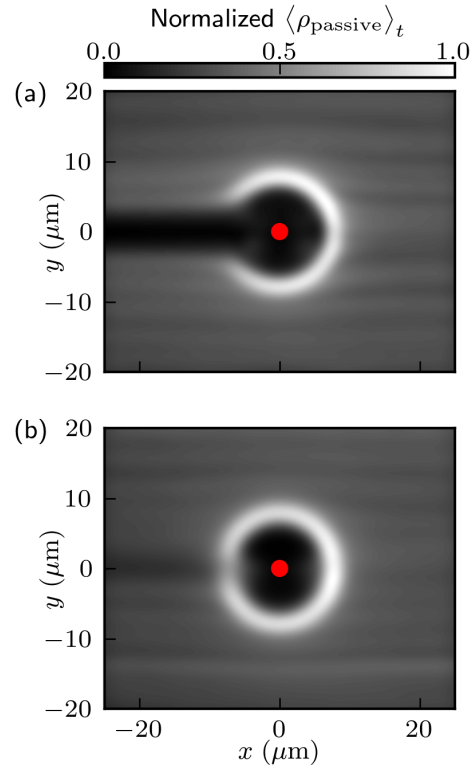


Figure C.3. **The depletion region is strongly affected by gravitational forces on the passive particles.** We performed two sets of simulations where we independently turn off near-field interactions and gravitational forces. In (a) we show the emergent pattern from simulations without near-field interactions between particles. The depletion region is unaffected by near-field interactions as it is still present in the pattern. Meanwhile, (b) is the emergent pattern from simulations with mass-less passive particles and observe that the depletion region is largely affected.

C.4. Supporting Tables

Parameter	Value	Units
Microroller radius	1.0×10^{-6}	m
Passive particle radius	1.0×10^{-6}	m
Microroller buoyant mass	3.1×10^{-15}	kg
Passive particle buoyant mass	2.5×10^{-16}	kg
Water viscosity	0.001	Pa s
ϵ_{cut}	2×10^{-21}	J
κ_{cut}	0.001×10^{-6}	m
Particle-particle $r_{\text{cutoff}}^{\text{Lubrication}}$	5×10^{-6}	m
Particle-particle $r_{\text{cutoff}}^{\text{Lubrication}}$	10^4	m
GMRES solver tolerance	10^{-6}	(dimensionless)
$\tau_{y \text{ max}}$	4.0×10^{-18}	N m

Table C.1. Parameters used in all simulations.

$\epsilon (10^{-18} J)$	$\kappa (\mu\text{m})$	height (μm)
0.0386	0.0756	1.212
0.0526	0.0816	1.246
0.029	0.29	1.339
0.06	0.17	1.415
0.06	0.21	1.467
0.08	0.19	1.498
0.12	0.21	1.615
0.19	0.22	1.734
0.29	0.23	1.853

Table C.2. Yukawa type potential parameters used in simulations to produce different microroller heights at $T = 0 \text{ K}$.

$\epsilon (10^{-18} J)$	$\kappa (\mu\text{m})$	height (μm)
0.00386	0.0756	1.229
0.00526	0.0816	1.266
0.0029	0.29	1.406
0.006	0.17	1.453
0.006	0.21	1.515
0.008	0.19	1.539
0.012	0.21	1.661
0.019	0.22	1.782
0.029	0.23	1.905

Table C.3. Yukawa type potential parameters used in simulations to produce different passive particle heights at $T = 0$ K.

$\epsilon (10^{-18} J)$	$\kappa (\mu\text{m})$	Average height (μm)
0.0386	0.0756	1.305 ± 0.143
0.0526	0.0816	1.335 ± 0.147
0.0346	0.1036	1.339 ± 0.158
0.029	0.29	1.394 ± 0.215

Table C.4. Yukawa type potential parameters used in simulations to produce different microroller heights at $T = 293$ K.

$\epsilon (10^{-18} J)$	$\kappa (\mu\text{m})$	Average height (μm)
0.00386	0.0756	1.964 ± 0.915
0.00526	0.0816	2.020 ± 0.939
0.00346	0.1036	1.973 ± 0.924
0.0029	0.29	2.1189103 ± 1.006

Table C.5. Yukawa type potential parameters used in simulations to produce different passive particle heights at $T = 293 \text{ K}$.